Computational Studies on the Mechanisms of Hydrogen Activation and Catalytic Hydrogenation by Cooperative Lewis Pairs

A Thesis

Submitted For the Degree of

DOCTOR OF PHILOSOPHY

in the Faculty of Science

by

Shubhajit Das

NEW CHEMISTRY UNIT
JAWAHARLAL NEHRU CENTRE FOR ADVANCED SCIENTIFIC RESEARCH
Bangalore – 560 064, India

SEPTEMBER 2018

To My Family

DECLARATION

I hereby declare that the matter embodied in the thesis entitled " **Computational Studies on the Mechanisms of Hydrogen Activation and Catalytic Hydrogenation by Cooperative Lewis Pairs**" is the result of investigations carried out by me at the New Chemistry Unit, Jawaharlal Nehru Centre for Advanced Scientific Research, Bangalore, India under the supervision of Prof. Swapan K Pati and that it has not been submitted elsewhere for the award of any degree or diploma.

In keeping with the general practice in reporting scientific observations, due acknowledgement has been made whenever the work described is based on the findings of other investigators. Any omission that might have occurred by oversight or error of judgement is regretted.

Shubhajit Das

CERTIFICATE

I hereby certify that the matter embodied in this thesis entitled " **Computational Studies on the Mechanisms of Hydrogen Activation and Catalytic Hydrogenation by Cooperative Lewis Pairs**" has been carried out by Mr. Shubhajit Das at the New Chemistry Unit, Jawaharlal Nehru Centre for Advanced Scientific Research, Bangalore, India under my supervision and that it has not been submitted elsewhere for the award of any degree or diploma.

Prof. Swapan K Pati
(Research Supervisor)

Acknowledgements

First and foremost, I would like to acknowledge my research supervisor Prof. Swapan K Pati for giving me an opportunity to explore the exciting research area of catalysis. I am thankful to him for his guidance, support, and encouragement throughout the journey of my Ph.D. career.

I convey my heartfelt gratitude to Prof. C. N. R. Rao for his vision of JNCASR. His presence & speeches are truly very inspiring.

I thank all my course instructors in JNCASR for the useful courses. I am very grateful to my excellent collaborators; Nagarjun, Suseela, Suman, Swadhin, Papri, Soumyabrata, Suman, Indranil, Narsina, Shiv, Rajarshi, Debdeep, Vivek, Prof. T. Govindaraju, Prof. Subi Jacob George, Prof. Sebastian C. Peter, Prof. Tapas Kumar Maji, Dr. Shabana Khan, Prof. H. W. Roesky, Dr. Jiten K Bera, and Dr. Anukul Jana. I would also like to thank all the faculty members of New Chemistry unit and Theoretical Sciences Unit.

I thank CSIR for fellowship. I sincerely acknowledge JNCASR for providing world-class research facilities. Especially, I thank all the academic, administrative, library, complab, mess, hostel staffs, and Dhanvantari for their support.

I am grateful to Anusooya ma'am and Sohan for all the support, love and affection.

I will take this opportunity to acknowledge all my past and present labmates; Pralok, Siam, Madhuri, Sharma, Pallavi, Dibyajyoti, Bradraj, Swastika, Arkamita, Somananda, Francesca, Abhiroop, Francesco, Monika, Silvia, Neha, Nisheal, Raju,

Madhulika, Pallavi, Asvini, Navamani, Sukanta, Ganesh, Sandhya, Srinivas, Supriti and Bidhan. Specifically, I want to thank Pralok and Arkamita for their help whenever required.

I thank all my football-buddies in JNC, and Nakul, Abhiroop and Madhulika for the musical endeavours.

A very special thanks to Anirban and Rajdeep for their delightful company. It's been a lot of fun with you two around.

I would like to thank my friend, philosopher and guide Amit, who also happens to be my elder brother. He will always be the one who I will look up to when the going gets tough. Thanks to Pallabi for being (patient!) with me and sharing all the moments of failure and success. Finally, I thank my parents, who have sacrificed so much and always provided the safety-net for me.

Abbreviations

DH	direct hydrogenation
TH	transfer hydrogenation
LA	Lewis acid
LB	Lewis base
TM	transition metal
THF	tetrahydrofuran
HOMO	highest occupied molecular orbital
LUMO	lowest unoccupied molecular orbital
FMO	frontier molecular orbital
FLP	frustrated Lewis pair
EC	encounter complex
BO	Born-Oppenheimer
DFT	density functional theory
Me	methyl
Et	ethyl
*n*Pr	n-propyl
*i*Pr	isopropyl
*n*Bu	n-butyl
*t*Bu	tert-butyl
Ph	phenyl

Bn	benzyl
Mes	mesityl
DABCO	1,4-diazabicyclo[2.2.2]octane
Col	collidine
BCF	$B(C_6F_5)_3$
DCB	1,2-dichlorobenzene
PES	potential energy surface
TS	transition state
IRC	intrinsic reaction coordinate
NPA	natural population analysis
NBO	natural bonding orbital
EDA	energy decomposition analysis
HDFE	hydride detachment free energy
ADFE	anion detachment free energy
FEHyAc	free energy of hydrogen activation
HyAcB	hydrogen activation barrier
FA	formic acid
HT	hydride transfer
PT	proton transfer
BAA	Brønsted acid activation
LAA	Lewis acid activation
DHR	dihydrogen release

Synopsis

Catalytic hydrogenation ranks among the most fundamental transformations in chemistry and finds broad applications at all scales of chemical production. Despite the existence of several well-established homogeneous and heterogeneous hydrogenation protocols, researchers continue to explore fresh and novel approaches to effect this important class of reaction. The past decade has witnessed the ability of the main group systems to catalyse hydrogenations, primarily, owing to the emergence of so-called frustrated Lewis pairs (FLPs). These are combinations of Lewis acids (LAs) and Lewis bases (LBs), which are sterically prevented from making any dative contact with each other. The cooperative action of these unquenched Lewis pairs allows activation of a wide range of chemical bonds featuring chemistry that has long been associated with transition metal compounds. Particularly interesting and relevant for the present thesis, is their ability to cleave hydrogen molecule (H_2) into proton and hydride (H^+/H^-) equivalents, which can subsequently be transferred from FLP to a suitable unsaturated substrate. In fact, the inclusion of these two steps into a catalytic cycle has led to the development of transition metal-free hydrogenation protocols for various polar and nonpolar organic substrates.

As with other branches in chemistry, development in catalysis also depends on the conceptual understanding of the underlying fundamental processes. Rational design of efficient FLP hydrogenation protocols requires a detailed knowledge of the mechanism of key reaction steps, central to which are H_2 activation and subsequent

hydrogen release. With this aim in mind, I have been involved in computational studies of a few recently reported catalytic hydrogenation processes, which are either directly FLP-mediated or relies heavily on the cooperative action between Lewis pairs. Based on quantum chemical calculations at various levels of density functional theory (DFT), we have been able to explore the relevant potential energy surfaces of these intriguing reactions. Gratifyingly, in a couple of studies, a thorough molecular-level understanding of the mechanism paved the way towards rational design of promising new candidates for potential catalytic applications.

The thesis is divided into following seven chapters.

Chapter 1 provides an introduction to the field of FLP chemistry with particular emphasis on the H_2 activation and the corresponding catalytic hydrogenation processes. A brief overview of the applied computational methodology is also included in this chapter.

In **Chapter 2**, we have explored the reaction mechanism of the metal-free $B(C_6F_5)_3$-catalysed hydrogenation of carbonyl compounds to the corresponding alcohols by DFT calculations. Possible reaction routes have been investigated in detail and the results provide solid support for the experimental observations. The critical role of the ether solvent, as an active participant in the hydrogenation process, is highlighted with the ether/borane Lewis pair shown to be involved in the heterolytic activation of H_2. The feasibility of an alternative direct hydrogenation route featuring carbonyl/borane-mediated H_2 cleavage has also been examined. We have also investigated the moisture sensitivity of the catalyst and possible decomposition routes. We found that the catalyst shows appreciable water-tolerance and that even in the presence of moisture, the hydrogenation proceeds through the same mechanism as that followed under anhydrous conditions.

In **Chapter 3**, the mechanism of H_2 activation by recently reported Sn/N Lewis pairs is unravelled using the representative $i\mathrm{Pr}_3\mathrm{SnOTf}$/DABCO combination. DFT computations provide evidence for weak intermolecular associations between LA and

LB, in which the counter-anion to cationic LA fragment plays a critical role. Two different encounter complexes (EC), in which the iPr$_3$SnOTf and DABCO units are held together by weak noncovalent interactions, are observed; an unprecedented counter-anion-mediated LA/LB association is characterised along with the trivial EC structure. H_2 activation in iPr$_3$SnOTf/DABCO Lewis pairs occurs through cooperative electron transfer processes involving the Sn/N centres. The present findings could provide a general mechanistic framework for H_2 activation by FLPs having an ion-pair LA component.

Chapter 4 describes a comprehensive DFT study on the mechanism of Sn/N FLP-catalysed hydrogenation of carbonyl compounds to corresponding alcohols. The reaction begins with a Sn/N FLP-mediated heterolytic cleavage of the H_2 molecule to release active hydrogens in solution. Our results reveal that, instead of the usual Brønsted acid activation, the carbonyl substrate is activated by LA-complexation, followed by subsequent hydride and proton delivery to complete the hydrogenation process. Additionally, we have also examined the feasibility of an autocatalytic pathway. The main feature of this reaction route is a Sn/O FLP-mediated H_2 cleavage, which has a comparable barrier to H_2 splitting by Sn/N FLPs. Overall, our computational mechanistic model is consistent with the experimental findings and the computed free energy barriers are in good agreement with the observed reactivity at experimental temperature. Insights obtained from this study are crucial for rational development of Sn-based FLP hydrogenation catalysts.

In **Chapter 5**, guided by the mechanistic understanding obtained in the previous two chapters, we have proposed a series of base-stabilized stannylium species (**1-R-X**) and computationally examined their reactivity towards H_2 activation. **1-R-X** exists as intramolecular Sn/N classical Lewis pairs in which the prospective LA/LB sites are found to be mutually quenched. Despite the adduct formation, **1-R-X** activates H_2 in the manner of FLPs. DFT computations reveals that H_2 activation by **1-R-X** proceeds through initial Sn-N bond elongation to provide an EC-like structure, which

permits the heterolytic cleavage of the H_2 molecule by cooperative action of the Sn and N centres. Our calculations reveal that the kinetics and thermodynamics of the H_2 activation step generally depends on the coordination strength of the counter-anion; weaker anion coordination leads to lower activation barrier as well as more exergonic reaction. Furthermore, the subsequent release of the active hydrogens to multiple bonds occurs in a concerted manner enabling hydrogenation of the corresponding unsaturated organic substrates.

In **Chapter 6**, with the aid of DFT calculations, we have elucidated the mechanism of the catalytic hydrogenation of CO_2 to formate using the recently reported dihydroxybipyridine-based Mn(I)-complex. Plausible catalytic pathways are unravelled thoroughly and the computational results account for the experimental findings. The critical roles of the external base additive and pendant oxygen ligands, as active participants in the hydrogenation process, are examined in detail. The overall mechanism includes two main steps; heterolytic dihydrogen cleavage and hydride transfer to CO_2 . The initial hydrogen splitting step is assisted by the external base. Pendant oxygen atoms take part neither in the hydrogen cleavage nor directly during the subsequent hydride transfer. Nevertheless, their presence is crucial for the hydrogenation reactivity of the catalyst as they have an indirect effect in determining the feasibility of the final hydride transfer step. Furthermore, guided by detailed mechanistic understanding, we have proposed a series of Mn(I)-complexes based on an acylmethylpyridinol ligand for catalysing the hydrogenation of CO_2 to formic acid.

Finally, **Chapter 7** provides the summary of the thesis in which some of the key features emerging out from our computational mechanistic models are discussed. It also contains future research directions regarding the possible extension of the works described in the previous chapters.

List of Publications

Publications related to thesis work

1. *"On the Mechanism of Frustrated Lewis Pair Catalysed Hydrogenation of Carbonyl Compounds"*

   Shubhajit Das, Swapan K Pati

   Chemistry-A European Journal, 2017, 23, 1078-1085

2. *"Mechanistic Insights into Hydrogen Activation by Frustrated N/Sn Lewis Pairs"*

   Shubhajit Das, Sukanta Mondal, Swapan K Pati

   Chemistry-A European Journal, 2018, 24 (11), 2575-2579

3. *"Unravelling the Mechanism of Tin-based Frustrated Lewis Pair Catalysed Hydrogenation of Carbonyl Compounds"*

   Shubhajit Das, Swapan K Pati

   Catalysis Science and Technology, 2018 DOI: 10.1039/C8CY01227J

4. *"Activation of Hydrogen and Hydrogenation Catalysis by Intramolecular Sn/N Lewis Pairs"*

   Shubhajit Das, Swapan K Pati

   (Submitted, 2018)

5. *"Mechanistic Insights into Catalytic CO_2 Hydrogenation using Mn(I)-complexes with Pendant Oxygen Ligands"*

Shubhajit Das, Swapan K Pati

Catalysis Science and Technology, 2018, 8, 3034-3043

Other publications by the author

6. *"Watson-Crick Base Pairing, Electronic and Photophysical Properties of Triazole Modified Adenine Analogues: A Computational Study"*

   Shubhajit Das, Pralok K Samanta, Swapan K Pati

   New Journal of Chemistry, 2015, 39 (12), 9249-9256

7. *"Computational Investigations on the Mechanism of Fluoride-Catalysed CO_2 Reduction to CO using Disilanes"*

   Shubhajit Das, Swapan K Pati

   (manuscript under preparation)

8. *"Sequence-Specific Recognition of DNA Minor Groove by an NIR-Fluorescence Switch-on Probe and its Potential Applications"*

   Nagarjun Narayanaswamy, **Shubhajit Das**, Pralok K Samanta, Khadija Banu, Guru Prasad Sharma, Neelima Mondal, Suman K Dhar, Swapan K Pati, T Govindaraju

   Nucleic Acids Research, 2015, 43 (18), 8651-8663

9. *"Imidazolyl-Naphthalenediimide-Based Threading Intercalators of DNA"*

   YV Suseela, **Shubhajit Das**, Swapan K Pati, T Govindaraju

   ChemBioChem, 2016, 17 (22), 2162-2171

10. *"Unique Approach to Copper-(I)-Silylene Chalcogenone Complexes"*

    Nasrina Parvin, Shiv Pal, Shabana Khan, **Shubhajit Das**, Swapan K. Pati, Herbert W. Roesky

    Inorganic Chemistry, 2017, 56 (3), 1706-1712

11. *"Cobalt-Based Coordination Polymer for Oxygen Reduction Reaction"*
Prabu Mani, Anjaiah Sheelam, **Shubhajit Das**, Guanxiong Wang, Vijay K Ramani, Kothandaraman Ramanujam, Swapan K Pati, Sukhendu Mandal
ACS Omega, 3 (4), 3830-3834

12. *"Neutral and Anionic Phosphate-Diester as Molecular Template for the Encapsulation of Water Dimer"*
Vivek Gupta, Debdeep Mandal, **Shubhajit Das**, Biswajit Santra, Ramakirushnan Suriya Narayanan, Nicolas Chrysochos, Carola Schulzke, Swapan K Pati, Vadapalli Chandrasekhar, Anukul Jana
(submitted, 2018)

13. *"Designed Synthesis of Donor-Acceptor Porous Organic Polymer Photocatalysts for Visible-Light Driven Hydrogen Evolution"*
Venkata M. Suresh, Papri Sutar, Parul Verma, **Shubhajit Das**, Swapan K Pati, Tapas Kumar Maji
(submitted, 2018)

14. *"N-Heterocyclic Germylene and Stannylene Catalyzed Selective Cyanosilylation and Hydroboration of Aldehydes"*
Rajarshi Dasgupta, **Shubhajit Das**, Swapan K Pati, Shabana Khan
(submitted, 2018)

15. *"Diphosphene acts Simultaneously as a Lewis Acid and a Lewis Base: NHC-Coordinated Diphosphene as a Precursors to Phosphinidenes and a Au(I)-Complex"*
Debabrata Dhara, **Shubhajit Das**, Pankaj Kalita, Ramakirushnan Suriya Narayanan, Swapan K Pati, David Scheschkewitz, Vadapalli Chandrasekhar, Anukul Jana
(manuscript under preparation)

16. *"The Role of Heterometallic Connectivity in Relative Activity of Decavanadate-based Hybrids for Electrocatalytic HER"*

    Soumyabrata Roy, Rajkumar Jana, **Shubhajit Das**, Saurav Ch Sarma, Sebastian C. Peter

    (manuscript under preparation)

17. *"Aqueous Phase Phosphorescence: Ambient Triplet Harvesting of Purely Organic Phosphors via Supramolecular Scaffolding"*

    Suman Kuila, K. Venkata Rao, Pralok K Samanta, **Shubhajit Das**, Swapan K Pati, M. Eswaramoorthy, Subi J George

    (manuscript under preparation)

18. *"Annulated aNHC-Ru Complex: A Highly Efficient Catalyst for Chemoselective Alkyne Semihydrogenation in Water"*

    Suman Yadav, Indranil Dutta, **Shubhajit Das**, Swapan K Pati, Jiten K Bera

    (manuscript under preparation)

Contents

List of Figures

List of Tables

Chapter 1

Introduction

1.1 H_2 activation and catalytic hydrogenation

Hydrogenation is one of the most fundamental transformations in chemistry, and its applications range from the chemical industry to laboratory scale organic synthesis [1]. The formal definition of hydrogenation includes the addition of hydrogens across an unsaturated chemical bond, usually in the presence of a catalyst. There are two strategies to effect hydrogenation; direct hydrogenation (DH) and transfer hydrogenation (TH). The latter requires a non-H_2 hydrogen source, often organic molecules, acting as the hydrogen donors. Some of the popular academic examples of TH include Birch reduction of arenes with sodium in ammonia [2], Meerwein-Ponndorf-Verley (MPV) reduction with sacrificial alcohols as hydrogen donors [3], hydride transfer from Hantszch ester [4], *etc.* Nevertheless, with respect to the reducing agents, all these reactions are stoichiometric and hence leads to the formation of an equivalent amount of waste. This renders such hydrogenations relatively ineffective for industrial applications. DHs, which utilize H_2 gas as the source of hydrogen, are comparatively more economical and atom-efficient. Since all investigated catalytic reactions in this thesis belong to DH, we will restrict our discussion to this particular class of hydrogenation.

DH has its genesis almost 100 years ago in the seminal works of Paul Sabatier

who achieved this transformation using H_2 pressure over finely divided metals [5]. These catalysts are essentially heterogeneous (reduced form of a metal or, metal deposited on a substrate), which are still frequently used in industry. Much later, in the 1960s, came homogeneous hydrogenation catalysts based on precious metals Ru, Rh, Ir *etc.*, enabling catalysis in solution. Homogeneous catalysis has its own set of advantages; (i) first of all, it involves well defined molecular complexes as catalysts, which can be monitored easily in solution (with suitable spectroscopic or computational techniques); (ii) it provides better chemoselectivity and enantioselectivity compared to its heterogeneous counterpart; (iii) the active sites are quite well-defined and can be readily optimized to obtain the desired reactivity (iv) the working conditions are often mild. This makes homogeneous hydrogenation catalysts particularly attractive in pharmaceuticals and food industry. An early example is the Wilkinson's Rhodium

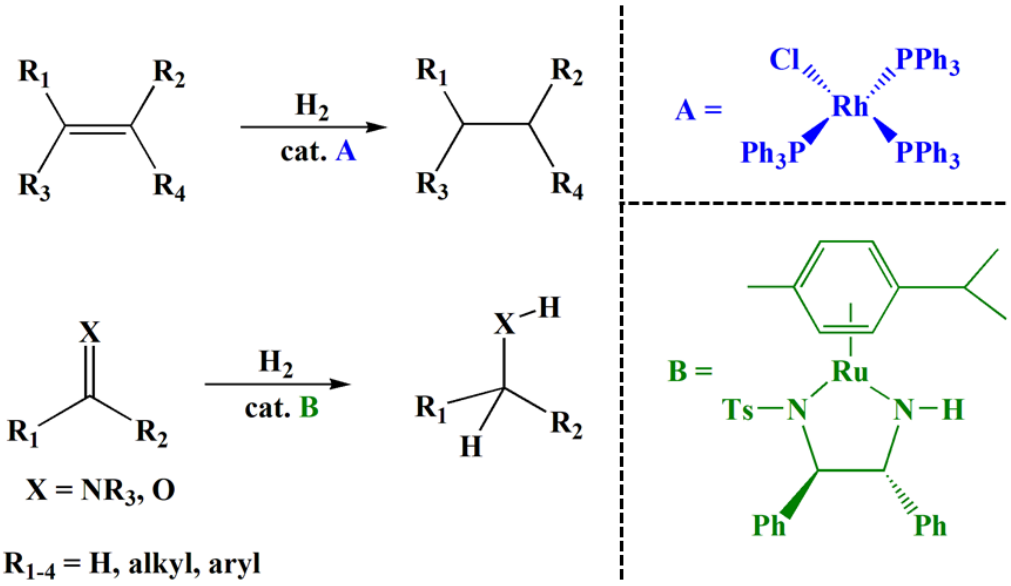

Figure 1.1: Examples of transition metal-catalysed hydrogenations.

catalyst for hydrogenation of olefins with molecular H_2 [6]. The catalyst is discovered in 1960s and still finds application in a wide range of hydrogenation processes. Apart from the applications, several studies on the Wilkinson's catalyst have immensely helped in the growth and development of organometallic catalysis. More recently, Noyori's Ru-based hydrogenation catalysts, which found much application in the

pharmaceutical industry, have enabled enantioselective hydrogenation of unsaturated polar substrates like carbonyls, imines, *etc* [7].

H_2 activation is at the heart of DH catalysis. Since molecular H_2 gas is used as the hydrogen source and under ambient conditions H_2 is not a reactive molecule, any catalytic DH process inherently relies on the step(s) of H_2 activation. Thus, systems that activate H_2 can potentially act as DH catalysts. In principle, these catalysts could be obtained by assembling elements from the entire periodic table. Unfortunately, as it stands, only a handful of chemical systems are capable of activating H_2 under mild conditions. Be it nature's or human-made, the majority of the H_2 activating systems are comprised of transition metal (TM) complexes. Their seemingly unique

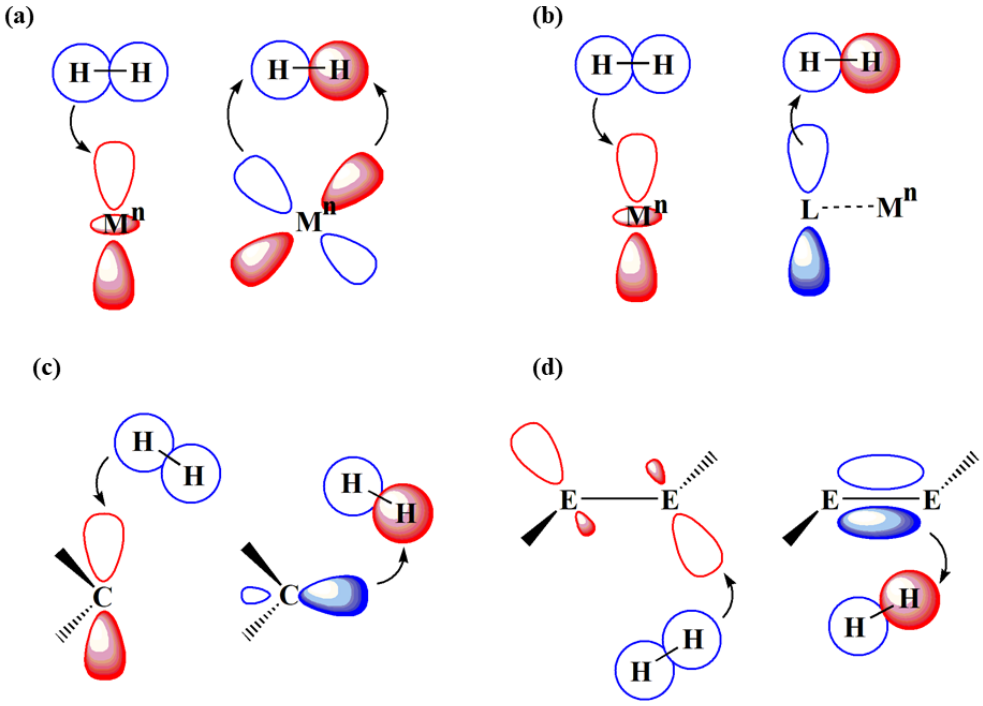

Figure 1.2: Frontier orbital model for various modes of H_2 activation. (a) Homolytic by transition metals. Heterolytic by (b) transition metals (c) singlet carbene, and (d) E_2Ar_2 (E= Ge, Sn) compounds. Occupied donor orbitals are shown in blue. Unoccupied acceptor orbitals are shown in red.

ability to effect H_2 activation is attributed to the presence of partially occupied d-shell featuring both empty and occupied frontier orbitals on the same centre within

a small energy window. Nevertheless, depending on the metal-ligand framework, several H_2 activation modes are reported in the literature, and some of these are depicted in Figure 1.2 [8, 9]. Ru and Ir hydrogenation catalysts often activate H_2 by oxidative addition to generate the corresponding metal dihydride along with a two-unit increment in the formal oxidation state of the TM centre [8, 10]. Two cooperative electron transfer (ET) processes featuring electron donation from the σ-bonding orbital of H_2 into an empty d-orbital and a back donation from a filled d-orbital into empty σ^*-antibonding orbital of H_2, lead to the homolytic cleavage of the H-H bond. Another possibility is the heterolytic cleavage of the H-H bond if a ligand (L) assists in the H_2 activation process. In that case, instead of a back donation from the metal centre, σ^*(H-H) accepts electrons coming from a filled ligand orbital. Therefore, H_2 cleavage occurs via the combination of TM$\leftarrow\sigma$(H-H) and L$\rightarrow\sigma^*$(H-H) cooperative ETs. This is typically observed in Ru-based catalysts or hydrogenase enzymes [8, 10, 11].

It can be readily envisaged that main group compounds featuring similar electronic configurations to TM complexes might also manifest identical reactivity towards H_2. The area of main group-mediated H_2 activation has received much attention lately with the ultimate goal of replacing the TMs in many important catalytic applications. This is particularly relevant for the cases in which the toxicity, cost, and abundance of precious TMs pose serious concerns. Carbenes are one such system having both an empty (p) and a filled orbital (sp^2) on the same carbon atom. As reported in the works of Bertrand *et al.* alkylamino carbenes are capable of activating H_2 in ambient temperature and pressure [12]. The mechanism is similar as that found in the oxidative addition of H_2 to a TM centre; the empty orbital and the lone pair of the carbene are involved in two ET processes with the σ(H-H) and σ^*(H-H) orbitals of the H_2 molecule. The other higher analogues of carbenes, such as (amido)(boryl)silylenes [13], diaryl germylenes [14], and diaryl stannylenes [15] are also found to engage in similar H_2 activation reactions. Another class of H_2 activating systems are the bent

relatives of acetylene, ArGeGeAr′ [16] and ArSnSnAr′ [17]. Again such reactivity is associated with the ET processes involving the frontier orbitals located on the unsaturated bond and H_2.

The recent years have witnessed a new player in the field of TM-free H_2 activation, the so-called frustrated Lewis pairs (FLPs). Pioneering works by Stephan *et al.* in 2007 showed that the cooperative action between sterically-crowded Lewis acid-base pairs leads to the heterolytic activation of H_2 molecule in the manner of TMs. Their remarkable ability to cleave molecular hydrogen played a pivotal role towards the developement of transition metal-free routes to catalytic hydrogenations, which was mostly considered to be a hypothetical area of research even a decade ago. Although the field was initially developed with a case-by-case basis, slowly the concept of FLPs is emerging as a new paradigm in chemistry. All the research works presented in this thesis are connected to the chemistry exhibited by FLPs. Therefore, in the next section, a detailed background on the key concepts of FLP chemistry is discussed.

1.2 Introduction to FLP chemistry

1.2.1 Historical context

Almost a century ago, Gilbert N. Lewis classified molecules in terms of their electron donating or accepting capabilities [18]. Molecules that behave as electron pair donors were termed as Lewis bases (LBs) while electron pair acceptors were referred to as Lewis acids (LAs). A simple combination of LA and LB usually neutralizes each other by forming strong dative adducts. This reactivity typically stems from an interaction between the lone pair of electrons in the high-lying highest occupied molecular orbital (HOMO) in the LBs and the low-lying lowest unoccupied molecular orbital (LUMO) in the LAs. In fact, not only adduct formation, any chemical reaction arising from the overlap between a filled doubly occupied orbital and an empty orbital can be, in principle, rationalized in terms of LA/LB interaction. Such reactions are abundant in much of the main group/TM-chemistry, and hence, the

concept of LA/LB is of fundamental significance in understanding chemical reactivity in general.

Since the formalization of the LA/LB concept, there have been occasional reports of systems showing that not all LA/LB combinations form adducts. One of the early examples includes the chemistry reported by Brown and co-workers in 1942. While examining the LA/LB interaction between pyridines and boranes, they found out that the combination of lutidine and BMe_3 failed to form a dative adduct [19]. This

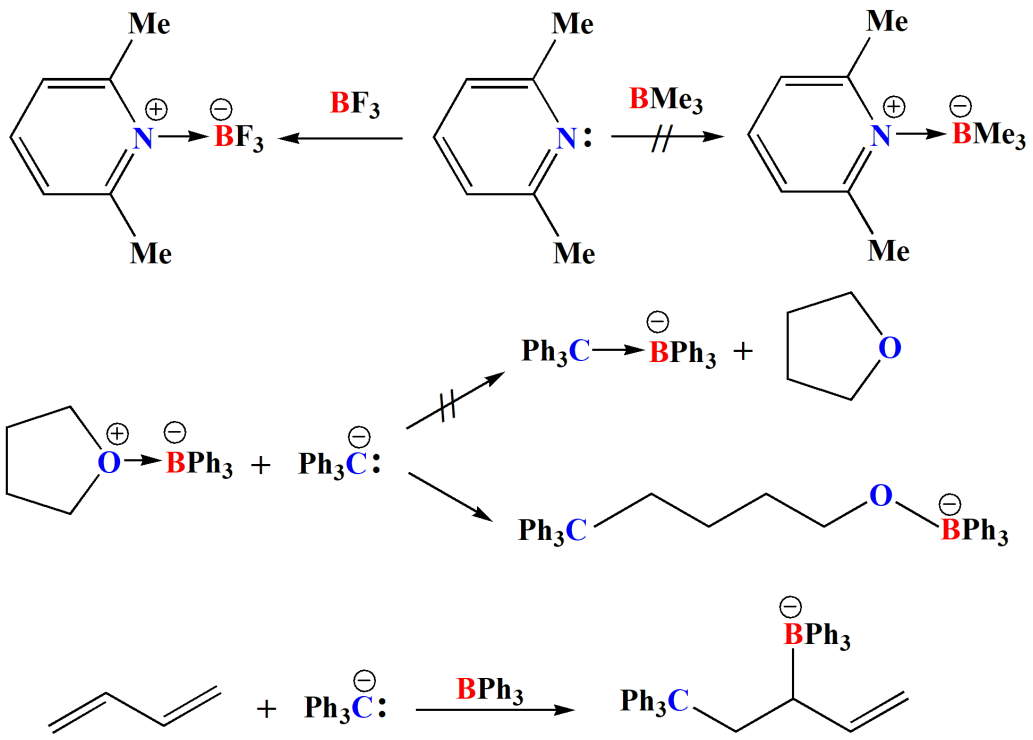

Figure 1.3: A few early examples of non-classical reactivity between sterically crowded Lewis acid and Lewis bases.

was contrasted with the observation that lutidine forms a dative adduct with BF_3 (see Figure 1.3) [19, 20]. The reason was thought to be steric congestion; the conflict between the *o*-methyl substituents in lutidine and methyl groups in BMe_3 prevented a dative interaction. Another example was provided by Wittig and co-workers who reported the reaction of Ph_3C anion with the tetrahydrofuran (THF)-adduct of BPh_3. They observed a ring opening reaction rather than the expected formation of BPh_3-Ph_3C adduct via displacement of THF; the reaction occurs at a sterically more

available carbon in comparison to the Lewis acidic boron centre [21]. More examples include Tochtermann's study on the polymerisation of butadiene in the presence of Ph_3C anion and LA BPh_3. Again, no classical adduct between BPh_3 and Ph_3C was observed. Instead, a trapping product was formed due to the 1,2-addition to butadiene [22]. These examples prove that the reactions involving bulky Lewis pairs are of special nature and often find alternative channels other than self-quenching/adduct formation.

1.2.2 Recognising FLP reactivity: H_2 activation

Early on, it was recognised that the Lewis pairs involved neither in adduct formation nor in alternative reactivity, could find interesting applications in chemistry. Moreover, tethering the LA and LB functional groups together in a single molecule gives rise to an ambiphilic environment, which could be exploited in TM-coordination chemistry as versatile ligands. In fact, several of such ambiphilic molecules are reported in the literature [23–25], and some of the examples are shown in Figure 1.4.

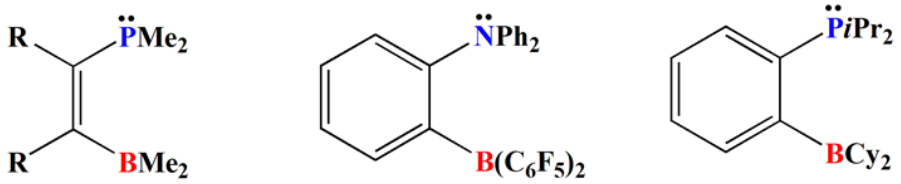

Figure 1.4: A few examples of ambiphilic molecules.

Pertaining to their interest in designing ambiphilic molecules in which the Lewis pairs are sterically prevented from adduct formation, the group of Douglas W. Stephan examined the reactivity of phosphine-borane compounds. A breakthrough discovery was made in 2006, when Stephan and co-workers synthesized a zwitterionic phosphonium hydridoborate, $[Mes_2PHC_6F_4BH(C_6F_5)_2]$, comprising of a protic hydrogen and a hydridic hydrogen in the same molecule [26]. Interestingly, when heated to 150 °C, it was found to release molecular H_2 gas, leading to the formation of $[Mes_2PC_6F_4B(C_6F_5)_2]$. Perhaps more striking was the observation that the

resulting phosphinoborane rapidly converts back to the original phosphonium hydridoborate when reacted to H_2 in room temperature. This represents an intramolecular phosphinborane-mediated heterolytic cleavage of H_2 molecule into a proton and a hydride equivalent, a reaction that is normally associated with TM chemistry. Subsequently, in 2007, Stephan and Welch demonstrated that the connection between the LA and LB fragments is not an essential criterion. H_2 cleavage is still possible with intermolecular phosphine/borane combination. The Lewis pair combination of tBu$_3$P

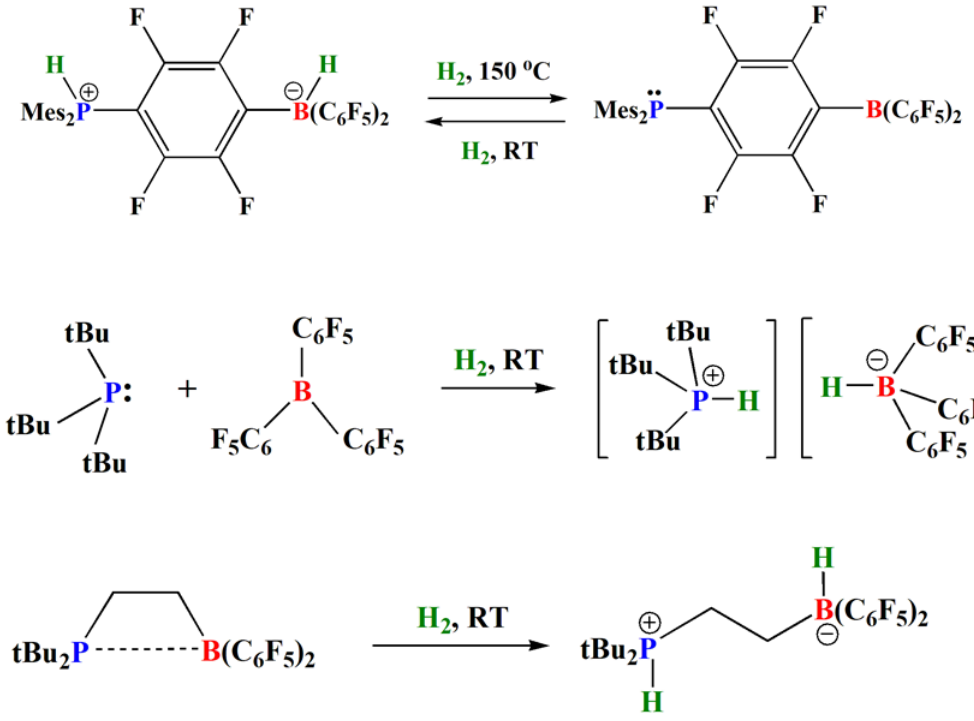

Figure 1.5: First few examples of heterolytic activation of H_2 by intramolecular/intermolecular FLPS.

and B$(C_6F_5)_3$ (BCF), that does not form a dative adduct, is able to effect H_2 cleavage in ambient temperature and pressure [27]. Another report came from the Erker group, who synthesized an ehtylene-bridged intramolecular phosphine-borane Lewis pair capable of facile H_2 cleavage [28]. The unique TM-like reactivity of these main group Lewis pairs was attributed to their inability to form a classical adduct due to steric bulk on the LA and LB centres. Thus, the unquenched LA and LB centres remain available for an interaction with a third, in the present case, H_2 molecule. Stephan

et al. coined the term "*Frustrated Lewis Pairs*" to represent such combinations of bulky LAs and bulky LBs [29]. Since these landmark discoveries, a broad spectrum of intermolecular as well as intramolecular LA and LB combinations have been shown to exhibit FLP reactivity. The list of LAs employed for H_2 activation include boranes, alanes, cationic boreniums, silyliums, phosphoniums, stannyliums, acridinums, carbocations, zirconocenes, *etc* [27, 30–37]. The LBs range from phosphines, amines, ethers, phosphazenes, carbenes to even exotic bases, such as carbodiphosphorans, *etc* [38–43]. Some of these examples are shown in Figure 1.6.

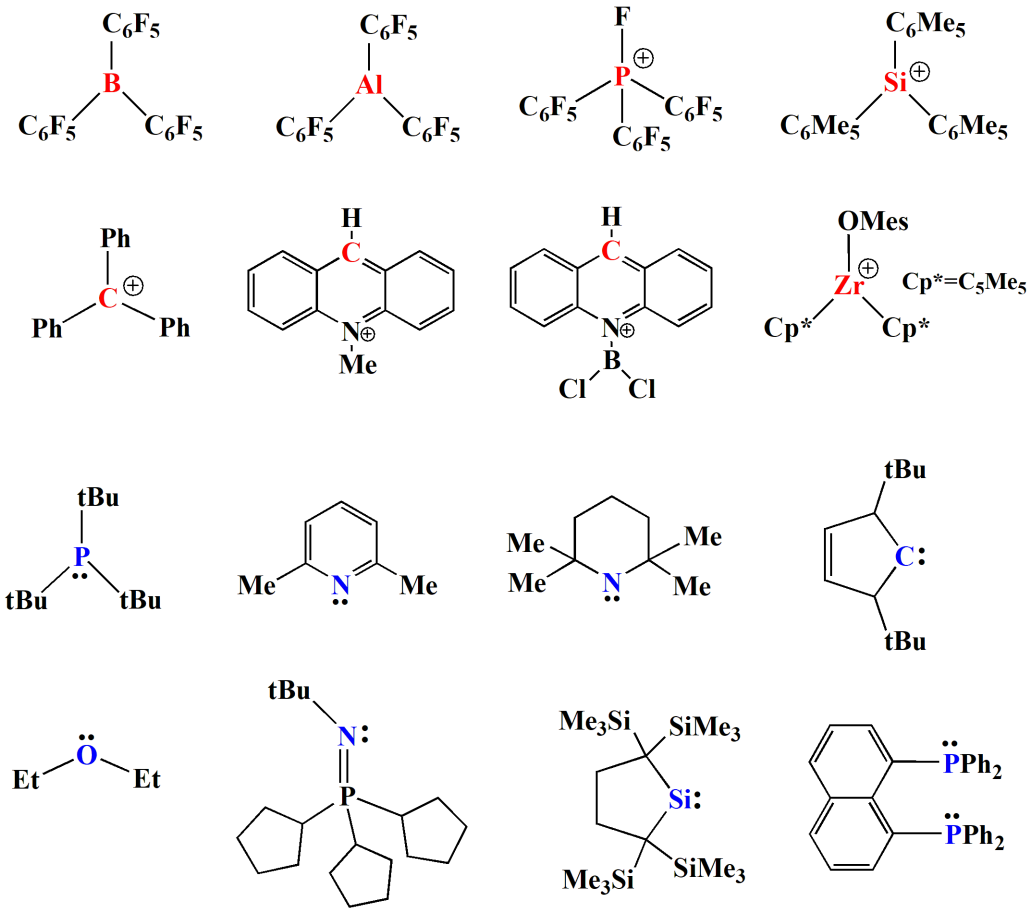

Figure 1.6: Examples of FLP LA (top) and LB (bottom) components described in the literature.

1.2.3 Activation of other small molecules

Although activation of H_2 is the most celebrated example of FLP chemistry, FLPs can capture a wide variety of other small molecules, which are kinetically inert or

not reactive to either of the Lewis components individually [44–46]. Some of the examples of the small molecules include CO_2, SO_2, N_2O, CO, NO, *etc* [47]. Apart

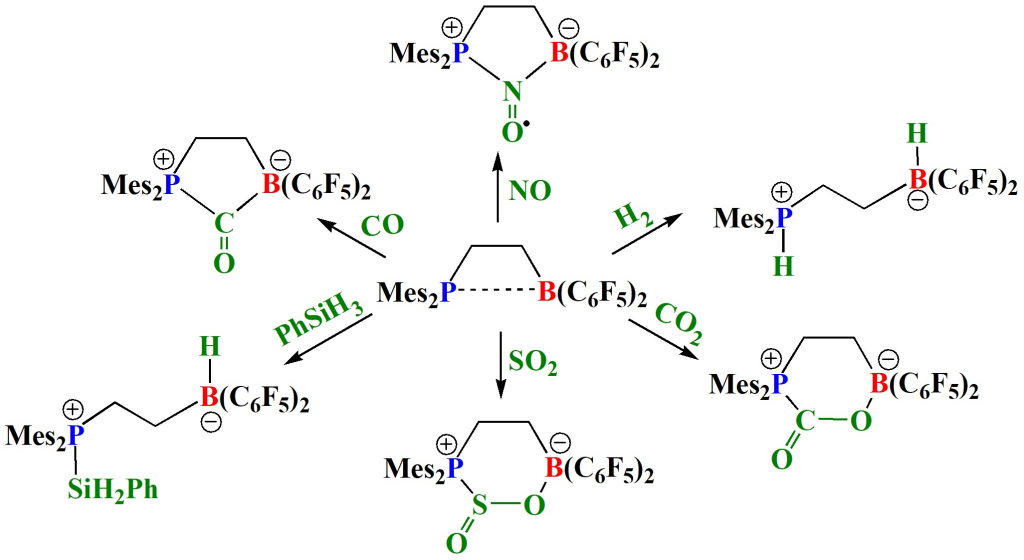

Figure 1.7: Selected represented examples of FLP activation of small molecules.

from that, FLPs can also react with various organic functionalities. Typical examples include ring-opening of cyclic ethers, E-H bond activation, addition reactions with alkenes, alkynes and cyclopropanes [44, 45, 48–50]. The concept of FLPs was also used in TM-based systems for activation of small molecules [44, 45, 51].

1.2.4 Mechanism of H_2 activation

Stephan's early mechanistic proposal for FLP-mediated H_2 activation involved a sequential action of LA and LB with H_2. Either a side-on-coordination of H_2 to LB or an end-on-coordination of H_2 to LA, was proposed to initiate the reaction, followed by the attack of the complementary Lewis component [27]. However, no experimental evidence was found to support such interactions, even at a low temperature. Subsequently, theoretical chemists analyzed such reactions and Pápai *et al.*came up with a different mechanistic proposal. They suggested the formation of a so-called encounter complex (EC) in which the LA and LB components are held together by weak noncovalent interactions [52]. Such an association ensures a preorganisation of the LA/LB centre for optimal interaction with the H_2 molecule. Molecular dynamics

studies suggested that the relative concentration of the EC is extremely low under the reaction condition; for example, the Lewis pair association was predicted to be only 2% at ambient temperature in toluene solution for tBu$_3$P/B(C$_6$F$_5$)$_3$ FLP [53]. The dominance of the weak dispersion interaction in ECs is also indicated by NMR

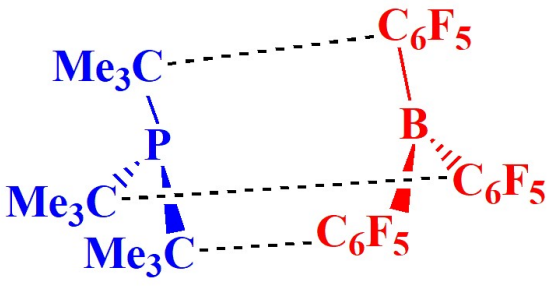

Figure 1.8: FLP (tBu$_3$P/B(C$_6$F$_5$)$_3$) "encounter complex".

studies of Mes$_3$P/B(C$_6$F$_5$)$_3$ FLP in which no specific orientation of the Lewis pair association was identified [54]. Within the EC cavity, H_2 activation occurs through a concerted TS in which two synergistic ET processes are observed featuring electron donations from a filled orbital on the donor centre to the empty $\sigma^*(H_2)$-antibonding orbital and $\sigma(H_2)$-bonding orbital to an empty orbital on the acceptor centre. The synergistic action of the Lewis pair gradually weakens the H-H bond and eventually, it is cleaved heterolytically to form two new, LB-H and LA-H, fragments [27, 55].

Grimme *et al.* proposed a conceptually different mechanistic scenario in which an electric field generated in between the LA/LB centres was thought to polarise the H-H bond, leading to its heterolytic cleavage [56]. The entrance of the H_2 molecule into the interrior of the EC was described to be the only energy demanding process while the H_2 splitting under the influence of the strong electric field was said to be barrierless. As it stands, most of the computational studies reported in the literature tend to converge into the former mechanism involving concerted ET between the LA/LB and H_2 molecule. Nevertheless, it is worth pointing out that, with a few exceptions, the majority of these studies explored quite a narrow range of Lewis pair combinations, such as amine or phosphine bases in partnership with borane Lewis acids.

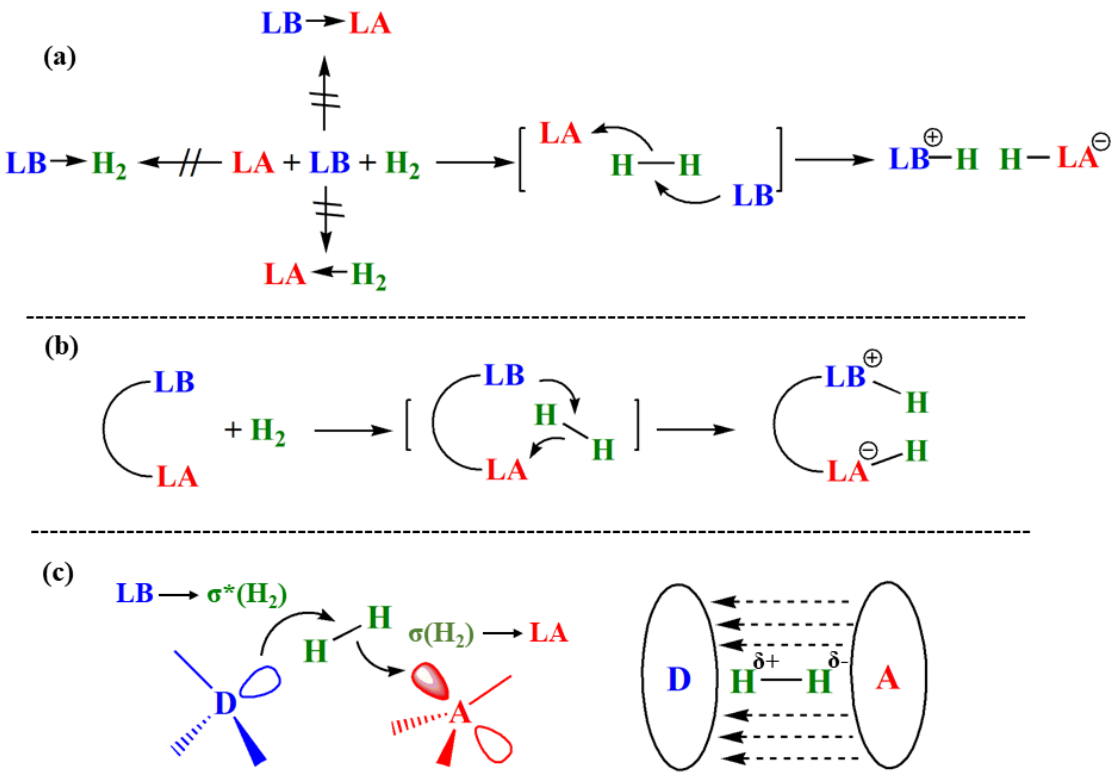

Figure 1.9: Mechanism of H_2 activation by (a) intermolecular (b) intramolecular FLPs. (c) The proposed reactivity models for heterolytic cleavage of H_2.

The thermodynamic aspect of FLP-mediated H_2 activation was also studied in detail by Pápai and co-workers [57]. They introduced an energy partitioning scheme, which quantitatively relates the acid-base strength of the FLPs with the thermodynamic requirement of H_2 splitting. According to this scheme, shown in Figure 1.10, the reaction free energy of H_2 activation is presented as the energetic sum of five hypothetical, yet chemically meaningful steps including the cleavage of the H_2 molecule into proton and hydride, separation of the LA and LB, proton attachment to LB, hydride attachment to LA, and the stabilisation of the H_2-activated product. On the basis of studies on a large variety of intermolecular and intramolecular FLPs, Pápai *et al.* concluded that the thermodynamics of H_2 splitting is largely governed by the cumulative strength of the LA and LB, which is estimated from the 3rd and the 4th term of the partitioning scheme. These two terms are expected to differ significantly

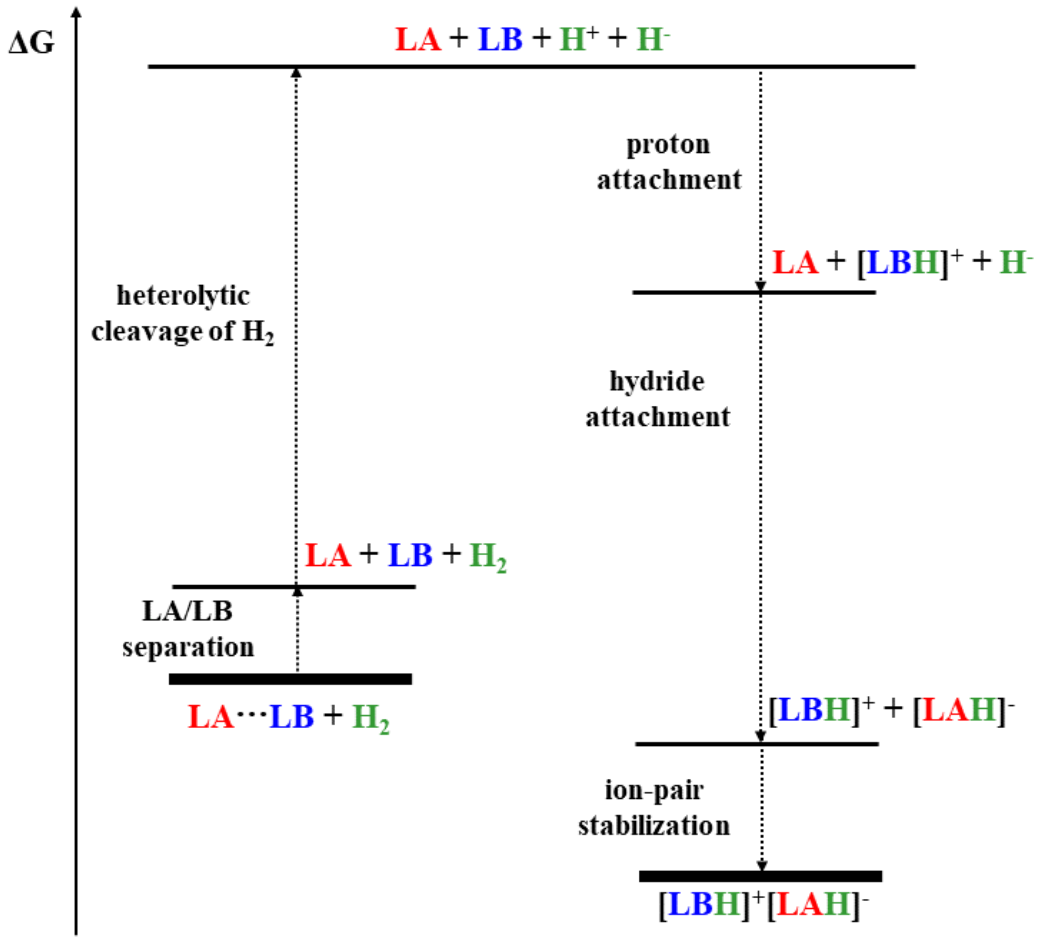

Figure 1.10: The partioning scheme proposed by Pápai *et al.* to understand the thermodynamic requirements of H_2 activation by FLPs.

in different combinations of FLPs and hence, by estimating these values, one can determine the likelihood of H_2 splitting by a given FLP of interest. A good proxy for the experimental determeination of the proton attachment term is the pK_a values of the employed LBs which are readily available in the literature [58]. On the contrary, determining the hydride attachment term experimentally is a far less trivial task. Qualitative estimates can be obtained from the available Gutmann-Beckett values although one should be careful while linking these values with the hydride affinity [59]. Fortunately, computational estimation of hydride affinity is straightforward and for a variety of FLP LA candidates, these values are available in the literature [60].

1.2.5 Catalytic hydrogenation

It can be readily envisaged that the heterolytic cleavage of H_2 by FLPs presented a possiblity of achieving metal-free hydrogenation catalysis. The idea seems fairly simple with the goal of sequential proton and hydrogen delivery to an unsaturated organic substrate following which the FLP would be regenerated again (see Figure 1.11).

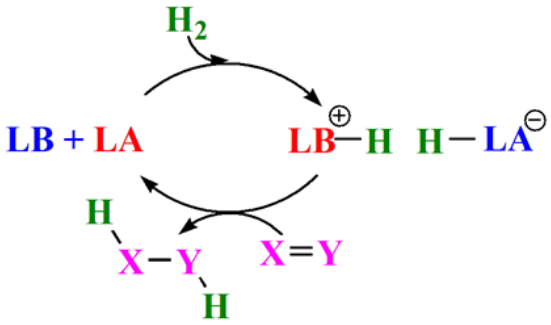

Figure 1.11: The proposed FLP-catalysed hydrogenation cycle for an unsaturated substrate, X=Y.

Soon after the discovery of the FLPs, Stephan *et al.* reported hydrogenation of imines, aziridines and protected nitriles using $[Mes_2PHC_6F_4BH(C_6F_5)_2]$ or BCF as the catalysts [61]. The strategy has been further extended to a wider variety of polar substrates such as enamines, enones, silyl enol ethers, and oximes [62–64]. While using a sterically encumbered basic substrate, which is the case for bulky imines, catalysis is often possible only with the LA component with the substrate serving the purpose of LB. But, in those cases too, if the substrate is not basic enough, the addition of a catalytic amount of LB might be necessary to accelerate the hydrogenation process. Noticeably absent from this group of polar substrates were carbonyl compounds, which were proved to be challenging for catalytic hydrogenation. However, this was eventually achieved by the group of Stephan and Ashley using BCF as the catalyst in the ethereal solvents [65, 66]. FLP-catalysed hydrogenation of carbonyl compounds will be discussed again in Chapater 2 and 4.

For nonpolar substrates such as simple olefins, slightly different hydrogenation

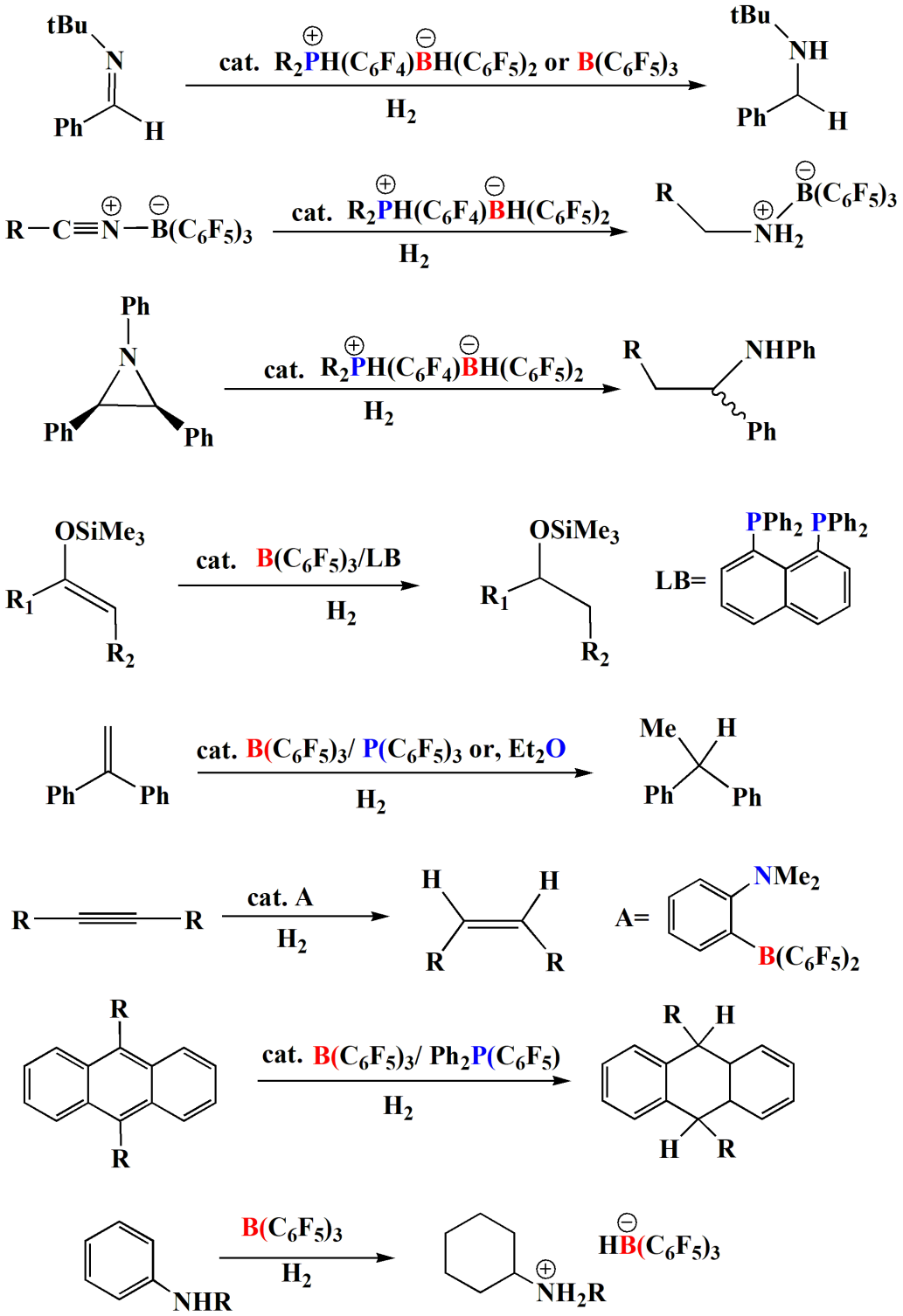

Figure 1.12: Examples of FLP-catalysed hydrogenation of polar and nonpolar substrates.

protocols were employed [41, 67]. In this case, much weaker LBs were used in combinations with BCF so that the conjugate acid is strong enough to protonate

the substrate, which would then accept the hydride from the borohydride [67]. A combination of BCF and $P(C_6F_5)_3Ph_2$ was shown to effect hydrogenation of 1,1-disubstituted olefins. Paradies *et al.* expanded the substrate scope to nitroolefins [68] and Alcarazo *et al.* reported hydrogenation of allenic esters using a combination of BCF/DABCO [69]. Repo *et al.* reported hydrogenation of nonfunctionalized alkynes to cis-alkenes using an intramolecular *ansa*-aminoborane as the FLP catalyst [70].

Aromatic substrates such as hydroanthracenes and hydrotetracenes can also be hydrogenated employing a combination of weakly basic LB and BCF [71]. Reduction of the aromatic rings is also possible as reported by Stephan *et al.* wherein hydrogenation of anilines afforded cyclohexylammonium salts in the presence of BCF [72]. Similar arene reductions of N-heterocycles such as pyridines, acridines, quinolines, and quinoxalines are also reported [73].

Noticeable among most of these hydrogenations is the use of boranes as the LA component. Even in the intramolecular examples reported in the literature, the LA fragment consists of B as the active site. This is even more surprising if we compare the diverse range of LAs employed in stoichiometric FLP H_2 activation with the narrow range of LAs used in catalytic hydrogenations. In fact, there have been only been a few reports for catalytic hydrogenations with non-boron based FLPs. Erker's report of Zr-based FLPs for hydrogenation for a range of polar and nonpolar substrates [74–76] and Stephan's reports of phosphonium based FLPs for hydrogenations of alkenes [33] are some of the examples. Even within the family of boranes, there have been very little variety in the choice of LAs with the majortity of studies focusing on BCF. Nevertheless, the current focus of FLP chemistry is gradually shifting towards the design of alternative FLP LAs. Ashley *et al.* demonstrated that Sn(IV)-LAs can be promising candidates, which in combination with amine bases were shown to catalyse the hydrogenation of imines and carbonyl compounds [36, 77]. The Sn(IV)-based LAs will be discussed in Chapter 2, 4, and 5.

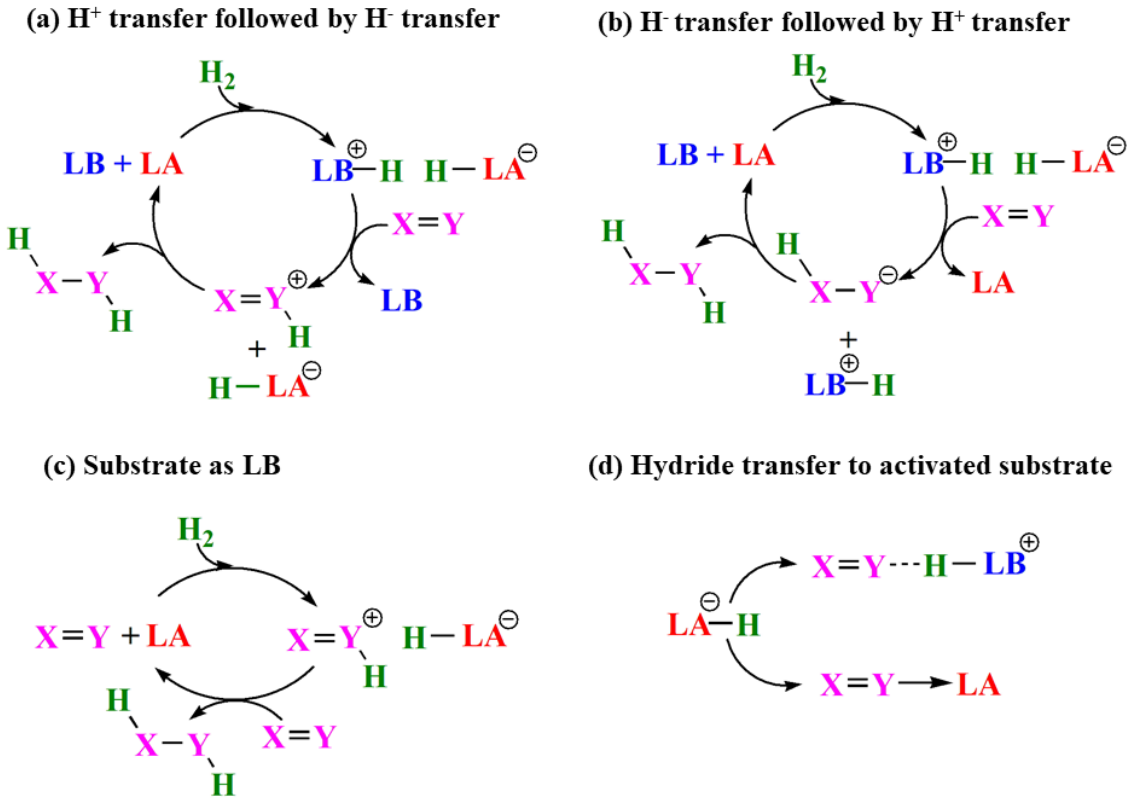

Figure 1.13: Mechanism of catalytic hydrogenation by FLPs for a general substrate X=Y which is basic at Y. Various mechanistic possibilities are shown.

1.2.6 Mechanism of catalytic hydrogenation

The general mechanism of FLP catalysed hydrogenation cycle involves initial H_2 activation to release the active hydrogens which are then transferred into an unsaturated substrate and the FLP catalyst is recovered. However, the sequence of proton and hydrogen delivery largely depends on the strength of the Lewis components. A major portion of FLP hydrogenations reports proton transfer prior to hydride transfer. The reason behind such mechanism lies in the frequent use of strongly electrophilic boranes as the LA component resulting in borohydrides that are not powerful enough to transfer hydride to unactivated substrate [61, 78–81]. Therefore, it is necessary to activate the substrate, either via full protonation or via forming hydrogen bonding interaction to the proton, so that it becomes sufficiently hydridophilic to complete the hydrogenation. If an alternate mechanism is to operate, *i.e.* hydride transfer prior to proton transfer, the substrate needs to be activated by other means, such as

coordinating with another LA molecule [36, 82]. One other possibility is the concerted transfer of proton and hydride to the substrate.

1.2.6.1 Factors controlling FLP hydrogenation

• Strength of LA and LB

As mentioned earlier, the strength of the Lewis components determines the thermodynamic feasibility of the H_2 activation step. While a combination of both very weak LA and LB is incapable of H_2 cleavage, a strong LA and LB combination often leads to very stable H_2 activation product which may not allow further release of the proton/hydride inhibiting catalytic hydrogenation process. For an optimal

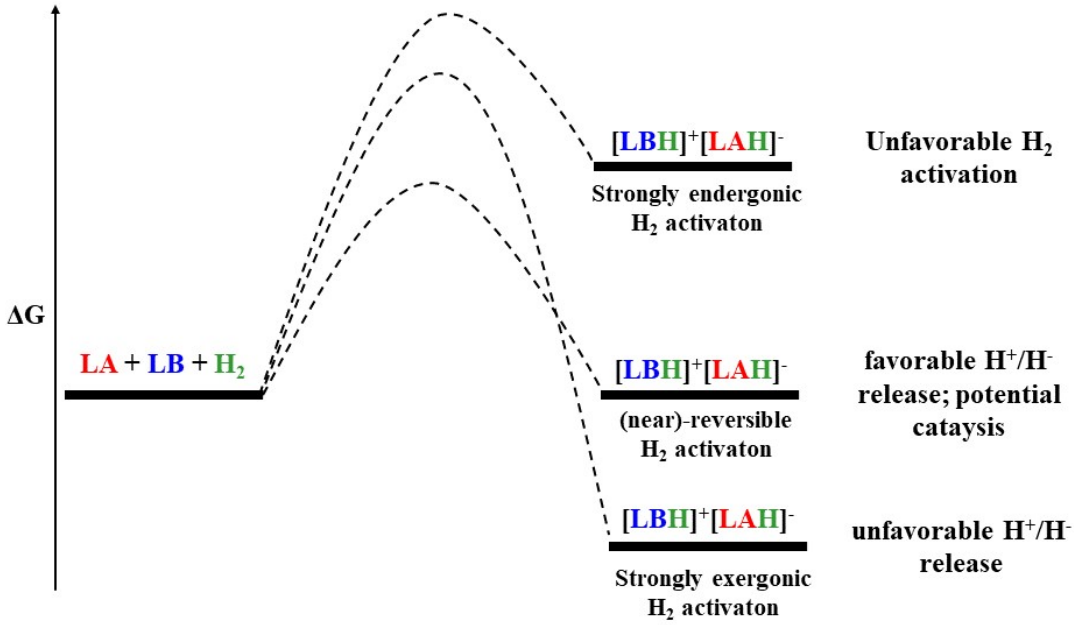

Figure 1.14: Effect of LA/LB strength on the thermodynamics of H_2 activation.

performance, one would like to have a reversible or near-reversible H_2 activation, which will render the subsequent hydrogen transfer facile. If the reaction proceeds via a substrate activation through protonation, which is often the case, it is crucial to balance the relative basicities of the LB and the substrate so that the protonation becomes feasible. An elegant example can be found in the reports of Stephan and Paradies. In order to hydrogenate alkenes, a weak fluorine-substituted phosphine base, which would result in a strong Brønsted acid upon H_2 activation, was employed

instead of a regular phosphine [67]. A similar approach was successfully demonstrated in the hydrogenation of carbonyl compounds in which a weak LB (ether) is used to generate a sufficiently strong BA to protonate the substrate [65, 66].

• **Steric bulk around the LA/LB centres**

The concept of FLP reactivity is, by definition, to utilize steric bulk to segregrate the Lewis components so that they do not form a strong unreactive classical adduct. However, it is well recognised by now that this is not an essential criterion to access FLP chemistry. These are the cases with less bulky LA and LBs, which might form a dative adduct at room temperature although at a higher temperature it can be dissociated to yield the active FLP *in situ*. This is typically known as the principle of "*thermally-induced frustration*" in FLP chemistry [83]. It is easy to see that the

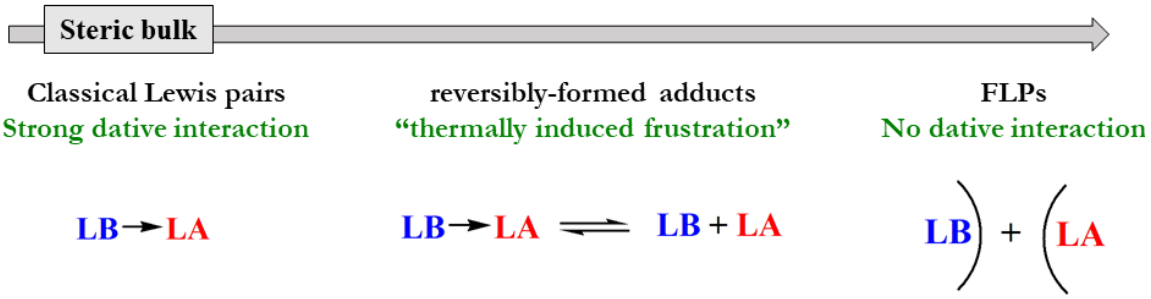

Figure 1.15: Variation of LA/LB interaction strength with steric bulk of the Lewis pairs.

extra energy required to separate the FLP components adds up to the activation barrier of the H_2 cleavage. Nevertheless, it gives the opportunity to explore a much wider range of LA/LB combinations with different steric profiles for potential FLP catalysis. In fact, steric bulk around the LA centre could play an important role in determining the functional group tolerance and substrate scope. For example, a less bulky LA forms a more reactive $[LA\text{-}H]^-$ facilitating the hydride transfer step while excessively bulky $[LA\text{-}H]^-$ might render this step kinetically infeasible. This is demonstrated in the work of Vanka *et al.* who showed that less bulky FLP combinations are better hydrogenation catalysts [84]. Soós *et al.* also reported a "size-exclusion principle" in the FLP hydrogenation, in which bulky LAs were

deliberately employed to hydrogenate less bulky imine substrates prohibiting the LA-amine (product) adduct formation [85].

• **Intramolecular or Intermolecular Lewis pairs**

Intramolecular FLPs, featuring LA and LB units tethered together in a single molecule, are expected to be more active hydrogenation catalysts compared to their intermolecular counterparts. The improved reactivity is attributed to a reduced entropic barrier of the bimolecular H_2 activation instead of a formally termolecular step. This was proved in the Erker's report of an intramolecular FLP, $Mes_2P(CH_2)_nB(C_6F_5)_2$, which showed enhanced activity as a hydrogenation catalyst compared to P/B intermolecular FLPs [28]. However, it was soon recognized that the reactivity also depends

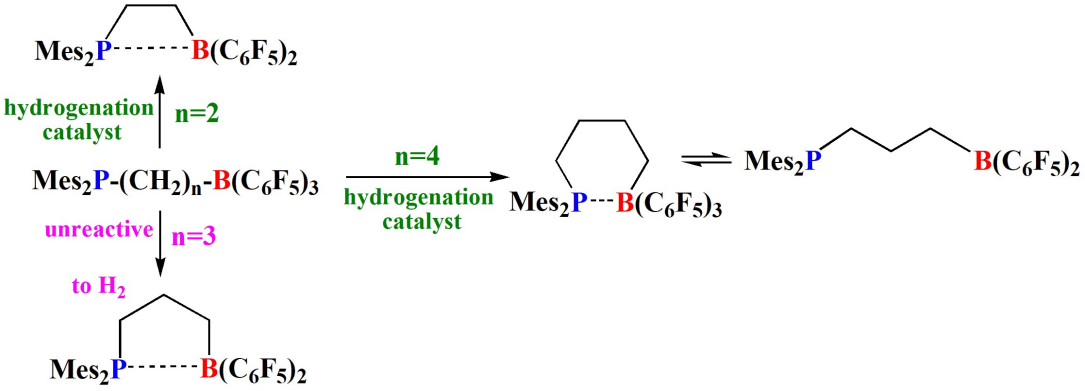

Figure 1.16: The reactivity of intramolecular phosphine borane Lewis pairs with different linker length.

on the linker that connects the LA/LB fragments. Note that, while n= 2 and 4 showed catalytic activity, n=3 linker renders the catalyst unreactive towards hydrogen [86, 87]. The rigidity of the linker is also equally important. In fact, the initially developed $Mes_2PC_6F_4B(C_6F_5)_2$ activates H_2 in an intermolecular manner despite being an intramolecular FLP due to the rigid tetrafluorophenylene linker which does not allow the P and B centres to come in close proximity [26, 88]. Thus, an optimal linker should be chosen carefully to achieve the desired improvement in the reactivity and at the same time, this should not additionally complicate the synthetic routes which is itself more complicated than the non-linked LA and LBs. One of the great benifits of intermolecular FLPs is the easily tunable independent Lewis components

(often available commercially) which can be varied rationally to screen a large number of Lewis pair combinations. In actuality, mechanistic investigations are also often easier with intermolecular FLPs. Therefore, one must keep these factors in mind while designing intramolecular FLP catalysts.

1.2.7 Analogies to TM-mediated H_2 activation

We will conclude this section by mentioning some apparent degrees of similarities between the mechanism of FLP-mediated H_2 activation and that of TM-mediated H_2 activation. For example, the H_2 cleavage by Noyori-bifunctional catalysts [7] bears close resemblance with FLP activation of H_2. In the former case, the H_2 splitting is also concerted with Lewis acidic metal accepting the hydride while the Lewis basic N centre accepts the proton. Also, closely related is the oxidative addition of H_2 to a metal centre, which also relies on the ETs involving its frontiers orbitals. Admittedly, in this case, both the donor and acceptor orbitals are located on the same metal centre while in the FLPs these are spatially separated. Nevertheless, the basic requirements of H_2 activation are the same; availabilities of an empty and a filled orbital, capable of interacting with the bonding and antibonding orbital of H_2 molecule, respectively. We will discuss such analogies again in Chapter 6.

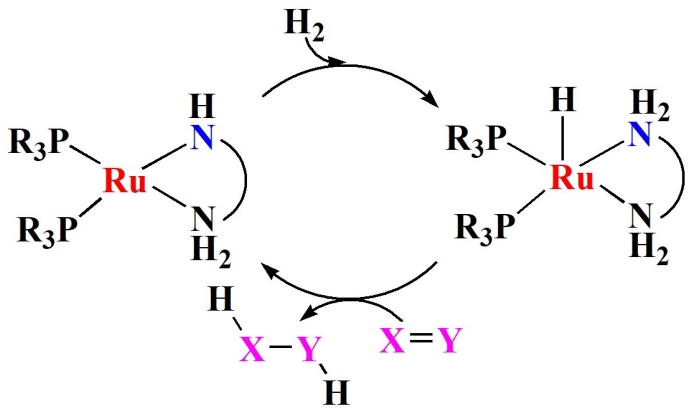

Figure 1.17: Schematic representation of H_2 activation and hydrogenation by Noyori catalysts.

1.3 Computational methodology

1.3.1 General aspects

Despite the incredible progress in the computational methods and computer technologies, accurate modelling of chemical reactions in solution remains a challenging task. Reaction mechanisms in catalytic processes are far from trivial. Apart from the inherent complexity associated with the charge, oxidation state, coordination and even spin states of the catalytic intermediates, external factors such as solvent or additives could further complicate any effort to unravel the mechanistic intricacies of the process. Solvents, in particular, may have a profound influence on catalytic mechanism either by simply perturbing the potential energy profile of the reaction or through active participation in the key reaction steps. Polar solvents preferentially stabilising ionic intermediates or protic solvents stabilising intermediates through hydrogen bonding interactions are typical examples of solvent effects. Also, noteworthy is the electronic and steric effect of the ligands, carried by the active catalytic sites, in determining the reactivity and selectivity of the process. However, with a wise choice of computational methods and a proper analysis of the results, it is possible to obtain a meaningful mechanistic description for a wide range of chemical reactions.

We have chosen a static approach to explore the potential energy surface (PES) for a chemical reaction in terms of the stationary points (reactants, products, intermediates, transition states) only. This decision is taken on the basis of the nature of the reactions studied and considering the available computer resources. Quantum chemical calculations at various levels of density functional theory have been used to locate the stationary points on the PES. The nature of the stationary points is characterized by a harmonic vibrational frequency analysis. Transitions states (TSs) are further verified with intrinsic reaction coordinate (IRC) calculations by checking their connection to the desired minima on either side of the saddle point. Most of the TS search calculations are preceded by relaxed scan calculations to map the

relevant part of the PES following the mechanistic rationale. In the scan calculations, all degrees of freedoms are fully relaxed while a single geometric variable (reaction coordinate) is scanned in a stepwise manner.

In order to take into account solvent effects, we have mostly considered a dielectic continuum model for solvation. Since the experimentally used solvents are polar/moderately polar and aprotic in nature, we do not expect active participation of the solvent molecule in the reaction pathways except in Chapter 2 for which we have used explicit solvent molecules to compute the mechanism. Note that, the present computational approach is not expected to provide very accurate Gibbs free energies. The uncertainties in estimating the free energy values stem from two main sources; (i) the empirical ingredients of the solvation model (SMD) used for the solvent correction, and (ii) the ideal gas-rigid-rotor-harmonic oscillator model used to estimate the gas phase entropic contributions. Therefore, while drawing conclusions, we kept all these factors in mind. Overall, in the present thesis, our aim has been to extract the key mechanistic features, rationalize experimental observations and identify underlying principles that may prove useful in designing new reactions. For this purpose, we think that the present computational framework is fairly reasonable.

1.3.2 Schrödinger equation for solving electronic structure

The foundation of any electronic structure calculation is the Schrödinger equation (SE), which can be solved to obtain the total energy of a system. The non-relativistic time-independent SE reads as,

$$\hat{H}\Psi = E\Psi \tag{1.1}$$

where, $\hat{H}$ is the Hamiltonian operator, Ψ is the many-body wavefunction containing all information about the quantum mechanical system and E is the total energy. The complete Hamiltonian for a system of interacting nuclei and electrons is given by

[89–91],

$$\hat{H} = -\sum_i \frac{\hbar^2}{2m_e}\nabla_i^2 - \sum_I \frac{\hbar^2}{2M_I}\nabla_I^2 - \sum_{i,I} \frac{Z_I e^2}{|\mathbf{r}_i - \mathbf{R}_I|} + \sum_{i \neq j} \frac{e^2}{|\mathbf{r}_i - \mathbf{r}_j|} + \sum_{I \neq J} \frac{Z_I Z_J e^2}{|\mathbf{R}_I - \mathbf{R}_J|} \quad (1.2)$$

where, m_e and M_I represent the masses of an electron and I-th nucleus, respectively. Electrons have a charge e and Z_I is the atomic number of the I-th nucleus. $\mathbf{r}_i$ and $\mathbf{R}_I$ are the positions of i-th electron and I-th nucleus, respectively. These five terms in equation 1.2 include, from left to right, kinetic energy of the electrons, kinetic energy of the nuclei, potential energy of the electrostatic attraction between electrons and nuclei, potential energy of the electron-electron repulsive interaction and finally, potential energy of the nucleus-nucleus repulsion. The complete many-body Hamiltonian can also be expressed in a much simpler way from the point-of-view of electrons as given by the equation,

$$\hat{H} = \hat{T}_e + \hat{T}_n + \hat{V_{ext}} + \hat{V_{int}} + \hat{V_{nn}} \quad (1.3)$$

Note that, in this picture, the potential offered by the nuclei are considered as external while the electronic potential is viewed as internal. Unfortunately, it is impossible to obtain an exact solution to SE for any but the smallest systems. Hence, any electronic structure method involves approximations to simplify the many-body Hamiltonian.

1.3.3 Born-Oppenheimer approximation

Born-Oppenheimer (BO) approximation is the first of such approximations to simplify the Hamiltonian in equation 1.2 by separating the electronic and nuclear motion. Since the nuclei are about thousands of times heavier than electrons, it seems reasonable to consider that the nuclei effectively remain stationary in the electronic time-scales. In other words, the electrons can be considered as moving in a static field

formed by the frozen nuclei. Within the BO approximation, it is possible to solve the electronic part of the SE independently. The total wave function ($\Psi_{tot}(\mathbf{r}_i, \mathbf{R}_I)$) can be broken down into nuclear and electronic parts which give rise to two separate SEs.

$$\Psi_{tot}(\mathbf{r}_i, \mathbf{R}_I) = \Psi_e(\mathbf{r}_i, \mathbf{R}_I)\Psi_n(\mathbf{R}_I) \tag{1.4}$$

where, $\Psi_e(\mathbf{r}_i, \mathbf{R}_I)$ and $\Psi_n(\mathbf{R}_I)$ are the eletronic and nuclear part of the wave function, respectively. The electronic part of the SE becomes,

$$\hat{H}_e\Psi_e(\mathbf{r}_i, \mathbf{R}_I) = E_e(\mathbf{R}_I)\Psi_e(\mathbf{r}_i, \mathbf{R}_I) \tag{1.5}$$

where $\hat{H}_e = \hat{T}_e + \hat{V_{ext}} + \hat{V_{ee}} + \hat{V_{nn}}$. and E_e is the electronic eigenvalue, which depends parametrically on the nuclear positions. Often, $\hat{V_{nn}}$ term is also excluded from the electronic part of the Hamiltonian. This is justified since coulombic nuclear repulsion only provides a constant-shift to the eigenvalues. It can always be added at a later stage to the electronic energy to obtain the total energy. The nuclear part of the SE turns out to be,

$$[\hat{T_n} + E_e(\mathbf{R}_I)]\Psi_n(\mathbf{R}_I) = E\Psi_n(\mathbf{R}_I) \tag{1.6}$$

where E is the total energy of the system. Thus, BO approximation reduces the complexity of the many-body Hamiltonian to some extent by separating the nuclear and electronic degrees of freedom.

1.3.4 Density functional theory

Even after introducing BO approximation, a solution to SE remains a challenging task. Nevertheless, density functional theory (DFT) provides a way to reformulate the problem using electron density as an alternative to many-body wave function to describe the system of interest. As already stated by the BO approximation, the electronic and nuclear motions are separated from each other, which makes electrons to relax in a static external potential $V_{ext}(\mathbf{r})$ created by the nuclei. The electronic

Hamiltonian (omitting the Coulombic nuclear repulsion term) is given by,

$$\hat{H}_e = -\sum_{i=1}^{N} \frac{\hbar^2}{2M_I}\nabla_i^2 + \sum_{i\neq j} \frac{e^2}{|\mathbf{r}_i - \mathbf{r}_j|} + \sum_i V_{ext}(\mathbf{r}_i) \tag{1.7}$$

The solution to equation 1.7 is difficult due to the electron-electron repulsion term. However, the first step towards achieving a solution lies in the Hohenberg-Kohn theorems that associate ground state particle density with all physical properties of the system.

1.3.4.1 Hohenberg-Kohn theorems

At the heart of DFT, there lies two ingeniously simple theorems put forward by Hohenberg and Kohn in 1964 [92–94].

- **Theorem 1:** *In any system of interacting particles, the external potential* $V_{ext}(\mathbf{r})$ *is uniquely determined (up to a constant) by the ground state particle density* $n_0(\mathbf{r})$

- **Theorem 2:** *For any* $V_{ext}(r)$ *we can define the energy functional,* $E[n(\mathbf{r})]$*, in terms of particle density* $n(\mathbf{r})$*. The density that minimizes* $E[n(\mathbf{r})]$ *is the correct ground state density* $n_0(\mathbf{r})$

Note that, the first two terms in equation 1.7 are dependent only on the electrons and the same for any N-electron system. It follows that the ground state density that fixes the $V_{ext}(\mathbf{r})$ also uniquely determines the Hamiltonian and hence the many-body wave functions are also determined. Therefore, in principle, all the properties of the systems can be derived from the ground state density although establishing such a connection between them might not be a trivial task. Nonetheless, it is straightforward to write an expression for the total energy in terms of $n(\mathbf{r})$. Omitting the kinetic energy and the coulombic repulsion term for the nuclei, the equation 1.3 transforms

to,

$$E_{HK}[n(\mathbf{r})] = T_e[n(\mathbf{r})] + E_{int}[n(\mathbf{r})] + \int d^3r V_{ext}(\mathbf{r})n(\mathbf{r}) = F_{HK}[n(\mathbf{r})] + \int d^3r V_{ext}(\mathbf{r})n(\mathbf{r}) \tag{1.8}$$

in which $F_{HK}[n(\mathbf{r})]$ is given by,

$$F_{HK}[n(\mathbf{r})] = T_e[n(\mathbf{r})] + E_{int}[n(\mathbf{r})] \tag{1.9}$$

where, $F_{HK}[n(\mathbf{r})]$ contains the kinetic energy of the electrons and the electron-electron repulsion term and is a universal density-dependent functional. It can easily be envisaged that if $F_{HK}[n(\mathbf{r})]$ is known, ground state density for a truly interacting system can simply be determined by performing a minimization of the total energy with respect to variations in the density function $n(\mathbf{r})$. In this sense, DFT is an exact many-body theory. However, there is no known way to obtain the functional that has to be minimized except for the definition involving many-body N-electron wave functions. However, a smart way to circumvent this problem was provided by Kohn and Sham in 1965. In fact, it is this Kohn-Sham formulation that puts DFT to practical use.

1.3.4.2 Kohn-Sham approach

The approach of Kohn and Sham was to replace the many-body interacting system by an auxiliary non-interacting particle system, and it was assumed that the two systems have exactly the same ground state density [93]. The auxiliary system can be solved more easily since the electrons are considered to be independent particles. In this non-interacting picture, each electron experiences an effective potential which depends solely on particle density. This leads to a reformulation of the original many-body problem to an independent particle problem in which densities interact with each other instead of wavefunctions. Thus, with the Kohn-Sham approximation,

the calculations can be performed on a set of independent particle SEs,

$$\hat{H} = (-\frac{\hbar^2}{2m_e}\nabla^2 + V_{KS})\phi_i(\mathbf{r}) = \epsilon_i\phi_i(\mathbf{r}) \tag{1.10}$$

where $\{\phi_i\}$ are the set of independent particle orbitals, which are also known as Kohn-Sham orbitals. For a N electron system, the ground state can be obtained by solving N such independent particle SEs. Each ϕ_i is occupied by one electron with the corresponding lowest eigenvalue ϵ_i. The density of the auxiliary system is obtained by summing the squares of the Kohn-Sham orbitals as given in equation 1.11.

$$n(\mathbf{r}) = \sum_i^N |\phi_i(\mathbf{r})|^2 \tag{1.11}$$

subjected to the conditon, $\int n(\mathbf{r})d\mathbf{r} = N$, that Kohn-Sham orbitals reproduce the density of the original many-body interacting system.

The kinetic energy functional for the auxialiary system is given by,

$$T_S[n(\mathbf{r})] = -\frac{\hbar^2}{2m_e}\sum_i^N \langle\phi_i(\mathbf{r})|\nabla^2|\phi_i(\mathbf{r})\rangle \tag{1.12}$$

Therefore, the universal $F_{HK}[n(\mathbf{r})]$ becomes,

$$F_{HK}[n(\mathbf{r})] = T_S[n(\mathbf{r})] + E_H[n(\mathbf{r})] + E_{XC}[n(\mathbf{r})] \tag{1.13}$$

where the classical Coulomb self-interaction term from $E_{int}[n(\mathbf{r})]$ is extracted and has been denoted as Hartree energy, $E_H[n(\mathbf{r})]$. $E_{XC}[n(\mathbf{r})]$ is the exchange-correlation (XC) energy containing the difference in kinetic energy between the fully-interacting many-body system and the non-interacting auxiliary system along with the non-classical contribution of the electron-electron interaction. Thus, the expression for $E_{XC}[n(\mathbf{r})]$ becomes,

$$E_{XC}[n(\mathbf{r})] = T_e[n(\mathbf{r})] - T_S[n(\mathbf{r})] + E_{int}[n(\mathbf{r})] - E_H[n(\mathbf{r})] \tag{1.14}$$

Thus, the ground state HK energy functional can be rewritten using Kohn-Sham approximation as,

$$E_{KS}[n(\mathbf{r})] = T_S[n(\mathbf{r})] + \int d^3r V_{ext}(\mathbf{r})n(\mathbf{r}) + E_H[n(\mathbf{r})] + E_{XC}[n(\mathbf{r})] \tag{1.15}$$

The XC energy is the only unknown term in the equation 1.15, and usually, it is approximated as a local or a semi-local functional. The success of the Kohn-Sham approach depends on the extent to which this $E_{XC}[n(\mathbf{r})]$ term can recover the lost many-body effects during the shift from a fully-interacting to a non-interacting auxiliary system. Nonetheless, the Kohn-Sham formulation at least makes it feasible to calculate the ground-state properties of a many-body system.

The ground-state energy can be obtained by minimizing $E_{KS}[n(\mathbf{r})]$ with respect to the constraint that total no. of electrons remains constant. In practice, one begins with a guess density from which the effective potential is calculated by differentiating the total energy functional. The effective potential is given by the expression,

$$V_{KS} = V_{ext}(\mathbf{r}) + \int \frac{n(\mathbf{r}')}{|\mathbf{r} - \mathbf{r}'|} d\mathbf{r}' + \frac{\delta E_{XC}[n(\mathbf{r})]}{\delta n(\mathbf{r})} \tag{1.16}$$

With the calculated V_{KS}, the single-electron equation 1.10 is solved for N electrons. Equation 1.10 is an eigenvalue problem, solving which we get the Kohn-Sham orbitals. From the Kohn-Sham orbitals, a new density is constructed employing equation 1.11 and this is taken as the new guess density to start the process all over again. Typically, instead of using the new density directly, an average of the new density and the density from the previous step is considered as the new guess density. These series of steps are repeated until we obtain a self-consistent solution, and final density is taken as the ground state electron density for the system under investigation.

1.3.4.3 Exchange-correlation functionals

The Kohn-Sham approximation simplifies the fully-interacting many-body problem into a set of independent particle SEs which can be solved more easily. However,

the Kohn-Sham equations are only solvable if the exact form of the $E_{XC}[n(\mathbf{r})]$ is known. Fortunately, even with gross approximations of the $E_{XC}[n(\mathbf{r})]$, it is possible to predict various properties of many systems to a fair degree of accuracy. Of these approximations, we will discuss a few which has been found to be extensively used in the literature.

- **Local density approximation (LDA)**

It is probably the simplest approximation in DFT. In LDA [95], XC energy per electron is approximated to be same as the XC energy of a homogeneous electron gas (HEG) of exactly same density. Thus, the expression for $E_{XC}[n(\mathbf{r})]$ for a spin unpolarized system is given by,

$$E_{XC}^{LDA}[n(\mathbf{r})] = \int d\mathbf{r} \epsilon_{XC}^{HEG}(n(\mathbf{r})) \cdot n(\mathbf{r}) \tag{1.17}$$

For a spin polarized system, the LDA can be genalized to a local spin density approximation (LSDA), which is given by,

$$E_{XC}^{LSDA}[n_{\uparrow}(\mathbf{r}), n_{\downarrow}(\mathbf{r})] = \int d\mathbf{r} \epsilon_{XC}^{HEG}(n_{\uparrow}(\mathbf{r}), n_{\downarrow}(\mathbf{r})) \cdot n(\mathbf{r}) \tag{1.18}$$

Despite the simplicity, LDA has been quite successful and works reasonably well for bulk solids. Since the inhomogeneties of the electron density is ignored under LDA, often the performance is poor when the density varies rapidly. For example, in the cases of defects in solids LDA makes erroneous predictions. Also, the binding energy is often overestimated while the ground state energies, ionization energies and band gaps of semiconductors are significantly underestimated with LDA. This had led to other approximations of XC functional beyond LDA.

- **Generalized gradient approximations (GGA)**

Mathematically, the obvious improvement to LDA is to consider density as well as

gradient of density at a given point, which leads to the GGA expression,

$$E_{XC}^{GGA}[n(\mathbf{r})] = \int d\mathbf{r}\epsilon_{XC}(n(\mathbf{r}), \vec{\bigtriangledown} n(\mathbf{r})) \cdot n(\mathbf{r}) \tag{1.19}$$

Three commonly used forms of GGAs are proposed by Becke [96] (B88), Perdew *et al.* [97], and Perdew, Burke and Enzerhof [96] (PBE). GGA usually shows a much improvement over LDA results in predicting binding energies and structural parameters, which is behind its extensive use in computational chemistry community. However, sometimes it tends to overcorrect LDA predictions as in ionic crystals in which the latter is found to yield better results compared to GGA. However, LDA and GGA perform equally badly for bandgap determination.

- **Meta-GGA functionals**

The next level of improvement on GGA can be obtained using the Laplacian of density along with the density gradient and density itself. These are called meta-GGA functionals, which often works well over GGA in many aspects [98, 99].

- **Hybrid functionals**

Further improvements can be made with the so-called hybrid functionals, which attempts to correct the self-interaction error in LDA/GGA by including a certain portion of exact non-local Hartree-Fock exchange along with XC description from other sources (LDA or GGA). For example, a commonly used hybrid functional is B3LYP [100], which is extremely popular in the chemistry community and has the following description,

$$E_{XC}^{B3LYP} = E_X^{LDA} + a_0[E_X^{HF} - E_X^{LDA}] + a_X[E_X^{GGA} - E_X^{LDA}] + a_C[E_C^{GGA} - E_C^{LDA}] + E_C^{LDA} \tag{1.20}$$

where, $a_0 = 0.20$, $a_X = 0.72$ and $a_C = 0.81$.

- **Long-range corrected functionals**

The LDA and GGA functionals neglect the long-range electron-electron exchange

interaction, which can not possibly be represented by a functional of one-electron quantity. Thus, these functionals are not suitable for modelling processes such as van der Waals interactions or non-covalent interactions. Various long-range exchange correction schemes have been proposed to handle such cases. CAM-B3LYP [101] and ωb97xd [102] are a couple of typical examples of long-range corrected functionals.

1.3.5 Softwares used

We have used several software packages to obtain the results reported in this thesis. All electronic structure calculations with DFT, geometry optimizations, vibrational frequency computations, thermochemical data, and solvent corrections were carried out using the Gaussian package (releases G16 A.03 and G09 A.02). We have employed NBO 3.1 package featured as a part of Gaussian programs for bonding analysis. The energy decomposition analysis calculations were performed using ADF2017.01. For visualization and graphical analyses, we have used Gaussview, VMD, Jmol, and Xmgrace. Whenever necessary, home-developed codes were used to analyse the computed data.

1.4 Scope of the thesis

In this thesis, we chiefly dealt with catalytic hydrogenations which are either directly mediated by FLPs or relies heavily on the cooperative action between Lewis pairs. We aimed to understand how the catalysts work at the molecular level by identifying the key intermediates and reaction pathways that form the basis of the H_2 activation and catalytic hydrogenation processes. To this end, we have explored the relevant potential energy surfaces corresponding to these reactions using quantum chemical calculations at various levels of density functional theory.

The present chapter provides a brief discussion on the H_2 activation and hydrogenation catalysis by FLPs along with a brief overview of the computational methodology used to perform the mechanistic studies. In the subsequent chapter, we have explored the detailed mechanism of $B(C_6F_5)_3$-catalysed hydrogenation of

carbonyl compounds. The next three chapters are devoted to the H_2 activation and hydrogenation catalysis by the Sn(IV)-based FLPs. The mechanism of H_2 activation by Sn/N FLPs is discussed in Chapter 3. Comprehensive mechanistic studies on the catalytic hydrogenation of carbonyl compounds by Sn/N FLPs are presented in Chapter 4. Chapter 5 deals with the computational design of intramolecular Sn/N Lewis pairs for catalytic applications. Finally, the mechanism of catalytic hydrogenation of CO_2 using Mn(I)-complexes with pendant oxygen ligands is discussed in Chapter 6. At the outset, this chapter does not appear to have any connection with the FLPs. However, while investigating the reaction, we came across several mechanistic features from which direct analogies can be drawn to FLP chemistry. The thesis ends with a brief summary of the results and an outlook towards possible future research and development.

Bibliography

[1] Rylander, P.; Elvers, B.; Rounsaville, J.; Schulz, G. Ullmanns Encyclopedia of Industrial Chemistry. 2005.

[2] Birch, A. J. *Journal of the Chemical Society (Resumed)* **1944**, 430–436.

[3] Meerwein, H.; Schmidt, R. *Justus Liebigs Annalen der Chemie* **1925**, *444*, 221–238.

[4] Hantzsch, A. *Berichte der deutschen chemischen Gesellschaft* **1881**, *14*, 1637–1638.

[5] Sabatier, P. *Industrial & Engineering Chemistry* **1926**, *18*, 1005–1008.

[6] Osborn, J. A.; Jardine, F.; Young, J. F.; Wilkinson, G. *Journal of the Chemical Society A: Inorganic, Physical, Theoretical* **1966**, 1711–1732.

[7] Noyori, R. *Angewandte Chemie International Edition* **2002**, *41*, 2008–2022.

[8] Kubas, G. J. *Chemical reviews* **2007**, *107*, 4152–4205.

[9] Berke, H. *ChemPhysChem* **2010**, *11*, 1837–1849.

[10] Vries, J. G. d. *The handbook of homogeneous hydrogenation*; Wiley-Vch, 2007.

[11] Siegbahn, P. E.; Tye, J. W.; Hall, M. B. *Chemical reviews* **2007**, *107*, 4414–4435.

[12] Frey, G. D.; Lavallo, V.; Donnadieu, B.; Schoeller, W. W.; Bertrand, G. *Science* **2007**, *316*, 439–441.

[13] Protchenko, A. V.; Birjkumar, K. H.; Dange, D.; Schwarz, A. D.; Vidovic, D.; Jones, C.; Kaltsoyannis, N.; Mountford, P.; Aldridge, S. *Journal of the American Chemical Society* **2012**, *134*, 6500–6503.

[14] Peng, Y.; Guo, J.-D.; Ellis, B. D.; Zhu, Z.; Fettinger, J. C.; Nagase, S.; Power, P. P. *Journal of the American Chemical Society* **2009**, *131*, 16272–16282.

[15] Peng, Y.; Ellis, B. D.; Wang, X.; Power, P. P. *Journal of the American Chemical Society* **2008**, *130*, 12268–12269.

[16] Spikes, G. H.; Fettinger, J. C.; Power, P. P. *Journal of the American Chemical Society* **2005**, *127*, 12232–12233.

[17] Peng, Y.; Brynda, M.; Ellis, B. D.; Fettinger, J. C.; Rivard, E.; Power, P. P. *Chemical Communications* **2008**, 6042–6044.

[18] Lewis, G. N. *Valence and the Structure of Atoms and Molecules*; Chemical Catalog Com.; New York, 1923.

[19] Brown, H. C.; Schlesinger, H.; Cardon, S. Z. *Journal of the American Chemical Society* **1942**, *64*, 325–329.

[20] Brown, H. C.; Kanner, B. *Journal of the American Chemical Society* **1966**, *88*, 986–992.

[21] Wittig, G.; Rückert, A. *Justus Liebigs Annalen der Chemie* **1950**, *566*, 101–113.

[22] Tochtermann, W. *Angewandte Chemie International Edition in English* **1966**, *5*, 351–371.

[23] Bontemps, S.; Bouhadir, G.; Miqueu, K.; Bourissou, D. *Journal of the American Chemical Society* **2006**, *128*, 12056–12057.

[24] Hudnall, T. W.; Kim, Y.-M.; Bebbington, M. W.; Bourissou, D.; Gabbai, F. P. *Journal of the American Chemical Society* **2008**, *130*, 10890–10891.

[25] Roesler, R.; Piers, W. E.; Parvez, M. *Journal of organometallic chemistry* **2003**, *680*, 218–222.

[26] Welch, G. C.; San Juan, R. R.; Masuda, J. D.; Stephan, D. W. *Science* **2006**, *314*, 1124–1126.

[27] Welch, G. C.; Stephan, D. W. *Journal of the American Chemical Society* **2007**, *129*, 1880–1881.

[28] Spies, P.; Erker, G.; Kehr, G.; Bergander, K.; Fröhlich, R.; Grimme, S.; Stephan, D. W. *Chemical Communications* **2007**, 5072–5074.

[29] Welch, G. C.; Cabrera, L.; Chase, P. A.; Hollink, E.; Masuda, J. D.; Wei, P.; Stephan, D. W. *Dalton Transactions* **2007**, 3407–3414.

[30] Farrell, J. M.; Hatnean, J. A.; Stephan, D. W. *Journal of the American Chemical Society* **2012**, *134*, 15728–15731.

[31] Schäfer, A.; Reißmann, M.; Schäfer, A.; Schmidtmann, M.; Müller, T. *Chemistry–A European Journal* **2014**, *20*, 9381–9386.

[32] Ménard, G.; Stephan, D. W. *Angewandte Chemie International Edition* **2012**, *51*, 8272–8275.

[33] vom Stein, T.; Peréz, M.; Dobrovetsky, R.; Winkelhaus, D.; Caputo, C. B.; Stephan, D. W. *Angewandte Chemie International Edition* **2015**, *54*, 10178–10182.

[34] Clark, E. R.; Ingleson, M. J. *Angewandte Chemie* **2014**, *126*, 11488–11491.

[35] Metters, O. J.; Forrest, S. J.; Sparkes, H. A.; Manners, I.; Wass, D. F. *Journal of the American Chemical Society* **2016**, *138*, 1994–2003.

[36] Scott, D. J.; Phillips, N. A.; Sapsford, J. S.; Deacy, A. C.; Fuchter, M. J.; Ashley, A. E. *Angewandte Chemie* **2016**, *128*, 14958–14962.

[37] Weicker, S. A.; Stephan, D. W. *Bulletin of the Chemical Society of Japan* **2015**, *88*, 1003–1016.

[38] Sumerin, V.; Schulz, F.; Nieger, M.; Leskelä, M.; Repo, T.; Rieger, B. *Angewandte Chemie International Edition* **2008**, *47*, 6001–6003.

[39] Chase, P. A.; Stephan, D. W. *Angewandte Chemie* **2008**, *120*, 7543–7547.

[40] Holschumacher, D.; Bannenberg, T.; Hrib, C. G.; Jones, P. G.; Tamm, M. *Angewandte Chemie* **2008**, *120*, 7538–7542.

[41] Hounjet, L. J.; Bannwarth, C.; Garon, C. N.; Caputo, C. B.; Grimme, S.; Stephan, D. W. *Angewandte Chemie* **2013**, *125*, 7640–7643.

[42] Li, H.; Aquino, A. J.; Cordes, D. B.; Hung-Low, F.; Hase, W. L.; Krempner, C. *Journal of the American Chemical Society* **2013**, *135*, 16066–16069.

[43] Mummadi, S.; Unruh, D. K.; Zhao, J.; Li, S.; Krempner, C. *Journal of the American Chemical Society* **2016**, *138*, 3286–3289.

[44] Stephan, D. W.; Erker, G. *Angewandte Chemie International Edition* **2010**, *49*, 46–76.

[45] Stephan, D. W.; Erker, G. *Angewandte Chemie International Edition* **2015**, *54*, 6400–6441.

[46] Stephan, D. W. *Science* **2016**, *354*, aaf7229.

[47] Stephan, D. W.; Erker, G. *Chemical Science* **2014**, *5*, 2625–2641.

[48] Stephan, D. W. *Accounts of chemical research* **2014**, *48*, 306–316.

[49] McCahill, J. S.; Welch, G. C.; Stephan, D. W. *Angewandte Chemie* **2007**, *119*, 5056–5059.

[50] Dureen, M. A.; Stephan, D. W. *Journal of the American Chemical Society* **2009**, *131*, 8396–8397.

[51] Chang, K.; Wang, X.; Fan, Z.; Xu, X. *Inorganic chemistry* **2018**, *57*, 8568–8580.

[52] Rokob, T. A.; Hamza, A.; Stirling, A.; Soós, T.; Pápai, I. *Angewandte Chemie International Edition* **2008**, *47*, 2435–2438.

[53] Bakó, I.; Stirling, A.; Bálint, S.; Pápai, I. *Dalton Transactions* **2012**, *41*, 9023–9025.

[54] Rocchigiani, L.; Ciancaleoni, G.; Zuccaccia, C.; Macchioni, A. *Journal of the American Chemical Society* **2013**, *136*, 112–115.

[55] Hamza, A.; Stirling, A.; András Rokob, T.; Pápai, I. *International Journal of Quantum Chemistry* **2009**, *109*, 2416–2425.

[56] Grimme, S.; Kruse, H.; Goerigk, L.; Erker, G. *Angewandte Chemie International Edition* **2010**, *49*, 1402–1405.

[57] Rokob, T. A.; Hamza, A.; Pápai, I. *Journal of the American Chemical Society* **2009**, *131*, 10701–10710.

[58] Bordwell, F. G. *Accounts of Chemical Research* **1988**, *21*, 456–463.

[59] Beckett, M. A.; Strickland, G. C.; Holland, J. R.; Varma, K. S. *Polymer* **1996**, *37*, 4629–4631.

[60] Heiden, Z. M.; Lathem, A. P. *Organometallics* **2015**, *34*, 1818–1827.

[61] others,, et al. *Inorganic chemistry* **2011**, *50*, 12338–12348.

[62] Paradies, J. *Angewandte Chemie International Edition* **2014**, *53*, 3552–3557.

[63] Hounjet, L. J.; Stephan, D. W. *Organic Process Research & Development* **2014**, *18*, 385–391.

[64] Stephan, D. W. *Organic & biomolecular chemistry* **2012**, *10*, 5740–5746.

[65] Mahdi, T.; Stephan, D. W. *Journal of the American Chemical Society* **2014**, *136*, 15809–15812.

[66] Scott, D. J.; Fuchter, M. J.; Ashley, A. E. *Journal of the American Chemical Society* **2014**, *136*, 15813–15816.

[67] Greb, L.; Oña-Burgos, P.; Schirmer, B.; Grimme, S.; Stephan, D. W.; Paradies, J. *Angewandte Chemie* **2012**, *124*, 10311–10315.

[68] Greb, L.; Daniliuc, C.-G.; Bergander, K.; Paradies, J. *Angewandte Chemie International Edition* **2013**, *52*, 5876–5879.

[69] Palomas, D.; Holle, S.; Inés, B.; Bruns, H.; Goddard, R.; Alcarazo, M. *Dalton Transactions* **2012**, *41*, 9073–9082.

[70] Chernichenko, K.; Madarász, Á.; Pápai, I.; Nieger, M.; Leskelä, M.; Repo, T. *Nature Chemistry* **2013**, *5*, 718–723.

[71] Segawa, Y.; Stephan, D. W. *Chemical Communications* **2012**, *48*, 11963–11965.

[72] Mahdi, T.; Heiden, Z. M.; Grimme, S.; Stephan, D. W. *Journal of the American Chemical Society* **2012**, *134*, 4088–4091.

[73] Geier, S. J.; Chase, P. A.; Stephan, D. W. *Chemical Communications* **2010**, *46*, 4884–4886.

[74] Xu, X.; Kehr, G.; Daniliuc, C. G.; Erker, G. *Journal of the American Chemical Society* **2013**, *135*, 6465–6476.

[75] Xu, X.; Kehr, G.; Daniliuc, C. G.; Erker, G. *Journal of the American Chemical Society* **2015**, *137*, 4550–4557.

[76] Flynn, S. R.; Metters, O. J.; Manners, I.; Wass, D. F. *Organometallics* **2016**, *35*, 847–850.

[77] Cooper, R. T.; Sapsford, J. S.; Turnell-Ritson, R. C.; Hyon, D.-H.; White, A. J.; Ashley, A. E. *Phil. Trans. R. Soc. A* **2017**, *375*, 20170008.

[78] Tussing, S.; Greb, L.; Tamke, S.; Schirmer, B.; Muhle-Goll, C.; Luy, B.; Paradies, J. *Chemistry–A European Journal* **2015**, *21*, 8056–8059.

[79] Tussing, S.; Kaupmees, K.; Paradies, J. *Chemistry–A European Journal* **2016**, *22*, 7422–7426.

[80] Greb, L.; Tussing, S.; Schirmer, B.; Ona-Burgos, P.; Kaupmees, K.; Lokov, M.; Leito, I.; Grimme, S.; Paradies, J. *Chemical Science* **2013**, *4*, 2788–2796.

[81] Whittemore, S. M.; Autrey, T. *Israel Journal of Chemistry* **2015**, *55*, 196–201.

[82] Das, S.; Pati, S. *Catalysis Science & Technology* **2018**,

[83] Rokob, T. A.; Hamza, A.; Stirling, A.; Pápai, I. *Journal of the American Chemical Society* **2009**, *131*, 2029–2036.

[84] Mane, M. V.; Vanka, K. *ChemCatChem* **2017**, *9*, 3013–3022.

[85] Erős, G.; Nagy, K.; Mehdi, H.; Pápai, I.; Nagy, P.; Király, P.; Tárkányi, G.; Soós, T. *Chemistry–A European Journal* **2012**, *18*, 574–585.

[86] Özgün, T.; Ye, K.-Y.; Daniliuc, C. G.; Wibbeling, B.; Liu, L.; Grimme, S.; Kehr, G.; Erker, G. *Chemistry–A European Journal* **2016**, *22*, 5988–5995.

[87] Wang, X.; Kehr, G.; Daniliuc, C. G.; Erker, G. *Journal of the American Chemical Society* **2014**, *136*, 3293–3303.

[88] Guo, Y.; Li, S. *Inorganic chemistry* **2008**, *47*, 6212–6219.

[89] Jensen, F. *Introduction to computational chemistry*; John Wiley & Sons, 2013.

[90] Koch, W.; Holthausen, M. C. *A chemist's guide to density functional theory*; 2001; Vol. 2.

[91] Szabo, A.; Ostlund, N. S. *Modern quantum chemistry: introduction to advanced electronic structure theory*; Dover Publications, 1996.

[92] Hohenberg, P.; Kohn, W. *Phys. Rev.* **1964**, *136*, B864–B871.

[93] Kohn, W.; Sham, L. J. *Phys. Rev.* **1965**, *140*, A1133–A1138.

[94] Kohn, W. *Rev. Mod. Phys.* **1999**, *71*, 1253–1266.

[95] Ceperley, D.; Alder, B. *Phys. Rev. Lett* **1980**, *45*, 566–569.

[96] Perdew, J. P.; Burke, K.; Ernzerhof, M. *Physical review letters* **1996**, *77*, 3865.

[97] Perdew, J. P.; Chevary, J. A.; Vosko, S. H.; Jackson, K. A.; Pederson, M. R.; Singh, D. J.; Fiolhais, C. *Physical Review B* **1992**, *46*, 6671.

[98] Zhao, Y.; Truhlar, D. G. *Theor. Chem. Acc.* **2008**, *120*, 215–241.

[99] Zhao, Y.; Truhlar, D. G. *J. Phys. Chem. A* **2006**, *110*, 13126–13130.

[100] Becke, A. D. *J. Chem. Phys.* **1993**, *98*, 5648–5652.

[101] Yanai, T.; Tew, D. P.; Handy, N. C. *Chem. Phys. Lett.* **2004**, *393*, 51–57.

[102] Chai, J.-D.; Head-Gordon, M. *Phys. Chem. Chem. Phys* **2008**, *10*, 6615–6620.

Chapter 2

On the Mechanism of $B(C_6F_5)_3$-Catalysed Hydrogenation of Carbonyl Compounds*

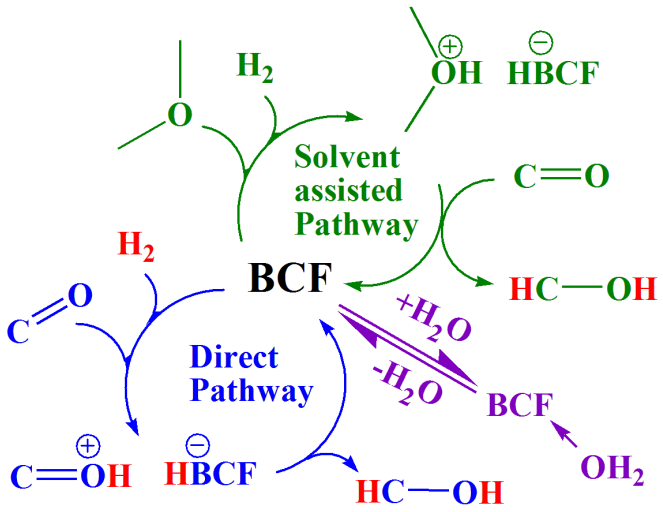

BCF : $B(C_6F_5)_3$

*Work reported in this chapter is published in: Shubhajit Das, Swapan K Pati, Chemistry-A European Journal, 2017, 23, 1078-1085. Reproduced with permission from John Wiley and Sons.

2.1 Introduction

Over the last decade, FLPs have been successfully employed for the reduction of a variety of unsaturated organic substrates including imines [1], nitriles, enamines [2], N-heterocycles [3], olefines [4], etc. Nonetheless, FLP-catalysed hydrogenation of organic carbonyl compounds has been particularly challenging. This is perhaps surprising as in 2007 Erker *et al.* reported stoichiometric hydrogenation of benzaldehyde by an intramolecular phosphine-borane FLP, $Mes_2PCH_2CH_2B(C_6F_5)_2$ [5]. Also, in 2009, Privalov *et al.* [6] computationally predicted $B(C_6F_5)_3$ (hereafter denoted as BCF)-catalysed direct hydrogenation of ketones to secondary alcohols. Unfortunately, in an attempt to realize this experimentally, Repo *et al.* [7] found that the BCF-catalysed hydrogenation of aromatic carbonyls follows stoichiometric deoxygenation route, resulting in aryl-substituted methane. Similar findings have also been reported by Stephan *et al.* [8] with aliphatic ketones. It took almost seven years to formulate a catalytic protocol until 2014, when the group of Stephan [9] and that of Ashley [10] simultaneously accomplished metal-free catalytic hydrogenation of carbonyl compounds to the corresponding alcohols (see Figure 2.1). These reactions involve direct use of H_2 as the hydrogen source, and the reaction is performed in ether solvents in the presence of catalytic amount of BCF. Alternatively, under similar conditions, instead of ether, these reactions can also be performed with oxygen-containing materials such as cyclodextrin or molecular sieves [11]. Very recently, moisture-tolerant FLP catalysts [12] for catalytic hydrogenation of aldehyde and ketones have also been reported.

As shown in Figure 2.1, two mechanisms for the BCF-catalysed hydrogenation of carbonyl compounds in ethereal solvent have been proposed. The first possibility is a transfer hydrogenation pathway where the solvent (ether) itself plays an active role. Heterolytic hydrogen clevage by a ether-borane Lewis pair has been proposed to generate a protonated ether and a hydridoborate anion; subsequent proton and hydride delivery complete the carbonyl reduction to alcohol. The initial ether-borane

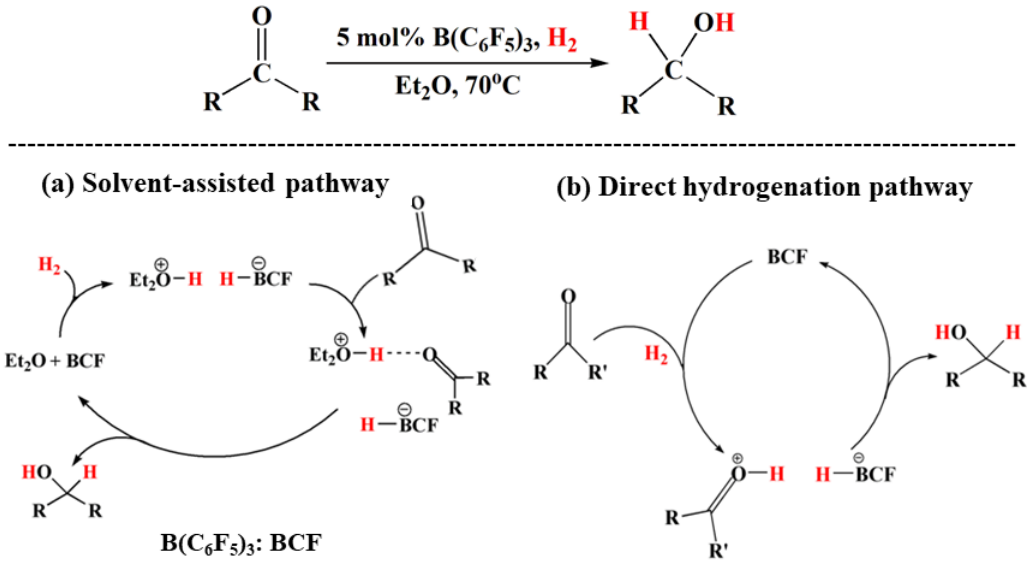

Figure 2.1: Possible reaction routes for BCF-catalysed hydrogenation of carbonyl compounds.

mediated H_2 activation, which has already been described in previous studies, provides solid support to this mechanism [13]. However, an alternate hydrogenation pathway, consisting of direct carbonyl-borane mediated H_2 activation, prior to the hydride transfer step, can not be ruled out. Infact, this reaction route is reminiscent of the mechanism of BCF-catalysed hydrogenation of imines [14]. This has prompted us to perform a detailed computational study to elucidate the full mechanism of metal-free carbonyl hydrogenation mediated by BCF. In order to gain detailed insight into the possible reaction pathways, we have resorted to density functional theory (DFT) based calculations.

2.2 Computational Details

All electronic structure calculations are performed at the DFT level using the dispersion corrected, range-separated hybrid $\omega B97XD$ [15, 16] exchange-correlational functional. 6-31+G(d,p) basis set is used for geometry optimization of all the investigated species. Additional single-point energy calculations are performed employing larger basis set, 6-311++G(d,p), for refining the energies.The ultra-fine integration grid is used for numerical integrations. The stationary points are characterized by

vibrational analysis to recognise the structures as minima (all positive frequencies) or transition state(s) (one negative frequency). Transition states (TSs) are verified through intrinsic reaction coordinate (IRC) calculations. All thermochemical data are estimated within the ideal gas-rigid rotor-harmonic oscilltor approximation at 343.15 K. SMD [17] model is used to take into account solvent effects at the $\omega B97XD$/6-31+G(d,p) level. All DFT calculations are performed using the Gaussian 09 [18] suit of programs.

Note that, we have used the following atom colouring to visualize the molecular geometries: C (grey), H (white), O (red), F (green), and B (pink).

2.3 Results and Discussions

2.3.1 Stoichiometric reaction

On the basis of experimental findings, the hydrogenation of carbonyl compounds proceeds at 70 °C and 60 atm of H_2 pressure in the presence of 5 mol% BCF with diethylether (Et_2O) as the solvent [9]. We first analyze the potential energy surface (PES) related to the stoichiometric reaction of carbonyl compound with BCF and H_2 in order to gain insights into the mechanism for the hydrogenation process. For the present study, we have chosen 4-heptanone (hereby denoted as Pr_2CO) as the prototype carbonyl substrate and diethylether as the solvent.

2.3.1.1 Solvent-assisted pathway

We start the discussion by exploring the solvent-assisted reaction route as shown in pathway **a**. The catalyst BCF, H_2, solvent Et_2O and the substrate Pr_2CO molecules are used as the zero energy reference. The reaction course is thought to begin with the heterolytic H_2 splitting by the ether-borane FLP. We indeed have identified a noncovalent association between ether and borane molecules, resulting in a encounter complex (EC) structure, Et_2O/BCF. The structure of this FLP reveals a B-O distance of 3.83 Å (which is much longer compared to that in the Et_2O/BCF dative adduct, 1.63 Å). Also, the central BC_3 unit in BCF remains almost planar, indicating the

absence of any ether-borane dative bond. The EC is stabilized by -9.2 kcal/mol with respect to BCF+Et_2O. The Et_2O/BCF EC reacts with molecular hydrogen, leading to the formation of zwitterion, $[Et_2OH]^+[BCFH]^-$, containing protonated ether and hydridoborate anion. In analogy with the previously reported FLP activation of H_2 [14, 19], we anticipated a single, concerted, transition state for H_2 splitting reaction. However, all efforts made towards locating a single transition state for synergistic, concerted H_2 splitting have failed. Instead, we have found that Et_2O/BCF EC activates H_2 in a stepwise manner [20]. First, H_2 coordinates to EC to form an initial adduct complex **INT1-a**. To achieve H_2 activation, **INT1-a** is rearranged to form **INT2-a** via **TS-H2act-1-a** where H_2 approaches towards the boron center in an asymetrical side-on fashion and the corresponding energy barrier is fairly low, 5.3 kcal/mol. **TS-H2act-1-a** features slightly elongated H-H distance of 0.77 Å (compared to 0.74 Å in H_2 itself) and the B-H distances are 1.65 Å and 1.79 Å, revealing significant interaction between the boron and the hydrogen atoms. The bonding situation in **TS-H2act-1-a** is furthur analysed by NBO calculations which suggest two B-H bond orders as 0.20 and 0.26. The computed structure of **INT2-a** shows further elongated H-H distance, 0.79 Å and two B-H distances are of 1.43 Å and 1.56 Å (bond orders are 0.39 and 0.30 respectively). Interestingly, the oxygen center is also engaged in weak contact with one of the H atoms. The corresponding O-H distance is lesser than the sum of the van der Waal radii of the oxygen (1.55 Å) and hydrogen atoms (1.20 Å). The subsequent deprotonation process, occuring with very low energy barrier (0.9 kcal/mol), by the ethereal oxygen leads to the hydrogen activated product via **TS-H2act-2-a** which shows a H-H distance of 0.86 Å and the partially fromed B-H (1.34 Å) and O-H (1.46 Å) bonds. In the structure of the zwitterionic product , $[Et_2OH]^+[BCFH]^-$, the protic and the hydridic hydrogen atoms are only 1.22 Å apart, which indicates the presence of a O-H...H-B dihydrogen bond. Splitting of H_2 by Et_2O/BCF FLP is exothermic by 9.4 kcal/mol. Infact, an additional ether molecule can provide extra stabiization to $[Et_2OH]^+[BCFH]^-$

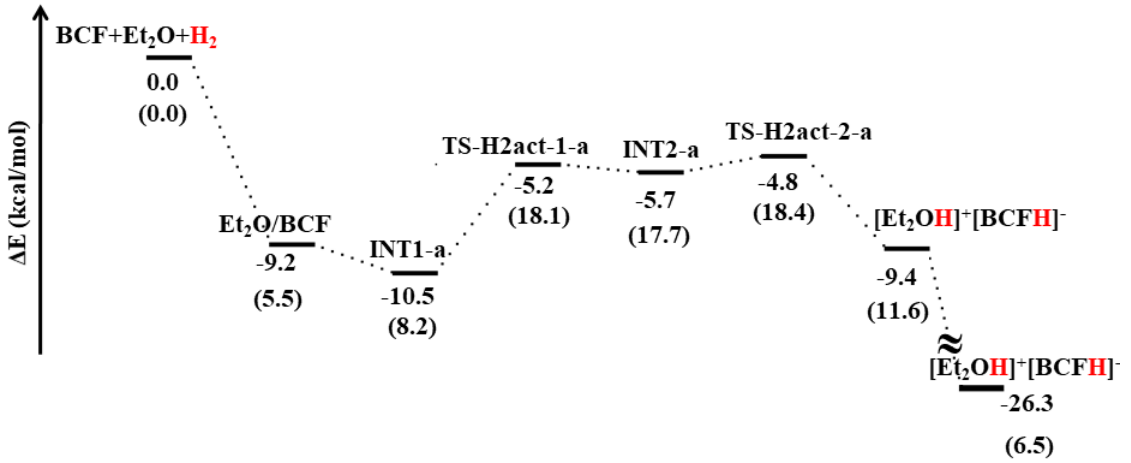

Figure 2.2: The potential energy profile for the H_2 activation in the pathway **a** of BCF-catalyzed hydrogenation of 4-heptanone. The energy values reported in this figure are $\omega B97XD$/6-311++G(d,p)// $\omega B97XD$/6-31+G(d,p) gas-phase electronic energies. Computed Solution phase Gibbs free energy values (at T=343.15 K) are given in parenthesis.

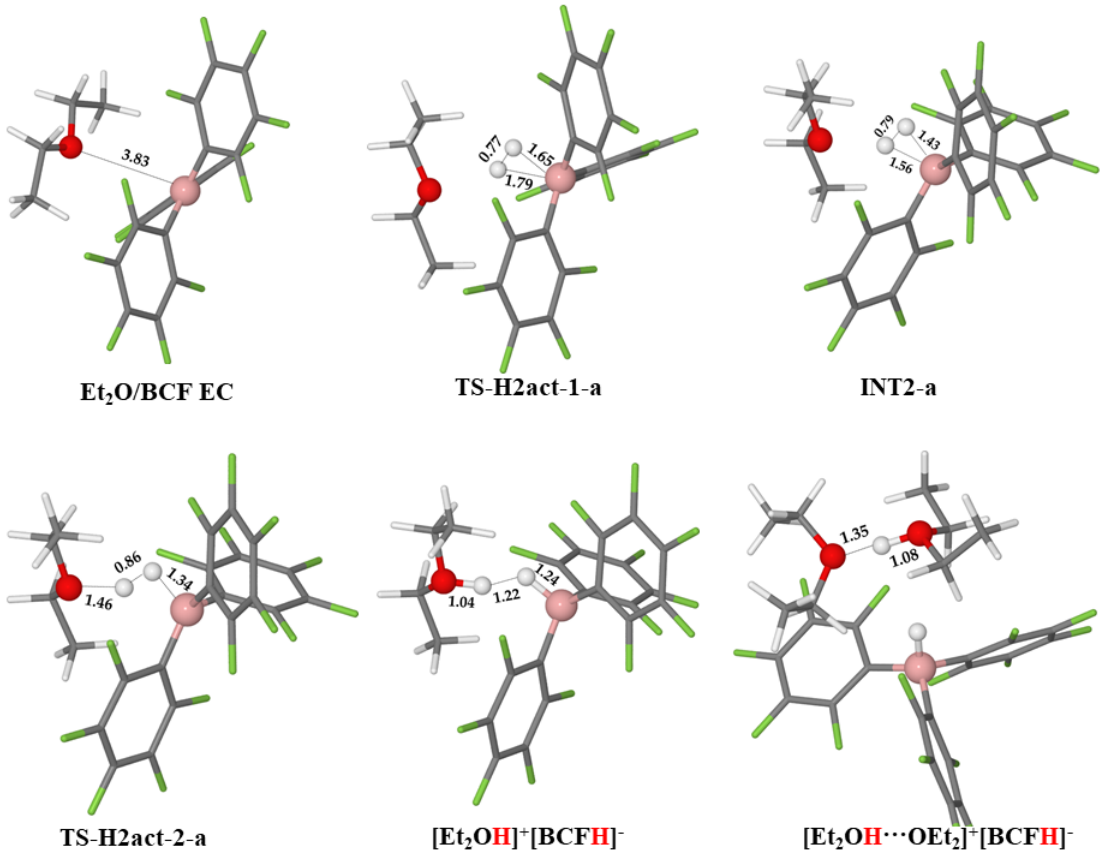

Figure 2.3: Geometry optimized structures of the intermediates/TSs for the H_2 activation step in the pathway **a** of BCF-catalyzed hydrogenation of 4-heptanone. All distances shown in the figure are in Å unit.

ion-pair by explicit solvation of the proton. The second ether molecule forms a strong hydrogen bond (O...H distance 1.35 Å) with the protonated ether moiety resulting in $[Et_2OH\cdots OEt_2]^+[BCFH]^-$ ion-pair which is about 16.9 kcal/mol more stable in the potential energy landscape than the former ion-pair. The corresponding relative energy profile and the geometry optimized structures of the intermediates/TSs involved in the H_2 activation step are shown in Figure 2.2 and Figure 2.3, respectively.

However, instead of a second ether molecule, a substrate molecule (Pr_2CO) can similarly associate itself to the protonated ether through hydrogen bonding interaction, leading to the formation of $[Et_2OH\cdots OCPr_2]^+[BCFH]^-$ ion-pair through **TS-COact-a**. The reaction begins with the coordination of the Pr_2CO molecule to the $[Et_2OH]^+[BCFH]^-$ ion-pair to form a ternary complex, $[Et_2OH]^+[BCFH]^-Pr_2CO$, imparting a stabilization of about 17.6 kcal/mol. This complex shows a relatively weakened dihydrogen bond as shown by the increased H-H distance of 1.46 Å (compared to 1.22 Å in $[Et_2OH]^+[BCFH]^-$) and also, the carbonyl oxygen establishes a contact with the proton attached to the ether unit. In **TS-COact-a**, the dihydrogen bond weakens further as the H-H distance increases to 1.72 Å while the carbonyl oxygen-proton distance lowers down to 1.91 Å indicating significant interaction. Eventually, the carbonyl oxygen hydrogen bonds to the protonated ether in $[Et_2OH\cdots OCPr_2]^+[BCFH]^-$ with a $O\cdots H$ distance of 1.38 Å.

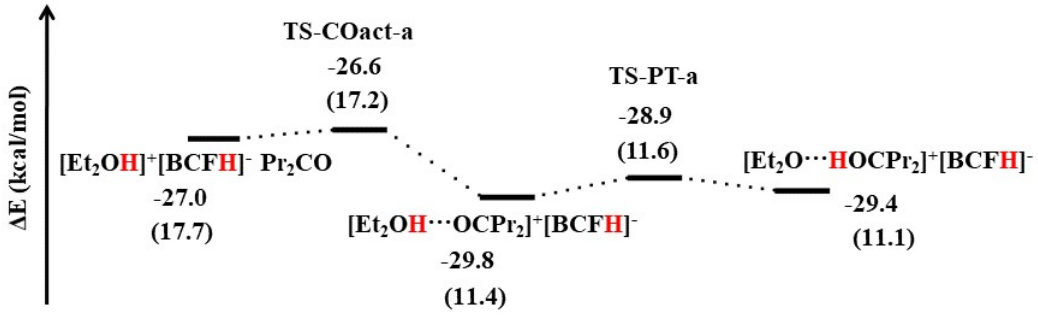

Figure 2.4: The potential energy profile for the substrate activation and PT steps in the pathway **a** of BCF-catalyzed hydrogenation of 4-heptanone. The energy values reported in this figure are $\omega B97XD$/6-311++G(d,p)// $\omega B97XD$/6-31+G(d,p) gas-phase electronic energies. Computed Solution phase Gibbs free energy values (at T=343.15 K) are given in parenthesis.

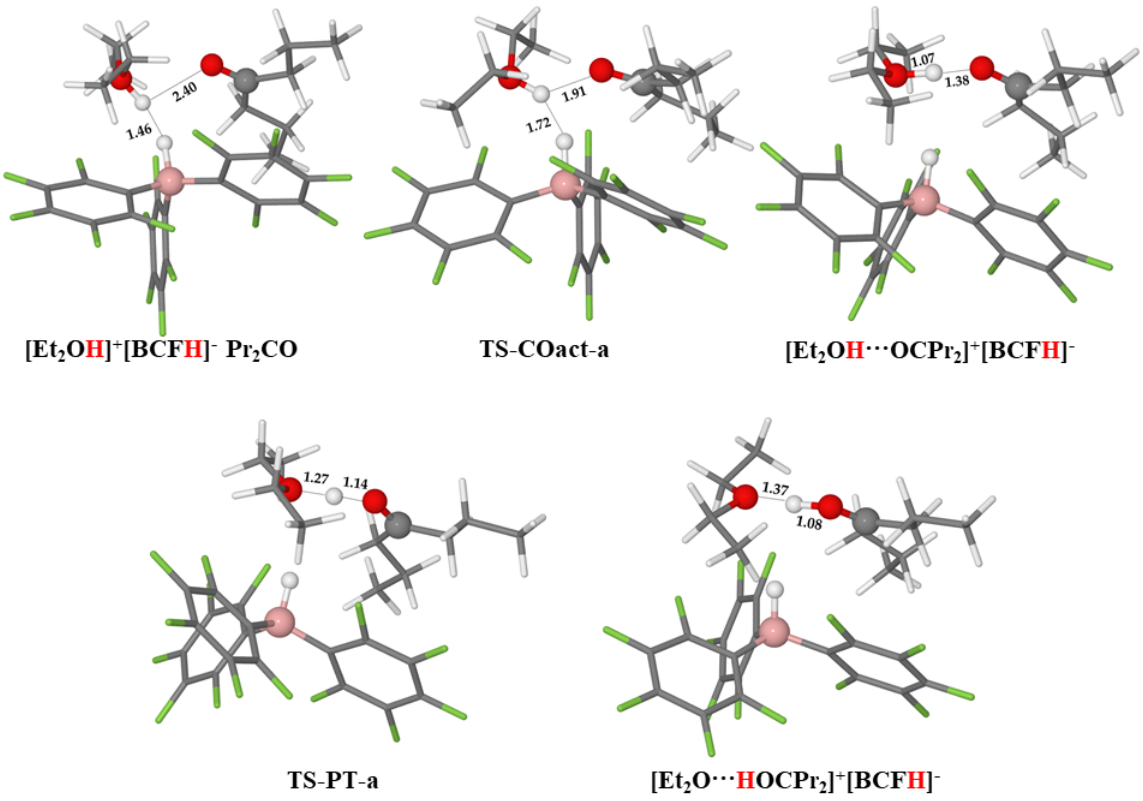

Figure 2.5: Geometry optimized structures of the intermediates/TSs for the substrate activation and PT steps in the pathway **a** of BCF-catalyzed hydrogenation of 4-heptanone. All distances shown in the figure are in Å unit.

Following the substrate activation, we find that a proton transfer (PT) can occur between the ethereal oxygen and the carbonyl oxygen via **TS-PT-a** generating the ion-pair, $[Et_2O\cdots HOCPr_2]^+[BCFH]^-$. **TS-PT-a** features a proton residing between two oxygen atoms with O-H distances of 1.14 Å (carbonyl oxygen) and 1.27 Å (ether oxygen). The PES corresponding to substrate activation and proton transfer is found to be quite flat with relative activation energy barriers of 0.4 and 0.9 kcal/mol, respectively. The structure of $[Et_2O\cdots HOCPr_2]^+[BCFH]^-$ shows that the transferred proton still remains associated to the ethereal oxygen by strong hydrogen bonding interaction. Moreover, we also find that the carbonyl carbon atom has increased positive NPA atomic charges (0.758 compared to 0.629 in free Pr_2CO) and thereby increasing its philicity towards hydride from the $[BCFH]^-$ anion. The corresponding

relative energy profile and the geometry optimized structures of the intermediates/TSs involved in the carbonyl activation and the PT steps are shown in Figure 2.4 and Figure 2.5, respectively.

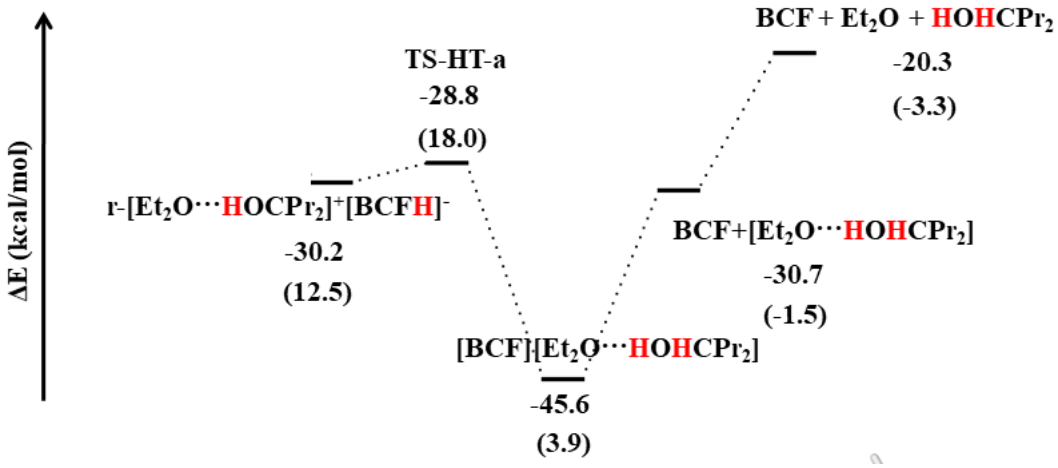

Figure 2.6: The potential energy profile for the HT step in the pathway **a** of BCF-catalyzed hydrogenation of 4-heptanone. The energy values reported in this figure are $\omega B97XD$/6-311++G(d,p)// $\omega B97XD$/6-31+G(d,p) gas-phase electronic energies. Computed Solution phase Gibbs free energy values (at T=343.15 K) are given in parenthesis.

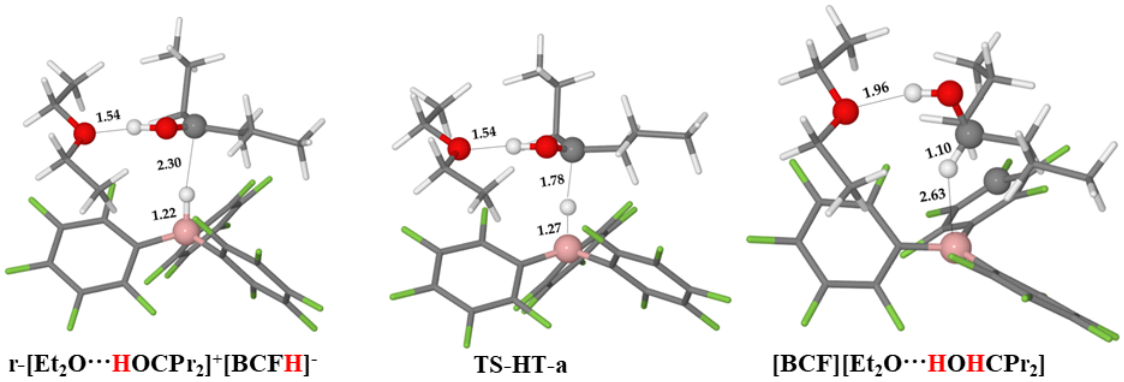

Figure 2.7: Geometry optimized structures of the intermediates/TSs for the HT step in the pathway **a** of BCF-catalyzed hydrogenation of 4-heptanone. All distances shown in the figure are in Å unit.

After the PT step, the B-H bond reorients itself to give isomer, r-$[Et_2O\cdots HOCPr_2]^+$ $[BCFH]^-$ wherein the B-H bond points directly towards the carbonyl carbon atom. Thereafter, the hydride transfer (HT) readily occurs via **TS-HT-a**, and throughout the HT process, the ether molecule remains hydrogen-bonded to the protonated

carbonyl moiety. **TS-HT-a** features B-H and C-H distances of 1.27 and 1.78 Å along with a B-H-C angle of 172.4 ° . The HT step is exothermic by 15.4 kcal/mol yielding [BCF][$Et_2O\cdots HOHCPr_2$] which can be dissociated to release the product alcohol (4-heptanol) and the borane catalyst. The corresponding relative energy profile and the geometry optimized structures of the intermediates/TSs involved in the HT step are shown in Figure 2.6 and Figure 2.7, respectively.

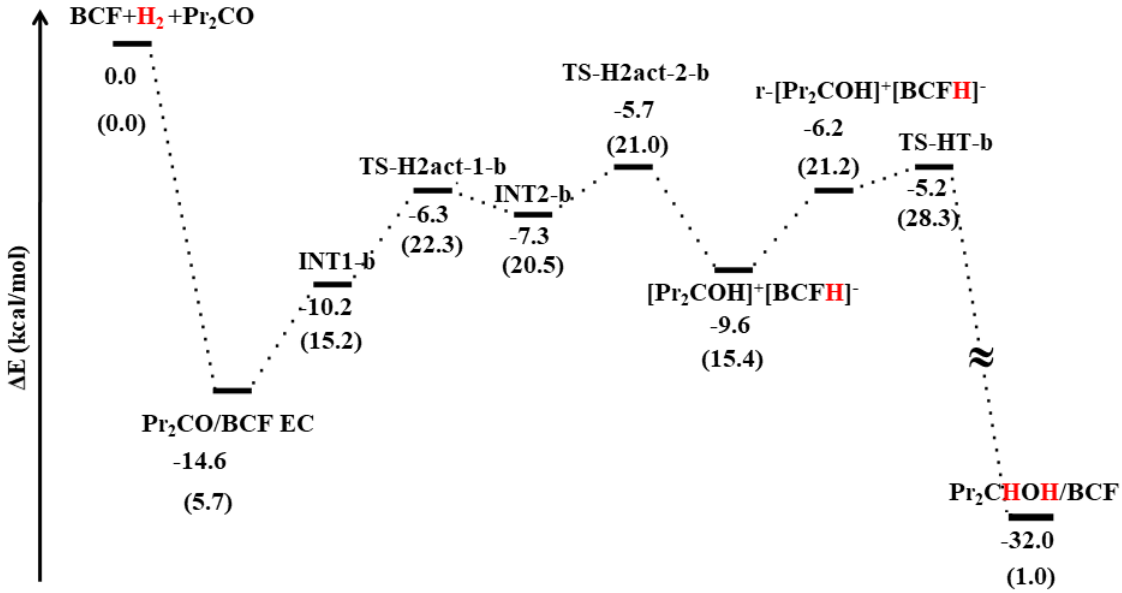

Figure 2.8: The potential energy profile for the pathway **b** of BCF-catalyzed hydrogenation of 4-heptanone. The energy values reported in this figure are $\omega B97XD$/6-311++G(d,p)// $\omega B97XD$/6-31+G(d,p) gas-phase electronic energies. Computed Solution phase Gibbs free energy values (at T=343.15 K) are given in parenthesis.

2.3.1.2 Direct Hydrogenation Pathway

Next, we focus on the direct hydrogenation route as shown in pathway **b**. The relative energy profile for the computed detailed reaction pathway is shown in Figure 2.8. In this pathway, the substrate, Pr_2CO, itself acts as a base partner to BCF and therefore, the reaction course begins with a ketone-borane mediated H_2 activation, leading to the formation of $[Pr_2COH]^+[BCFH]^-$ ion-pair. This H_2 activation step shares a number of common features with the previously described H_2 splitting by Et_2O/BCF FLP. As per our expectation, we have located a Pr_2CO/BCF EC on the PES and the species has a binding energy of -14.6 kcal/mol. The EC is predicted to

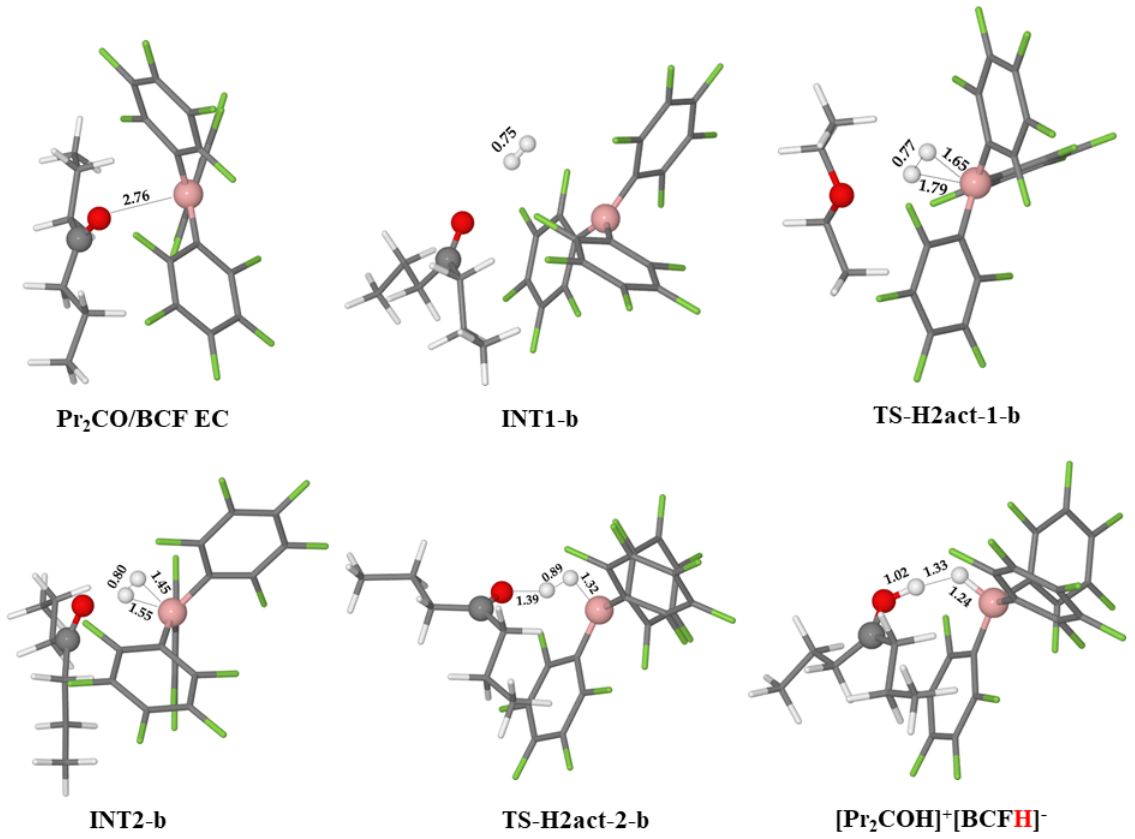

Figure 2.9: Geometry optimized structures of the intermediates/TSs for the H_2 activation step in the pathway **b** of BCF-catalyzed hydrogenation of 4-heptanone. All distances shown in the figure are in Å unit.

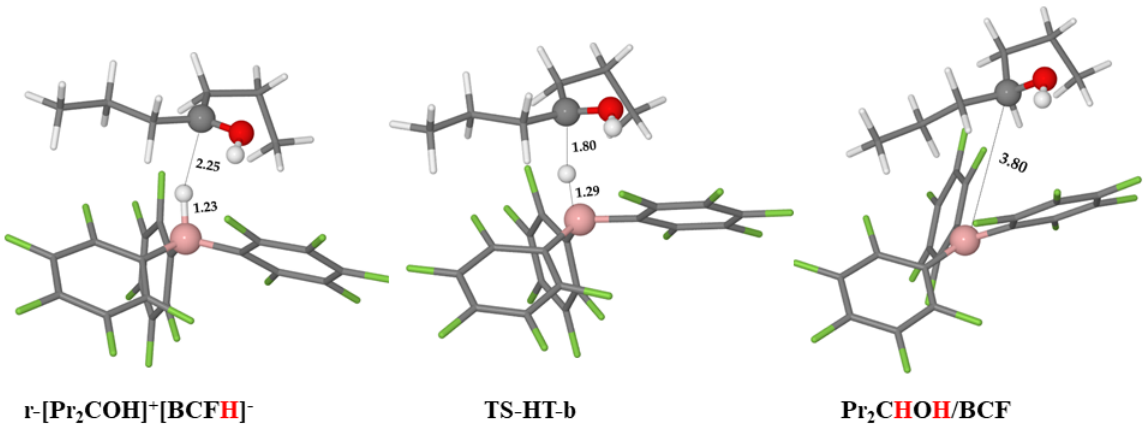

Figure 2.10: Geometry optimized structures of the intermediates/TSs for the HT step in the pathway **b** of BCF-catalyzed hydrogenation of 4-heptanone. All distances shown in the figure are in Å unit.

react with H_2 in a similar way as Et_2O/BCF EC; stepwise activation of H_2 involving two TSs. First, an initial adduct complex, **INT1-b**, is formed between the FLP

and the H_2 molecule. In analogy to pathway **a**, the dihydrogen molecule approaches towards the boron centre in an assymetrical side-on fashion leading to the formation of **INT2-b** through **TS-H2act-1-b**, which lies 3.9 kcal/mol above **INT1-b**. The structure of **INT2-b** shows a H-H distance of 0.80 Å and B-H distances of 1.45 Å and 1.55 Å. **INT2-b** is converted to the H_2 activated product via **TS-H2act-2-b** and the corresponding barrier is also found to be quite low (1.6 kcal/mol). **TS-H2act-2-b** features a H-H distance of 0.89 Å and the partially fromed B-H (1.32 Å) and O-H (1.39 Å) bonds. The calculated structures of $[Pr_2COH]^+[BCFH]^-$ shows a dihydrogen bond with a H-H distance of 1.33 Å which is slightly higher than that in $[Et_2OH]^+[BCFH]^-$ ion-pair. Similarly, like pathway **a**, prior to HT step, $[Pr_2COH]^+[BCFH]^-$ ion-pair undergoes an internal rearrangement to suitably orient the B-H bond towards the carbonyl carbon. Subsequently, HT takes place to complete the hydrogenation process. The HT transtion state, **TS-HT-b**, shows similar key geometrical features compared to **TS-HT-a**. The B-H and C-H distances are of 1.29 and 1.80 Å, respectively, which are found to be very similar to those found in **TS-HT-a**. However, after the HT step, the resulting species dissociates to give the alcohol product. Overall, direct hydrogenation route comprises of two main steps: H_2 splitting by ketone-borane FLP and subsequent HT. The geometry optimized structures of the intermediates/TSs involved in the direct hydrogenation pathway are shown in Figure 2.9 and Figure 2.10.

2.3.2 Catalytic Process

The above computational results provided us with important mechanistic information for the two plausible routes, proposed for carbonyl hyrogenation reaction. Now, we aim to examine the catalytic hydrogenation process by determining the kinetic and thermodynamic feasibility of all the basic reaction steps involved in these two reaction pathways, **a** and **b**. Figure 2.11 shows the relative Gibbs free energy profile (computed at T=70 °C) for the main basic steps of the hydrogenation process.

Carbonyl hydrogenation may begin with two alternative pathways; H_2 activation

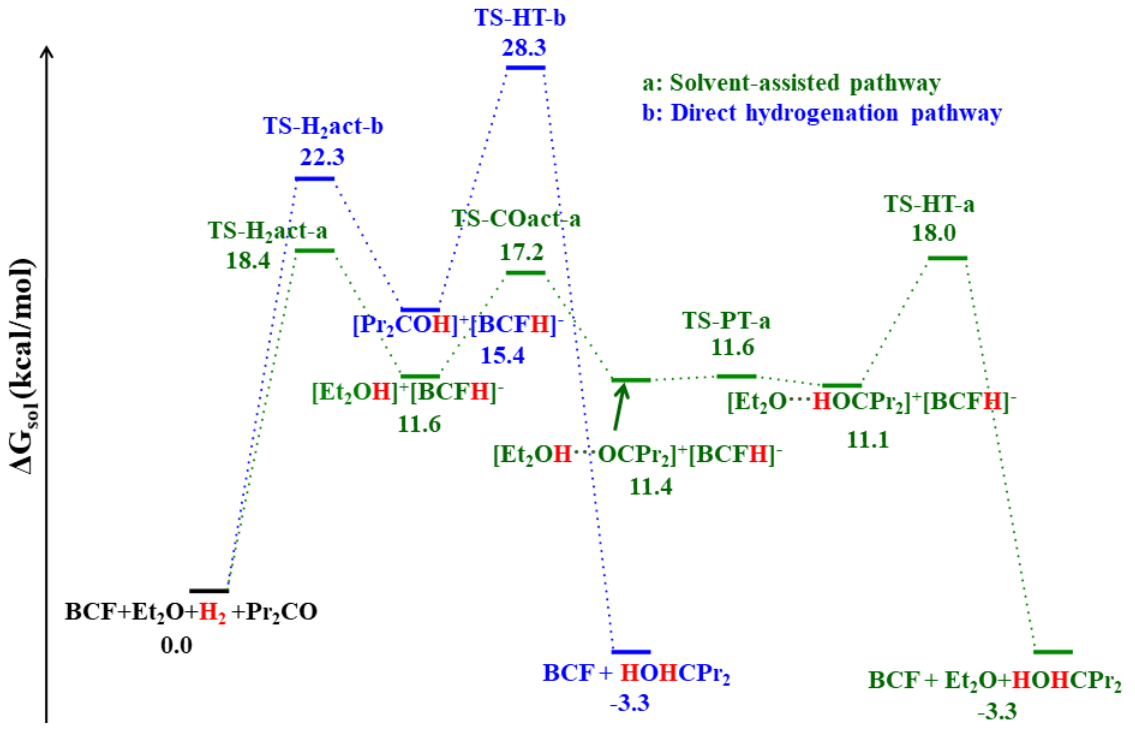

Figure 2.11: Solvent-corrected Gibbs free energy profile at T=70 °C for both solvent-assisted and direct hydrogenation pathwats. For simplicity, only the main reaction steps are shown.

by Et_2O/BCF pair in solvent-assisted pathway or by Pr_2CO/BCF pair in direct hydrogenation pathway. According to the computed free energies, the direct hydrogenation route has a higher H_2 activation barrier (22.3 kcal/mol) compared to the solvent-assisted route, making the former pathway kinetically less favorable than the latter one. The free energy barrier for H_2 cleavage step in solvent-assisted pathway is estimated to be 18.4 kcal/mol (**TS-H2act-2-a**) which is consistent with the observed reactivity at elevated temperature. The zwitterionic H_2-activated product, $[Et_2OH]^+[BCFH]^-$ which is the main active catalyst species for hydrogenation, is 11.6 kcal/mol higher in free energy compared to the reactants, indicating that this reactive intermediate is present only in very low concentrations in solution. This result is consistent with the experimental observation that reaction of a toluene solution of 5 mol% BCF and 1:1 ratio of Et_2O/Pr_2CO at 70 °C under 4 atm of H_2 afforded low yields of 4-heptanol (30%) [9]. However, as shown by the experiment, increament in H_2 pressure and Et_2O/Pr_2CO-ratio resulted in improved yields.

Eventually, quantitative yields were obtained at 70 °C under H_2 pressure, as high as 60 atm using Et_2O as solvent. Clearly, such reaction conditions have important implications, particularly, when compared to the corresponding H_2 activation by BCF/*t*Bu_3P FLP which takes place under milder reaction condition (1 atm H_2, 25 °C, toluene solvent) [19]. Basically, increasing H_2 pressure leads to high concentration of H_2 which in turn increases the degree of H_2 activation in solution. Also, large excess of one of the reactants, Et_2O (as it is used as solvent), favours the reaction equilibrium towards forward direction. Therefore, although the Et_2O/BCF-mediated H_2 activation is found to be endergonic, very high H_2 pressure as well as huge excess of Et_2O clearly shifts the equilibrium towards the H_2-activated product, maintaining significant equilibrium concentrations of $[Et_2OH]^+[BCFH]^-$. Following the H_2 activation, the protonated ether activates the carbonyl fragment via H-bonding interaction in an almost thermodymanically neutral process via **TS-COact-a** which lies at 17.2 kcal/mol. Although the subsequent PT which takes place in a very flat free energy surface, is also close to neutral in terms of free energy change, the final HT step and the dissociation of the $[BCF][Et_2O\cdots HOHCPr_2]$ species renders the overall hydrogenation thermodynamically feasible. Apparently, the exergonic HT step and the entropy release due to dissociation of the products appears to be necesssary to provide the stabilization along the reaction pathway. The hydride transfer TS, **TS-HT-a**, resides at 18.0 kcal/mol which is similar in free energy for the TSs of H_2 activation and the substrate activation step. Interestingly, in direct hydrogenation pathway, free energy of the TS for hydride transfer step is found to be significantly higher than that in the solvent-assisted pathway. This result indicates that the main stabilizing effect in **TS-HT-a** is the explicit solvent ether molecule involved in hydrogen-bonding interaction with the protonated carbonyl moiety. Overall, our computational results clearly show that carbonyl hydrogenation would kinetically prefer the solvent-assisted pathway over the direct hydrogenation route.

Note that, we have also considered and ruled out an alternative mode for the

substrate activation step in the solvent-assisted pathway. After the H_2 activation step,

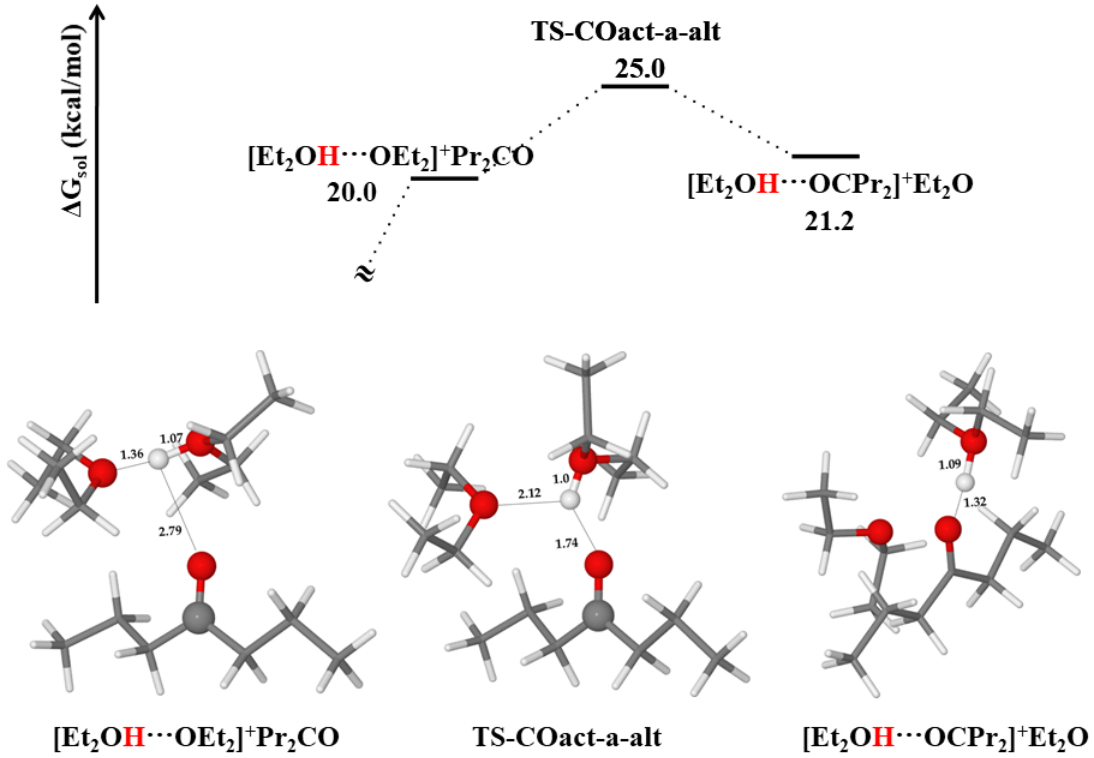

Figure 2.12: Solvent-corrected Gibbs free energy profile at T=70 °C for alternative substrate activation mode. The relative free energies (kcal/mol) are calculated with the reference to the free reactants such as BCF, H_2 , solvent Et_2O and the substrate Pr_2CO. All distances shown in the figure are in Å unit.

the $[Et_2OH]^+[BCFH]^-$ ion-pair can be further stabilized through hydrogen-bonding interaction with another ether molecule and thereby forming $[Et_2OH\cdots OEt_2]^+[BCFH]^-$ ion-pair which is 6.5 kcal/mol higher than the reactants. This ion-pair can dissociate, and the $[Et_2OH\cdots OEt_2]^+$ ion can activate the carbonyl moiety of Pr_2CO. First, a ternary cationic complex is formed when a substrate molecule associates itself with $[Et_2OH\cdots OEt_2]^+$ ion. Eventually, as shown in Figure 2.12, through **TS-COact-a-alt**, Pr_2CO molecule establishes a hydrogen bonding interaction with the protonated ether moiety. However, **TS-COact-a-alt** resides at 25.0 kcal/mol which is significantly higher than **TS-COact-a**. Thus, the alternative substrate activation mode is kinetically less favourable and accordingly, we did not pursue along this reaction route.

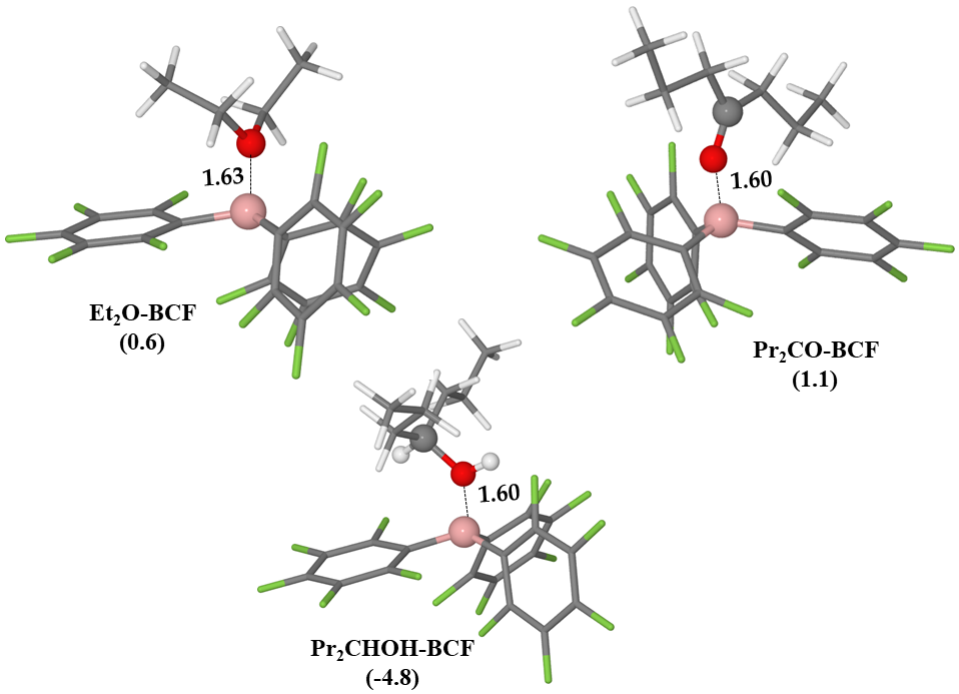

Figure 2.13: Geometry optimized structures of Et_2O-BCF, Pr_2CO-BCF and Pr_2CHOH-BCF dative complexes. Solvent-corrected Gibbs free energy value of these complexes are mentioned in parenthesis in kcal/mol. All distances shown in the figure are in Å unit.

However, a crucial point of the FLP-catalysed hydrogenation of carbonyl compounds by boranes is the catalytic turnover of the process. As the reaction proceeds, the alcohol (product) concentration builds up in the reaction mixture and this could lead to reduction in the catalytic efficiency through inhibition by the product. Basically, the alcohol binds with the borane catalyst to form a dative adduct, Pr_2CHOH-BCF. In order to reuse the catalyst, BCF, thermal dissociation of the adduct is necessary. This suggests that after the first reaction cycle, the association free energy of the alcohol-borane dative adduct must be included in the subsequent H_2 activation barrier. As a result, the effective free energy barrier for H_2 splitting increases by 4.8 kcal/mol. In fact, BCF also forms a dative-adduct with the Lewis basic Et_2O as well as with the substrate, Pr_2CO. The association Gibbs free energies of the Et_2O-BCF (0.6 kcal/mol) and Pr_2CO-BCF (1.1 kcal/mol) adducts suggest that these can be easily dissociated at higher temperature. The optimized structures of the dative-adducts are shown in Figure 2.13.

2.3.3 Moisture sensitivity of the catalyst and decomposition routes

One of the most serious limitations of BCF-catalysed hydrogenations is the extreme moisture sensitivity of the processes. As a result, these reactions are to be performed under anhydrous condition that requires extensive drying of the solvents. Actually, BCF being extremely oxophilic, in presence of water (H_2O), readily establishes an equilibrium with the dative-adduct, BCF-H_2O. This BCF-H_2O adduct can be irreversibly deprotonated by various bases present in the reaction medium. Alternatively, the adduct may also undergo a protodeborylation (**pdeb**) reaction which leads to the decomposition of the catalyst. However, these two processes constitute the main deactivation routes for BCF in presence of H_2O (see Figure 2.14). To adreess this issue, very recently Ashley *et al.* have reported notable water tolerance for BCF-catalysed hydrogenation of carbonyl compounds in ethereal solvents [21]. In fact, this protocol allows the use of non-anhydrous commercial solvents in the hydrogenation process, while keeping almost similar reaction condition as mentioned in the previous section. No catalyst decomposition was observed and the hydrogenation proceeded cleanly with practically no difference in the reaction outcome. Motivated by these intriguing results, we have extended our computational investigation to provide structural and thermochemical foundations for the experimental observations.

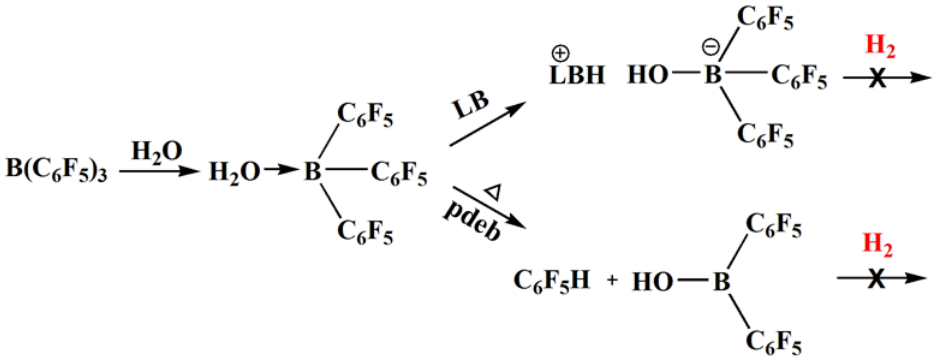

Figure 2.14: The possible decomposition routes of BCF in presence of moisture.

First, the 1:1 dative complex between BCF and water is subjected to computational

analysis. The BCF-H_2O adduct formation is only slightly endergonic (1.0 kcal.mol) in Et_2O. The pK_a of the adduct, BCF-H_2O, has been found to be similar to that of HCl [22–24] and irreversible deprotonation is possible in the presence of moderately strong bases. However, our calculations predict that the formal deprotonation of the

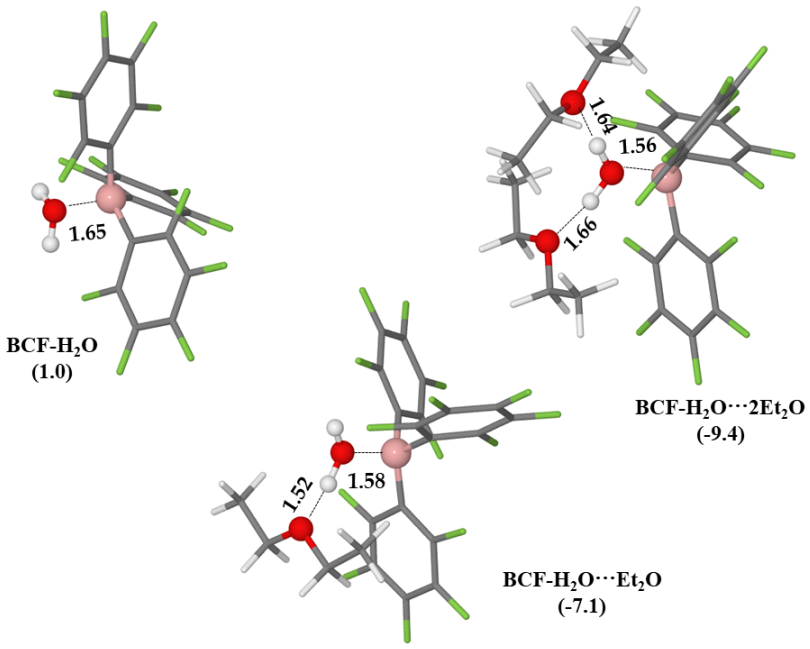

Figure 2.15: Geometry optimized structures of BCF-H_2O, and BCF-$H_2O\cdots Et_2O$ and BCF-$H_2O\cdots 2Et_2O$ complexes. Solvent-corrected Gibbs free energy value of these complexes are mentioned in parenthesis in kcal/mol. All distances shown in the figure are in Å unit.

BCF-H_2O complex (into $[Et_2OH]^+$ and $[BCF\text{-}OH]^-$ ions) by Et_2O, acting as base, is strongly endergonic by 26 kcal/mol. Although a second molecule of Et_2O can provide extra stabilization of the protonated ether (by forming $[Et_2OH\cdots OEt_2]^+$), the reaction still remains endergonic by 13.8 kcal/mol. The unfavourable thermodynamics of the reaction which can be attributed to the weak Bronsted basicity of the Et_2O, definitely rules out the possibility of an irreversible deprotonation. All attempts to locate a TS for the deprotonation reaction have failed and thus, we refrain from reaching to a pertinent kinetic prediction at this point. Rather, our calculations suggest that the adduct will be significantly stabilized by forming hydrogen bonds with the solvent molecules. In fact, this is in line with the experimenatal observations

which suggest strong interaction between the solvent and the BCF-H_2O adduct. The first ether molecule imparts a stabilization of about -8.1 kcal/mol, while the second ether molecule stabilizes the adduct further to -9.4 kcal/mol. The optimized structures of these complexes are depicted in Figure 2.15 and the O$\cdots$H bond distances found in these adducts clearly indicate H-bonding interaction between the coordinated water molecule and solvent molecules.

Next, we look at the **pdeb** route for catalyst decomposition. In **pdeb** reaction, the ipso carbon atom (C_{ipso}) on a C_6F_5 ring in BCF is protonated yielding C_6F_5H and $B(C_6F_5)_2OH$ [25]. This process is thermodynamically favoured and is computed to be strongly exergonic by 26.3 kcal/mol. For **pdeb** of BCF-H_2O, the source of labile proton is the water molecule itself which is datively bonded to B atom. The other possible source of proton can be a protonated ether, Et_2OH, which is generated in Et_2O-BCF mediated H_2-splitting, as the cationic part of the zwitterionic product. However, this possibility can be discounted as the dissociation of the zwitterion, prior to substrate activation, is not kinetically favourable. Therefore, the water molecule can directly deliver the proton to C_{ipso} and the TS for this process, **TS-pdeb-1**, lies at 35.4 kcal/mol. In **TS-pdeb-1**, the B-C_{ipso} bond is noticeably elongated to 1.87 Å (compared to 1.62 Å in BCF-H_2O) and the C_{ipso}-H and O-H distances are 1.35 and 1.27 Å, respectively. We then anticipated that a solvent ether molecule may assist in the proton delivery and help reducing the barrier for **pdeb**. As per our calculation, Et_2O-assisted proton delivery takes place in one single step via **TS-pdeb-2** which corresponds to a free energy activation barrier of 32.6 kcal/mol (2.8 kcal/mol less than **TS-pdeb-1**). An alternative two step pathway, featuring a deprotonation by an ether molecule prior to the proton delivery, can be ruled out since we already have shown that such deprotonation is strongly endergonic. This is also confirmed by IRC calculation which connects **TS-pdeb-2** directly with BCF-$H_2O\cdots Et_2O$ as the reactant. The structure of **TS-pdeb-2** features corresponding B-C_{ipso}, C_{ipso}-H and O-H distances of 1.95, 1.45, 1.16 Å, respectively. The optimized structures of

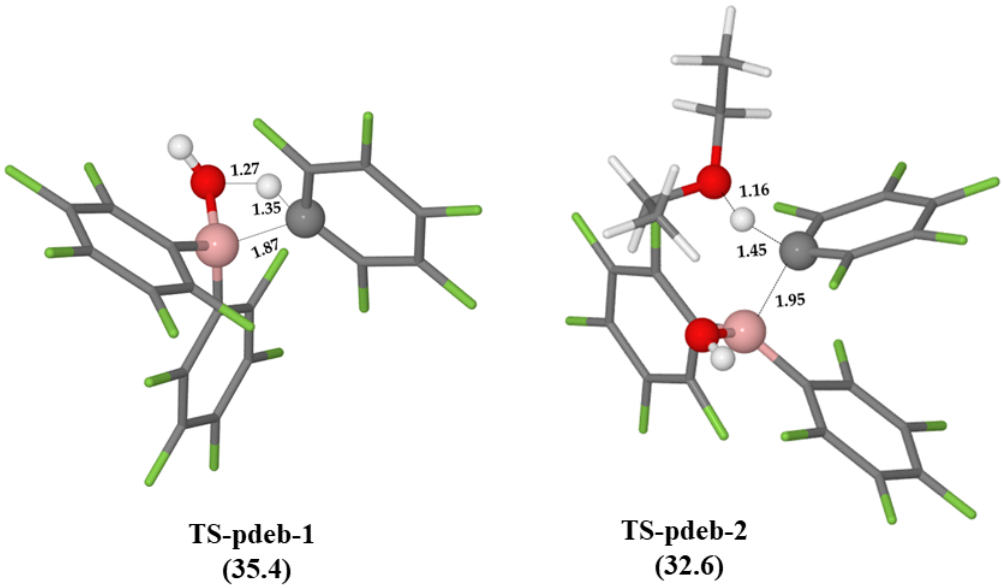

Figure 2.16: Geometry optimized structures of the TSs involved in the **pdeb** reaction. Solvent-corrected Gibbs free energy value of these complexes are mentioned in parenthesis in kcal/mol. These values are calculated with respect to the corresponding reactants obtained after IRC calculations, followed by geometry optimization to the respective minima. All distances shown in the figure are in Å unit.

TS-pdeb-1 and **TS-pdeb-2** are shown in 2.16. However, the free energy activation barrier for **pdeb** is found to be significantly high, particularly, when compared to that of hydrogenation pathway which is only around 18 kcal/mol. As a result, although **pdeb** is thermodynamically favoured, we expect the process to be kinetically very slow or hindered at the reaction temperature. This is consistent with the experimental observation that no catalyst decomposition is detected under the employed reaction condition. In fact, Ashley *et al.* observed protodeborylation in BCF-H_2O adduct in the presence of tetramethylpiperidine at temperature as high as 160 °C which is higher than reaction temperature in the present case [25].

Overall, we suggest, in non-anhydrous solvent, BCF forms dative-adduct with water, BCF-H_2O which strongly interacts with the solvent. While deprotonation of the adduct is thermodynamically disfavoured owing to the weakly basic nature of the solvent, kinetic barrier hinders the **pdeb** route for catalyst decomposition. However, thermal dissociation of the adducts at reaction temperature renders equilibrium

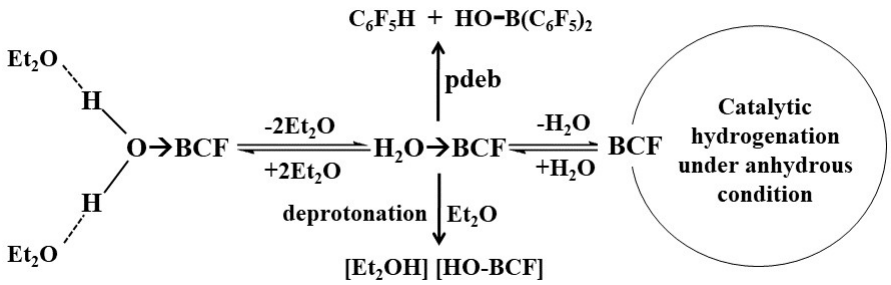

Figure 2.17: The schematic of equilibrium among BCF, BCF-H_2O adduct and corresponding solvent stabilizations. Two decomposition routes are also shown.

between datively bound and free BCF which is then expected to be available for FLP reactivity. This hypothesis is in accordance with the observed catalytic activity of BCF, even in non-anhydrous solvent. Hence, under the equilibrium condition, the adducts can be considered as the resting state of the reaction while the hydrogenation process proceeds as in anhydrous condition (see Figure 2.17).

2.4 Conclusion

Our results suggest that the BCF-catalysed hydrogenation of carbonyl compounds in ether solvent proceeds through a solvent-assisted pathway which begins with a ether-borane mediated hydrogen activation, followed by substrate activation, proton transfer and hydride transfer to complete the process. An alternative direct hydrogenation route featuring carbonyl-borane mediated hydrogen splitting is found to be kinetically unfavourable compared to the former pathway. Moreover, we find the catalyst, BCF, to be significantly moisture-tolerant and the hydrogenation can proceed even in the presence of water as it does under anhydrous condition. We are hopeful that these mechanistic findings will provide useful insights into FLP-mediated hydrogenation process.

Bibliography

[1] Chase, P. A.; Welch, G. C.; Jurca, T.; Stephan, D. W. *Angewandte Chemie International Edition* **2007**, *46*, 8050–8053.

[2] Spies, P.; Schwendemann, S.; Lange, S.; Kehr, G.; Fröhlich, R.; Erker, G. *Angewandte Chemie International Edition* **2008**, *47*, 7543–7546.

[3] Geier, S. J.; Chase, P. A.; Stephan, D. W. *Chemical Communications* **2010**, *46*, 4884–4886.

[4] Greb, L.; Oña-Burgos, P.; Schirmer, B.; Grimme, S.; Stephan, D. W.; Paradies, J. *Angewandte Chemie* **2012**, *124*, 10311–10315.

[5] Spies, P.; Erker, G.; Kehr, G.; Bergander, K.; Fröhlich, R.; Grimme, S.; Stephan, D. W. *Chemical Communications* **2007**, 5072–5074.

[6] Nyhlén, J.; Privalov, T. *Dalton Transactions* **2009**, 5780–5786.

[7] Lindqvist, M.; Sarnela, N.; Sumerin, V.; Chernichenko, K.; Leskelä, M.; Repo, T. *Dalton Transactions* **2012**, *41*, 4310–4312.

[8] Longobardi, L. E.; Tang, C.; Stephan, D. W. *Dalton Transactions* **2014**, *43*, 15723–15726.

[9] Mahdi, T.; Stephan, D. W. *Journal of the American Chemical Society* **2014**, *136*, 15809–15812.

[10] Scott, D. J.; Fuchter, M. J.; Ashley, A. E. *Journal of the American Chemical Society* **2014**, *136*, 15813–15816.

[11] Mahdi, T.; Stephan, D. W. *Angewandte Chemie International Edition* **2015**, *54*, 8511–8514.

[12] Gyomore, A.; Bakos, M.; Foldes, T.; Pápai, I.; Domján, A.; Soós, T. *ACS Catalysis* **2015**, *5*, 5366–5372.

[13] Hounjet, L. J.; Bannwarth, C.; Garon, C. N.; Caputo, C. B.; Grimme, S.; Stephan, D. W. *Angewandte Chemie* **2013**, *125*, 7640–7643.

[14] Rokob, T. A.; Hamza, A.; Stirling, A.; Pápai, I. *Journal of the American Chemical Society* **2009**, *131*, 2029–2036.

[15] Chai, J.-D.; Head-Gordon, M. *The Journal of chemical physics* **2008**, *128*, 084106.

[16] Chai, J.-D.; Head-Gordon, M. *Physical Chemistry Chemical Physics* **2008**, *10*, 6615–6620.

[17] Marenich, A. V.; Cramer, C. J.; Truhlar, D. G. *The Journal of Physical Chemistry B* **2009**, *113*, 6378–6396.

[18] Frisch, M. J. et al. Gaussian 09 Revision A.01. Gaussian Inc. Wallingford CT 2009.

[19] Welch, G. C.; Stephan, D. W. *Journal of the American Chemical Society* **2007**, *129*, 1880–1881.

[20] Lu, Z.; Cheng, Z.; Chen, Z.; Weng, L.; Li, Z. H.; Wang, H. *Angewandte Chemie International Edition* **2011**, *50*, 12227–12231.

[21] Scott, D. J.; Simmons, T. R.; Lawrence, E. J.; Wildgoose, G. G.; Fuchter, M. J.; Ashley, A. E. *ACS catalysis* **2015**, *5*, 5540–5544.

[22] Bergquist, C.; Bridgewater, B. M.; Harlan, C. J.; Norton, J. R.; Friesner, R. A.; Parkin, G. *Journal of the American Chemical Society* **2000**, *122*, 10581–10590.

[23] Di Saverio, A.; Focante, F.; Camurati, I.; Resconi, L.; Beringhelli, T.; D'Alfonso, G.; Donghi, D.; Maggioni, D.; Mercandelli, P.; Sironi, A. *Inorganic chemistry* **2005**, *44*, 5030–5041.

[24] Beringhelli, T.; Maggioni, D.; D'Alfonso, G. *Organometallics* **2001**, *20*, 4927–4938.

[25] Ashley, A. E.; Thompson, A. L.; O'Hare, D. *Angewandte Chemie International Edition* **2009**, *48*, 9839–9843.

Chapter 3

Mechanistic Insights into H_2 Activation by Frustrated Sn/N Lewis Pairs*

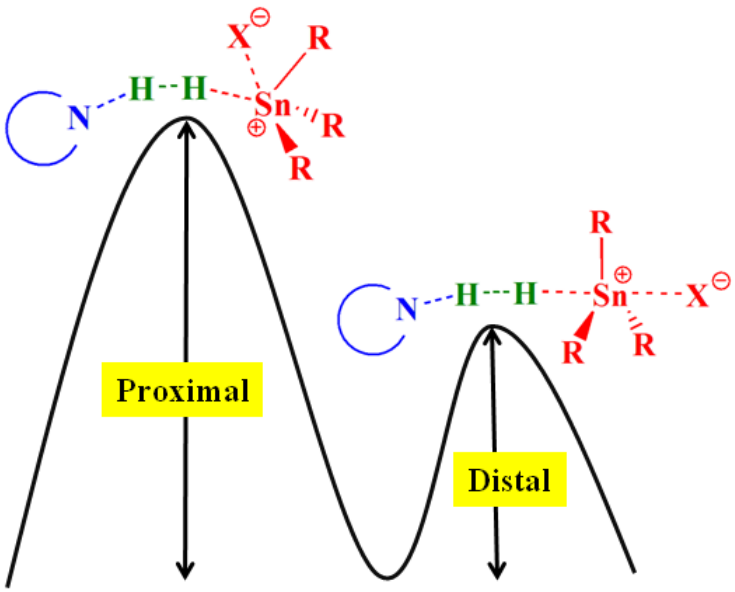

*Work reported in this chapter is published in: Shubhajit Das, Sukanta Mondal, Swapan K Pati, Chemistry-A European Journal, 2018, 24 (11), 2575-2579. Reproduced with permission from John Wiley and Sons.

3.1 Introduction

Despite the rapid expansion of the field over the last decade, FLP hydrogenations have heavily been reliant on early main-group LAs, the most common being perfluorinated boranes and derivatives thereof. Such confined attention on boranes is even more surprising considering the apparent drawbacks of this particular class of LAs. In fact, moisture sensitivity and low functional group tolerance of the commonly employed borane LAs has been an omnipresent concern in FLP community [1–4]. To mitigate this problem, researchers sought for alternative FLP LAs [5]; several

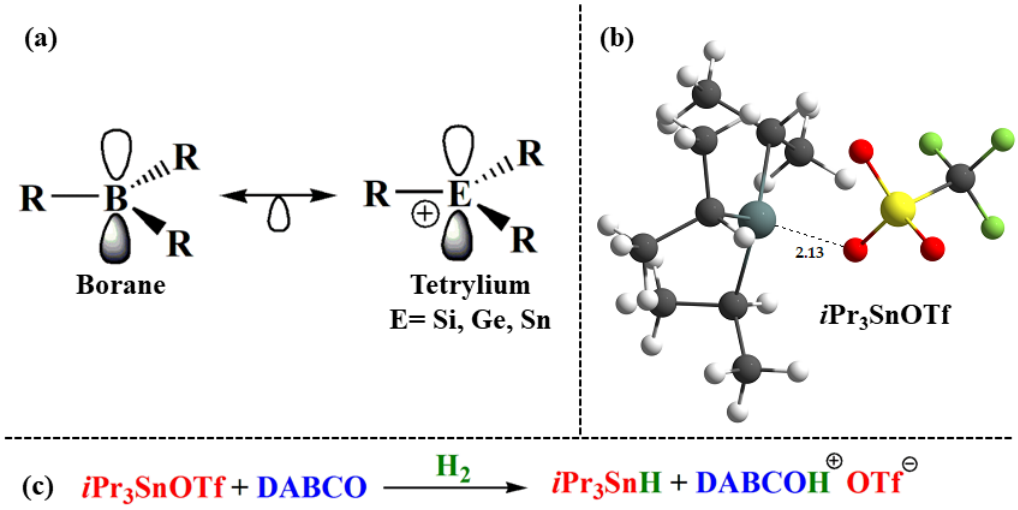

Figure 3.1: (a) Isolobal structures of borane and tetrylium LAs (b) Geometry optimized structures of triisopropylstannylium triflate. The distance shown in the figure is in Å unit. (c) H_2 activation by *i*Pr_3SnOTf/DABCO Lewis Pair.

research endeavours were taken to develop LAs based on heavier p-block elements, which received meager attention in FLP chemistry so far. Of particular interests were the Gr 14-based cationic tetrylium (R_3E^+; E=Si, Ge, Sn) LAs, which exhibit many properties akin to the commonly employed LAs, such as boranes (R_3B).

Tetrylium LAs emerged into FLP chemistry with the pioneering works by M´uller *et al.* wherein a silylium-phosphine Lewis pair was shown to activate H_2 [6, 7]. Later, Ashley *et al.* synthesized a thermally robust silylium-phosphine adduct which was also found to be capable of H_2 activation [8]. Surprisingly, the heavier congeners of the Gr 14 elements, germanium (Ge) and tin (Sn), received much less attention

compared to silicon. Manners *et al.* first introduced stannylium (R_3Sn^+)-based LAs in FLP chemistry with a trialkylstannylium triflate (R_3SnOTf, OTf=CF_3SO_3) which primarily acts as a surrogate for the R_3Sn^+ ion [9]. Unfortunately, H_2 activation was not possible with nBu$_3$SnOTf/amine combination. Very recently, Ashley *et al.* used much bulkier stannylium triflates (R = iPr or Bn) which were capable of activating H_2 when partnered with nitrogenous bases, thereby, constituting the first examples of Sn/N FLP-mediated H_2 activation [10, 11]. In particular, iPr$_3$SnOTf/DABCO (1,4-Diazabicyclo[2.2.2]octane) combination was shown to engage in H_2 cleavage in room temperature. Moreover, Sn/N-mediated H_2 activation was further utilized to design an efficient catalytic hydrogenation protocol which exhibited excellent moisture tolerance as well as a wide range of substrate scope. These observations represent significant advances in the main group alternative FLP LA chemistry. Further improvements, however, require a thorough molecular level understanding of the underlying mechanism of these processes. To this end, in this chapter, we report a computational study on the mechanism of H_2 activation by Sn/N Lewis pairs using the representative iPr$_3$SnOTf/DABCO combination reported by Ashley *et al.* We have performed density functional theory (DFT) calculations to identify the possible reaction pathways and intermediates involved in the H_2 activation pathway.

3.2 Computational details

All molecular geometries are optimized by DFT using M062X [12, 13] functional along with 6-311G(d,p) basis set on lighter atoms (C, H, N, F, O, S, Cl) and def2TZVP on Sn atom including Stuttgart-Dresden effective core potential [14]. This basis set combinatio is hereafter denoted as BS1. M062X functional is highly recommended for main group themochemistry and the present computational approach has been previously shown to yield reliable geometries for the related Sn(IV)-systems [15]. Additionally, in order to account for the non-covalent interactions,

Grimme's D3 dispersion model [16] is employed. The electronic energies are refined with single point energy calculations using a higher basis set 6-311++g(d,p) for the lighter atoms. Hereafter, we have denoted the basis set combination 6-311++G(d,p)(C,H,N,O,S,F)+(def2TZVP+ECP)(Sn)// 6-311G(d,p)(C,H,N,O,S,F) + (def2TZVP+ECP)(Sn) as BS2. For each optimized structure, harmonic vibrational frequencies are computed to characterise the stationary points either as minima (no imaginary frequency) or first order saddle points (one imaginary frequency). Transition states are further verified by intrinsic reaction coordinate (IRC) calculations by checking their connection to two respective minimum structures. All thermochemical data are obtained with the ideal gas-rigid rotor-simple harmonic oscillator approximations at 298.15 K and 1 atm. However, Gibbs free energies are subjected to a concentration correction for c = 1 mol/dm^3 condition in the solvent. The solvent (o-DCB) effects are taken into account by SMD solvation model [17]. All geometry optimizations and single point energy calculations are performed with Gaussian16 suit of programs [18]. To achieve a quantitative account of these secondary interactions, a Ziegler-Rauk-type energy decomposition analyses (EDA) [19–24] are performed on the M062X-D3/BS1 optimized geometries using PBE-D3/TZ2P method as implemented in ADF2017.01[25]. Here, PBE-D3/TZ2P level is used due to the nonavailability of M062X-D3 functional in ADF package. Reliability of PBE-D3/TZ2P level of theory in taking care of the weak noncovalent interactions of FLPs has also been shown by Skara et al [26]. Computations were carried out without frozen core approximation using all-electron basis set. Scalar relativistic effects were considered using the zeroth-order regular approximation [27, 28]. Interaction energy ($\Delta E_{interaction}$) between the fragments can be partitioned into electrostatic interaction (ΔE_{elstat}), Pauli repulsion (ΔE_{Pauli}), orbital interaction (ΔE_{orb}), and dispersion energy (ΔE_{disp}) terms.

3.3 Results and discussions

3.3.1 General aspects

R_3Sn^+ cations are isolobal, iso(valence)electronic as well as isostructural with boranes. The central Sn(IV) atom is sp^2 hybridised and features an empty p acceptor orbital which is primarily responsible for its Lewis acidity. Nevertheless, we envisaged that coordination with the counteranion would inevitably cause a reduction in the stannylium character. This is supported by our computed hydride affinity (HA) values which indicate significantly lower HA for *i*Pr_3SnOTf compared to naked *i*Pr_3Sn^+. OTf^- coordinates to the Sn centre through one of its three equivalent oxygen atoms (hereby denoted as O*) with a Sn-O* distance of 2.13 Å. The Sn-OTf interaction is further exemplified by the pyramidalization (% pyramidalization = 36.1) about the Sn atom. NBO analysis suggests a lone pair(O*) → p(Sn) donor-acceptor interaction, which pushes electron density to the p orbital on Sn centre (population 0.18e vs. practically zero in *i*Pr_3Sn^+). Furthermore, the association between the ion-pair, *i*Pr_3Sn^+ and OTf^-, is computed to be strongly exergonic (ΔG=-28.7 kcal/mol) in *o*-DCB. Overall, these results together confirm the existence of appreciable Sn-OTf interaction, which is also captured in the NMR spectra of *i*Pr_3SnOTf [10]. Nevertheless, we would stress here that despite OTf^- coordination, the Lewis acidity of the Sn centre is not fully quenched as notable stannylium character is still retained. *i*Pr_3SnOTf is still able to function as a LA albeit weaker than its naked form.

3.3.2 Sn/N Lewis pair associations

Having demonstrated Sn-OTf interaction, we turned our attention to inquire how DABCO interacts with *i*Pr_3SnOTf. To this end, we examined the potential energy profiles for *i*Pr_3SnOTf/DABCO interaction with respect to Sn-N(DABCO) distance, $\mathbf{d_{Sn-N}}$. We surmised that OTf^-, being attached to the Sn centre, might intervene in the interaction between DABCO and *i*Pr_3Sn^+ core. And accordingly, there could be two possibilities depending upon the mutual positioning of DABCO and OTf^-;

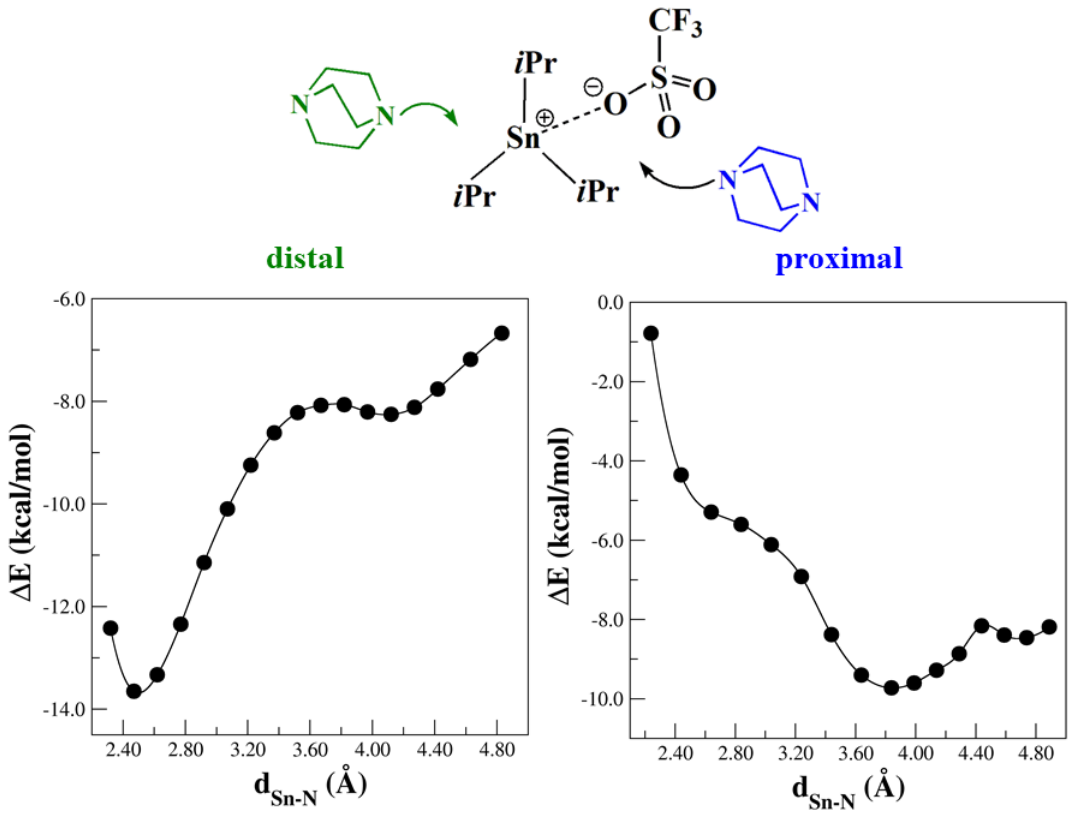

Figure 3.2: Potential energy profiles for distal and proximal interaction in iPr$_3$SnOTf/DABCO Lewis pairs. The data points are obtained by performing a relax PES scan with respect to Sn-N separation at M062X-D3/BS1 level, followed by single point energy calculations at the M062X-D3/BS2 level of theory.

(1) DABCO interacts with iPr$_3$Sn$^+$ while remaining in the close vicinity of the OTf$^-$ (proximal interaction) and (2) DABCO interacts with iPr$_3$Sn$^+$ from the opposite side of the OTf$^-$ (distal interaction). The corresponding potential energy profiles for distal and proximal interaction are depicted in Figure 3.2.

In the distal interaction, we have been able to locate a datively bound complex, **A**, at $\mathbf{d_{Sn-N}}$=2.51 Å as a minimum on the energy profile. Note that, evidence of such dative interaction was observed in the NMR spectra of a solution of iPr$_3$SnOTf and DABCO, wherein a rapid exchange with the free form of LA and LB was also duly noted [10]. However, the structure of **A** consists of a hypervalent Sn atom, in a near trigonal bipyramid (TBP) geometry, with three carbon atoms (from the iPr substituents) forming the equatorial plane while the DABCO nitrogen and O* occupying the apical positions. The structural features are consistent with the

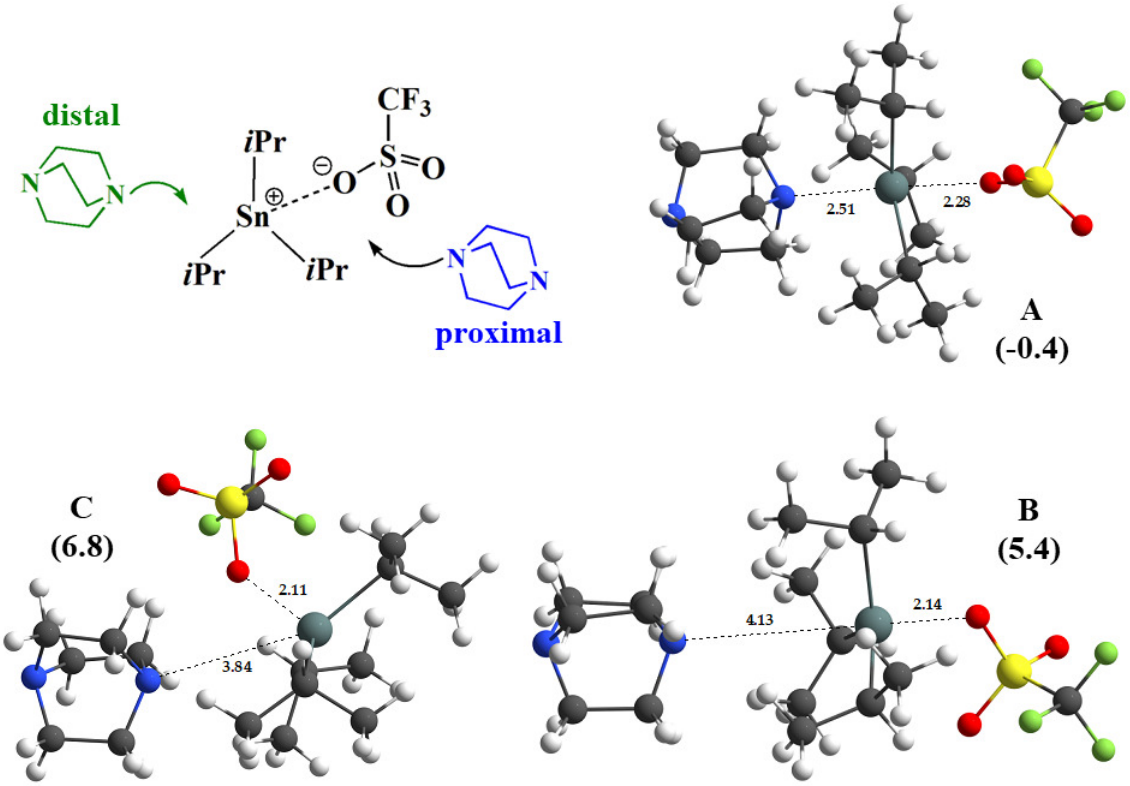

Figure 3.3: Distal and proximal modes of interaction between *i*Pr_3SnOTf and DABCO. Geometry optimized structures of classical Lewis adduct (**A**) and encounter complexes (**B** and **C**) between *i*Pr_3SnOTf and DABCO. All distances shown in the figure are in Å unit. Solvent-corrected Gibbs free energy values are given in parenthesis. Atom colour code: C (grey), H (white), N (blue), O (red), S (yellow), F (green), and Sn (dark green).

experimental observation that Sn-OTf interaction is still retained in the dative adduct [29]. Nevertheless, the dative interaction with DABCO weakens the Sn-OTf interaction, as indicated by an elongated Sn-O* distance (2.28 Å in **A** *vs.* 2.13 Å in free *i*Pr_3SnOTf). However, formation of **A** is computed to be marginally exergonic (-0.4 kcal/mol); therefore, dissociation of this complex into the individual components is very likely at room temperature, as suggested by the NMR spectra of *i*Pr_3SnOTf/DABCO solution [10].

Further examination of the energy profiles allowed us to identify two other weak associations (**B** in distal interaction and **C** in proximal interaction) between *i*Pr_3SnOTf and DABCO at much longer Sn-N separations, (4.13 and 3.83 Å in **B** and **C**, respectively *vs.* 2.51 Å in **A**) which impede any Sn-N dative interaction. Bonding

Table 3.1: EDA results for the ECs considering *i*Pr$_3$SnOTf and DABCO as the two fragments. All energy values are in kcal/mol. The percentage values of contribution towards the total attractive interaction ($\Delta E_{attraction}$=ΔE_{elstat}+ΔE_{orb}+ΔE_{disp}) are given in parenthesis.

EC	$\Delta E_{interaction}$	ΔE_{elstat}	ΔE_{pauli}	ΔE_{orb}	ΔE_{disp}
C	-8.4	-11.0(43.8)	16.7	-5.9	-8.2(32.7)
B	-7.1	-7.2(39.3)	11.4	-4.5	-6.7(36.8)

in these associations is characterised by a combination of multiple C-H$\cdots$F and C-H$\cdots$O hydrogen bonds along with dispersion interactions. In order to obtain a quantitative estimate of such secondary interaction, we have performed an energy decomposition analysis (EDA) calculations on the EC structures considering DABCO and *i*Pr$_3$SnOTf as the interacting fragments and the corresponding results are provided in Table 3.1. These LA/LB ECs are formed mainly due to electrostatic and dispersion interactions with the former contributing 43.8% (**C**), 39.3% (**B**) and the later 32.7% (**C**), 36.8% (**B**) towards the total attractive interaction. The dominance of electrostatic contributions is apparent due to the presence of an ion-pair LA. Thus, **B** and **C** are considered to be encounter complexes (ECs) between *i*Pr$_3$SnOTf and DABCO. **B** represents the expected EC structure in which DABCO interacts with only *i*Pr$_3$Sn$^+$ (through the substituents) without any interference of the OTf$^-$ anion. Interestingly, OTf$^-$interacts strongly with DABCO and plays a crucial role in stabilising the structure of **C**; the -SO$_3$ and -CF$_3$ fragments in OTf$^-$ provides alternative means of noncovalent interactions through C-H$\cdots$F or C-H$\cdots$O contacts. However, **B** and **C** are bound by -8.2 and -9.7 kcal/mol, although the favorable association energy is overcompensated by the entropy loss. Therefore, formation of these ECs is predicted to be slightly endergonic in *o*-DCB at room temperature, which is in accord with the fact that such noncovalent associations were not observed experimentally. **B** and **C** have comparable stabilities in solution with a slight preference for the former association. The existence of two structurally different ECs for a particular LA/LB combination is without precedence and is a direct consequence of using a cationic LA

which tends to associate with its counteranion. Note that, this could be a general feature of all Lewis pair combinations with an ion-pair LA component.

The frontier molecular orbitals (FMOs) of the ECs are depicted in Figure 3.4. For both the FLPs, HOMO is mainly concentrated on the DABCO part with lone pair of the N atom being the major constituent. The LUMO, which is localized on the *i*Pr$_3$SnOTf fragment, is mainly composed by the empty p orbital on the Sn atom. This suggests that the FLP association hardly affects the individual FMO characteristics of the LB and LA components. The relative orientations of the HOMO and LUMO are different for two FLPs indicating that, compared to **C**, in **B** the HOMO and the LUMO are better preorganized for simultaneous interaction with the incoming H_2 molecule.

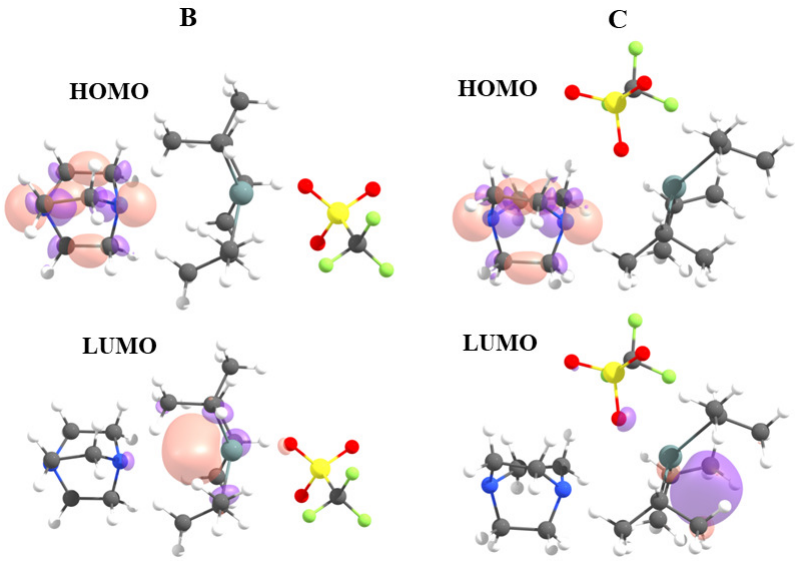

Figure 3.4: Relevant frontier molecular orbitals of the it iPr$_3$SnOTf/DABCO FLPs. Atom colour code: C (grey), H (white), N (blue), O (red), S (yellow), F (green), and Sn (dark green).

3.3.3 H_2 activation by *i*Pr$_3$SnOTf/DABCO Lewis pair

We next focus on the mechanism of heterolytic H_2 activation by Sn/N Lewis pair. Considering the Sn-N distances, both the ECs are capable of accommodating a small molecule, such as H_2, in the cavity between the Sn and the N atoms. Following

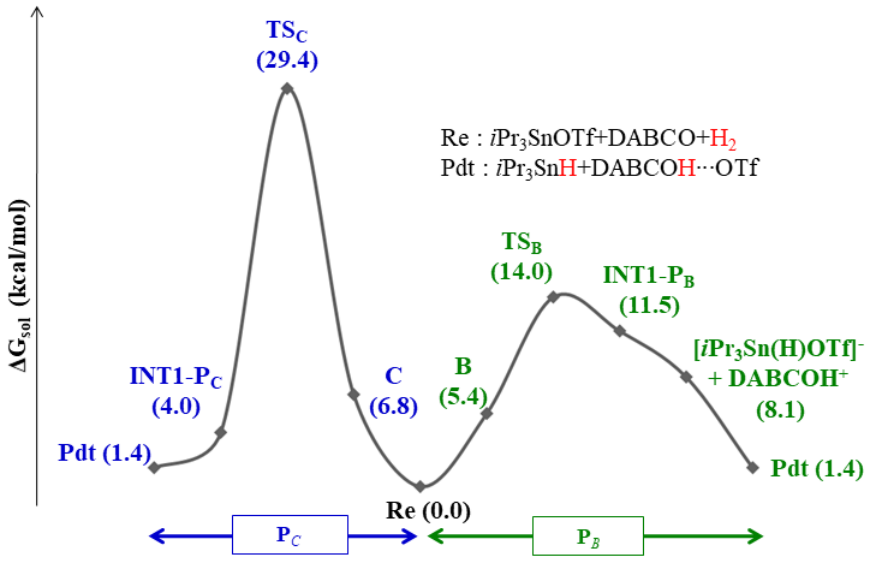

Figure 3.5: Relative free energy profile of H_2 activation by it iPr_3SnOTf/DABCO Lewis pair. Solvent-corrected Gibbs free energy values are given in parenthesis. Re and Pdt refer to reactants and products, respectively.

the entrance, the H_2 molecule may engage in interactions with the active LA/LB centres. Thus, we propose dual H_2 activation pathways, $\mathbf{P_B}$ and $\mathbf{P_C}$, mediated by **B** and **C** respectively. We have found that both the ECs react with H_2 via single concerted transition states ($\mathbf{TS_B}$ and $\mathbf{TS_C}$) resulting in heterolytic cleavage of the H-H bond. The corresponding free energy profiles are depicted in Figure 3.5. The formation of the final products, iPr$_3$SnH and DABCOH$\cdots$OTf, are calculated to be slightly endergonic in terms of Gibbs free energy change (ΔG=1.4 kcal/mol). The most striking observation is that the computed free energy activation barrier for H_2 activation is found to be much lower in $\mathbf{P_B}$ compared to $\mathbf{P_C}$; $\mathbf{TS_B}$ lies 15.4 kcal/mol lower than $\mathbf{TS_C}$. Therefore, $\mathbf{P_B}$ is kinetically favoured over $\mathbf{P_C}$ and consequently, H_2 activation is predicted to proceed through the former pathway. The computed activation barrier for H-H cleavage in $\mathbf{P_B}$ is consistent with the observed reactivity at room temperature.

$\mathbf{TS_C}$ initially relaxes to a primary product complex, $\mathbf{INT1-P_C}$, which lies 2.8 kcal/mol below than to **C**+H_2. In the structure of $\mathbf{INT1-P_C}$, the H-H atoms are 2.35 Å distance apart. The N-H and Sn-H bond distances are 1.05 Å and 1.75 Å,

respectively. OTf^- is involved in a N-H$\cdots$O hydrogen bonding interaction with the DABCO unit. The Sn-O* distance is found to be 2.85 Å, which indicates very weak interaction with the Sn centre. Eventually, $\mathbf{INT1-P_C}$ dissociates into the final products, iPr$_3$SnH and DABCOH$\cdots$OTf. The primary product of H_2 activation in $\mathbf{P_B}$ is $\mathbf{INT1-P_B}$ which resembles $\mathbf{TS_B}$ in structure. $\mathbf{INT1-P_B}$ features a rather close H-H contact of 1.21 Å. Such close H-H separation is ensured by the stable TBP geometry around the Sn centre. The N-H and Sn-H bond lengths are 1.14 Å and 1.97 Å, respectively. The Sn-O* bond distance is found to be 2.31 Å. $\mathbf{INT1-P_B}$ lies about 6.1 kcal/mol higher than FLP+H_2. However, it can readily dissociate into [iPr$_3$Sn(H)OTf]$^-$ and $DABCOH^+$. An alternative dissociation route resulting in iPr$_3$SnH-HDABCO and OTf^- is calculated to be thermodynamically less favorable compared to the former dissociation. In [iPr$_3$Sn(H)OTf]$^-$, the Sn-H bond distance becomes 1.79 Å and Sn-OTf interaction further weakens compared to

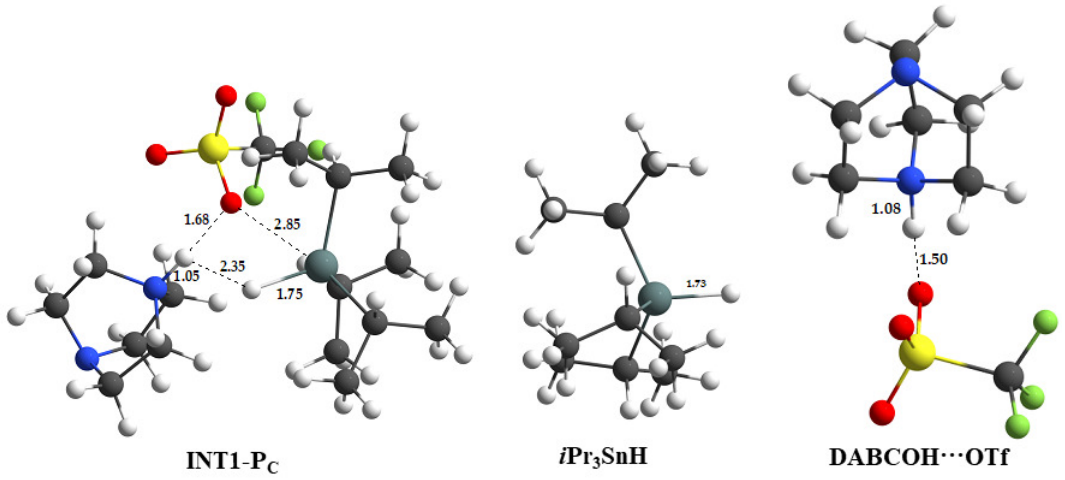

Figure 3.6: Geometry optimized structures of $\mathbf{INT1-P_C}$, iPr$_3$SnH and DABCOH$\cdots$OTf. All distances shown in the figure are in Å unit. Atom colour code: C (grey), H (white), N (blue), O (red), S (yellow), F (green), and Sn (dark green).

$\mathbf{INT1-P_B}$. We find that $DABCOH^+$ establishes hydrogen bonding interaction with one of the other two oxygen atoms (not attached to Sn centre) of OTf^-, leading to the formation of $\mathbf{INT2-P_B}$. $\mathbf{INT2-P_B}$ is 3.2 kcal/mol lower than FLP+H_2. Later, OTf^- is completely released from the Sn centre and the final products are formed.

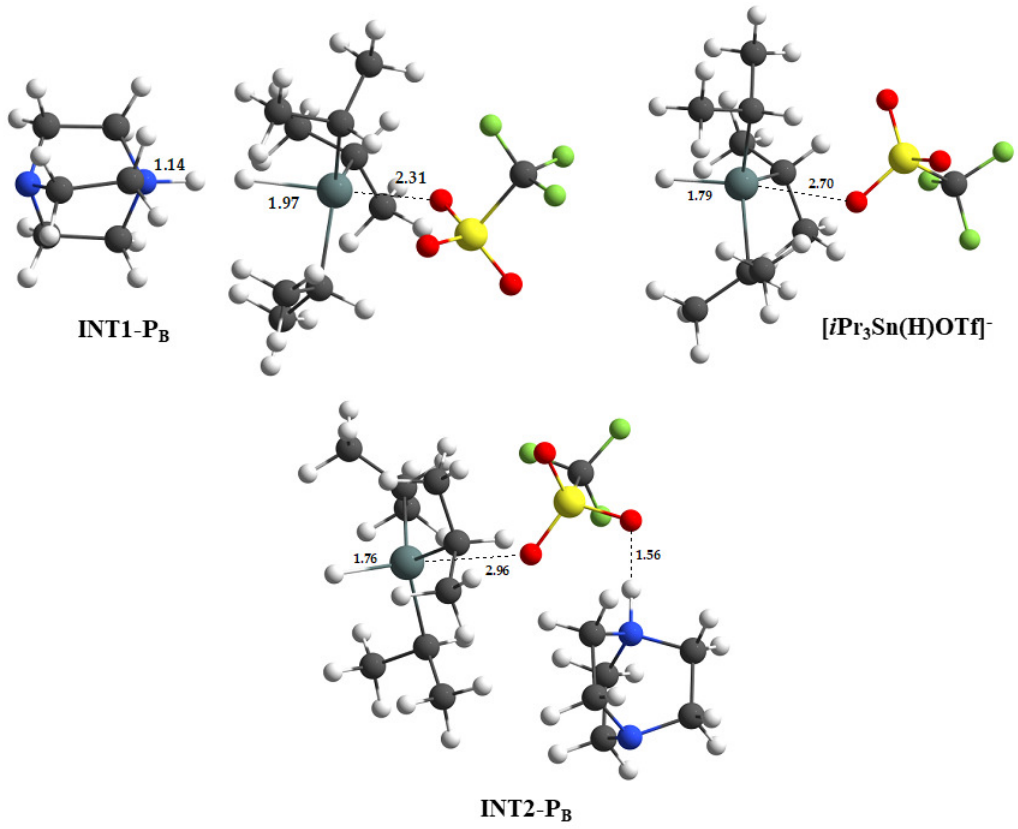

Figure 3.7: Geometry optimizd structures of $\mathbf{INT1-P_B}$, $[i\mathrm{Pr_3Sn(H)OTf}]^-$, and $\mathbf{INT2-P_B}$. All distances shown in the figure are in Å unit. Atom colour code: C (grey), H (white), N (blue), O (red), S (yellow), F (green), and Sn (dark green).

The dissociation steps, involving $\mathbf{INT1-P_B} \rightarrow [i\mathrm{Pr_3Sn(H)OTf}]^- + \mathrm{DABCOH}^+ \rightarrow \mathbf{INT1-P_B} \rightarrow i\mathrm{Pr_3SnH} + \mathrm{DABCOH}\cdots\mathrm{OTf}$, are downhill in free energy and occur without any barrier. The optimized geometries for all these intermediates are shown in Figure 3.6 and Figure 3.7.

Note that, experimentally, H_2 activation by $i\mathrm{Pr_3SnOTf/DABCO}$ does not proceed beyond 50% at room temperature [29]. At first glance, this appears to be a mere consequence of the computed energetics. However, the absence of H_2/D_2-scrambling under the reaction condition rules out the possibility of a reversible situation. The incomplete reactivity may arise from a quenching of remaining LA due to coordination of OTf^- (to Sn centre) released upon H_2 activation, leading to the formation of a hypervalent Sn complex, $[i\mathrm{Pr_3Sn(OTf)DABCOH}\cdots\mathrm{OTf}]$ (see Figure 3.8 for structure). Formation of such a complex (with respect to $i\mathrm{Pr_3SnOTf+DABCOH}\cdots\mathrm{OTf}$) is

exergonic by 7.4 kcal/mol. Thus, an elevated temperature is required for thermal dissociation of the complex to set free iPr$_3$SnOTf for completion of the reaction. Nevertheless, the temperature used in the subsequent catalytic hydrogenation process is as high as 120 °C. Such high temperature will aid in the dissociation of the complex as well as it will shift the H_2 activation towards the forward direction. At this point, it should be mentioned that the ultimate goal of this H_2 activation process is to utilize the activated hydrogens in the hydrogenation process. The hydrogenation reaction involves the transfer of the activated hydrogens, proton and the hydride, into an unsaturated substrate. Note that, [iPr$_3$Sn(H)OTf]$^-$ and DABCOH$^+$, obtained after the dissociation of $\mathbf{INT1 - P_B}$, are likely to be suitable species that can easily transfer hydride/proton to the substrate. In that case, we might not observe the final products of H_2 activation in the form of iPr$_3$SnH and DABCOH$\cdots$OTf. We will address this issue in the next chapter while discussing the relative hydride donating ability of iPr$_3$SnH and [iPr$_3$Sn(H)OTf]$^-$.

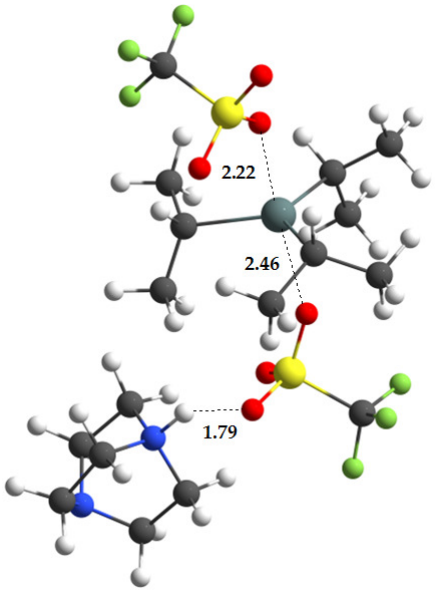

Figure 3.8: Geometry optimized structures of [iPr$_3$Sn(OTf)DABCOH$\cdots$OTf]. All distances shown in the figure are in Å unit. Atom colour code: C (grey), H (white), N (blue), O (red), S (yellow), F (green), and Sn (dark green).

When inspecting the TS structures (see Figure 3.9), certain differences become apparent. While $\mathbf{TS_C}$ features a rather early TS with $\mathbf{d_{H-H}}$= 0.87 Å and H-H bond

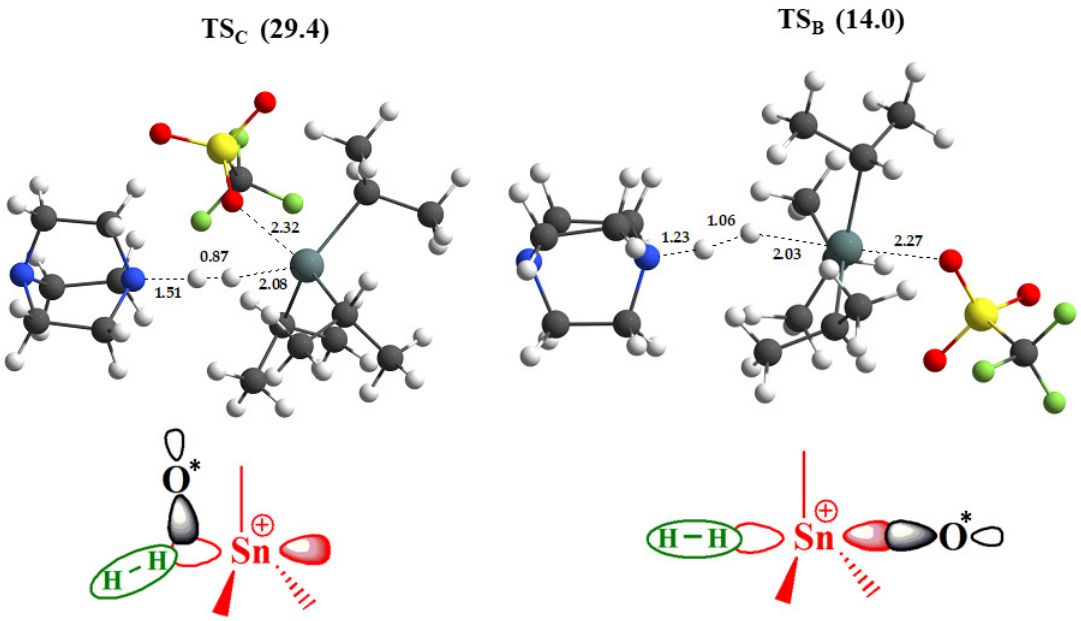

Figure 3.9: Geometry optimized structures of the transitions states for H_2 activation by iPr$_3$SnOTf/DABCO FLPs. All distances shown in the figure are in Å unit. The corresponding overlap situtaion of the three selected NBOs, $\sigma(H_2)$, empty p orbital on Sn and a O* orbital from the OTf^-, are shown below. Atom colour code: C (grey), H (white), N (blue), O (red), S (yellow), F (green), and Sn (dark green).

Table 3.2: Selected NBO interaction energies (computed at the second order pertubation level) in the **TS$_B$** and **TS$_C$**. All energies are in kcal/mol.

TS	$\Delta E^{int}_{N\rightarrow\sigma^*(H_2)}$	$\Delta E^{int}_{Sn\leftarrow\sigma(H_2)}$	$\Delta E^{int}_{Sn\leftarrow O*(sp^x)}$
TS$_B$	138.8	72.2	58.3
TS$_C$	58.3	31.8	34.5

order of 0.65, a further elongated H-H bond with $\mathbf{d_{H-H}}$= 1.06 Å and bond order of 0.44 in **TS$_B$** indicates a late TS. The calculated NPA atomic charges show that the H atom near to the Sn centre (H_A) grows a hydridic character, while the H atom close to N centre (H_D) becomes protonic (see Table 3.3) . The bonding picture in the TSs are further analyzed with NBO calculations, which reveal that donor(N)/acceptor(Sn) orbitals in FLPs are involved in cooperative interactions with the $\sigma^*(H_2)/\sigma(H_2)$ orbitals in H_2 molecule. In fact, both **B** and **C** activate H_2 in a similar way as borane/phosphine FLPs; single step H-H cleavage featuring a Sn-H-H-N interaction [30, 31]. The corresponding donor-acceptor interaction energies, estimated at the

Table 3.3: Selected distances (**d**), NPA charges (**q**), Wiberg bond indices (**WBI**) and angles in the *i*Pr_3SnOTf/DABCO ECs and the corresponding TS structures for H_2 activation. H_A and H_D refers to the hydrogen atoms near to the Sn and N, respectively. All distances are in Å unit.

Quantity	**B**	$\mathbf{TS_B}$	**C**	$\mathbf{TS_C}$
$\mathbf{d_{Sn-N}}$	4.13	4.22	3.84	3.98
$\mathbf{d_{N-H_D}}$	-	1.23	-	1.50
$\mathbf{d_{Sn-H_A}}$	-	2.03	-	2.08
$\mathbf{d_{H_D}-H_A}$	-	1.06	-	0.87
$\mathbf{d_{Sn-O*}}$	2.14	2.27	2.11	2.31
$\mathbf{q(N)}$	-0.548	-0.557	-0.549	-0.554
$\mathbf{q(Sn)}$	2.226	2.077	2.261	2.157
$\mathbf{q(H_A)}$	-	0.383	-	0.271
$\mathbf{q(H_D)}$	-	-0.395	-	-0.236
$\mathbf{WBI(N-H_D)}$	-	0.314	-	0.171
$\mathbf{WBI(Sn-H_A}$	-	0.303	-	0.208
$\mathbf{WBI(H_D-H_A)}$	-	0.447	-	0.653
$\mathbf{N-H_A-H_D}$	-	168.8°	-	167.5°
$\mathbf{Sn-H_D-H_A}$	-	150.6°	-	118.9°
$\mathbf{H_A-Sn-O*}$	-	177.6°	-	67.1°

second-order perturbation level are tabulated in Table 3.2.

The H_2 activation is concerted in both the pathways; the H-H bond cleavage is accompanied with concomitant N-H and Sn-H bond formation. However, consistent with a late TS, partial Sn-H and N-H bond formations in $\mathbf{TS_B}$ are in a more advanced stage compared to that in $\mathbf{TS_C}$. Note that, the Sn-OTf interaction is still retained in the TSs although it is weakened owing to the partial formation of the Sn-H bond. Along the reaction coordinate, the Sn centre progressively becomes pentacoordinated as the Sn-H bond begins to form. The H_A-Sn-O* angle is found to be 177.6° in $\mathbf{TS_B}$ resulting in a stable TBP environment around the Sn centre. Such a stable geometry is ensured by the optimal overlap between the $\sigma(H_2)$, p(Sn) and an O* orbital from the OTf^- as illustrated in Figure 3.9. The corresponding overlap in $\mathbf{TS_C}$ is less favorable because these orbitals are not properly oriented; a particular lobe of the p(Sn) orbital is shared by the other two orbitals. Consequently, the H_A-Sn-O* angle in $\mathbf{TS_C}$ is found to be 67.1°. Note that, the overlap situations qualitatively correlates

with the calculated barrier in these two pathways. However, in the final products, OTf^- helps in stabilising the proton through hydrogen bonding interaction with $DABCOH^+$. A few key geometric parameters are listed in Table 3.3.

3.3.4 Activation strain analysis

In order to understand the origin of such marked difference in H_2 activation barrier in these two reaction channels, we have carried out a thorough activation-strain analysis [32–35] considering a bimolecular reaction between *i*Pr_3SnOTf/DABCO EC and H_2. In this model, the activation energy is decomposed into strain energy and energy of interaction between the reactants in TS. The strain energy of each fragment is estimated by the energy change associated in going from optimized ground state geometry to the geometry it has in the TS. Interaction energy is calculated by the difference between activation energy and the total strain energy.

$$\begin{aligned} \Delta E &= \Delta E_{strain} + \Delta E_{int} \\ \Delta E_{strain} &= \Delta E_{strain}(FLP) + \Delta E_{strain}(H_2) \end{aligned} \tag{3.1}$$

We noted that in the present case the position of the two TSs, $\mathbf{TS_B}$ and $\mathbf{TS_C}$, are very different along the reaction coordinate. In such cases, as pointed out in the former studies [36, 37], simply employing the activation-strain model on the TS geometry might be inadequate to capture the actual effect of strain vs. interaction. Hence, we have performed the activation-strain analysis along the reaction coordinate as the H-H bond is gradually stretched. The data points are chosen from the corresponding IRC calculations. For each chosen geometry, single point calculations are performed at M062X-D3/BS2 level of theory.

Our results reveal that higher activation barrier in $\mathbf{P_C}$ is due to a much higher strain energy (ΔE_{strain}) curve at an early stage of the reaction, where the TS is located (see Figure 3.10). Such high strain energy, even when H-H bond is hardly elongated, stems from the geometric distortion of **C** caused by the movement of OTf^-

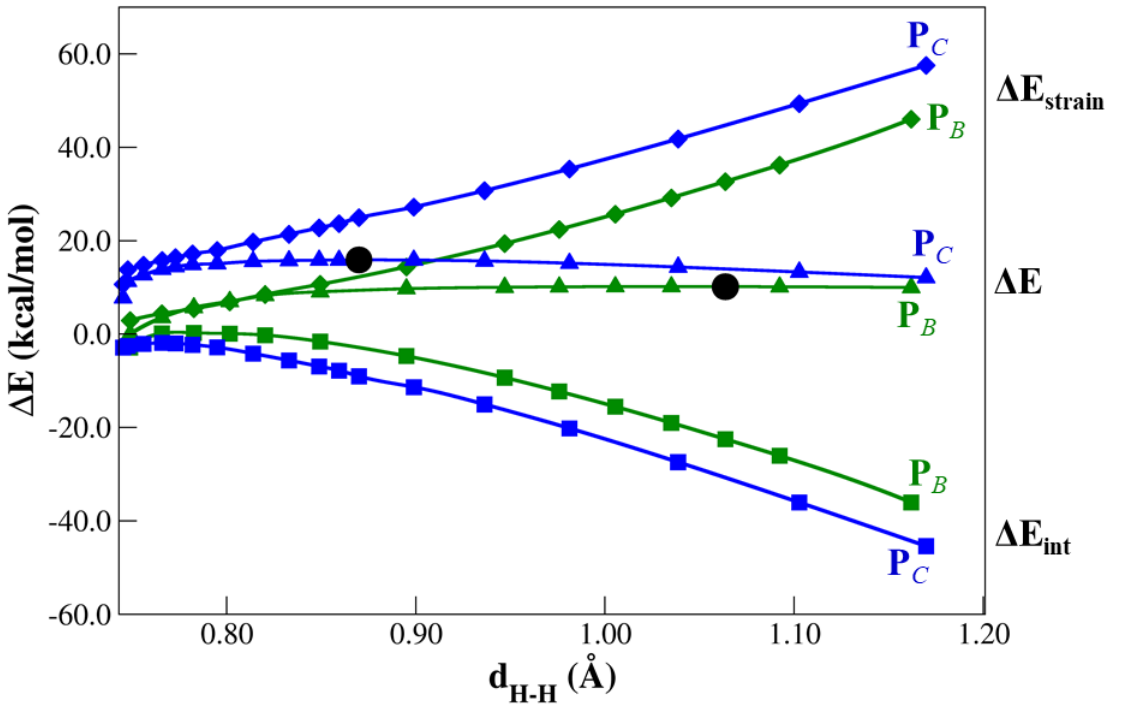

Figure 3.10: Activation strain analysis for the H_2 activation in the $\mathbf{P_B}$ (green) and $\mathbf{P_C}$ (blue) pathways. The black dots indicate TSs.

near the incoming H_2 molecule. Interaction energy (ΔE_{int}) curve is found to be much less stabilizing in this region. The effect of EC distortion is much less pronounced in **B** as OTf^- remains outside the EC cavity and H_2 is well accommodated. In the region of $\mathbf{TS_B}$, strain energy is still high due to a significantly elongated H_2 molecule although H-H stretch is compensated by newly forming Sn-H and N-H bonds. Additionally, efficient orbital overlaps as well as favorable geometry around Sn centre (*vide supra*) results in high interaction energy, which partially offsets the strain energy and leads to a low activation barrier in $\mathbf{P_B}$.

3.3.5 H_2 activation by *i*Pr_3SnX(X= Cl, NTf_2)/DABCO Lewis pairs

Finally, we examine the effect of the counteranions in H_2 activation by replacing OTf^- with Cl^- and NTf_2^- in *i*Pr_3SnX (X= Cl, NTf_2) LA. Likewise OTf^-, we have been able to locate two different EC associations, (**B**-like and **C**-like), for each *i*Pr_3SnCl/DABCO and *i*Pr_3SnNTf_2/DABCO Lewis pairs. Note that, in the following

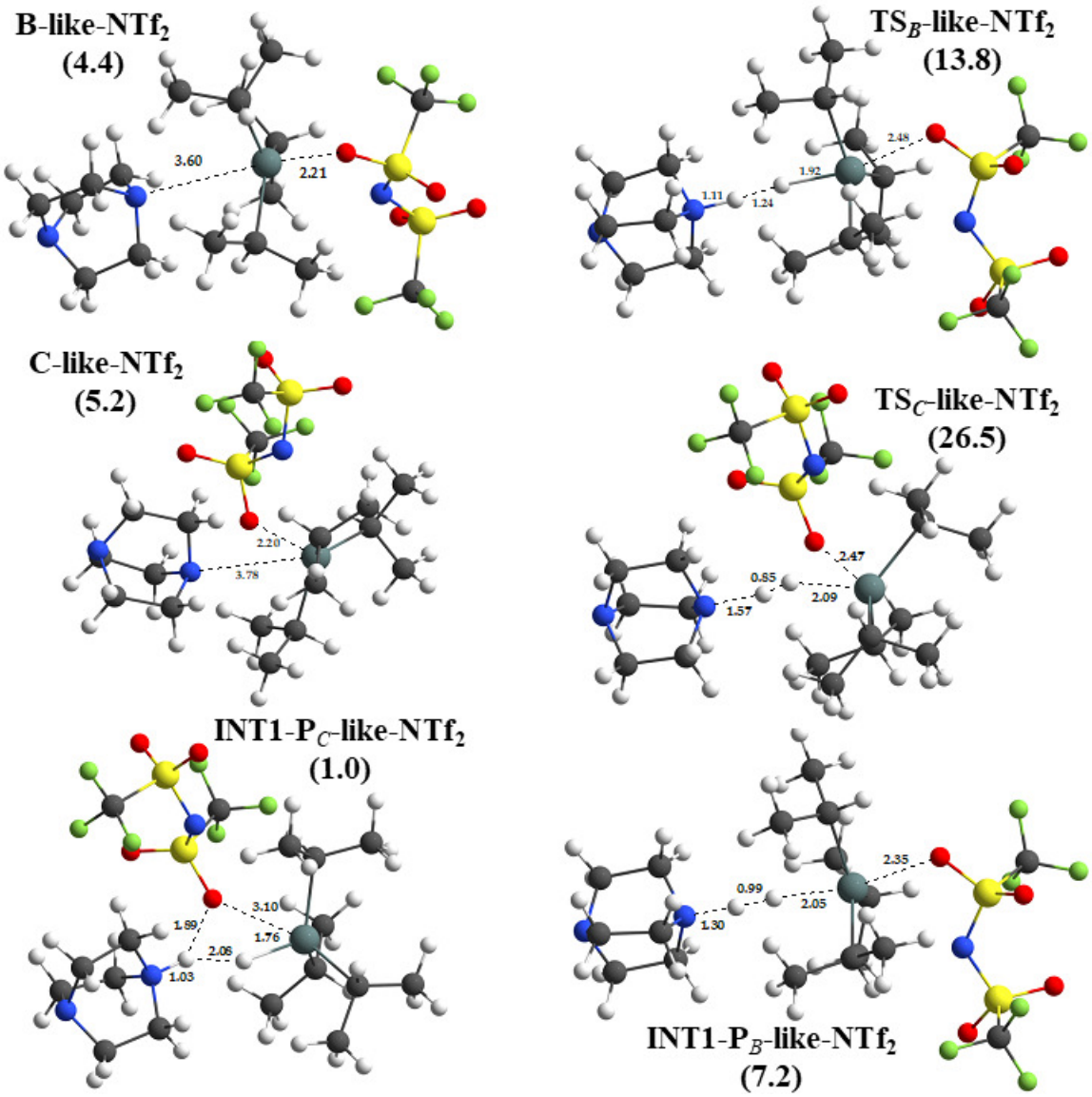

Figure 3.11: Geometry optimized structures of key stationary points for H_2 activation by iPr$_3$SnNTf$_2$/DABCO Lewis pair. All distances shown in the figure are in Å unit. Solvent-corrected Gibbs free energy values are given in parenthesis. Atom colour code: C (grey), H (white), N (blue), O (red), S (yellow), F (green), and Sn (dark green).

discussion, we have denoted H_2 activation mediated by **B**-like and **C**-like ECs as distal and proximal pathways, respectively. In the proximal pathway, for X= NTf$_2$ and Cl, the H_2 activation barriers are computed to be 26.5 kcal/mol and 36.4 kcal/mol, respectively. These differences in activation barriers directly correlate with the strength of the LA component; weaker LA (iPr$_3$SnCl) corresponds to higher activation barrier. As found with OTf$^-$, the distal pathway is kinetically more

favorable for NTf_2^- with much less activation barrier of 13.8 kcal/mol. The key stationary points for H_2 activation by *i*Pr_3SnNTf_2/DABCO Lewis pair are displayed in Figure 3.11.

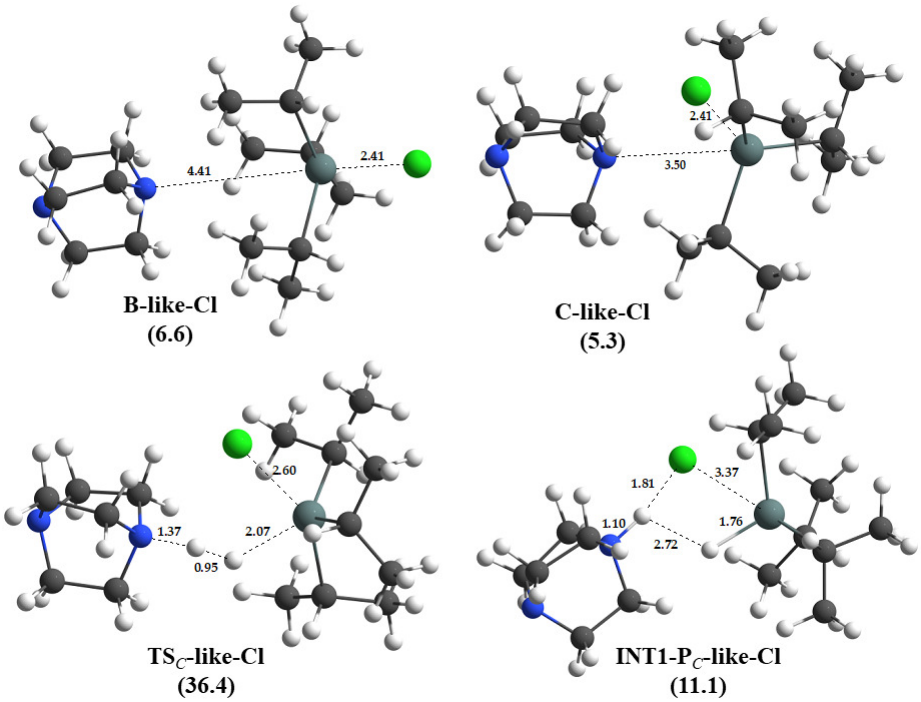

Figure 3.12: Geometry optimized structures of key stationary points for H_2 activation by *i*Pr_3SnCl/DABCO Lewis pair. All distances shown in the figure are in Å unit. Solvent-corrected Gibbs free energy values are given in parenthesis. Atom colour code: C (grey), H (white), N (blue), O (red), S (yellow), Cl (green), and Sn (dark green).

Interestingly, for X=Cl, all attempts to locate either $\mathbf{TS_B}$-like or $\mathbf{INT1\text{-}P}_B$-like structures were unsuccessful, which rules out the possibility of H_2 activation via the distal pathway. Although we have been able to locate a *i*Pr_3SnCl/DABCO EC in distal pathway along with the corresponding EC-bound H_2-adduct, relaxed PES scan calculations with respect to H-H distance show that a $\mathbf{INT1-P_B}$-like intermediate does not correspond to a local minimum (see Figure 3.13). On the contrary, $\mathbf{INT1-P_C}$-like intermediate exists in the proximal pathway, the reason being a favorable N-H$\cdots$Cl hydrogen bonding interaction with the nearby Cl^- anion, which tends to stabilise the structure. Such an interaction is not possible in the distal pathway as Cl^- remains away from the EC-cavity. Thus, in the absence of the

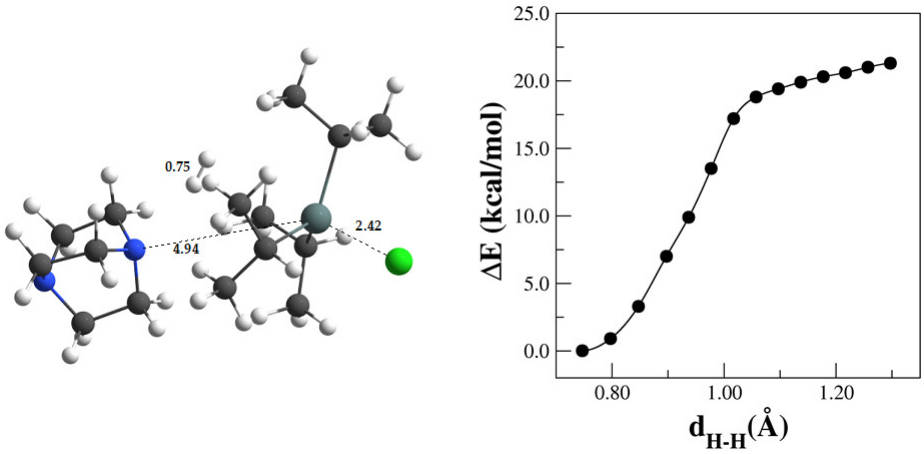

Figure 3.13: Potential energy profile for H_2 activation in the distal pathway for *i*Pr_3SnCl/DABCO Lewis pair. The data points are obtained by performing a relax PES scan with respect to H-H separation at M062X-D3/BS1 level, followed by single point energy calculations at the M062X-D3/BS2 level of theory. A weak *i*Pr_3SnCl/DABCO/H_2-adduct (structure is shown on the left hand side of the plot) is chosen as the starting point for the scan calculation. All distances shown in the figure are in Å unit. Atom colour code: C (grey), H (white), N (blue), O (red), S (yellow), Cl (green), and Sn (dark green).

distal pathway, H_2 activation by *i*Pr_3SnCl/DABCO could only proceed through the proximal pathway, implying the entailing importance of the latter one. Admittedly, the computed activation barrier is too high to achieve at room temperature and consequently, elevated temperature would be necessary to access such high-lying TS. The key stationary points for H_2 activation by *i*Pr_3SnCl/DABCO Lewis pair are depicted in Figure 3.12.

3.4 Conclusion

In summary, we have elucidated the mechanism of heterolytic H_2 activation by Sn/N Lewis pairs using DFT calculations. Our computational mechanistic model suggests the formation of noncovalent associations between LA and LB, leading to two types of ECs. Interestingly, an unprecedented counteranion-assisted EC structure is characterised along with the usual FLP. H_2 activation occurs through FLP-mediated synergistic cooperative electron transfer processes involving the LA/LB centres. We are hopeful that the present findings would not only provide a general mechanistic

framework for H_2 activation via (Sn/Sn) FLPs with an ion-pair LA component but can also help in designing effective Sn-based and other Gr. 14-based alternative FLP LAs.

Bibliography

[1] Das, S.; Pati, S. K. *Chem. Eur. J.* **2017**, *23*, 1078–1085.

[2] Gyomore, A.; Bakos, M.; Foldes, T.; Pápai, I.; Domján, A.; Soós, T. *ACS Catal.* **2015**, *5*, 5366–5372.

[3] Scott, D. J.; Simmons, T. R.; Lawrence, E. J.; Wildgoose, G. G.; Fuchter, M. J.; Ashley, A. E. *ACS Catal.* **2015**, *5*, 5540–5544.

[4] Bergquist, C.; Bridgewater, B. M.; Harlan, C. J.; Norton, J. R.; Friesner, R. A.; Parkin, G. *J. Am. Chem. Soc.* **2000**, *122*, 10581–10590.

[5] Weicker, S. A.; Stephan, D. W. *Bull. Chem. Soc. Jpn* **2015**, *88*, 1003–1016.

[6] Schäfer, A.; Reißmann, M.; Schäfer, A.; Saak, W.; Haase, D.; Müller, T. *Angew. Chem. Int. Ed.* **2011**, *50*, 12636–12638.

[7] Reißmann, M.; Schafer, A.; Jung, S.; Muller, T. *Organometallics* **2013**, *32*, 6736–6744.

[8] Herrington, T. J.; Ward, B. J.; Doyle, L. R.; McDermott, J.; White, A. J.; Hunt, P. A.; Ashley, A. E. *Chem. Comm.* **2014**, *50*, 12753–12756.

[9] Whittell, G. R.; Balmond, E. I.; Robertson, A. P.; Patra, S. K.; Haddow, M. F.; Manners, I. *Eur. J. Inorg. Chem.* **2010**, *2010*, 3967–3975.

[10] Scott, D. J.; Phillips, N. A.; Sapsford, J. S.; Deacy, A. C.; Fuchter, M. J.; Ashley, A. E. *Angew. Chem. Int. Ed.* **2016**, *55*, 14738–14742.

[11] Cooper, R. T.; Sapsford, J. S.; Turnell-Ritson, R. C.; Hyon, D.-H.; White, A. J.; Ashley, A. E. *Phil. Trans. R. Soc. A* **2017**, *375*, 20170008.

[12] Zhao, Y.; Truhlar, D. G. *Accounts of chemical research* **2008**, *41*, 157–167.

[13] Zhao, Y.; Truhlar, D. G. *Theoretical Chemistry Accounts: Theory, Computation, and Modeling (Theoretica Chimica Acta)* **2008**, *120*, 215–241.

[14] Andrae, D.; Haeussermann, U.; Dolg, M.; Stoll, H.; Preuss, H. *Theoretical Chemistry Accounts: Theory, Computation, and Modeling (Theoretica Chimica Acta)* **1990**, *77*, 123–141.

[15] Sindlinger, C. P.; Aicher, F. S.; Schubert, H.; Wesemann, L. *Angewandte Chemie International Edition* **2017**, *56*, 2198–2202.

[16] Grimme, S.; Antony, J.; Ehrlich, S.; Krieg, H. *The Journal of chemical physics* **2010**, *132*, 154104.

[17] Marenich, A. V.; Cramer, C. J.; Truhlar, D. G. *The Journal of Physical Chemistry B* **2009**, *113*, 6378–6396.

[18] Frisch, M. J. et al. Gaussian 16 Revision A.03. 2016; Gaussian Inc. Wallingford CT.

[19] Ziegler, T.; Rauk, A. *Inorganic Chemistry* **1979**, *18*, 1755–1759.

[20] Ziegler, T.; Rauk, A. *Theoretical Chemistry Accounts: Theory, Computation, and Modeling (Theoretica Chimica Acta)* **1977**, *46*, 1–10.

[21] Mitoraj, M.; Michalak, A. *Journal of molecular modeling* **2007**, *13*, 347–355.

[22] Srebro, M.; Michalak, A. *Inorganic chemistry* **2009**, *48*, 5361–5369.

[23] Mitoraj, M. P.; Michalak, A.; Ziegler, T. *Journal of chemical theory and computation* **2009**, *5*, 962–975.

[24] Michalak, A.; Mitoraj, M.; Ziegler, T. *The Journal of Physical Chemistry A* **2008**, *112*, 1933–1939.

[25] ADF2017, SCM, Theoretical Chemistry, Vrije Universiteit, Amsterdam, The Netherlands, https://www.scm.com.

[26] Skara, G.; Pinter, B.; Top, J.; Geerlings, P.; De Proft, F.; De Vleeschouwer, F. *Chemistry-A European Journal* **2015**, *21*, 5510–5519.

[27] van Lenthe, E.; Baerends, E.-J.; Snijders, J. G. *The Journal of chemical physics* **1994**, *101*, 9783–9792.

[28] van Lenthe, E.; Ehlers, A.; Baerends, E.-J. *The Journal of chemical physics* **1999**, *110*, 8943–8953.

[29] Scott, D. *Next generation "frustrated Lewis pairs"* **2016**, Imperial College London.

[30] Rokob, T. A.; Bako, I.; Stirling, A.; Hamza, A.; Papai, I. *J. Am. Chem. Soc.* **2013**, *135*, 4425–4437.

[31] Rokob, T. A.; Hamza, A.; Stirling, A.; Soós, T.; Pápai, I. *Angew. Chem. Int. Ed.* **2008**, *47*, 2435–2438.

[32] Diefenbach, A.; De Jong, G. T.; Bickelhaupt*, F. *Molecular Physics* **2005**, *103*, 995–998.

[33] Bickelhaupt, F. M.; Houk, K. N. *Angewandte Chemie International Edition* **2017**, *56*, 10002–10002.

[34] van Zeist, W.-J.; Bickelhaupt, F. M. *Organic & biomolecular chemistry* **2010**, *8*, 3118–3127.

[35] Fernández, I.; Bickelhaupt, F. M. *Chemical Society Reviews* **2014**, *43*, 4953–4967.

[36] de Jong, G. T.; Bickelhaupt, F. M. *ChemPhysChem* **2007**, *8*, 1170–1181.

[37] Green, A. G.; Liu, P.; Merlic, C. A.; Houk, K. *Journal of the American Chemical Society* **2014**, *136*, 4575–4583.

Chapter 4

Unravelling the Mechanism of Tin-based Frustrated Lewis Pair Catalysed Hydrogenation of Carbonyl Compounds*

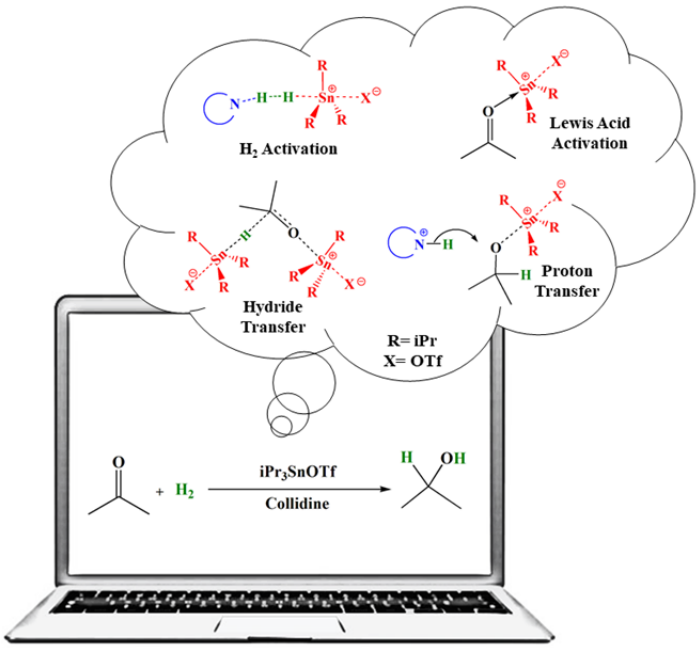

*Work reported in this chapter is based on: Shubhajit Das, Swapan K Pati, Catalysis Science and Technology, 2018 DOI: 10.1039/C8CY01227J. Reproduced with permission from The Royal Society of Chemistry.

4.1 Introduction

So far, we have presented studies on H_2 cleavage by Sn/N Lewis pairs. Typical Sn/N FLP-mediated H_2 cleavage along with an unprecedented counterion-assisted FLP reactivity was the mechanistic model that we examined in the previous chapter. Continuing along the same line, we now wish to extend our understanding to the full mechanism of the catalytic hydrogenation of carbonyl compounds using Sn/N Lewis pairs.

The Sn/N FLP-mediated H_2 activation led to the development of catalytic hydrogenation routes with unparalleled moisture tolerance and substrate scope. Particularly notable here was the ease at which a catalytic protocol for hydrogenation of carbonyls was accomplished using iPr$_3$SnOTf as the LA catalyst in the presence of an auxiliary base such as collidine (2,4,6-trimethylpyridine). These results can be compared with the early struggles to effect FLP hydrogenation of carbonyls using borane catalysts which was attributed to the inherent oxophilicity of boranes affording several inhibition and decomposition steps that prevent catalysis. We studied some of those decomposition routes towards the end of Chapter 2.

As shown in Figure 4.1, based on the experimental mechanistic studies, Ashley *et al.* formulated a putative catalytic cycle for the iPr$_3$SnOTf-catalysed carbonyl hydrogenation. The reaction was thought to begin with iPr$_3$SnOTf/collidine Lewis pair-mediated heterolytic cleavage of the H-H bond in giving proton and hydride fragments in solution. The key point of their mechanistic proposal was the LA activation (LAA) of the carbonyl substrate instead of the Bronsted acid activation (BAA) proposed in the corresponding B(C_6F_5)$_3$-catalysed hydrogenation process [1]. Substrate activation is followed by subsequent transfers of the hydride and the proton which lead to the formation of the alcohol and regenerates the catalyst in solution. Furthermore, an alternative H_2 activation involving iPr$_3$SnOTf/Sn-alkoxide Lewis pair (*in situ* generated) was also proposed to lead to the alcohol product. These results inspired us to initiate a computational study to explore possible reaction

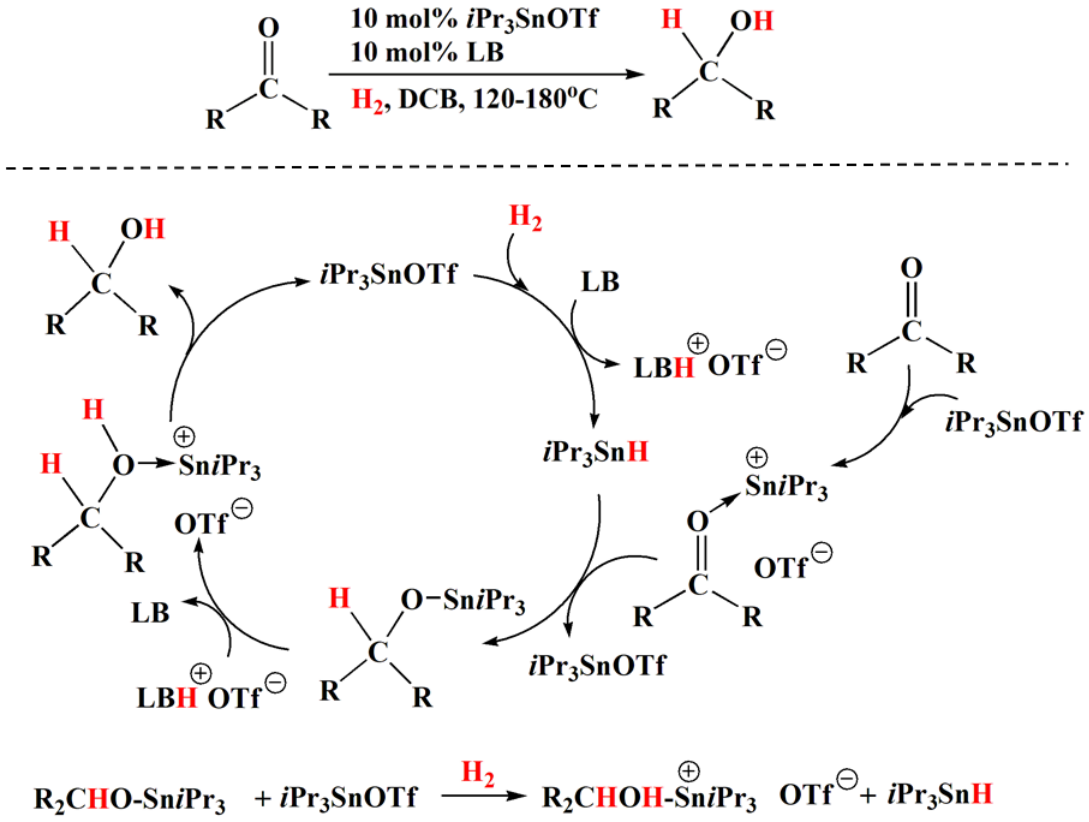

Figure 4.1: Hydrogenation of carbonyl compounds catalysed by iPr$_3$SnOTf as demonstrated in reference 24. The experimentally proposed mechanism by Ashley *et al.* is shown below.

intermediates and transition states (TSs) involved in the catalytic pathway of the Sn/N FLP catalysed carbonyl hydrogenation proces.

4.2 Computational Details

In order to make a direct comparison possible, we have used the same computational protocol as our previous chapter. All geometry optimizations are performed using M062X [2, 3] functional under the framework of DFT. We have employed Grimme's D3 dispersion model [4] to take into account noncovalent interactions. We have used 6-311G(d,p) basis set on lighter atoms (C, H, N, F, O, S), while for the Sn atom, def2TZVP along with Stuttgart-Dresden effective core potential [5] is used. This basis set combination is hereafter denoted by BS1. The electronic energies are further refined with single point energy calculations using a higher basis

set 6-311++g(d,p) for the lighter atoms. Each optimized structure is subjected to harmonic vibrational frequency analysis to determine the nature of the stationary points either as a minimum (no imaginary frequency) or first-order saddle point (one imaginary frequency). Transition states are confirmed by intrinsic reaction coordinate (IRC) calculations by checking their connection to the desired minima on either side of the saddle point. The thermochemical data are estimated within the framework of ideal gas-rigid rotor-simple harmonic oscillator approximations. Zero-point-energy corrections are included in the Gibbs free energy values along with a concentration correction for c = 1 mol/dm^3 condition in the solvent. The SMD solvation model is used to account for the solvent (DCB:*o*-dichlorobenzene) effects [6]. All calculations are performed with Gaussian16 suit of programs [7].

Note that, we have used the following atom colouring to visualize the molecular geometries: C (grey), H (white), N (blue), O (red), S (yellow), F (pale yellow), and Sn (cyan).

4.3 Results and discussions

4.3.1 General aspects

The use of a truly naked stannylium cation appears to be an impractical choice in FLP catalysis. Since these species are highly reactive in solution, a counterion must accompany the cationic core to improve chemical stability. To this end, Ashley *et al.* opted for *i*Pr$_3$SnOTf as the LA considering its easy synthesizability and thermally robust core structure. It was clear that OTf$^-$ coordination would quench the Lewis acidity of the cationic unit, rendering *i*Pr$_3$SnOTf as an inferior LA, compared to naked *i*Pr$_3$Sn$^+$. Nevertheless, NMR studies by Ashley *et al.* demonstrated that significant stannylium character would still be present in *i*Pr$_3$SnOTf [8]. This was supported by our recent computational study that despite OTf$^-$ coordination *i*Pr$_3$SnOTf still retains requisite Lewis acidity to engage in meaningful FLP chemistry [9].

careful experiments by Ashley and co-workers suggest that iPr$_3$SnOTf catalyses

the hydrogenation of carbonyl compounds in the presence of 10 mol% nitrogenous bases such as collidine under 10 atm of H_2 pressure in DCB solvent [8]. The reaction proceeds at 120 °C and it was found that increasing temperature results in improved yields. Eventually, near quantitative yields were obtained at a temperature as high as 180 °C without any decomposition of the catalyst. To understand mechanistic intricacies of the hydrogenation process, we first investigated the possible outcome of the stoichiometric reactions between the reactants present in the solution. Naturally, we began with the heterolytic activation of H_2, which is an essential mechanistic step for hydrogenation.

In the following studies, dimethylketone or acetone (Me_2CO) is chosen as the model substrate. We considered collidine (hereafter denoted as Col) as the auxiliary base as it has been shown to give the optimal performance experimentally. o-DCB is used as the solvent in accordance with the experiments. For the sake of clear representation, during the discussion of the mechanism, we have abbreviated the "*i*Pr_3Sn' moiety by **Sn**. The solvent-corrected Gibbs free energies for the reaction intermediates and transition states (TSs) are computed at T=120 °C (393.15 K) and 1 atm pressure, unless mentioned otherwise. For the description of the full catalytic cycle, separated reactants i.e. *i*Pr_3SnOTf, Col, H_2 and Me_2CO molecules are used as zero-energy-reference.

It is worth pointing out that we have also considered the possibility of a radical mechanism as this is quite common in the Sn-based reactions. This is particularly relevant because R_3SnH species (one of the reaction intermediates) are susceptible for homolytic Sn-H cleavage giving rise to radical chain mechanisms. However, the homolytic cleavage usually occurs in the presence of a radical initiator or UV radiations, the lack of which rules out the possibility of radical mechanism in the present case. This was also addressed in the experimental works of Ashley *et al.* While studying the hydrogenation of imines catalysed by *i*Pr_3SnOTf, Ashley *et al.* deliberately used a bromoaryl imine substrate to check whether a radical mechanism

is operative or not [8]. The NMR study showed a clean hydrogenation reaction with no experimental evidence of any side reaction such as hydrodebromination, the formation of $i\text{Pr}_3\text{Sn-Sn}i\text{Pr}_3$ or $i\text{Pr}_3\text{SnBr}$. This suggests that the radical Sn species is not involved during the $i\text{Pr}_3\text{SnOTf}$ catalysed hydrogenation reaction. So, it was proposed that the reaction follows a normal polar FLP-hydrogenation mechanism. Also, during their mechanistic study of the carbonyl hydrogenation process, Ashley *et al.* reported no evidence in favour of a radical mechanism. Therefore, considering these experimental observations, we ruled out possibility of a radical mechanism and did not further explore along this route. Instead, we focussed on the polar mechanism for hydrogenation of the carbonyl compound.

4.3.2 Heterolytic H_2 activation by SnOTf/Col Lewis pairs

The heterolytic activation of H_2 by Sn/N Lewis pairs was investigated experimentally by Ashley *et al.* [8]. The NMR studies were consistent with H-H bond cleavage, leading to the formation of Sn-H and N-H bonds in solution. In the previous chapter, we have already established the mechanism of such H_2 splitting with the representative **Sn**OTf/DABCO (1,4-Diazabicyclo[2.2.2]octane) Lewis pairs. Our results show that a similar mechanism prevails for H_2 activation by **Sn**OTf/Col Lewis Pairs although with some minor alterations, which can be associated with the slightly different steric profile and LB strength of Col compared to DABCO. Thus, we refrain from providing a detailed mechanistic description of this reaction Instead, we briefly mention the energetics and a few salient (structural) features of **Sn**OTf/Col-mediated H_2 splitting pathways as the outcome of this step is crucial for the overall catalytic hydrogenation cycle.

4.3.2.1 SnOTf/Col Lewis pair associations

In the former reports of tetrylium LAs in FLP chemistry, silylium (R_3Si^+) ions were usually paired with bulky inert noncoordinating anions, such as $B(C_6F_5)_4^-$ [10, 11]. Therefore, the LA was practically thought to remain in its bare cationic

form. Thus, the counteranion was found to hardly affect LA/LB interaction, and consequently, the formation of a so-called encounter complex (EC) involving only R_3Si^+ and LB was presumed. However, in the present case, the presence of the counter anion plays a critical role in EC formation. In fact, depending upon the mutual positioning of Col and OTf^-, there could be two different modes of interaction between LA and LB.

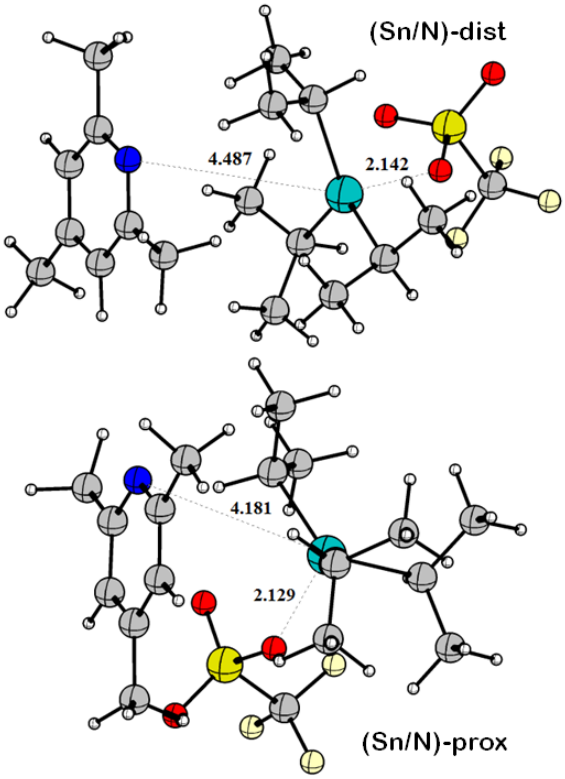

Figure 4.2: Geometry optimized structures of the **Sn**OTf/Col ECs. All distances are given in Å unit.

Accordingly, we have been able to locate two different weak associations between **Sn**OTf and Col in which the Sn and N centres are separated by 4.487 and 4.181 Å. Such long Sn-N distances prevent any dative interaction and thus, these loosely bound structures are characterised as **Sn**OTf/Col ECs, which are hereafter denoted by **(Sn/N)-dist** and **(Sn/N)-prox**. The geometry optimized structures of the **Sn**OTf/Col ECs are displayed in Figure 4.2. These structures are stabilized by means of noncovalent interactions; a combination of multiple C-H$\cdots$F and C-H$\cdots$O

hydrogen bonds along with dispersion interactions. Since the Sn centre is not electronically perturbed, the Sn-O(OTf) distances remain similar to that in **Sn**OTf. The geometries of these two ECs are significantly different. In the former structure, Col interacts with $\mathbf{Sn}^+$ from the opposite side to the OTf^- (distal interaction) while, in the latter, Col interacts to $\mathbf{Sn}^+$ from the same side as OTf^- (proximal interaction). This is reflected in the $\angle N - Sn - O$ angle which is found to be 152.7° and 85.8° in **(Sn/N)-dist** and **(Sn/N)-dist**, respectively. **(Sn/N)-dist** and **(Sn/N)-prox** are electronically bound by 8.9 and 14.2 kcal/mol. However, the entropic penalty for the LA/LB association makes the EC formations endergonic under experimental conditions. The association Gibbs free energies for **(Sn/N)-dist** and **(Sn/N)-prox** are computed to be 10.8 and 9.7 kcal/mol at 393.15 K, which indicates that the ECs will be present in low concentrations in solution.

Note that, apart from the weak associations, we have also been able to optimize a dative adduct between **Sn**OTf and Col via distal interaction. However, the formation of such dative adduct is found to be 13.2 kcal/mol uphill in free energy, presumably due to the high degree of strain caused by the steric repulsion between Me groups in Col and *i*Pr groups in **Sn**OTf. This result is consistent with the experimental observation that upon addition of Col in **Sn**OTf, there is a fairly small change in ^{119}Sn NMR spectrum, suggesting a weak interaction between LA and LB.

4.3.2.2 H_2 cleavage by SnOTf/Col Lewis pairs

Both **(Sn/N)-dist** and **(Sn/N)-prox** can react with H_2 and result in heterolytic cleavage of the H-H bond. Following the nomenclature of our previous report [9], the H_2 cleavage pathways are denoted by distal and proximal pathways mediated by **(Sn/N)-dist** and **(Sn/N)-prox**, respectively. The mechanism of H-H cleavage reveals two simultaneous donor-acceptor interactions involving the lone pair on N atom (N(LP)), $\sigma^*(H_2)$, $\sigma(H_2)$ and empty p-orbital on Sn atom (p(Sn)); electron donations occur from N(LP) to $\sigma^*(H_2)$ and from $\sigma(H_2)$ to empty p(Sn). Both of these electron transfers weaken the H-H bond and eventually, results in heterolytic

cleavage. The relative Gibbs free energy profiles for H_2 splitting by **Sn**OTf/Col Lewis pairs are depicted in Figure 4.3. The heterolytic H_2 cleavage occurs through **TS-**

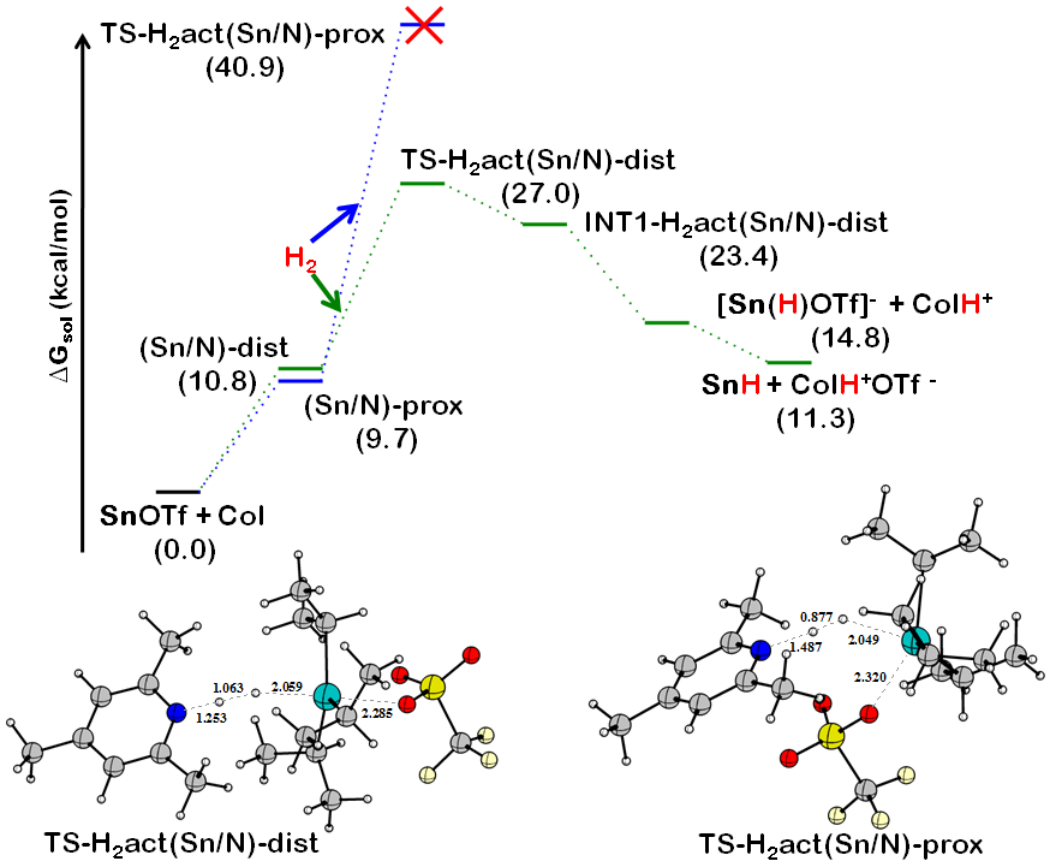

Figure 4.3: Relative Gibbs free energy profile of H_2 cleavage by **Sn**OTf/Col Lewis pairs. Solvent-corrected Gibbs free energy values are given in parenthesis. Geometry optimized structures of the TSs for H_2 cleavage in distal and proximal pathways are also shown. All distances are given in Å unit.

H_2act(Sn/N)-dist and **TS-H_2act(Sn/N)-prox** in distal and proximal pathway, respectively. The free energy activation barrier in the distal pathway is computed to be 27.0 kcal/mol, which is 13.9 kcal/mol lower than that in the proximal pathway, suggesting that the H_2 cleavage would proceed through the former pathway. This result is consistent with our previous computational work in which the **Sn**OTf/DABCO Lewis pair was shown to activate H_2 in the distal pathway [9]. The structure of **TS-H_2act(Sn/N)-dist** reveals that the H-H, Sn-H, and N-H bond distances are 1.063, 2.059 and 1.253 Å, respectively. **TS-H_2act(Sn/N)-dist** relaxes to **INT1-H_2act(Sn/N)-dist**, which readily dissociates into [**Sn**(H)OTf]$^-$ and ColH$^+$ through

a exergonic reaction step (ΔG= -8.6 kcal/mol). Later, OTf^- can also be released from the Sn centre, leading to the formation of **Sn**H and ColH$\cdots$OTf; this step is downhill in free energy by 12.1 kcal/mol with respect to **INT1-H_2act-dist**.

4.3.3 Substrate activation and transfer of active hydrogens

After H_2 cleavage, active hydrogens are available in the form of [**Sn**(H)OTf]$^-$ (or **Sn**H) and ColH$^+$ as hydride and proton sources, respectively, and subsequent transfer of these would complete the hydrogenation process. This can occur either in the sequence of proton transfer (PT) followed by hydride transfer (HT) or HT followed by PT. Thus, there is a question of which one would occur first. Nonetheless, prior to HT/PT, we examined the feasibility of a substrate activation step either by ColH$^+$ or by **Sn**OTf.

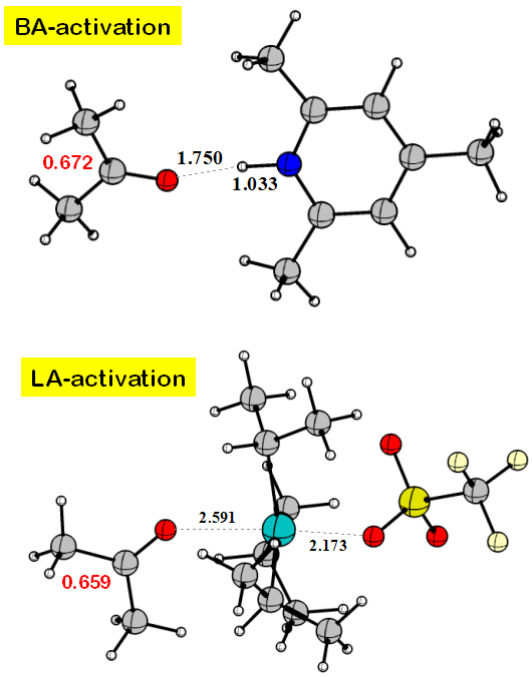

Figure 4.4: Bronsted acid activation and Lewis acid activation of the carbonyl substrate. Geometry optimized structures of the BA and LA-activated substrates are also shown. All distances shown in the figure are in Å. The NPA atomic charges on carboyl carbon atom are shown in red.

4.3.3.1 Bronsted acid activation (BAA)

We first contemplated a Bronsted acid (BA) activation mode (see Figure 4.4) in which ColH$^+$, liberated upon H_2 cleavage, turns on the substrate by forming a hydrogen-bonding interaction with the carbonyl oxygen. This notion was based on the previously studied $B(C_6F_5)_3$-catalysed hydrogenation of carbonyl compounds in ethereal solvents. In an attempt to elucidate the mechanistic picture of that reaction (as reported in Chapter 2), we proposed that the carbonyl substrate was activated via forming hydrogen-bonding interaction with a protonated ether molecule [1]. Also, note that in the $B(C_6F_5)_3$-catalysed process, substrate activation was immediately followed by a PT step which made the carbonyl carbon even more electrophilic and the subsequent HT occurred with low activation energy barrier. In the present case, the structure of $[Me_2CO\cdots HCol]^+$ shows a hydrogen bonding interaction with a N-H$\cdots$O distance of 1.750 Å. As a result, the NPA atomic charge in the carbonyl carbon is higher (0.672 *vs.* 0.607) compared to that in Me_2CO, which suggests increased hydridophilicity. However, we rule out the possibility of a further PT from Col to carbonyl oxygen as the reaction Me_2CO + ColH$^+$ $\rightarrow$ $[Me_2COH]^+$ + Col is computed to be strongly endergonic (ΔG= 29.9 kcal/mol), which is also consistent with the higher basicity of Col compared to Me_2CO. This stands in contrast with the $B(C_6F_5)_3$-catalysed hydrogenation, which represented a case of BAA through full protonation of the carbonyl substrate in order to facilitate subsequent HT [1]. Thus, we decided to examine the feasibility of HT to $[Me_2CO\cdots HCol]^+$.

We first attempted to locate a TS for HT to $[Me_2CO\cdots HCol]^+$ by [**Sn**(H)OTf]$^-$ and the corresponding Gibbs free energy profile is displayed in Figure 4.5. Surprisingly, we ended up optimizing a TS, **TS-HT/PT-BAA**, in which both the proton and the hydride are transferred into the carbonyl substrate in a concerted manner, and the desired alcohol product is formed in a single step. A similar concerted HT and PT has also been recently reported in the hydrogenation of CO_2 by Mn(I)-complexes, built with acylmethylpyridinol ligand [12]. However, the structure of **TS-HT/PT-BAA**

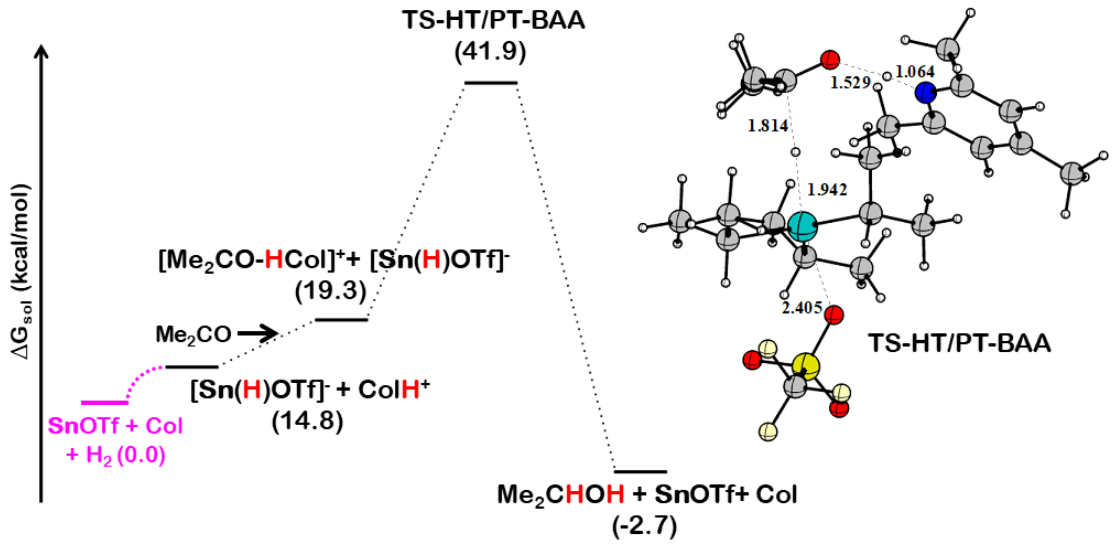

Figure 4.5: Relative Gibbs free energy profile of concerted HT and PT to the BA-activated carbonyl substrate. Solvent-corrected Gibbs free energy values are given in parenthesis. Geometry optimized structure of the **TS-HT/PT-BAA** is also shown. The magenta-colored segment in the free energy profile is used to mark the zero-energy-reference. All distances shown in the figure are in Å unit.

reveals a nearly linear arrangement of the N-H-O (171.3 °) and Sn-H-C (167.7 °) atom segments; the relevant N-H, O-H, C-H and Sn-H distances are found to be 1.064, 1.529, 1.814 and 1.942 Å respectively. Unfortunately, the free energy barrier for this concerted hydride and proton transfer is found to be prohibitively high (41.9 kcal/mol) with respect to separated reactants, **Sn**OTf+Col+H_2+Me_2CO. While considering HT to $[Me_2CO\cdots HCol]^+$ by **Sn**H, we have located another concerted TS analogous to **TS-HT/PT-BAA**, corresponding to an even higher activation barrier of 44.6 kcal/mol. Thus, accessing such TSs might not be feasible under experimental conditions, and we turned our attention to explore other relatively low-energy pathways.

4.3.3.2 LA activation (LAA)

Alternatively, as already suggested by Ashley *et al.*, the substrate may also be activated via dative coordination of a LA molecule with the carbonyl oxygen, leading to the formation of Me_2CO-**Sn**OTf [8]. The notion of LAA came from a direct experimental observation that the NMR spectrum of a solution of Me_2CO and **Sn**OTf

indicates substantial Sn-O interaction. Note that, prior computational works have also shown that the elctrophilicity of the carbonyl carbon can be significantly increased by complexation with $B(C_6F_5)_3$ LA [13, 14]. However, the optimized structure of Me_2CO-**Sn**OTf shows a near trigonal bipyramid-geometry around the Sn centre with the carbonyl oxygen and an OTf oxygen occupying the axial positions; the Sn-O(carbonyl) and Sn-O(OTf) distances are found to be 2.591 and 2.173 Å, respectively. The slight elongation in the latter distance compared to that in **Sn**OTf indicates Sn-carbonyl interaction. Our results show that formation of Me_2CO-**Sn**OTf adduct is nearly thermoneutral (ΔG= 0.6 kcal/mol at 393.15 K), which suggests an equilibrium between the dative adduct and the free components under experimental condition. Nonetheless, LA-coordination does make the carbonyl carbon more electrophilic, which is apparent from the increased NPA atomic charge on the carbon atom (0.659 *vs.* 0.607 in Me_2CO).

We now focus into the sequential transfer of the activated hydrogens i.e. HT to LA-activated carbonyl followed by PT. The possibility of PT before HT can safely be ruled out as the process Me_2CO-**Sn**OTf+ColH$^+$ $\rightarrow$ [Me_2COH-**Sn**OTf]$^+$+Col is computed to be strongly endergonic. HT to Me_2CO-**Sn**OTf may occur via two reaction pathways involving either [**Sn**(H)OTf]$^-$ or **Sn**H as the HT agent. The corresponding free energy profiles along with the optimized structures of the TSs are depicted in Figure 4.6.

[**Sn**(H)OTf]$^-$ directly transfers a hydride to the carbonyl carbon through **TS-HT-LAA-1**, which corresponds to a free energy activation barrier of 17.1 kcal/mol with respect to [**Sn**(H)OTf]$^-$+Me_2CO-**SnOTf**. The structure of **TS-HT-LAA-1** reveals a near linear arrangement of the Sn-H-C atoms as indicated by $\angle Sn-H-C$ angle of 172.0°. The transferring H atom remains almost equidistant from the Sn and the C atoms; the Sn-H and C-H distances are found to be 1.870 and 1.888 Å. The HT initially leads to the formation of [Me_2CHO-(**Sn**OTf)$_2$]$^-$ that features an "alkoxide" (Me_2CHO^-) sandwiched between two **Sn** units (see Figure 4.7). The alkoxide oxygen

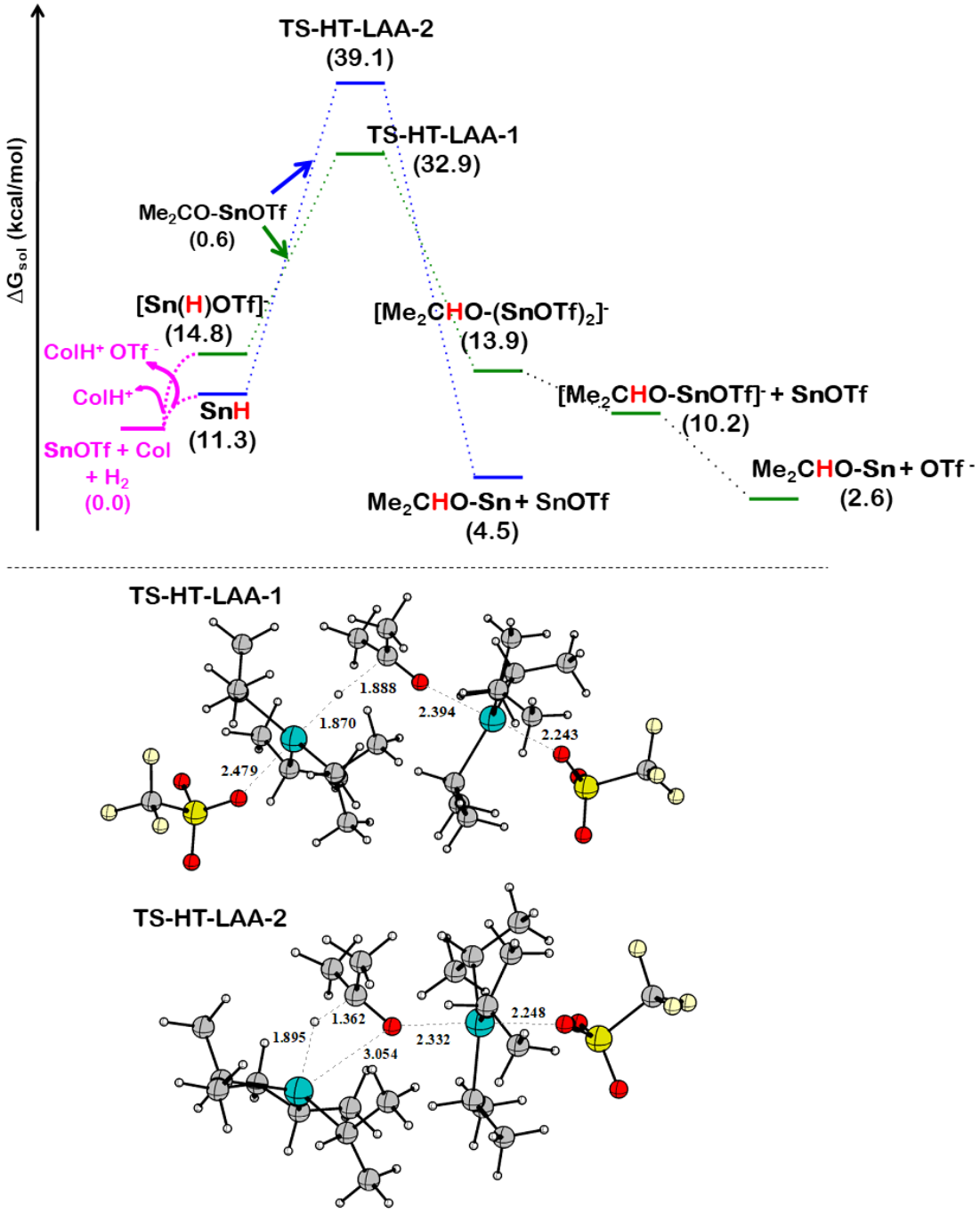

Figure 4.6: Relative Gibbs free energy profile of HT by [**Sn**(H)OTf]$^-$ and **Sn**H to Me_2CO-**Sn**OTf. Solvent-corrected Gibbs free energy values are given in parenthesis. The magenta-colored segment in the free energy profile is used to mark the zero-energy-reference. Geometry optimized structures of the TSs for HT are also shown. All distances shown in the figure are in Å unit.

binds to two Sn centres in a nearly symmetrical fashion as the two Sn-O(carbonyl) distances are found to be very similar (2.333 and 2.323 Å). [Me_2CHO-(**Sn**OTf)$_2$]$^-$

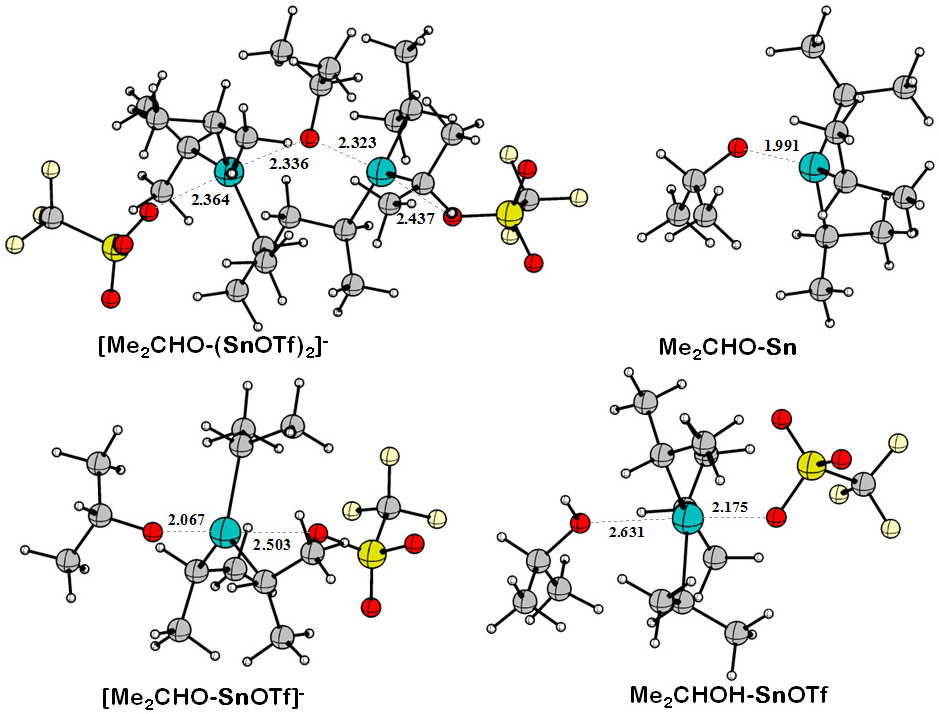

Figure 4.7: Geometry optimized structures of various reaction intermediates during HT and PT. All distances shown in the figure are in Å unit.

readily loses a LA molecule to form [Me_2CHO-**Sn**OTf]$^-$ and the process is exergonic by 3.7 kcal/mol. It can further lose an OTf^- to form Me_2CHO-**Sn**; this is even more exergonic with ΔG=-7.5 kcal/mol. The released OTf^- can be stabilized in the solution by forming a hydrogen bonding interaction with the ColH$^+$, liberated upon H_2 cleavage. We noticed that the Sn-O(alkoxide) distance in [Me_2CHO-**Sn**OTf]$^-$ is significantly smaller than the Sn-O(carbonyl) in Me_2CO-**Sn**OTf, indicating a greater extent of Sn-O interaction. This is owing to the more basic nature of the alkoxide oxygen compared to the carbonyl oxygen. Consequently, strong Sn-O(alkoxide) interaction results in weakening of the Sn-OTf interaction, which is reflected in the significantly longer Sn-O(OTf) distance in [Me_2CHO-**Sn**OTf]$^-$ compared to that in Me_2CO-**Sn**OTf. The Sn-O(alkoxide) distance is 2.067 Å in Me_2CHO-**Sn**, which is even shorter than the Sn-O distance in **Sn**OTf, suggesting a strong Sn-O interaction. However, the overall HT step [**Sn**(H)OTf]$^-$+Me_2CO-**Sn**OTf→Me_2CHO-**Sn**+**Sn**OTf+OTf^- is exergonic by 12.7 kcal/mol. If **Sn**H delivers the hydride to

carbonyl, the reaction proceeds via **TS-HT-LAA-2**. The computed activation barrier with respect to **Sn**H+Me_2CO-**SnOTf** is found to be 27.1 kcal/mol, which is about 10.0 kcal/mol higher than the former HT with [**Sn**(H)OTf]$^-$. Thus, on the basis of the computed free energy activation barrier, [**Sn**(H)OTf]$^-$-mediated HT pathway is found to be kinetically preferred over the **Sn**H-mediated HT.

At this point, we tried to understand the origin of higher barrier in the HT process promoted by **Sn**H. When we examined the structures of **TS-HT-LAA-1** and **TS-HT-LAA-2**, certain differences were observed. The most striking difference is the non-linear arrangement of the Sn-H-C atoms in **TS-HT-LAA-2** as indicated by $\angle Sn-H-C = 130.9°$. In fact, **TS-HT-LAA-2** seems like a four-membered ring transition state as the Sn-O(carbonyl) distance is much smaller compared to that in **TS-HT-LAA-1**. Qualitatively, we can argue that an anionic [**Sn**(H)OTf]$^-$ is more likely to lose a hydride compared to a neutral **Sn**H and thus, the former species, being a better hydride donor, promotes HT with a lower activation barrier. Nevertheless, to obtain a quantitative estimate, we have calculated the Gibbs free energies of hydride detachment (HDFE) according to the equation $EH^n \rightarrow E^{n+1}+ H^-$. A smaller HDFE suggests a higher hydride donating ability. We find that HDFE of [**Sn**(H)OTf]$^-$ is 27.5 kcal/mol, which is about 31.0 kcal/mol lower compared to that in **Sn**H. Therefore, [**Sn**(H)OTf]$^-$ is a much stronger hydride donor than **Sn**H. NBO calculations further confirm the picture. The H atom in [**Sn**(H)OTf]$^-$ bears a NPA atomic charge of -0.365, while the same in **Sn**H is found to be -0.283; the greater negative charge in the former species suggests a higher electron density on the H atom which is more prone to attack the π^*(C=O) orbital. Also, the higher lying σ(Sn-H) orbital in [**Sn**(H)OTf]$^-$ (-0.232 *vs.* -0.381 eV in **Sn**H) is better suited to donate electrons to the carbonyl moiety. Therefore, we propose that [**Sn**(H)OTf]$^-$ acts as the active HT agent in solution.

Once Me_2CHO-**Sn** is formed in the solution, the alkoxide oxygen can easily be protonated by Col$H^+ \cdots OTf^-$. The protonation step can be represented by the

reaction Me_2CHO-**Sn** + $ColH^+ \cdots OTf^-$ → Me_2CHOH-**Sn** + Col, which is computed to be exergonic by 5.6 kcal/mol. After PT, the carbonyl substrate is fully hydrogenated to the alcohol product, Me_2CHOH. Me_2CHOH initially forms in a LA-bound form, Me_2CHOH-**Sn**OTf. However, thermal dissociation of the complex liberates the free alcohol, releasing the LA catalyst. The overall catalytic reaction Me_2CO + H_2 + **Sn**OTf + Col → Me_2CHOH + **Sn**OTf + Col is thermodynamically favorable by 2.7 kcal/mol.

4.3.4 H_2 activation by SnOTf/alkoxide Lewis pairs

In their experimental work, Ashley *et al.* pointed out that the formation of alkoxide intermediate opens up the possibility of an additional pathway, which also leads to the alcohol product. The alkoxide possesses a Lewis basic oxygen atom, and in principle, it could activate another molecule of H_2 in conjunction with **Sn**OTf. To examine this additional pathway, we first considered H_2 activation for the LA/LB combination of **Sn**OTf/Me_2CHO-**Sn**. We did characterize a weak LA/LB EC in the distal pathway along with a corresponding LA/LB/H_2-adduct in which the H_2 molecule is weakly bound to the EC. Unfortunately, we could locate neither a TS for H_2 cleavage nor a putative H_2 activated product (i.e a zwitterionic structure in which the H-H bond is completely cleaved) along this reaction channel. In fact, relaxed potential energy scan calculations (starting from the H_2-adduct) with respect to H-H distance suggest that a H_2 activated product does not even correspond to a local minimum. Thus, we looked for alternative possibilities.

We noticed that [Me_2CHO-**Sn**OTf]$^-$, which is formed en-route to Me_2CHO-**Sn**, is a stronger base compared to Me_2CHO-**Sn**. This can be confirmed by the free energy change of the reaction [Me_2CHOH-**Sn**]$^+$+[Me_2CHO-**Sn**OTf]$^-$→Me_2CHO-**Sn**+Me_2CHOH-**Sn**OTf, which is computed to be -16.6 kcal/mol. The OTf coordination makes [Me_2CHO-**Sn**OTf]$^-$ a better electron donor as indicated from the slightly increased NPA atomic charge (-0.985 vs -0.969) on the alkoxide oxygen atom compared to Me_2CHO-**Sn**. Hence, we inquired the feasibility of H_2 activation

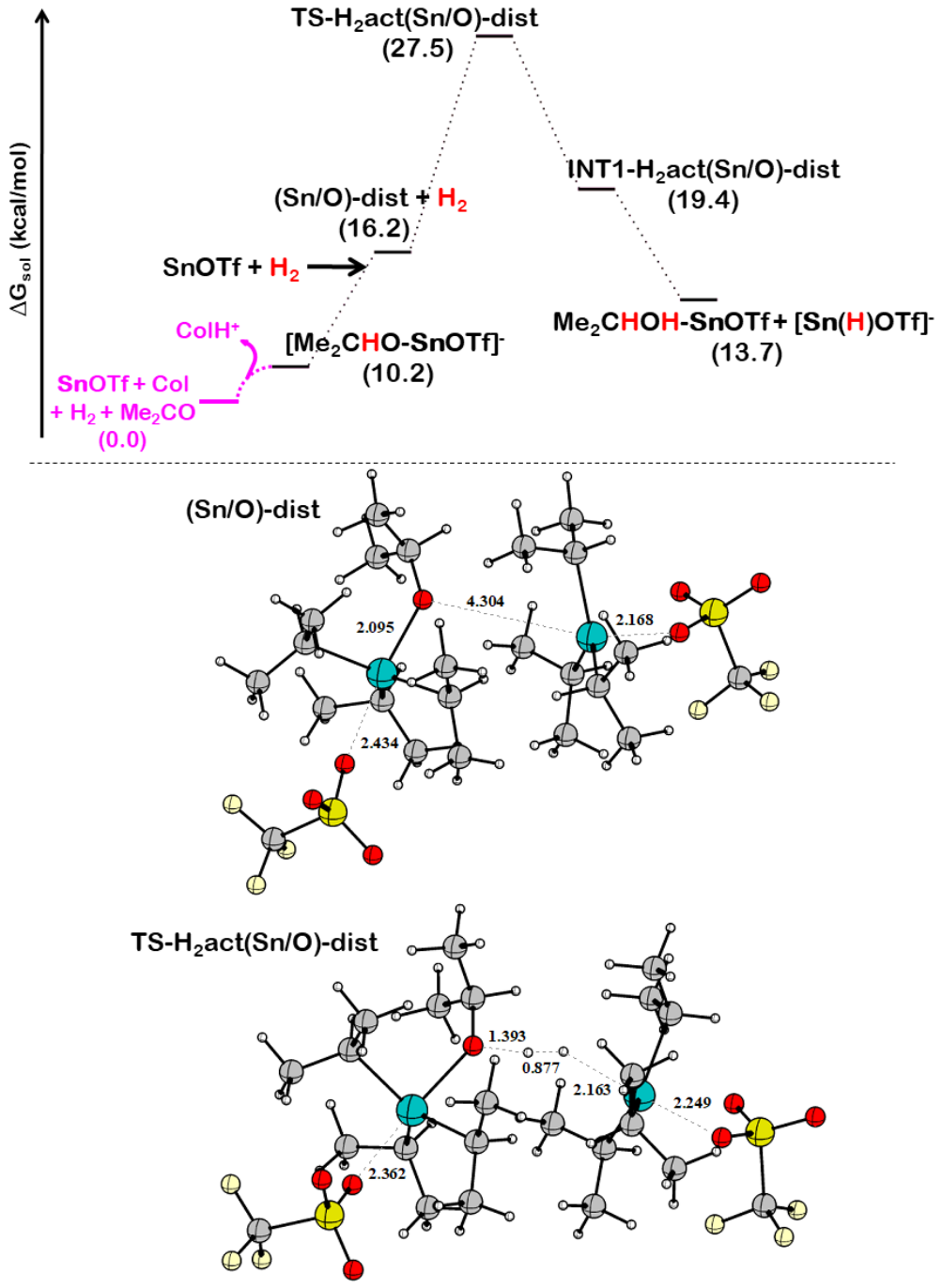

Figure 4.8: Relative Gibbs free energy profile for H_2 cleavage by **Sn**OTf/[Me_2CHO-**Sn**OTf]$^-$ Lewis pair. Solvent-corrected Gibbs free energy values are given in parenthesis. The magenta-colored segment in the free energy profile is used to mark the zero-energy-reference. Geometry optimized structures of the corresponding EC and TS for H_2 cleavage in distal pathway are given below. All distances shown in the figure are in Å unit.

mediated by **Sn**OTf/[Me_2CHO-**Sn**OTf]$^-$ combination and the corresponding relative free energy profile is depicted in Figure 4.8. Noncovalent association between **Sn**OTf

and [Me_2CHO-**Sn**OTf]$^-$ leads to the formation of an anionic EC, **(Sn/O)-dist**, via distal interaction. In the structure of this EC, OTf$^-$ and [Me_2CHO-**Sn**OTf]$^-$ remain on the opposite sides of **Sn**$^+$ unit. The Sn(LA)-O(LB) distance is found to be 4.304 Å. Note that, although several cationic FLP structures are dispersed in literature, examples of anionic FLP [15] combinations are relatively scarce. However, **(Sn/O)-dist** activates H_2 in a similar manner as Sn/N FLPs; concerted single step heterolytic H-H cleavage via **TS-H_2act(Sn/O)-dist**. The structure of **TS-H_2act(Sn/O)-dist** reveals a H-H distance of 0.877 Å along with Sn-H and O-H distances of 2.163 and 1.393 Å, respectively. NBO calculations reveal donor-acceptor interactions between the alkoxide oxygen lone pair, $\sigma^*(H_2)$, $\sigma(H_2)$ and empty p-orbital on Sn atom (p(Sn)). The computed activation barrier is found to be 17.3 kcal/mol with respect to [Me_2CHO-**Sn**OTf]$^-$+**Sn**OTf+H_2. The primary product of H_2 cleavage is **INT1-H_2act(Sn/O)-dist**, which features two H atoms in a distance of 1.426 Å. Dissociation of **INT1-H_2act(Sn/O)-dist** liberates LA-bound alcohol, Me_2CHOH-**Sn**OTf, along with [**Sn**(H)OTf]$^-$. After that, thermal dissociation of Me_2CHOH-**Sn**OTf releases the alcohol product. Note that, this reaction route provides an alternative pathway for the generation of alcohol without the involvement of the auxiliary base (or in other words, without the conventional PT step).

4.3.5 Full catalytic cycle

Our computational results described up to this point aided us to elucidate the mechanism of individual stoichiometric reaction steps involved in the Sn/N Lewis pair catalysed hydrogenation of carbonyl compounds. Now, we wish to collate these steps into a catalytic hydrogenation cycle. The relative Gibbs free energy profile for the full catalytic pathway is depicted in Figure 4.9. The hydrogenation necessarily begins with the formation of **Sn**OTf/Col EC, **(Sn/N)-dist**, which activates H_2 and splits the H-H bond, leading to the formation of active hydride ([**Sn**(H)OTf]$^-$) and proton (ColH$^+$) in solution. The free energy activation barrier for H_2 cleavage is 27.0 kcal/mol, which corresponds to **TS-H_2act(Sn/N)-dist**. H_2 activation is followed

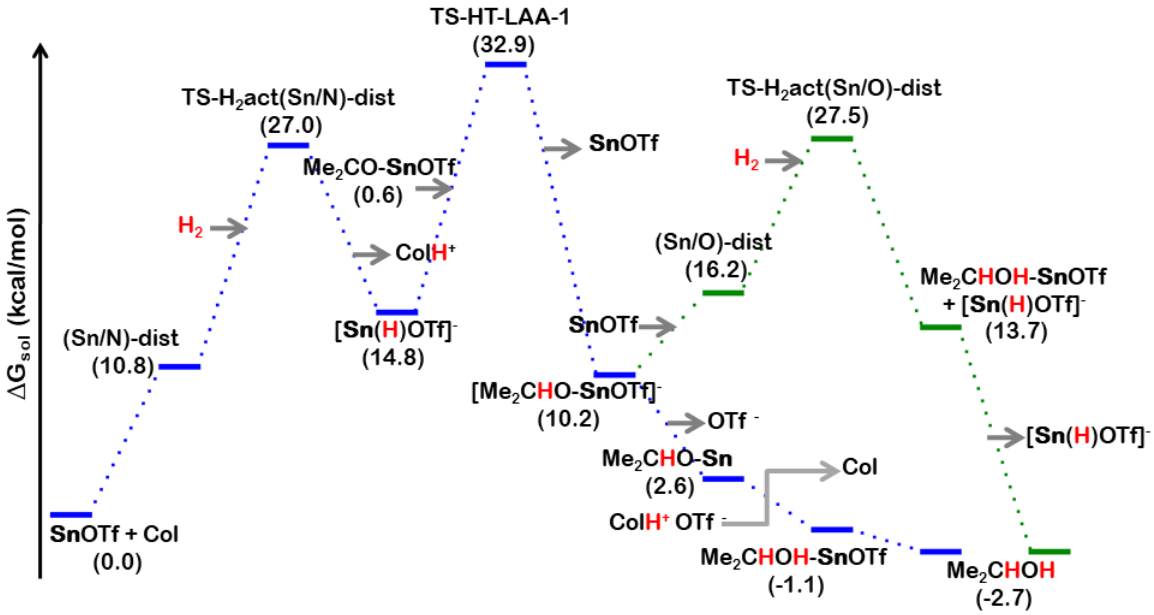

Figure 4.9: Relative Gibbs free energy profile for the complete catalytic hydrogenation cycle. Blue and green colour represent cycle **C-1** and **C-2**, repectively. Solvent-corrected Gibbs free energy values are given in parenthesis.

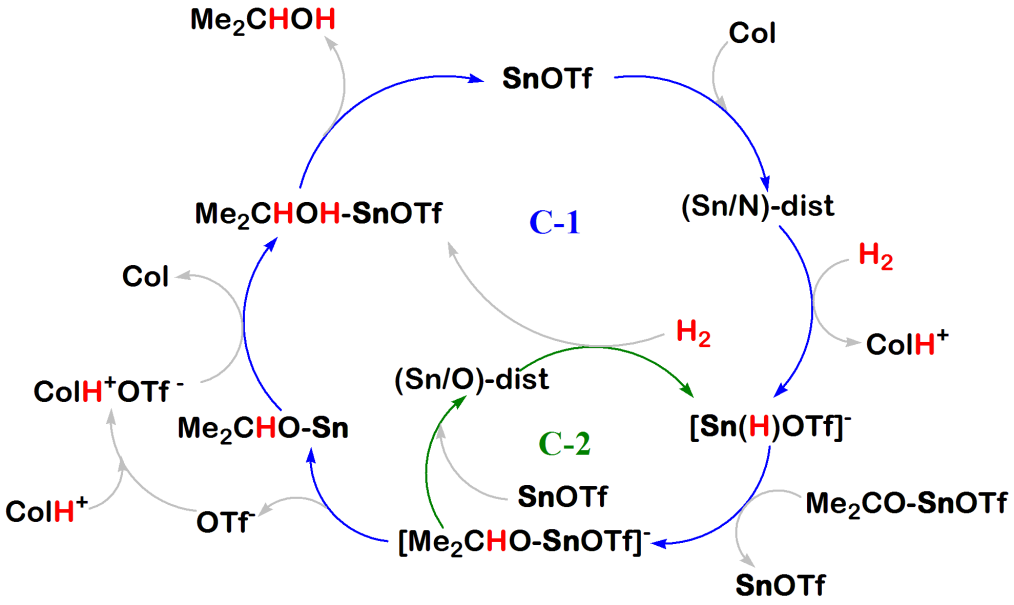

Figure 4.10: Plausible catalytic routes, **C-1** (blue) and **C-2** (green), for Sn/N FLP catalysed hydrogenation of carbonyl compunds.

by subsequent transfer of the hydride and proton to close the catalytic cycle. Prior to HT, a **Sn**OTf molecule activates the carbonyl moiety by coordinating with the carbonyl oxygen. [**Sn**(H)OTf]$^-$ directly transfers the hydride to the LA-activated substrate to generate an alkoxide intermediate. The free energy activation barrier for

the HT step is 32.9 kcal/mol, which corresponds to **TS-HT-LAA-1**. The alkoxide can readily be protonated by $ColH^+$ in solution forming the alcohol, which initially remains coordinated to a LA molecule. Thermal dissociation of the complex liberates the alcohol and regenerates the catalyst. Thus, the catalytic cycle, closed by the reaction sequence H_2 activation → substrate activation → HT → PT, is denoted by **C-1** and depicted by the outer cycle in Figure 4.10.

One key point emerging from our mechanistic model is the feasibility of an additional Sn/O FLP-mediated H_2 activation pathway, which extends **C-1** by another catalytic cycle **C-2**, shown by the inner cycle in Figure 4.10. After HT in **C-1**, $[Me_2CHO\text{-}\mathbf{Sn}OTf]^-$ is generated, which in combination with **Sn**OTf forms a FLP and splits a molecule of H_2. Note that, upon Sn/O-mediated H_2 activation, along with the alcohol product, $[\mathbf{Sn}(H)OTf]^-$ is also released, which is the active HT agent in the solution. Eventually, $[\mathbf{Sn}(H)OTf]^-$ would transfer the hydride to LA-activated substrate to generate more $[Me_2CHO\text{-}\mathbf{Sn}OTf]^-$ and close the catalytic cycle. Note that, **C-2** is a base-free autocatalytic route to alcohol, although it is not completely independent of **C-1**. Similar autocatalysis was also previously reported by Papai *et al.* in the mechanism of $B(C_6F_5)_3$-catalysed hydrogenation of imines to amines [16]. In that case, the hydrogenated product (amine) itself was capable of activating hydrogens in partnership with $B(C_6F_5)_3$ and these resulted in active hydrogens which would further reduce imine to amine. However, the present case is slightly different as the autocatalytic pathway begins not from the completely hydrogenated form of carbonyl, but rather from the alkoxide intermediate obtained after HT step.

Having examined the possible catalytic pathways, we now delve to settle the course of the reaction. We see that HT, which corresponds to the highest barrier in the free energy profile, is a common step in both **C-1** and **C-2**. Thus, in principle, none of these two cycles is as such kinetically favorable over the other. Also similar in **C-1** and **C-2** is the barrier for H_2 splitting since **TS-H_2act(Sn/N)-dist** and **TS-H_2act(Sn/O)-dist** lie very close in free energy. Therefore, the question remains

that which of these two pathways will ultimately prevail? As mentioned previously, the reaction must commence with **C-1**. After H_2 cleavage, substrate activation and HT, $[Me_2CHO\text{-}\mathbf{Sn}OTf]^-$ is formed. At this point, the reaction route may bifurcate and enter into **C-2**. Now, there can be two conceptually different scenarios. (1) If **C-2** prevails, the LB is no longer required. Since **C-2** is itself an autocatalytic route to product, the reaction might take this course and reach to the product. In that case, the outcome of the reaction becomes independent of the choice of the LB because it would then only be required for the initial H_2 cleavage step to release hydride so that HT could occur to provide an entry into **C-2**. (2) On the contrary, if **C-1** continues to resume after HT, the LB actively participates in the reaction during the PT step, and thus, we expect it to influence the outcome of the reaction. The experimental results suggest that the choice of LB is crucial for the hydrogenation. If DABCO, which is a stronger base than Col, is used, the yield is found to be lower, indicating the involvement of the LB in the hydrogenation pathway. Therefore, cycle **C-1** seems to be more consistent with the experimental observation. To confirm this, we have computed the Gibbs free energy change for the final protonation step in **C-1** and our results show that PT step is 2.2 kcal/mol endergonic for DABCO, which is qualitatively in agreement with the experiment. Note that, the same protonation is found to be 5.6 kcal/mol exergonic for Col. This can be rationalized by comparing the basic strength of DABCO and Col. DABCO, being a stronger base than Col, makes its conjugate acid, $DABCOH^+$, a weaker proton donor compared to $ColH^+$. Therefore, the hydrogenation proceeds through **C-1** pathway with an overall free energy activation barrier of 32.9 kcal/mol, which is consistent with the observed reactivity at experimental temperature.

4.4 Conclusion

In summary, we have explored the full mechanism of the hydrogenation of carbonyl compounds catalysed by frustrated Sn/N Lewis pairs using comprehensive DFT

calculations. By comparing the energy profiles of possible elementary reaction steps, we have been able to outline a mechanism for the catalytic hydrogenation process. The catalytic cycle is closed in four main basic steps. First step consists of a typical Sn/N FLP-mediated heterolytic splitting of H_2 by **Sn**OTf/Col Lewis pair to release active hydrogens in the solution. The second step, substrate activation, may proceed with two conceptually different modes namely BAA and LAA. Subsequent steps involve the delivery of the hydride and the proton to the activated substrate to complete the catalytic hydrogenation cycle. A concerted hydride and proton transfer following the BAA mode is found to be kinetically infeasible due to high activation energy barrier. This contrasts with the related $B(C_6F_5)_3$-catalysed hydrogenation of carbonyl compounds in which BAA mode is found to prevail. Instead, we found that hydride transfer to the LA-activated substrate followed by a proton transfer leads to the alcohol product through a low energy pathway. We have also explored the possibility of a competitive reaction pathway in which an alkoxide intermediate is shown to further assist in the H_2 activation process and this opens up an autocatalytic route to the alcohol product. The Sn/O-mediated H_2 activation shares a number of common features as that with Sn/N Lewis pairs and also proceeds with a comparable activation barrier. Furthermore, our results reveal that $[\mathbf{Sn}(H)OTf]^-$ is responsible for HT in solution instead of **Sn**H. In fact, the anion coordination makes the former a stronger hydride donor. This suggests the additional importance of OTf^- in aiding the HT step along with its trivial role in stabilizing the proton through hydrogen-bonding interaction. The mechanistic understanding obtained in the present work would assist in the rational design of Sn-based FLP hydrogenation catalysts, and our efforts in this regard are reported in the next chapter.

Bibliography

[1] Das, S.; Pati, S. K. *Chemistry-A European Journal* **2017**, *23*, 1078–1085.

[2] Zhao, Y.; Truhlar, D. G. *Theoretical Chemistry Accounts: Theory, Computation, and Modeling (Theoretica Chimica Acta)* **2008**, *120*, 215–241.

[3] Zhao, Y.; Truhlar, D. G. *Accounts of chemical research* **2008**, *41*, 157–167.

[4] Grimme, S.; Antony, J.; Ehrlich, S.; Krieg, H. *The Journal of chemical physics* **2010**, *132*, 154104.

[5] Andrae, D.; Haeussermann, U.; Dolg, M.; Stoll, H.; Preuss, H. *Theoretical Chemistry Accounts: Theory, Computation, and Modeling (Theoretica Chimica Acta)* **1990**, *77*, 123–141.

[6] Marenich, A. V.; Cramer, C. J.; Truhlar, D. G. *The Journal of Physical Chemistry B* **2009**, *113*, 6378–6396.

[7] Frisch, M. J. et al. Gaussian 16 Revision A.03. 2016; Gaussian Inc. Wallingford CT.

[8] Scott, D. J.; Phillips, N. A.; Sapsford, J. S.; Deacy, A. C.; Fuchter, M. J.; Ashley, A. E. *Angewandte Chemie International Edition* **2016**, *55*, 14738–14742.

[9] Das, S.; Mondal, S.; Pati, S. K. *Chemistry-A European Journal* **2018**, *24*, 2575–2579.

[10] Reißmann, M.; Schafer, A.; Jung, S.; Muller, T. *Organometallics* **2013**, *32*, 6736–6744.

[11] Schäfer, A.; Reißmann, M.; Schäfer, A.; Saak, W.; Haase, D.; Müller, T. *Angewandte Chemie International Edition* **2011**, *50*, 12636–12638.

[12] Das, S.; Pati, S. K. *Catalysis Science & Technology* **2018**, *8*, 3034–3043.

[13] Heshmat, M.; Privalov, T. *Chemistry-A European Journal* **2017**, *23*, 9098–9113.

[14] Heshmat, M.; Privalov, T. *The Journal of chemical physics* **2017**, *147*, 094302.

[15] Kyri, A.; Kunzmann, R.; Schnakenburg, G.; Qu, Z.-W.; Grimme, S.; Streubel, R. *Chemical Communications* **2016**, *52*, 13361–13364.

[16] Rokob, T. A.; Hamza, A.; Stirling, A.; Pápai, I. *Journal of the American Chemical Society* **2009**, *131*, 2029–2036.

Chapter 5

Activation of Hydrogen and Hydrogenation Catalysis by Intramolecular Sn/N Lewis Pairs*

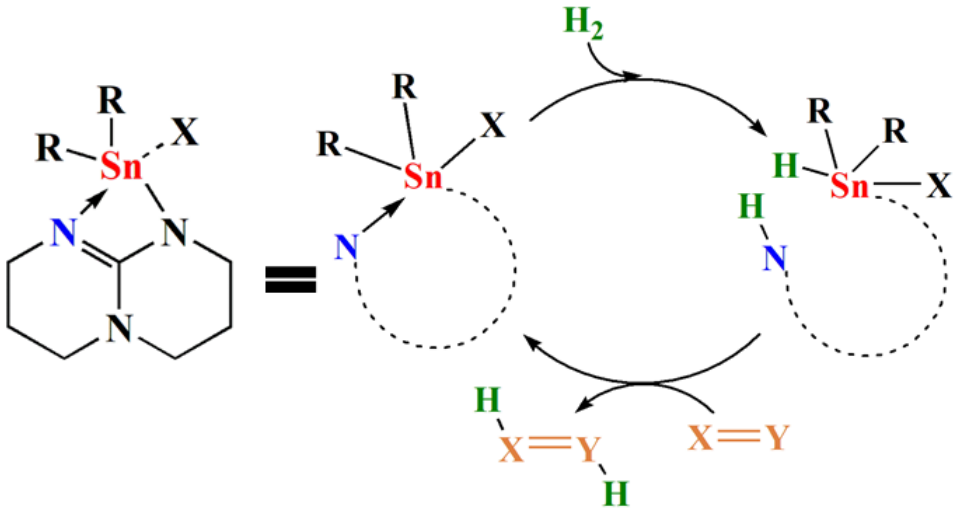

*Work reported in this chapter is based on: Shubhajit Das, Swapan K Pati, submitted (2018)

5.1 Introduction

The previous two chapters helped us to achieve a comprehensive understanding of the mechanism of H_2 activation and catalytic hydrogenation by intermolecular Sn/N FLPs. The molecular level insights obtained in those studies made us contemplate about designing intramolecular Sn-based FLPs with improved catalytic activity. In this chapter, we have proposed a new series of intramolecular Sn/N Lewis pairs (LP) and examined their H_2 activation/release propensities using DFT computations. Note that, we decided to keep the Lewis acidic and basic centres to Sn(IV) and N since the corresponding intermolecular analogues are experimentally realized and well-understood.

5.2 Design of intramolecular Sn/N Lewis pairs

We began by searching for a suitable linker to tether the LA and LB units together. The idea was to position the active Sn and N sites in the vicinal arrangements in analogy to the previously developed P/B systems [1]. Furthermore, we looked for an optimal backbone to embed the Sn/N centres which would provide structural integrity to the LP. Our interest was drawn to a cyclic guanidinate backbone, TBD, which was previously utilized by Cantat *et al.* to stabilise the silylium cations [2]. In that case, the base-stabilised silylium cations showed intramolecular FLP reactivity in partnership with a guandinate ring N atom. Inspired by this, we have designed intramolecular Sn/N LPs featuring the same backbone hoping to extract similar reactivity out of it. The general structural framework of the newly designed Sn/N LPs is shown in Figure 5.1.

Two structural features, the substituents (R) on the Sn centre and the counter anion (X), mainly determine the reactivity of Sn/N LPs. To create a diverse pool of LPs, we first look for suitable R and X groups. Three chosen candidates for X are Cl^-, OTf^- and NTf_2^-, which possess different coordination strength to Sn centre. Furthermore, choosing alkyl groups methyl (Me), benzyl (Bn) and isopropyl (*i*Pr)

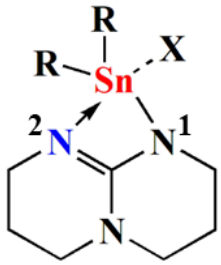

1-R-X

R/X	Cl	OTf	NTf_2
Me	1-Me-Cl	1-Me-OTf	1-Me-NTf_2
Bn	1-Bn-Cl	1-Bn-OTf	1-Bn-NTf_2
*i*Pr	1-*i*Pr-Cl	1-*i*Pr-OTf	1-*i*Pr-NTf_2

Figure 5.1: Structural framework of our proposed intramolecular Sn/N Lewis pairs along with the chosen nine candidates.

provides different steric environment around the Sn centre. Note that, these choices (of R/X) are made on the basis of their prevalence in the intermolecular Sn/N FLPs and corresponding intramolecular Si/N FLP systems [2–4]. Initially, to examine the basic reactivity pattern with H_2, we have considered all possible combinations of these R and X groups and prepared a set of total nine candidates. Hereafter, we have denoted the newly designed intramolecular Sn/N LPs by **1-R-X**.

5.3 Computational details

For the consistency, we have used the same computational protocol as used in Chapter 3 and 4. All geometry optimizations are performed using M062X [5, 6] functional under the framework of DFT. We have employed Grimme's D3 dispersion model [7] to take into account noncovalent interactions. We have used 6-311G(d,p) basis set on lighter atoms (C, H, N, F, O, S, Cl), while for the Sn atom, def2TZVP along with Stuttgart-Dresden effective core potential [8] is used. This basis set combination is hereafter denoted by BS1. The electronic energies are further refined with single point energy calculations using a higher basis set 6-311++g(d,p) for the lighter atoms. Each optimized structure is subjected to harmonic vibrational frequency analysis to determine the nature of the stationary points. Transition states are further confirmed by intrinsic reaction coordinate (IRC) calculations. The thermochemical data are estimated within the framework of ideal gas-rigid rotor-simple harmonic oscillator approximations. Zero-point-energy corrections are included in the Gibbs

free energy values along with a concentration correction for c = 1 mol/dm^3 condition in the solvent. We have used *o*-dichlorobenzene as the solvent (in analogy with the reactivity of corresponding intermolecular Sn/N FLPs) to estimate the relative stabilities of the reaciton intermediates/ TSs involved in the H_2 activation and the subsequent dihydrogen release step. The SMD solvation model is used to account for the solvent effects [9]. All reported free energy values are computed at T=298 K and P=1 atm pressure. All calculations are performed using Gaussian 16 package [10].

Note that, we have used the following atom colouring to visualize the molecular geometries: C (grey), H (white), N (blue), O (red), S (yellow), F (pale yellow), Cl (green) and Sn (cyan). For the sake of clarity, we have only shown the hydrogens attached to non-carbon elements.

5.4 Results and discussion

5.4.1 Structural features of 1-R-X

The optimized structures of all **1-R-X** candidates (see Figure 5.2) show similar features with the minor differences arising out from the different steric profile of the R groups and the coordinated X around the Sn centre. The shared structural features include a distorted TBP geometry around the Sn centre with two R groups and one of the guanidinate N atoms (N1) forming the equatorial plane. The apical positions are occupied by the other nitrogen atom (N2) in the guanidinate ring and X. Interestingly, N2, which is the perceived LB-site, remains datively coordinated with the Sn centre, rendering the LPs in a dormant closed form. Nevertheless, this does not seem to be an unusual occurrence as similar closed forms are also observed in other intramolecular Lewis pairs. However, in those cases, an active open from, which can serve the purpose of an encounter complex (EC), was also found to be readily accessible [11, 12]. Analogously, we also expected a closely-lying open active form of **1-R-X** which, surprisingly, we were unable to locate. This is confirmed by several relaxed potential energy surface (PES) scan calculations with respect to

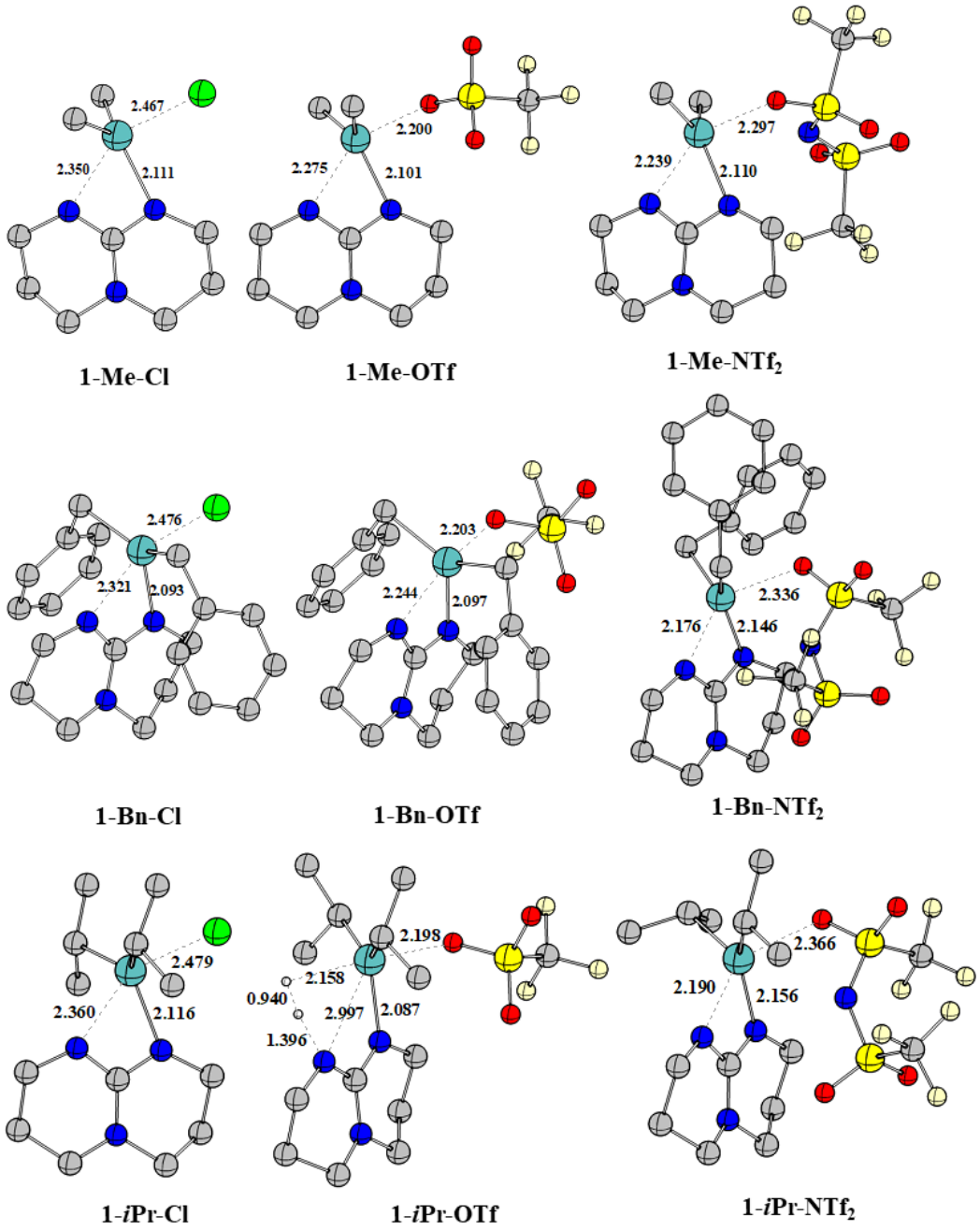

Figure 5.2: Geometry optimized structures of all **1-R-X** candidates. All distances are given in Å

.

Sn-N2 distance, which always shows monotonically increasing energy profiles as the Sn and N2 centres move away from each other. This raises an immediate question that whether or not **1-R-X** would show FLP reactivity at all? To find an answer to the question, we looked back to the reactivity of analogous intramolecular Si/N LPs

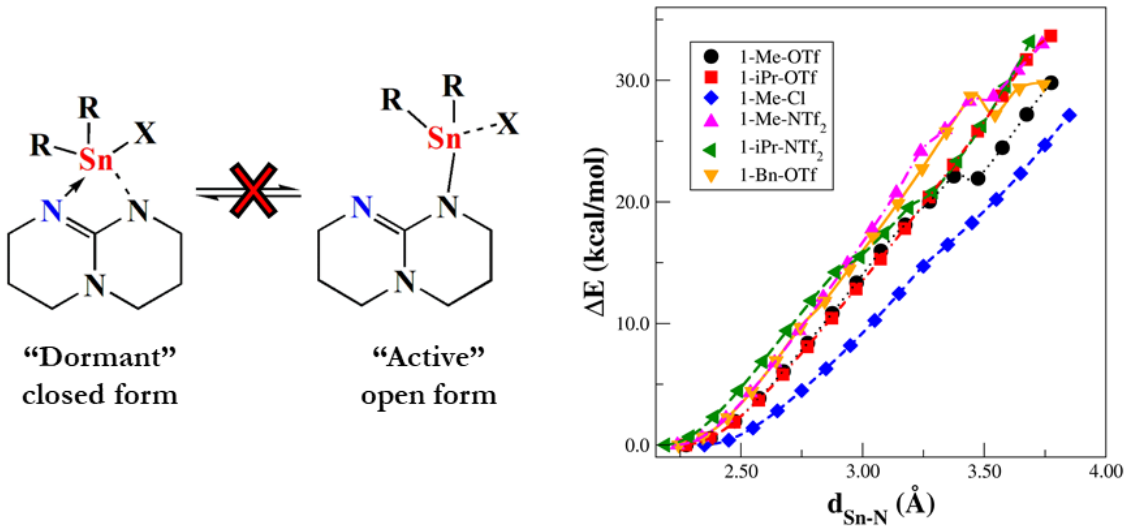

Figure 5.3: No open active from for **1-R-X** (left). Potential energy profiles along Sn-N2 distance for a few selected **1-R-X** candidates (right). The data points are obtained by performing a relax PES scan with respect to Sn-N2 separation at M062X-D3/BS1 level. For the sake of clarity, we have not shown the profiles for all the candidates.

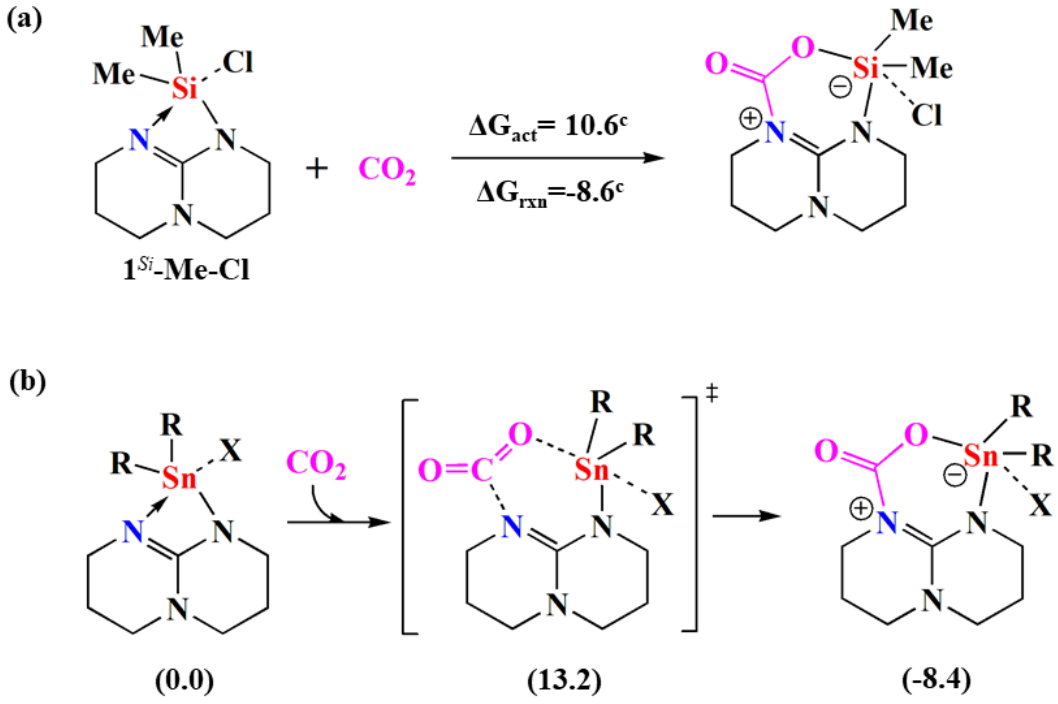

Figure 5.4: (a) CO_2 capture by $\mathbf{1}^{Si}$**-Me-Cl**. [c] taken from reference 2. (b) CO_2 activation by **1-R-X**. Relative Gibbs free energy values for R=*i*Pr and X=NTf_2 are given in parenthesis. All energy values are in kcal/mol.

($\mathbf{1}^{Si}$**-Me-Cl**) by Cantat *et al.*, which shares similar structural features as **1-R-X** [2].

Interestingly, $\mathbf{1}^{Si}$**-Me-Cl** captures CO_2 and forms a stable adduct. DFT calculation

indicated that the capture of CO_2 occurs with a low activation energy barrier in the manner of the FLPs [2]. To confirm that whether an open form exists or not in the case of **1**^{Si}**-Me-Cl**, we performed a similar relaxed PES scan with respect to Si-N distance. Note that, in this case, also, we did not see an open form as a local minimum; the energy profile was found to be similar as found in the case of **1-R-X**. These results instigated us to check the reactivity of **1-R-X** towards CO_2. As observed in **1**^{Si}**-Me-Cl**, we find similar CO_2 capture by all **1-R-X** candidates e.g. for **1-***i***Pr-NTf$_2$**, the formation of CO_2 adduct is exergonic by 8.4 kcal/mol with a low free energy activation barrier of 13.2 kcal/mol. This suggests that despite having a dative bond between the active centres, **1-R-X** can still activate CO_2 in the manner of FLPs, which made us hopeful that these intramolecular Sn/N FLPs might also react with H_2.

5.4.2 H_2 activation

Having demonstrated the FLP-type CO_2 activation, we turned our attention to the heterolytic cleavage of H_2 by **1-R-X**. Interestingly, we find that **1-R-X** is able to cleave the H-H bond, leading to the formation of **2-R-X**. The heterolytic splitting of the H_2 molecule occurs through a single concerted TS, **TS1-R-X**, the structure of which resembles the TS obtained in the distal pathway of H_2 activation

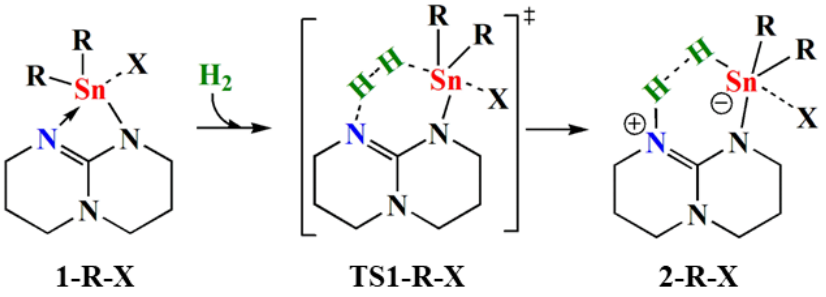

Figure 5.5: H_2 activation by **1-R-X** candidates.

by intermolecular Sn/N LPs [13, 14]. We have already shown in Chapter 3 that the intermolecular Sn/N LPs can activate H_2 in two different pathways, distal and proximal, which were characterized by the mutual positioning of counter anion and LB

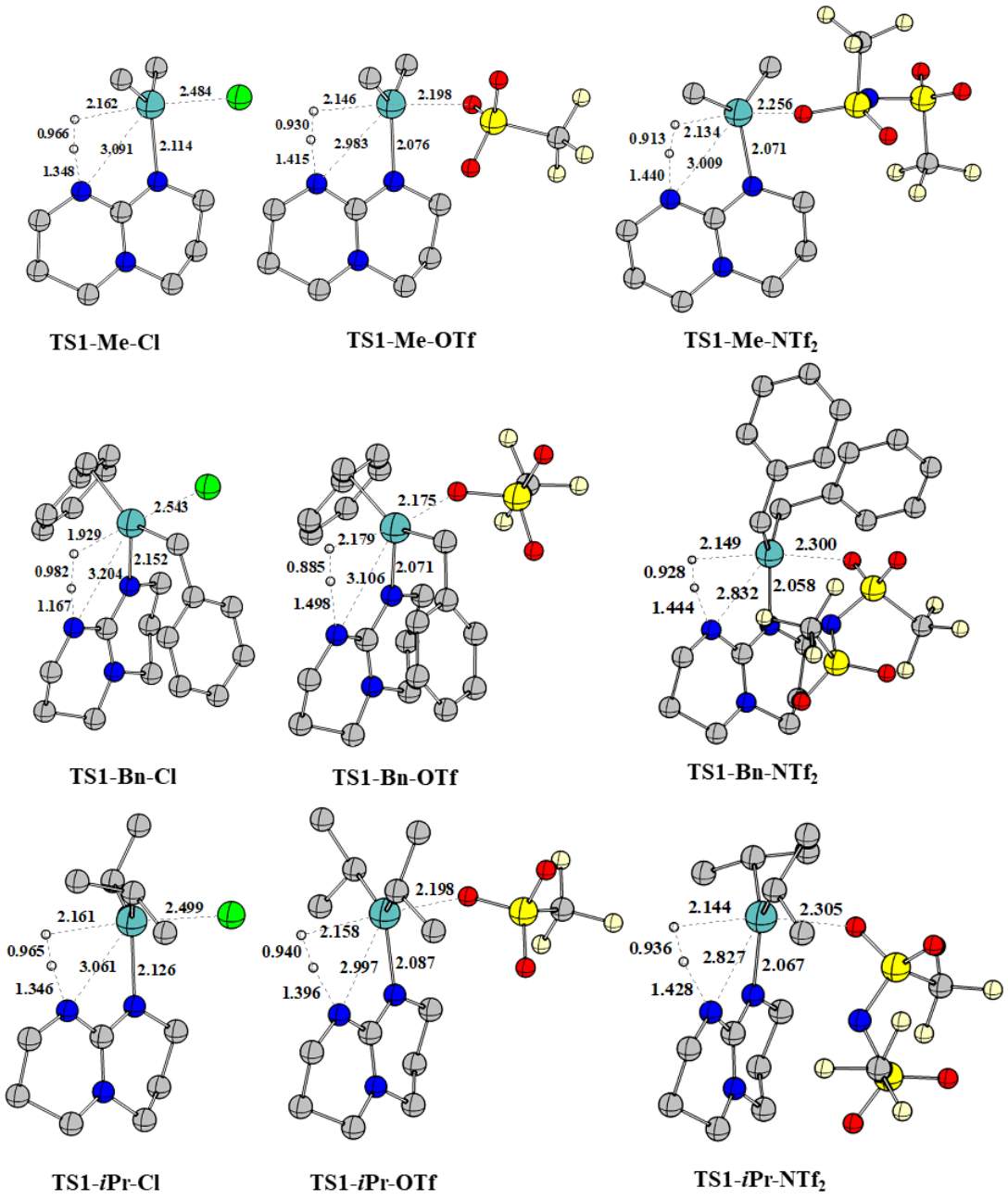

Figure 5.6: Geometry optimized structures of **TS1-R-X**. All distances are given in Å.

during the reaction course. Distal pathway, in which the LB remains in the opposite side of counter anion, was proposed to be kinetically more favorable over the proximal pathway featuring LB and counter anion in close vicinity of each other. Note that, in the present case, the intramolecular design of **1-R-X** itself keeps the X and the LB site in the opposite sides of the Sn centre and thereby, enables H_2 activation only in the

distal pathway. The free energy activation barriers for H-H cleavage range in between 25-33 kcal/mol for different **1-R-X** candidates. However, the thermodynamics of H_2 activation differs significantly among the candidates, ranging from nearly reversible, moderately endergonic to strongly endergonic. It is important to note that none of the **1-R-X**-mediated H_2 cleavage is strongly exergonic, which would render subsequent release of the active hydrogens infeasible. The geometry optimized structures of **TS1-R-X** and **2-R-X** are shown in Figure 5.6 and Figure 5.7, respectively.

5.4.2.1 Mechanism of H_2 activation

One key point emerging out from our mechanistic model is the activation of H_2 by **1-R-X**, starting from its closed dormant form. The H_2 activation profile of **1-R-X** resembles closely with that of intermolecular Sn/N FLPs [13]. The thought-provoking aspect is that it can not be rationalized with "thermally induced frustration", which settles that the absence of a dative adduct is not the sole criterion to exhibit FLP reactivity. LPs that form a dative adduct can also show FLP-characteristics, provided that the dative adduct formation is reversible under the reaction condition; H_2 activation is still feasible with the formally dissociated Lewis components through a normal FLP-type mechanism involving EC. However, this is not the case for **1-R-X**. In this case, an open (active) form, which would feature as an EC-like structure, does not exist (as a local minimum). Despite that, the structure of **TS1-R-X** suggests a typical FLP-type H_2 activation featuring a Sn-H-H-N interaction. NBO calculations further confirm the expected cooperativity between the LA/LB centres; two simultaneous donor-acceptor interactions can be characterised involving electron donation from a N lone pair to empty σ^* (H_2) and σ(H_2) to p orbital on the Sn centre. Given the normal FLP-type TS arising out of a classical Lewis acid-base adduct, we envisaged that further insights could be obtained analysing the pathway on the PES that connects the reactants to the TS. To this end, we have chosen **1-*i*Pr-OTf**-mediated H_2 activation as the prototype case for further analysis of the reaction pathway.

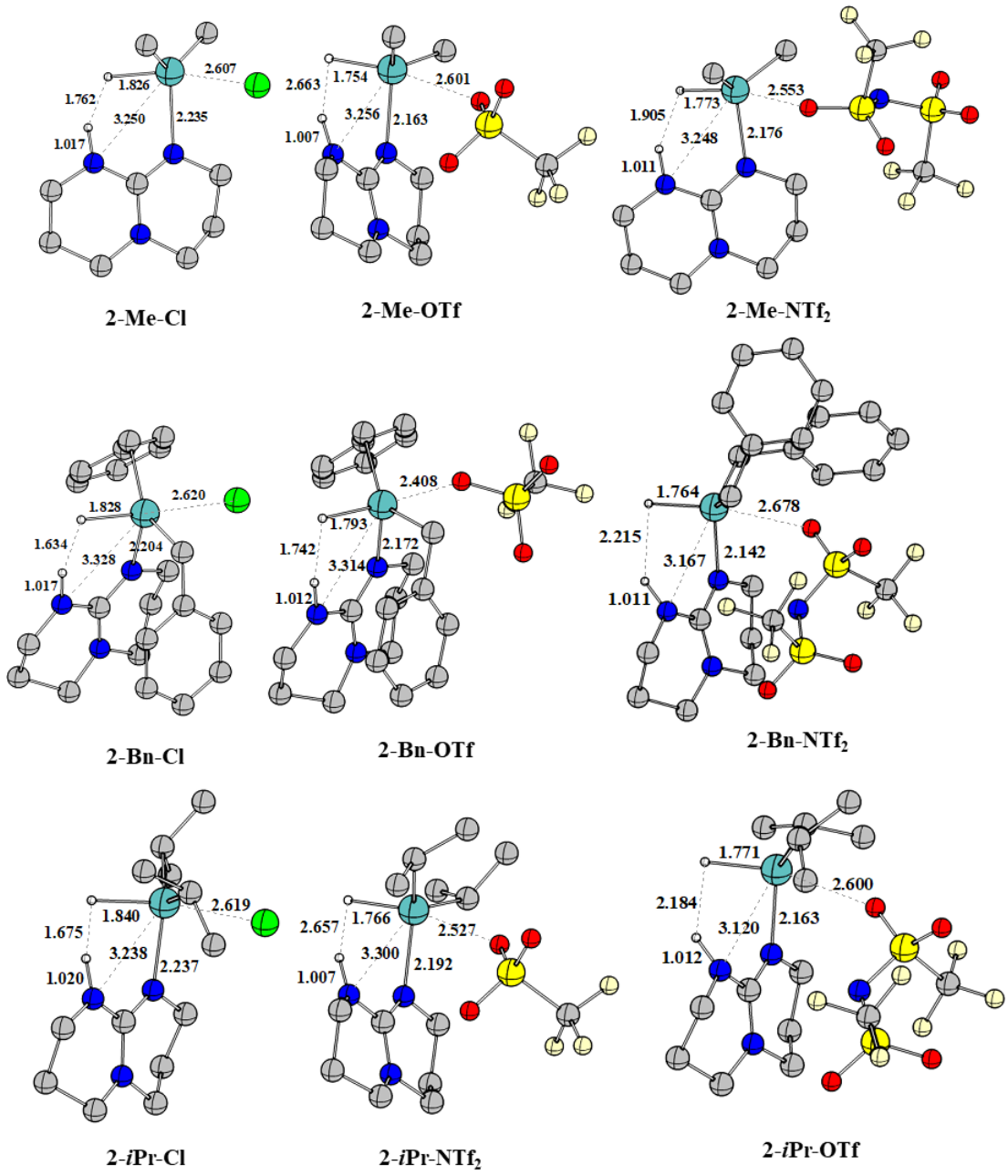

Figure 5.7: Geometry optimized structures of **2-R-X**. All distances are given in Å.

In general, the presence of LA-H-H-LB interaction can be characterised at the very early stage of a typical FLP-mediated H_2 activation [15]. As a result, from the beginning of the reaction itself, the H-H bond starts to elongate, and this becomes quite gradual as the reaction progresses. We find that such features are absent at the beginning of the present H_2 activation in **1-R-X** and appears at a much later stage. The reaction commences with an elongation of the Sn-N2 bond weakening the dative

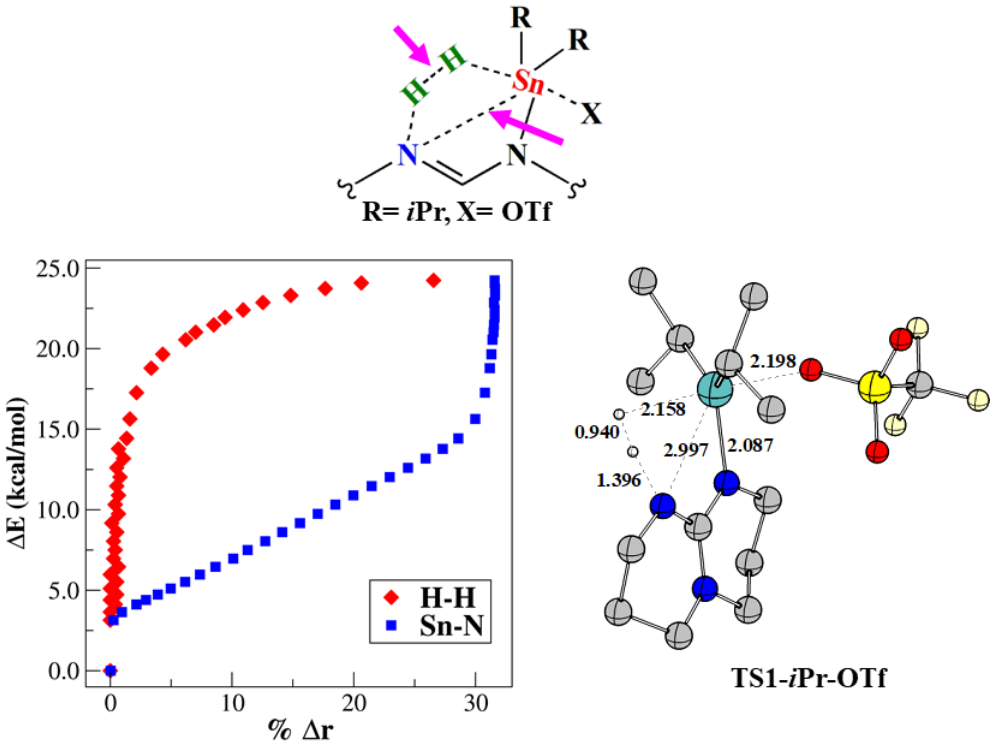

Figure 5.8: Potential energy profiles (up to TS) for the H_2 activation by **1-*i*Pr-OTf** with varying Sn-N2 (blue) and H-H (red) distances (left). The aforementioned distances are shown with the arrows (top). Geomery optimized structure of **TS1-*i*Pr-OTf** (right). All distances are given in Å.

interaction between the LA/LB site. This should be done to allow the interaction with the incoming H_2 molecule. Naturally, at this stage, the H_2 molecule remains far away from the Sn/N centre and the H-H bond length remains fixed at the equilibrium value. Only when the Sn-N2 interaction is weakened to a certain extent, H_2 molecule begins to interact with the LP. This is formally the starting point of H_2 splitting and as the reaction progresses, the H-H bond gradually elongates with increase in Sn-H-H-N interaction. It is interesting to notice that during this H_2 splitting stage, the Sn-N2 bond distance remains more or less constant until the TS is reached. In order to quantify these features, we have plotted the potential energy profile as a function of Sn-N2 and H-H bond elongation along the reaction pathway from reactant to TS. Note that, these bond elongations are scaled and represented in the form of a reduced bond streach ($\%\Delta r$), defined by the equation $\%\Delta r = (\frac{r}{r_0} - 1) \times 100$, where r is the bond length at any given point on the energy profile and r_0 is the equilibrium

bond length in isolated reactants. The two different stages of the reaction is clearly visible in the Figure 5.8, characterised by the asynchronicity of Sn-N2 and H-H bond elongation. It is possible to quantify the extent of Sn-N2 elongation, which roughly marks the begnning of the H_2 splitting stage and from the Figure 5.8, it is estimated to be around 31% *i.e.* at d(Sn-N2)= 2.979 Å. The energy requirement for this early weakneing of the Sn-N2 interaction amounts to 15-16 kcal/mol.

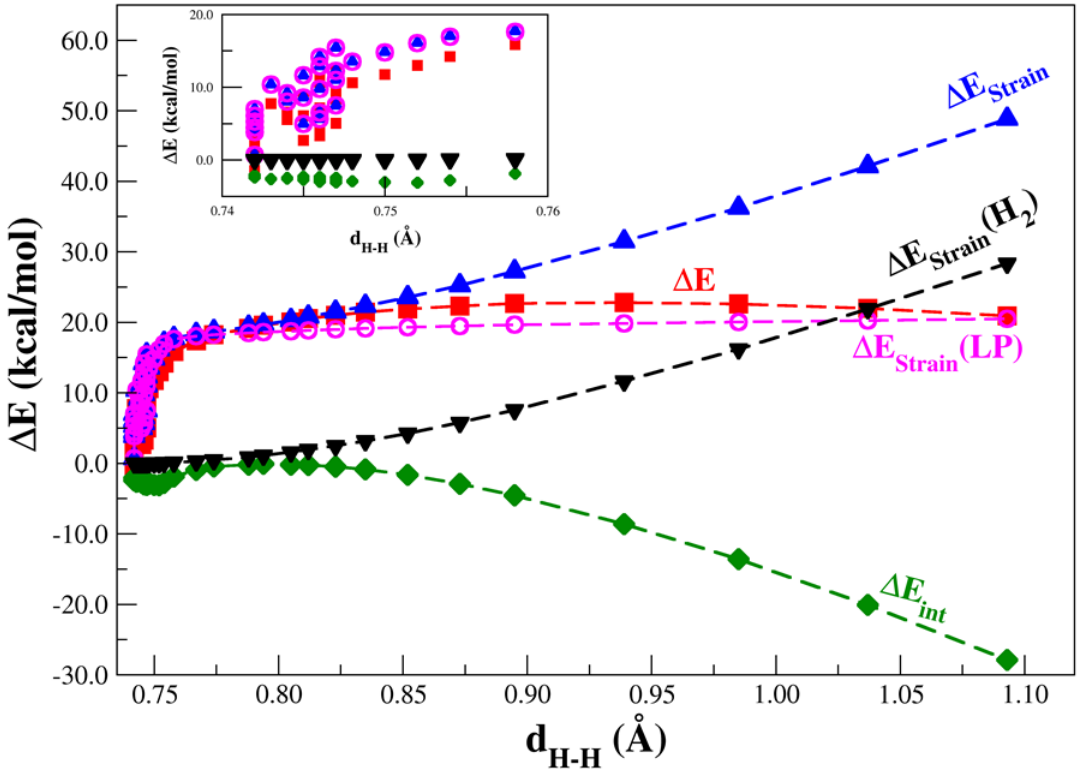

Figure 5.9: Activation strain analysis for the H_2 activation by **1-*i*Pr-OTf**. The variation of strain energy (along with the two individual contributions) at a very early stage of the reaction is shown in the inset.

Next, we further examine the situation by performing activation-strain analysis along the entire reaction pathway characterised by H-H streach. The computed variations in strain energy ($\mathbf{\Delta E_{strain}}$) and interaction energy ($\mathbf{\Delta E_{int}}$) is shown in Figure 5.9. Furthermore, $\mathbf{\Delta E_{strain}}$ is divided into two contributions, $\mathbf{\Delta E_{strain}(LP)}$ and $\mathbf{\Delta E_{strain}(H_2)}$, coming from each reactant, LP (*i.e.* **1-*i*Pr-OTf**) and H_2, respectively. Note that, in the former reactant, strain energy mainly originates from the Sn-N2 elongation while for the latter, H-H bond elongation is responsible for the strain

energy during the reaction pathway. At the early stage of the reaction, before the begining of H-H elongation, the strain energy curve rises very steeply; in this region $\mathbf{\Delta E_{strain}}$ is entirely contributed by the **1-*i*Pr-OTf** with the contribution from the H_2 molecule remaining constant at zero energy (this is better shown in the inset of Figure 5.9). Conversely, in the region of H-H bond elongation (*i.e.* the H_2 splitting stage), the reverse is true; almost entire $\mathbf{\Delta E_{strain}}$ contibution comes from the elongated H_2 molecule (indicated by the similar slope of the $\mathbf{\Delta E_{strain}}$ and $\mathbf{\Delta E_{strain}(H_2)}$ curve) while the $\mathbf{\Delta E_{strain}(LP)}$ contibutes no more to the strain energy curve (indicated by an almost zero slope in this region).

Note that, the examples of accessing FLP reactivity directly from a classical Lewis acid-base adduct are very rare in the literature. Ashley *et al.* demonstrated such reactivity in which a classical silylium-phosphine adduct was found to be capable of H_2 activation [16]. In this combined experimental-computational study, they concluded that an EC-like structure was directly formed due to transient elongation of the Si-P bond without the full dissociation of the Lewis components. More recently, Stephan *et al.* reported that despite a dative bond between P and B centres, a CO_2 adduct can be obtained from a intermolecular borane-proazaphosphatrane dative adduct [17]. In this case, also, the authors could not locate a suitable preorganization of the LA/LB centres prior to CO_2 capture. In the present case, we report H_2 activation by a closed intramolecular Sn/N LP which bypasses the formal disscociation of the active centres. Interestingly, transient elongation of the Sn-N bond allows the H-H cleavage via a FLP-like TS. In that sense, the reactivity of **1-R-X** may have broader implications in FLP chemistry.

5.4.2.2 Energetics of H_2 activation

In order to compare the reactivity among the candidates, we compute the binding strength of various X, employing the equation **1-R-X**$\rightarrow$**1-R**$^+$+ X^-, which estimates the anion detachment free energy (ADFE). For a particular choice of R, ADFE runs in the order of Cl > OTf > NTf_2. Along with the inherent coordination strength,

ADFE is also determined by a relative balance of the steric interaction between alkyl substituents on the Sn centre and X; bulkier R leads to smaller ADFE. Owing to the smaller size of Cl, ADFE remains more or less similar in the series of **1-R-Cl** for all the R groups. For OTf also, R does not have a very pronounced impact on ADFE. For Me and Bn, ADFE remains more or less similar while for *i*Pr the value is slightly less, consistent with the more steric bulk of the latter substituent. For bulkier NTf_2, ADFE strongly depends on the bulk of the R group and follows the expected ordering (considering the bulk on the α-carbon to the Sn centre) Me > Bn > *i*Pr.

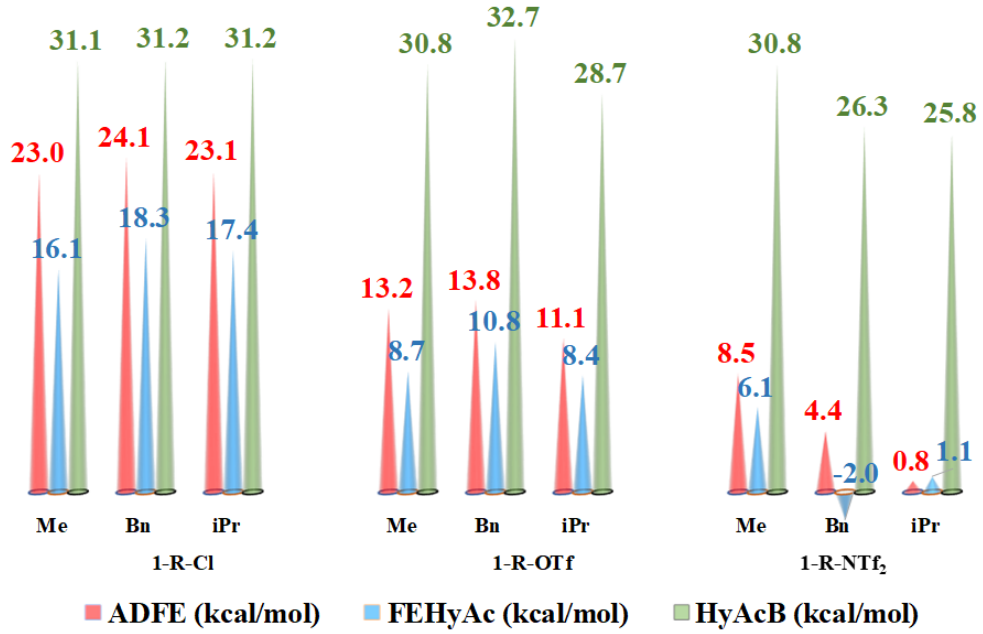

Figure 5.10: The computed values of ADFE, FEHyAc and HyAcB for all **1-R-X** candidates. All energy values are given in kcal/mol.

We find that the Gibbs free energy change for H_2 activation (FEHyAc) correlates well with ADFE; with increasing ADFE, the H_2 activation becomes more and more endergonic. To incorporate the H_2 activation step into a catalytic hydrogenation cycle, we would ideally require a reversible or a close to reversible H_2 activation. We find nearly reversible H_2 cleavage for **1-Bn-NTf$_2$** and **1-*i*Pr-NTf$_2$**. For **1-Me-OTf**, **1-Bn-OTf**, and **1-*i*Pr-OTf**, H_2 cleavage is moderately endergonic. However, for all Cl-containing candidates, the H_2 splitting is strongly endergonic. This can be rationalized from the stronger coordination of X leading to weaker Lewis acidity of

the Sn centre, resulting in less favorable thermodynamics.

Similar correlation is also obtained between ADFE and the H_2 activation barrier (HyAcB). As found in the intermolecular Sn/N FLPs, weaker X coordination results in lower barrier. For X=Cl, all candidates show similar HyAcB of around 31 kcal/mol. For NTf_2, the HyAcB varies smoothly with ADFE. **1-*i*Pr-NTf$_2$**, having the lowest ADFE, exhibits the lowest HyAcB of 25.8 kcal/mol. Although for a particular X , HyAcB correlates well with ADFE, however, between different family of candidates with diffrent X, the correlation is much weaker. Only when R=*i*Pr, we find a smooth variation of HyAcB with ADFE. For R=Me, the HyAcB remains more or less similar for all X, suggesting that HyAcB is insensitive to the choice of X. For R=Bn, instead of a decrease in the barrier on going from Cl to OTf, we see a slight increase in the barrier. In fact, **1-Bn-OTf** exhibits highest HyAcB among all the candidates. However, in **1-Bn-NTf$_2$**, the barrier decreases again to 26.3 kcal/mol. The variation of HyAcB and FEHyAc with ADFE for **1-R-X** candidates is depicted in Figure 5.10.

Comparing the FEHyAc and HyAcB values, we find that two NTf_2-containing candidates, **1-*i*Pr-NTf$_2$** and **1-Bn-NTf$_2$**, show the lowest activation barrier among the nine candidates and in both the cases, the H_2 activation is nearly reversible. Therefore, we have selected these two candidates to study their catalytic activity towards hydrogenation of unsaturated substrates.

5.4.3 Catalytic hydrogenation of carbonyls and imines

Given the reversible to moderately endergonic H_2 activation by a few **1-R-X**, we contemplated the possibility of dihydrogen release (DHR) from **2-R-X** to unsaturated organic substrates (X=Y) and thereby, constituting a closed catalytic hydrogenation cycle. The proposed hydrogenation scheme is shown in Figure 5.11. To this end, we first examine DHR from **2-*i*Pr-NTf$_2$** to two different substrates such as Me_2CO (model carbonyl substrate) and H_2C=NH (model imine substrate). The corresponding relative Gibbs free energy profiles for the full catalytic hydrogenation cycles (including the H_2 activation step) are depicted in Figure 5.12.

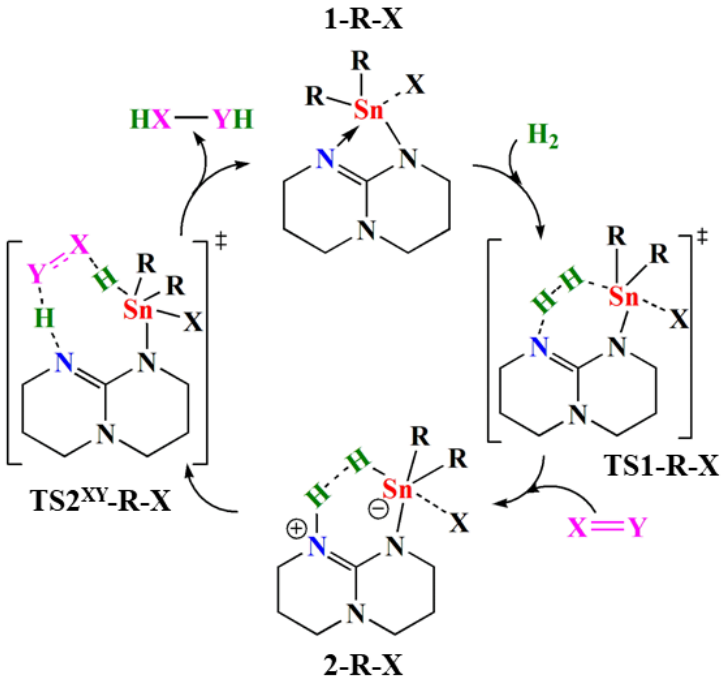

Figure 5.11: The proposed scheme for catalytic hydrogenation of an unsaturated substrate X=Y.

The catalytic cycle begins with H_2 cleavage by **1-*i*Pr-NTf$_2$** to yield **2-*i*Pr-NTf$_2$**, which we have already discussed in the previous section. We find that DHR to X=Y occurs in a single step and in a concerted manner. Prior to DHR, an initial reactant complex, **3**^{XY}**-*i*Pr-NTf$_2$** (*XY* represents *CO* and *im* for Me_2CO and H_2C=NH, respectively), is formed when **2-*i*Pr-NTf$_2$** establishes a N-H$\cdots$O/N hydrogen bonding interaction with the Lewis basic O/N atom of the substrate. The structure of the TS for DHR, **TS2**^{XY}**-iPr-NTf$_2$**, reveals a simultaneous migration of the hydride from the Sn centre towards carbonyl/imine carbon and a proton from N2 towards O/N atom. This is a typical case of Brønsted acid activation (BAA) in which the NH$\cdots$O/N H-bonding interaction activates the carbonyl/imine carbon towards the acceptance of the hydride. Note that, we have already examined the BAA mode for the hydrogenation of carbonyl compounds for intermolecular Sn/N LPs in the previous chapter [14]. In the BAA mode, we found a similar TS, **TS-HT/PT-BAA**, for concerted hydride and proton transfer to Me_2CO. The present TS, **TS2**^{XY}**-*i*Pr-NTf$_2$**, shares a number of common structural features with **TS-HT/PT-BAA**.

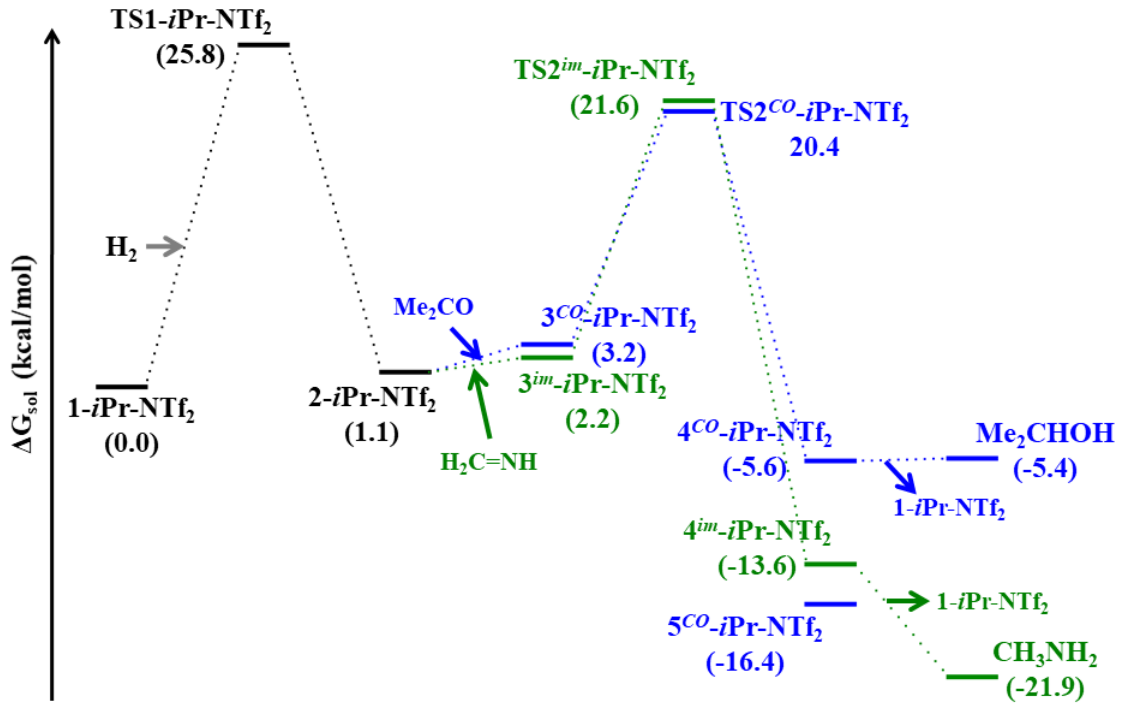

Figure 5.12: Relative Gibbs free energy profiles for catalytic hydrogenation of Me_2CO (blue) and $H_2C{=}NH$ (green) by **1-*i*Pr-NTf$_2$**. Solvent-corrected Gibbs free energy (kcal/mol) values are given in parenthesis.

Unfortunately, in the case of intermolecular Sn/N LPs, an alternative LAA mode in which the LA-coordination activated the carbobyl substrate was computed to be kinetically more favorable over the BAA mode and, accordingly, the reaction followed the former pathway.

After DHR, the product remains bound to the catalyst leading to **4^{XY}-R-NTf$_2$** and the Sn-N2 interaction is reformed again. Thermal dissociation of the hydrogenated product returns the catalyst **1-*i*Pr-NTf$_2$**. However, for hydrogenation of Me_2CO, we find that the alcohol product can also bind to the catalyst in a different manner, leading to the formation of **5^{CO}-R-NTf$_2$**. The structure of **5^{CO}-R-NTf$_2$** features a O-H dissociated alcohol with the formation of Sn-O(alkoxide) and N2-H bonds. As a result, the active Sn/N sites are blocked rendering the catalyst inactive towards further H_2 activation. Thermal dissociation of this complex is necessary to release the product and return **1-*i*Pr-NTf$_2$** to resume catalysis.

TS2^{XY}-*i*Pr-NTf$_2$ lies at 20.4 and 21.6 kcal/mol for Me_2CO and $H_2C{=}NH$,

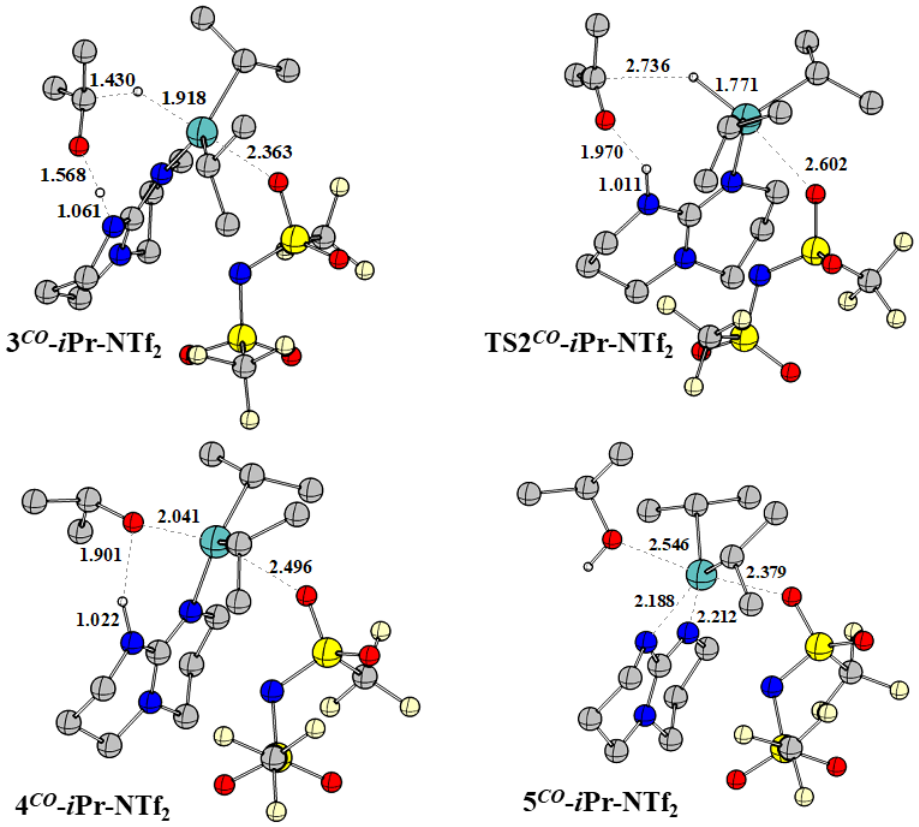

Figure 5.13: Geometry optimized structures of the intermidiate(s)/TS involved in the DHR of **2-*i*Pr-NTf$_2$** to Me_2CO. All distances are given in Å.

respectively, indicating that the activation barrier for the DHR is lower than that of H_2 activation. Thus, for both hydrogenation cycle, rate-determining barrier corresponds to **TS1-*i*Pr-NTf$_2$**, which lies at 25.8 kcal/mol and can be considered to be in the experimentally-accessible range. Note that, a high temperature will be required to obtain a catalytic turnover for the hydrogenation of Me_2CO since the alcohol product blocks the active centres of the catalyst by forming a stable complex and thus, the dissociation energy of the complex also contributes to the overall activation barrier. However, such a situation does not arise for the hydrogenation of imines. The dissociation of the amine-bound catalyst complex, **3^{CN}-R-NTf$_2$**, is 8.5 kcal/mol downhill in free energy to release the product and return the catalyst.

We have also examined the propensity of dimerization of **1-*i*Pr-NTf$_2$** which might hinder its catalytic activity. The dimerization energy is computed following the reaction 2·**1-*i*Pr-NTf$_2$** $\rightarrow$ [**1-*i*Pr**]$_2^{2+}$ + 2NTf$_2^-$. Our results reveal that free energy

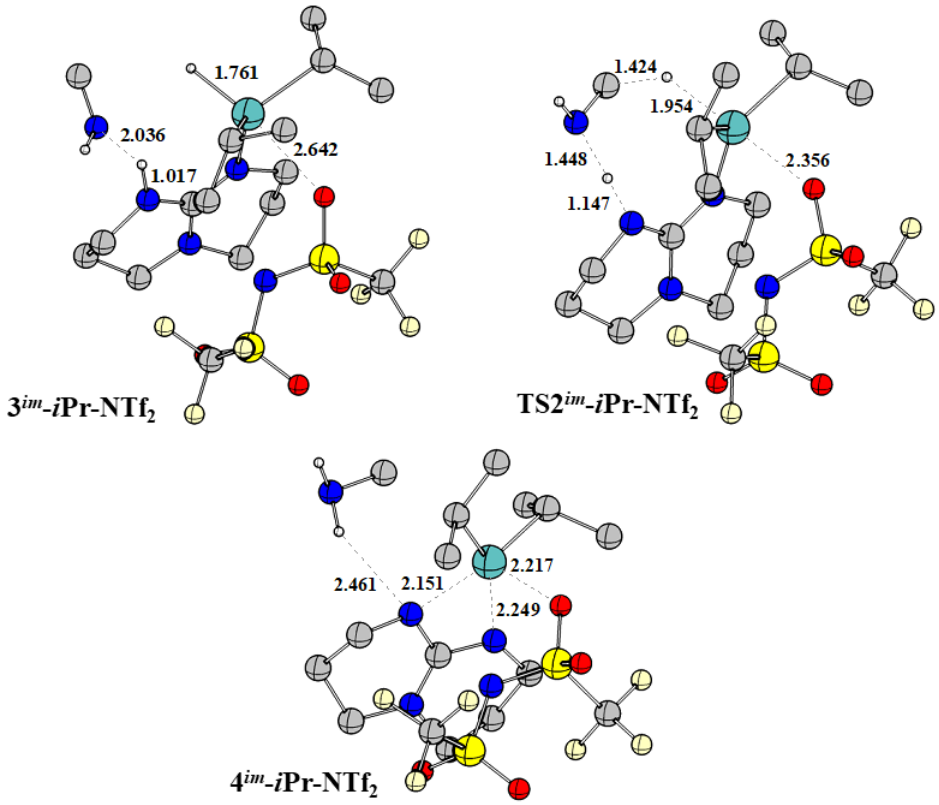

Figure 5.14: Geometry optimized structures of the intermidiate(s)/TS involved in the DHR of **2-*i*Pr-NTf$_2$** to H_2C=NH. All distances are given in Å.

for the dimerisation (-2.5 kcal/mol) will not affect the catalytic cycle since it is only marginally exergonic.

Finally, we have selected a few more NTf_2-containing candidates, **1-R-NTf$_2$**, by considering some additional alkyl substituents, which include Et, *n*Pr and *t*Bu. The computed values for FEHyAc, HyAcB, and activation barrier for DHR to H_2C=NH for these candidates are listed in Table 5.1. All of these candidates show nearly

Table 5.1: The computed values for FEHyAc, HyAcB and **TS2^{CN}-R-NTf$_2$** for catalytic hydrogenation of H_2C=NH by **1-R-NTf$_2$** candidates.

R	HyAcB	FEHyAcB	**TS2^{CN}-R-NTf$_2$**
Bn	26.3	-2.0	19.3
Et	25.4	-1.2	19.8
*n*Pr	26.8	-0.3	20.2
*t*Bu	24.8	0.7	21.4

reversible H_2 activation, and the variation in free energy barriers for both the steps remains within 2 kcal/mol. HyAcB for **1-*t*Bu-NTf$_2$** is found to be the lowest (24.8 kcal/mol) in the series of all **1-R-X** candidates. The computed activation barriers suggest that these newly designed **1-R-NTf$_2$** LPs may act as potential hydrogenation catalysts for imines.

5.5 Conclusion

In summary, we have designed a new series of intramolecular Sn/N Lewis pairs, (**1-R-X**) for hydrogen activation and hydrogenation catalysis. **1-R-X** assumes a closed dormant form with the active Sn and N sites involved in dative interaction with each other. With the aid of DFT calculations, we have examined their reactivity towards H_2 and found that **1-R-X** activates H_2 in the manner of the FLPs via single concerted TS, resulting from the expected cooperativity between the Sn and N centres. Our results reveal that the H_2 activation begins with an initial elongation of the Sn-N bond, directly leading to an "encounter complex"-like structure which allows the LA/LB centres to engage into H-H cleavage. We have also performed an activation-strain analysis to confirm this mechanistic picture. The coordination strength of X has a profound effect in determining the energetics of H_2 activation. Finally, we have investigated the hydrogenation of imines and carbonyls using a few selected **1-R-X** candidates. We find a concerted release of active hydrogens to the unsaturated bonds with an activation barrier lower than that of H_2 cleavage. Considering the overall free energy activation barriers, **1-R-NTf$_2$** candidates are proposed to be promising catalysts for the hydrogenation of imines.

Bibliography

[1] Spies, P.; Erker, G.; Kehr, G.; Bergander, K.; Fröhlich, R.; Grimme, S.; Stephan, D. W. *Chemical Communications* **2007**, 5072–5074.

[2] Von Wolff, N.; Lefèvre, G.; Berthet, J.-C.; Thuéry, P.; Cantat, T. *ACS Catalysis* **2016**, *6*, 4526–4535.

[3] Scott, D. J.; Phillips, N. A.; Sapsford, J. S.; Deacy, A. C.; Fuchter, M. J.; Ashley, A. E. *Angewandte Chemie International Edition* **2016**, *55*, 14738–14742.

[4] Cooper, R. T.; Sapsford, J. S.; Turnell-Ritson, R. C.; Hyon, D.-H.; White, A. J.; Ashley, A. E. *Phil. Trans. R. Soc. A* **2017**, *375*, 20170008.

[5] Zhao, Y.; Truhlar, D. G. *Theoretical Chemistry Accounts: Theory, Computation, and Modeling (Theoretica Chimica Acta)* **2008**, *120*, 215–241.

[6] Zhao, Y.; Truhlar, D. G. *Accounts of chemical research* **2008**, *41*, 157–167.

[7] Grimme, S.; Antony, J.; Ehrlich, S.; Krieg, H. *The Journal of chemical physics* **2010**, *132*, 154104.

[8] Andrae, D.; Haeussermann, U.; Dolg, M.; Stoll, H.; Preuss, H. *Theoretical Chemistry Accounts: Theory, Computation, and Modeling (Theoretica Chimica Acta)* **1990**, *77*, 123–141.

[9] Marenich, A. V.; Cramer, C. J.; Truhlar, D. G. *The Journal of Physical Chemistry B* **2009**, *113*, 6378–6396.

[10] Frisch, M. J. et al. Gaussian 16 Revision A.03. 2016; Gaussian Inc. Wallingford CT.

[11] Chernichenko, K.; Kótai, B.; Pápai, I.; Zhivonitko, V.; Nieger, M.; Leskelä, M.; Repo, T. *Angewandte Chemie International Edition* **2015**, *54*, 1749–1753.

[12] Zeonjuk, L. L.; Petkov, P. S.; Heine, T.; Röschenthaler, G.-V.; Eicher, J.; Vankova, N. *Physical Chemistry Chemical Physics* **2015**, *17*, 10687–10698.

[13] Das, S.; Mondal, S.; Pati, S. K. *Chemistry-A European Journal* **2018**, *24*, 2575–2579.

[14] Das, S.; Pati, S. *Catalysis Science & Technology* **2018**,

[15] Rokob, T. A.; Bako, I.; Stirling, A.; Hamza, A.; Papai, I. *Journal of the American Chemical Society* **2013**, *135*, 4425–4437.

[16] Herrington, T. J.; Ward, B. J.; Doyle, L. R.; McDermott, J.; White, A. J.; Hunt, P. A.; Ashley, A. E. *Chemical Communications* **2014**, *50*, 12753–12756.

[17] Johnstone, T. C.; Wee, G. N.; Stephan, D. W. *Angewandte Chemie* **2018**, *130*, 5983–5986.

Chapter 6

Mechanistic Insights into Catalytic CO_2 Hydrogenation using Mn(I)-Complexes with Pendant Oxygen Ligands*

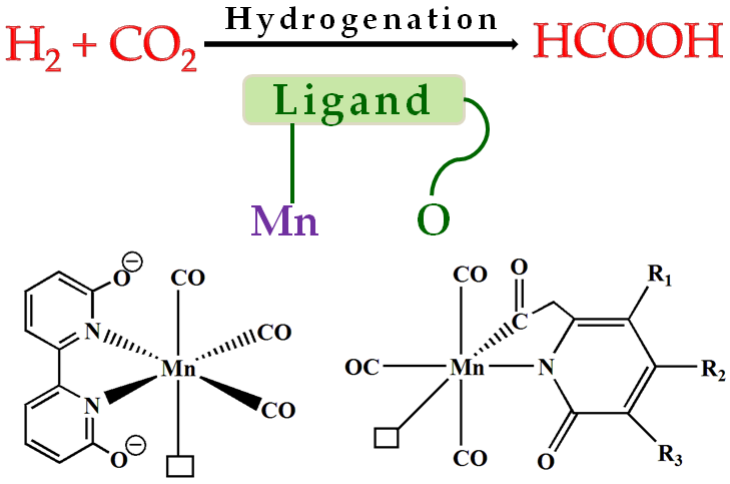

*Work reported in this chapter is published in: Shubhajit Das, Swapan K Pati, Catalysis Science and Technology, 2018, 8, 3034-3043. Reproduced with permission from The Royal Society of Chemistry.

6.1 Introduction

The final work-chapter of this thesis deals with hydrogenation of CO_2 to formic acid (FA)/formate by Mn(I)-complexes bearing pendant oxygen ligands. Although the reaction falls under the category of TM-catalysed hydrogenation, we will show that the basic mechanism of hydrogenation exploits the strategy of cooperativity between the Lewis pairs. It points to the simplicity and transferability of this concept to the other branches of chemistry.

In the last few decades, utilization of carbon dioxide (CO_2) as a chemical feedstock has been a hot research topic. While the appealing features of CO_2 stem from its low toxic, inexpensive and highly abundant nature, high kinetic and thermodynamic stability has restricted its use in synthetic chemistry and industrial processes [1, 2]. Hydrogenation of CO_2 to FA is one promising strategy to utilize CO_2 for production of value-added chemicals [3]. Apart from being a potential hydrogen carrier, FA finds a wide range of applications in the laboratory as well as in the industry as reductant, acid, and carbon source [4–6]. Although direct hydrogenation of CO_2 to FA, using gaseous H_2 as the reductant (H_2+ CO_2 $\rightarrow$ HCOOH) is a thermodynamically unfavorable process, the problem can be tackled by addition of an external base, which neutralises FA to drive the reaction towards forward direction [7].

Precious transition metal (TM) complexes based on Ru, Rh, Ir etc. have long been predominantly used as catalysts for CO_2 hydrogenation. For example, in 2009, Nozaki introduced a PNP pincer Ir(III)-trihydride complex with a turn-over number (TON) of 350000 for CO_2 hydrogenation to formate in basic aqueous solution [8]. In 2011, the group of Hazari synthesized a similar Ir complexes that achieved a TON of 348000 for hydrogenation of CO_2 [9]. Himeda and co-workers reported an iridium dihydroxybipyridine complex capable of catalysing CO_2 hydrogenation under mild reaction condition in aqueous medium with TON of 308000 [10]. More recently, Pidko *et al.* synthesized ruthenium PNP pincer complexes, which also exhibited significantly high TON (>90000) for hydrogenation of CO_2 [11]. In contrast to such precious

TM complexes, earth-abundant TMs received much less attention. The triphos ligand based Fe and Co-complexes reported by Beller's group showed good catalytic activity as CO_2 hydrogenation catalysts although the turnovers were reported to be much less compared to the previous examples of precious TM complexes [12–14]. Milstein and co-workers synthesized PNP pincer complexes of iron, capable of hydrogenating CO_2 to formate in basic aqueous medium [15]. In recent years, Yang *et al.* computationally examined a few promising Fe and Co-complexes as catalysts for CO_2 hydrogenation [16–19]. Surprisingly, despite being an earth-abundant and non-toxic metal, manganese has been given scant attention in homogeneous CO_2 hydrogenation so far. Gratifyingly, the reports on Mn-based catalysts for hydogenation of CO_2 have been increasing since last year. Gonsalvi *et al.* reported TON as high as 30,000 for a Mn PNP pincer complex in the presence of a Lewis acid co-catalyst [20]. Pathak *et al.* computationally proposed a series of Mn-based complexes as promising CO_2 hydrogenation catalysts [21, 22]. However, of particular interest is the bioinspired approach by Nervi/Khusnutdinova and co-workers, who have developed Mn(I)-complexes for hydrogenation of CO_2 to FA [23]. These complexes are built with 6,6′-dihydroxy-2,2′bipyridine (DHBP) and CO ligands. TON upto 6250 is reported for

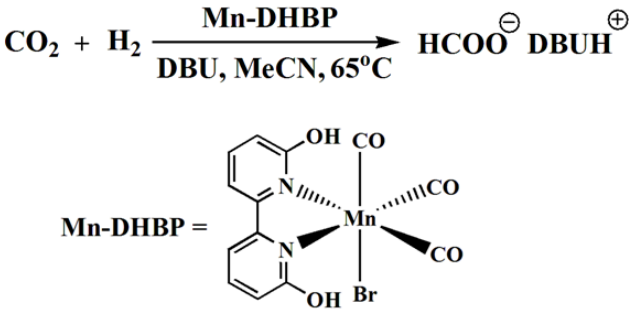

Figure 6.1: Hydrogenation of CO_2 to formate catalysed by **Mn-DHBP**

$Mn(DHBP)Br(CO)_3$ (hereafter denoted as **Mn-DHBP**) using DBU as an external base at 65 °C in acetonitrile solvent (see Figure 6.1). This represents a significant advancement for not only broadening the spectrum of CO_2 hydrogenation catalysts based on earth-abundant metals but also for a number of practical reasons such as

easy handling of the catalyst, the use of inexpensive nonphosphine ligands along with relatively milder reaction conditions.

DHBP ligands were previously introduced in Ir, Rh and Co-half-sandwich complexes and employed for CO_2 hydrogenation by Himeda and co-workers in protic solvents such as water [24–26]. These processes were examined in detail using density functional theory (DFT) calculations which suggested the role of pendant hydroxyl groups in facilitating the H_2 activation through a proton-relay mechanism involving a solvent (water) molecule [26, 27]. Moreover, these pendant groups were also shown to have a profound effect in reducing the activation barrier of the hydride transfer step by stabilizing the transition state (TS) via hydrogen-bonding interactions. Since **Mn-DHBP** operates in an aprotic solvent, we were curious about the role of the pendant hydroxyl moieties during the course of hydrogenation; whether or not these oxygens actively participate in the heterolytic H_2 cleavage and hydride transfer. This prompted us to launch a comprehensive computational study to unveil the mechanism of **Mn-DHBP**-catalysed hydrogenation of CO_2 to FA using density functional theory calculations. To our delight, the thorough molecular level understansing of the mechanism served as a guiding principle for rational design of potential Mn(I)-based CO_2 hydrogenation catalysts.

6.2 Computational details

All molecular geometries are optimized with M06 [28] exchange-correlation functional using 6-31+G(d,p) basis set for lighter atoms (C, H, O, N) and LanL2DZ basis set along with the corresponding effective core potential for Mn. The basis set combination is hereby denoted as BS-I. To refine the electronic energies obtained at the M06/BS-I level, single point calculations are performed with higher basis set 6-311++g(d,p) for C, H, O, N and SDD along with Stuttgart-Dresden effective core potential for Mn; this basis set combination is denoted as BS-II. Solvent (acetonitrile) effects are considered under the framework of SMD model by Truhlar and Cramer

[29]. All geometry optimizations are followed by a harmonic vibrational analysis to characterise the nature of the stationary points; transition states (one imaginary frequency) or minima (no imaginary frequencies). Transition state structures are further verified with intrinsic reaction coordinate (IRC) calculations to check its connection to the desired minima on either side of the saddle point. All thermochemical data are obtained within the framework of ideal gas-rigid rotor-simple harmonic approximation and the computed Gibbs free energy values include zero-point energy corrections. All calculations are performed using Gaussian 16 package [30].

Note that, we have used the following atom colouring to visualize the molecular geometries: C (grey), H (white), N (blue), O (red), and Mn (magenta).

6.3 Results and discussion

6.3.1 Mechanism of CO_2 hydrogenation catalysed by 1

The hydrogenation of CO_2 catalysed by **Mn-DHBP** is previously investigated experimentally by Nervi/Khusnutdinova *et al.* and this has provided important mechanistic information for the catalytic cycle. Results of NMR experiments indicate that the actual catalyst, $Mn(DHBP)Br(CO)_3$ complex readily loses Br^- in the acetonitrile solvent under experimental conditions. It was also shown in the experiment that the pendant hydroxyl groups could be deprotonated in the presence of DBU. We have computed the Gibbs free energy change for such a deprotonation process and our results suggest that both the hydroxy groups can be deprotonated by DBU; the process ($Mn(DHBP)(CO)_3$ + 2DBU→ $Mn(dDHBP)(CO)_3$ + $2DBUH^+$ where dDHBP represents a doubly deprotonated DHBP moiety) is calculated to be thermodynamically favored by 27.1 kcal/mol. If we consider a solvent molecule occupying the vacant coordination site, the double deprotonation ($Mn(DHBP)(CO)_3(MeCN)$ + 2DBU→ $Mn(dDHBP)(CO)_3(MeCN)$ + $2DBUH^+$) is computed to be thermodynamically favored by 20.4 kcal/mol. In fact, the presence of a doubly deprotonated anionic ligand was also confirmed by Nervi/Khusnutdinova, through spectroscopic studies.

Taking account of all these facts, the deprotonated monoanionic complex, **1**, is chosen as the active form of the catalyst in solution. Figure 6.2 shows the mechanism for the hydrogenation of CO_2 to FA catalysed by **1**. The corresponding relative Gibbs free energy profile is depicted on Figure 6.3.

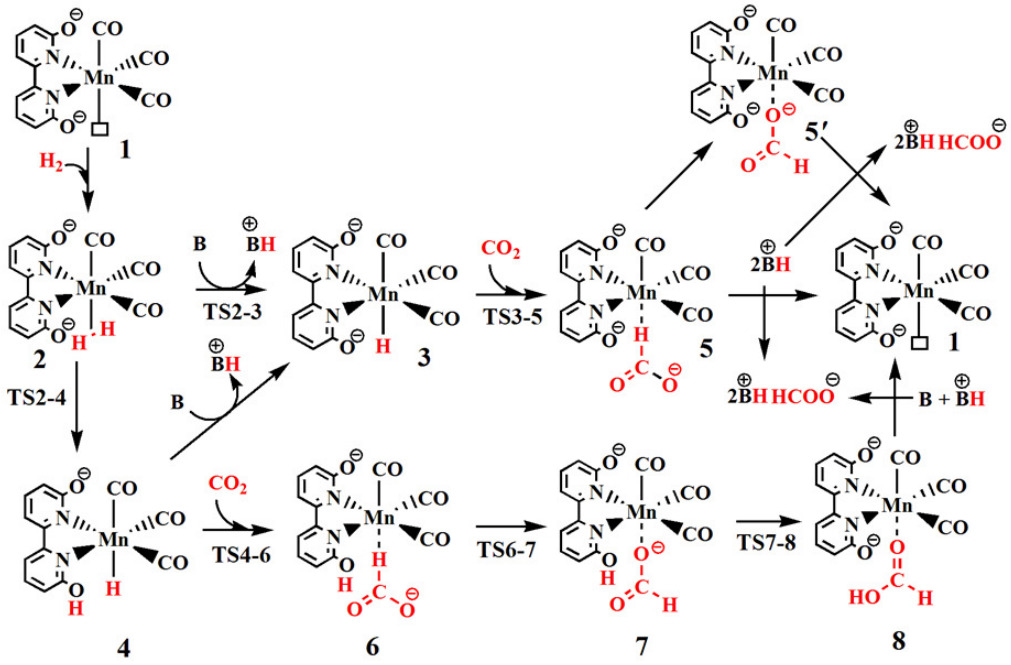

Figure 6.2: Mechanism of hydrogenation of CO_2 to FA catalysed by **1**. **B** denotes the external base, DBU. The square box in **1** represents a vacant coordination site. While the complexes **1**, **2**, **4**, **6**, **7** and **8** are monoanionic, **3**, **5** and **5′** are dianionic.

1 is a five-coordinated Mn-complex with one doubly deprotonated DHBP and three CO ligands; two of the CO ligands occupy the equatorial sites while the remainder takes the axial position. The bidentate bipyridine ligand with the pendant ortho oxygens remain in the equatorial positions while the sixth(axial) coordination site remains either vacant or occupied by a solvent molecule. Infact, a solvent-bound **1** is found to be 3.1 kcal/mol more stable than **1**+ MeCN. At the beginning of the catalytic process, H_2 molecule occupies the vacant site (or exchanges with the solvent molecule) to form a Mn-H_2 σ-complex, **2**. Formation of **2** is computed to be 4.6 kcal/mol uphill in free energy. The structure of **2** features a slightly stretched

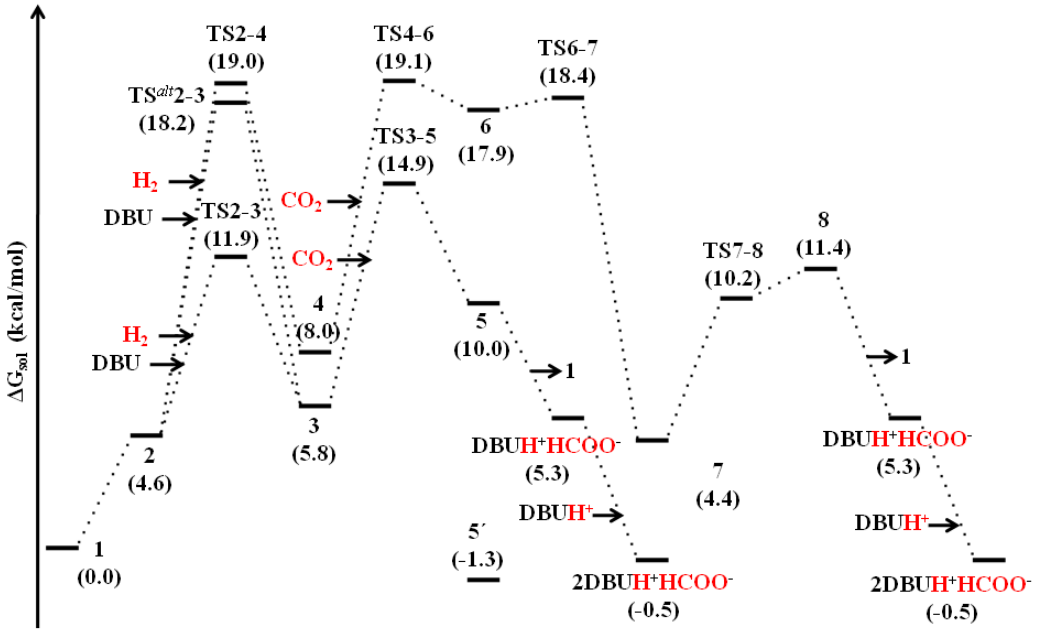

Figure 6.3: Relative Gibbs free energy profile (at T=338.15 K) for hydrogenation of CO_2 to FA catalysed by **1**. All free energy values are in kcal/mol.

H_2 molecule coordinated to Mn centre in η_2 fashion with H-H distance of 0.802 Å (compared to 0.742 Å in isolated H_2 itself). Thereby, the σ-complex would initiate the heterolytic H_2 cleavage towards the formation of Mn-hydride.

In the present case, H_2 cleavage could occur in two ways; with or without the involvement of the external base, DBU. In the latter case, one of the pendant oxygens, attached to the ortho position of the dDHBP ligand, assists in the H_2 cleavage. We shall discuss these two cases separately.

The deprotonation of **2** by DBU proceeds through **TS2-3**, leading to the formation of Mn-hydride complex, **3**. **TS2-3** corresponds to a free energy activation barrier of 11.9 kcal/mol. The H-H distance in **TS2-3** is elongated to 1.028 Å while the Mn-H and N-H distances are found to be 1.662 and 1.266 Å, respectively. The structure of **TS2-3** features a set of noncovalent interactions. The methylene hydrogens of DBU are involved in C-H$\cdots$O and C-H$\cdots\pi$ interactions with the pendant oxygen atoms and the bpy moiety. Interestingly, we have located another high energy TS, **TS^{alt}2-3**, for the DBU-assisted deprotonation process, which is 6.3 kcal/mol higher than **TS2-3**. These two TS structures mainly differ in the mutual positioning of the

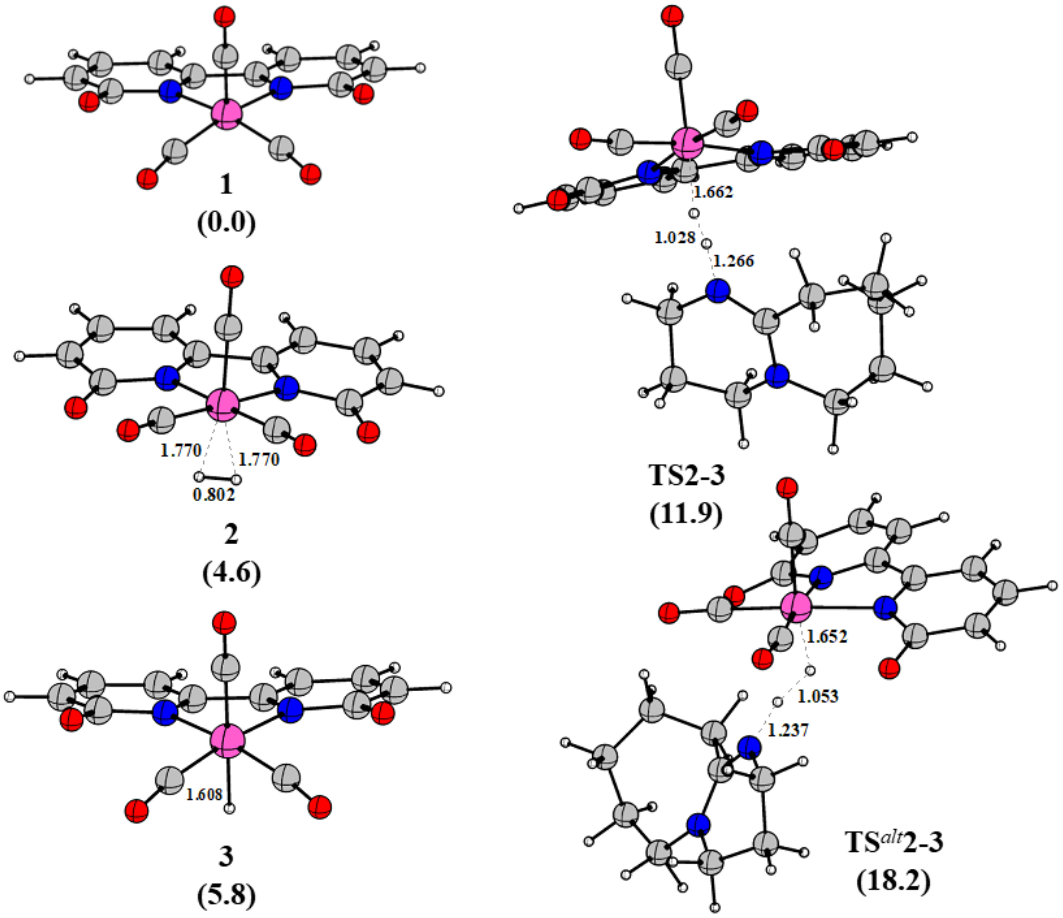

Figure 6.4: Geometry optimised structures of the key stationary points for heterolytic cleavage of H_2 during hydrogenation of CO_2 to FA catalysed by **1**. All distances are given in Å. Solvent-corrected Gibbs free energy values (in kcal/mol) are given in parentheses.

DBU and the bpy ligand. While in **TS2-3**, DBU and bpy remain in close vicinity on the same side of the H_2 , these two are located on the opposite side of H_2 in **TS^{alt}2-3**. Consequently, a few noncovalent contacts are absent in the latter TS structure. It is evident that these weak interactions play a crucial role to stabilize the TS and reduce the activation free energy barrier in **TS2-3**. On the basis of computed barrier height, deprotonation is predicted to occur through **TS2-3**. Overall, H_2 splitting by DBU is found to be slightly endergonic by 1.2 kcal/mol. The optimized structures of the key stationary points for the heterolytic cleavage of H_2 in the DBU-assisted pathway are depicted in Figure 6.4.

In an alternative pathway, H_2 molecule in **2** can be cleaved by the cooperative

action of Mn and the pendant oxygen atom in the manner of frustrated Lewis pair (FLP)-mediated heterolytic H_2 activation. Note that, similar H_2 splitting mechanism is also reported in a computational study of borane/ether(B/O) intermolecular FLPs [31]. The TS for Mn/O-mediated H_2 cleavage, **TS2-4** (see Figure 6.6 for structure), lies at 19.0 kcal/mol, which is slightly higher in free energy than **TS2-3**. **TS2-4** features a H-H distance of 0.998 Å; the Mn-H and O-H distances are 1.725 and 1.293 Å, respectively. In the resulting Mn-H complex **4**, the H_2 molecule is completely cleaved as the H atoms are 2.419 Å apart from each other. Formation of **2**→**4** is endergonic by 3.4 kcal/mol.

After the heterolytic cleavage of H_2, the subsequent hydride delivery to CO_2 completes the hydrogenation process. This can occur via two possible reaction pathways involving either **3** or **4** as the hydride transfer (HT) agent. In the former case, **3** transfers the hydride directly to a CO_2 molecule wherein the Mn-H bond points towards the carbon atom. Hydride transfer into CO_2 occurs through **TS3-5** which lies 9.1 kcal/mol above **3**. $\angle Mn-H-C$ angle in **TS3-5** is found to be 163.2° while the Mn-H and C-H distances are 1.644 and 1.890 Å, respectively. **TS3-5** initially relaxes to a H-bound formate complex, **5**, in which the Mn-H and C-H distances become 1.812 and 1.211 Å, respectively. After that, **5** may undergo a formate ion dissociation in an exergonic step (ΔG=-4.4 kcal/mol). Alternatively, the formate can also bind to the Mn centre through its oxygen end, leading to the formation of **5′**. Thermal dissociation is necessary to liberate the formate from **5′**. Once released from the Mn centre, formate can exist in solution as an ion pair $DBUH^+HCOO^-$. It can be further stabilized by forming hydrogen-bonding interactions with another $DBUH^+$ ion in the form of $2DBUH^+HCOO^-$. The geometry optimized structures of the relevant stationary points involved in the HT step are shown in Figure 6.5.

HT by **4** proceeds through **TS4-6** with an activation barrier of 19.1 kcal/mol. Interestingly, the pendant hydroxyl does not take part in the process. Note that, such hydroxyl-assisted HT was reported by Zhao *et al.* in Ir complexes with DHBP

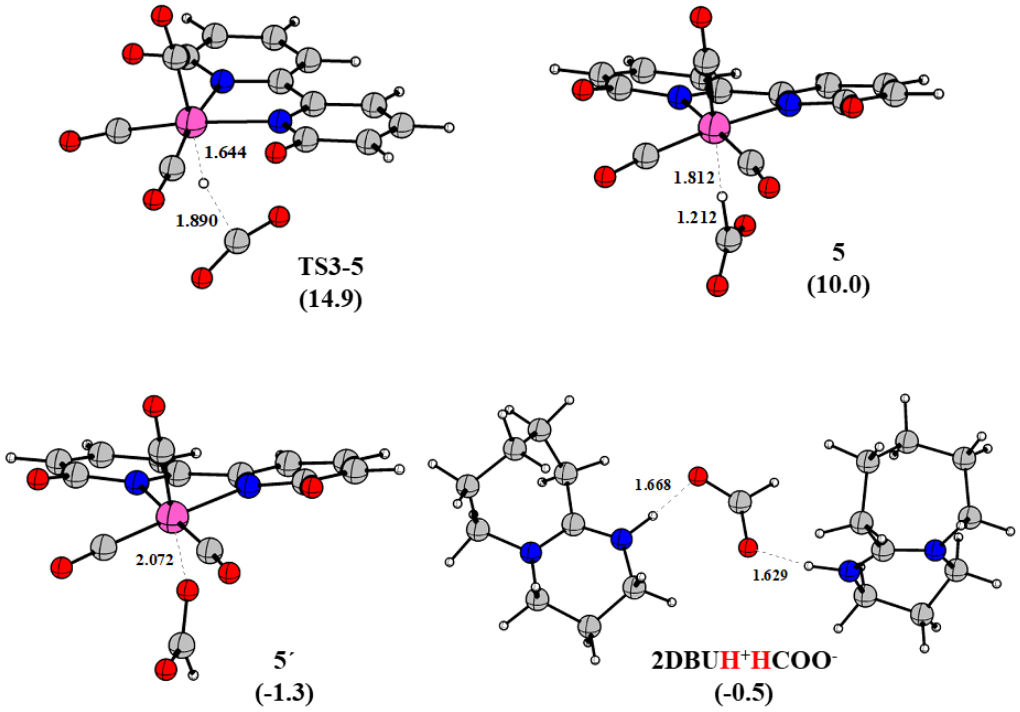

Figure 6.5: Geometry optimised structures of **TS3-5**, **5**, **5′** and 2DBUH$^+$HCOO$^-$. All distances are given in Å. Solvent-corrected Gibbs free energy values (in kcal/mol) are given in parentheses.

ligands [27]. In fact, they located a six-membered TS in which hydroxyl group is involved in hydrogen bonding interaction with one of the CO_2 oxygen. Attaining such stable TS geometry might not be feasible in the present case as the pendant hydroxyl remains far away from the CO_2; basically, the former moiety resides in equatorial plane while the latter approaches from the axial direction. Thus, **TS4-6** resembles in structure with **TS3-5**; the only difference is a pendant hydroxyl group, which remains in a deprotonated state for the latter structure. **TS4-6** lies 4.3 kcal/mol higher than **TS3-5**. This can be rationalized by comparing the hydride donating ability between **3** and **4**. To this end, we have computed the hydride detachment free energy (HDFE) following the equation $\mathbf{MH} \rightarrow \mathbf{M}^+ + \mathrm{H}^-$. HDFE reflects the ease at which the hydride can be detached from the Mn centre; smaller HDFE indicates better hydride donating ability. Our calculation results show that HDFE of **4** is about 10.9 kcal/mol higher than that of **3**, suggesting much inferior hydride donating ability of the former species. In fact, the NPA atomic charges also show that the H

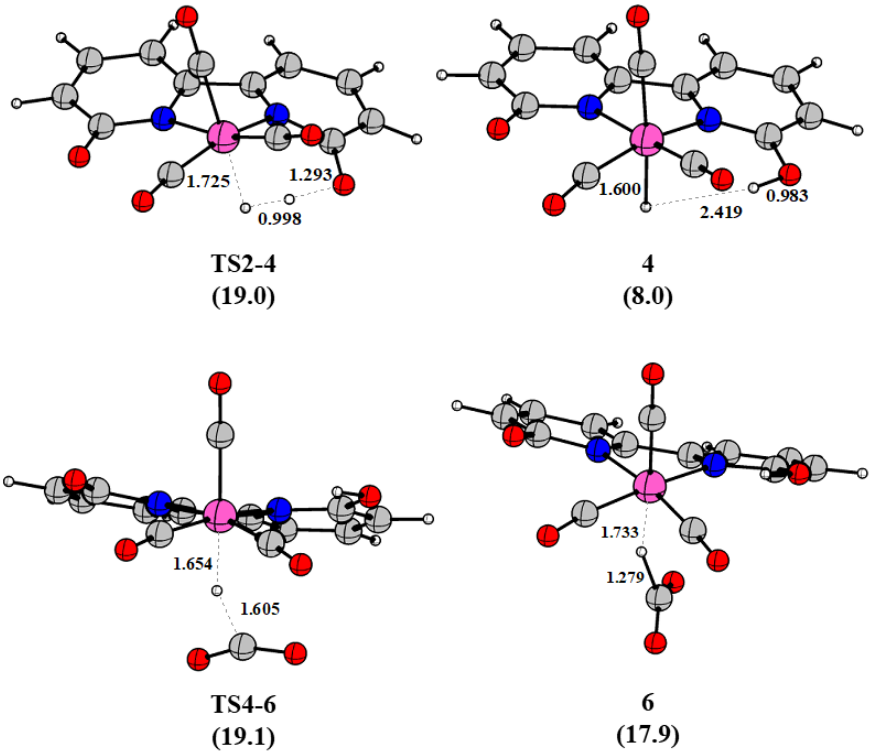

Figure 6.6: Geometry optimised structures of **TS2-4**, **4**, **TS4-6** and **6**. All distances are given in Å. Solvent-corrected Gibbs free energy values (in kcal/mol) are given in parentheses.

atom in **3** is more negative compared to that in **4**, suggesting that the hydride in **3** has a greater electron density and more prone to attack the CO_2. However, the Mn-H and C-H distances are 1.654 and 1.604 Å in **TS4-6**. **6** features a H-bound formate complex similar to **5**. Following its formation, the formate in **6** rotates to form more stable O-bound formate complex, **7**. The bond rotation occurs in a low barrier step through **TS6-7**. In **TS6-7**, one of the formate oxygen moves closer to the pendant hydroxyl group and forms a hydrogen bonding interaction. The O$\cdots$H distance is found to be 1.512 Å along with O$\cdots$H-O angle of 170.5°. Incidentally, **7** is 13.5 kcal/mol more stable than **6**. The pendant hydroxyl group in **7** can deliver a proton to the Mn-bound oxygen through **TS7-8**, which lies at 7.1 kcal/mol. In the structure of **8**, the FA molecule is bound to the Mn centre with its hydroxyl oxygen end and at the same time maintaining a H-bonding interaction with the pendant oxygen. Upon dissociation, **8** releases **1** and FA, which forms 2DBUH$^+$HCOO$^-$ in

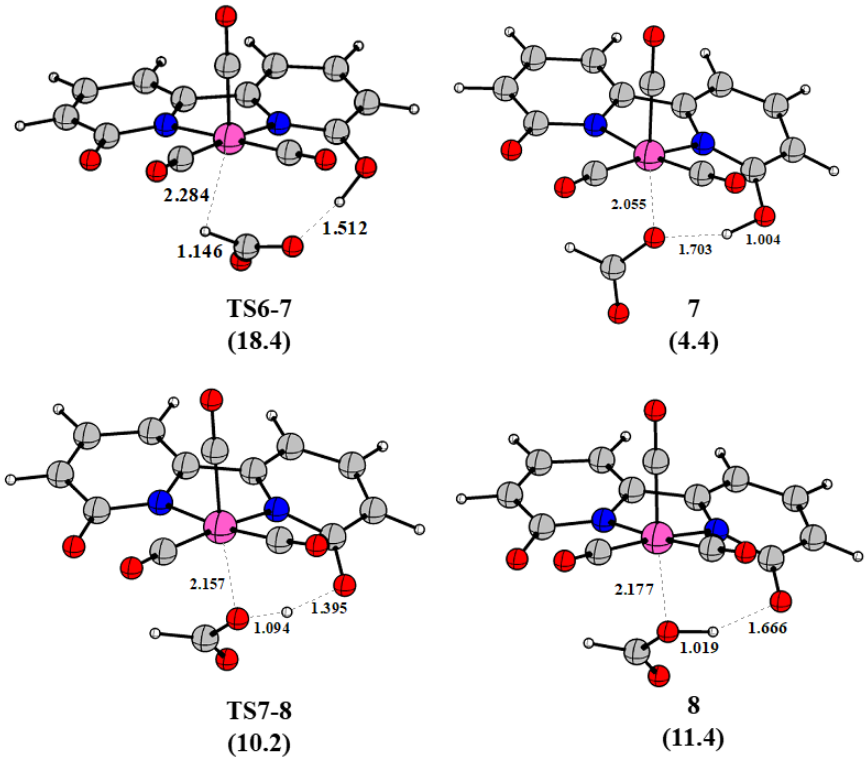

Figure 6.7: Geometry optimised structures of **TS6-7**, **7**, **TS7-8** and **8**. All distances are given in Å. Solvent-corrected Gibbs free energy values (in kcal/mol) are given in parentheses.

solution. The optimized geometries of the relevant stationary points for the pendant oxygen-assisted H_2 cleavage and subsequent HT are shown in Figure 6.6 and Figure 6.7.

It is worth mentioning that we also considered another alternative pathway which involves isomerisation of the initial catalyst **1**. The pentacoordinated complex **1** can be isomerised to its configurational isomer,$\mathbf{1}_{iso}$, in which the vacant coordination site is located in the equatorial plane and trans to one of the pyridine nitrogens. $\mathbf{1}_{iso}$ would then catalyse the hydrogenation of CO_2. However, $\mathbf{1}_{iso}$ lies 17.1 kcal/mol higher than **1** in the free energy profile. The TS for such an isomerisation process could not be located. Nevertheless, assuming that it has to lie even higher than 17.1 kcal/mol, this reaction route becomes noncompetetive with the DBU-assisted H_2 cleavage pathway (which has a barrier of 11.9 kcal/mol). Thus, we rule out the possibility of the isomerisation pathway.

As can be seen from the energy profile in Figure 6.3, CO_2 hydrogenation catalysed by **1** could proceed through two pathways, which are hereby denoted as $\mathbf{P}_A$ and $\mathbf{P}_B$, respectively. In $\mathbf{P}_A$, the catalytic cycle is closed by the following intermediate sequence, **1**→**2**→**3**→**5**(and **5′**)→**1** while that in $\mathbf{P}_B$ involves **1**→**2**→**4**→**6**→**7**→**8**→**1** (for a simplified description see Figure 6.8). In $\mathbf{P}_A$, external base DBU actively participates in H_2 cleavage by deprotonating the initial Mn-H_2 σ-complex. The resulting Mn-hydride complex transfers the hydride to CO_2 and completes the hydrogenation process. $\mathbf{P}_B$ is essentially a base-free hydrogenation pathway where Mn and the pendant oxygen acts cooperatively to cleave the H_2. Next, the hydride and the proton are transferred to CO_2 yielding FA. Following H_2 activation in the $\mathbf{P}_B$ pathway, the

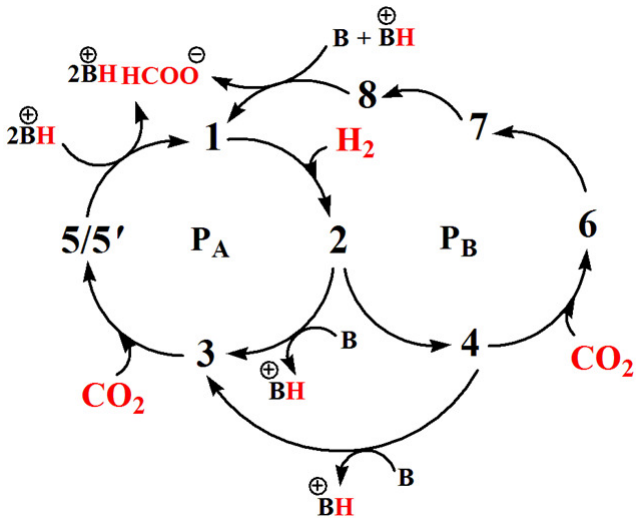

Figure 6.8: Plausible catalytic routes for hydrogenation of CO_2 to formate catalysed by **1**. **B** denotes the external base, DBU.

resulting complex **4** can be deprotonated by DBU to give **3** from which HT may proceed via $\mathbf{P}_A$. In fact, formation of **4**→**3** is thermodynamically favorable by 2.2 kcal/mol. Thus, even if the reaction begins via $\mathbf{P}_B$, it can switch over to $\mathbf{P}_A$ after H_2 activation. The benefit is that the HT step in $\mathbf{P}_A$ occurs with much less activation barrier (via **TS3-5**) when compared to that (via **TS4-6**) in $\mathbf{P}_B$.

The overall catalytic reaction **1**+H_2+CO_2+DBU+$DBUH^+$→**1**+2$DBUH^+HCOO^-$ is almost thermoneutral(ΔG=-0.5 kcal/mol) in acetonitrile. The activation barrier for

H-H cleavage is computed to be much lower in $\mathbf{P}_A$ compared to $\mathbf{P}_B$ and consequently, the H_2 splitting is predicted to proceed via the former pathway under the reaction condition. We have analysed the Gibbs free energy profile for the CO_2-hydrogenation catalysed by **1** through energy span model [32]. **TS2-3** is the TOF-determining TS (TDTS) and **5′** is the TOF-determining intermediate (TDI). Thus, the free energy span is computed to be 14.9-(-1.3)+(-0.5) = 15.7 kcal/mol, which is consistent with the observed reactivity at experimental temperature.

6.3.2 Mechanism of CO_2 hydrogenation catalysed by $\mathbf{1}_{OMe}$

In order to further elucidate the role of the pendant oxygen ligands, we have examined the mechanism of CO_2 hydrogenation by replacing the anionic oxygen ligands on the bpy moiety of **1** with methoxy (OMe) groups. The resulting complex is denoted as $\mathbf{1}_{OMe}$. The corresponding actual catalyst, **Mn-DMBP** (Mn(DMBP)Br$(CO)_3$; DMBP=6,6′-dimethoxy-2,2′bipyridine), was experimentally found to be inactive towards hydrogenation of CO_2 to formate in presence of DBU [23]. Thus, we next explore the CO_2 hydrogenation reactivity of the **Mn-DMBP** complex. Like **Mn-DHBP**, we find similar mechanism for the initial DBU-assisted H_2 cleavage by **Mn-DMBP**. First, H_2 binds to the active form of the catalyst, $\mathbf{1}_{OMe}$, to yield the σ-complex, $\mathbf{2}_{OMe}$. $\mathbf{2}_{OMe}$ is deprotonated by DBU, leading to the formation of the hydride $\mathbf{3}_{OMe}$. The TS for the depronotation, $\mathbf{TS2}_{OMe}$-$\mathbf{3}_{OMe}$, corresponds to free energy activation barrier of only 5.9 kcal/mol. The geometry optimized structures of the key stationary points in the DBU-assisted H_2 cleavage by $\mathbf{1}_{OMe}$ are depicted in Figure 6.9. $\mathbf{3}_{OMe}$ is supposed to transfer the hydride to CO_2 to complete the hydrogenation. Unfortunately, all our attempts to locate a TS for the HT step were unsuccessful. Although, we were able to optimize a weak $\mathbf{3}_{OMe}$-CO_2 adduct, we could not locate a minimum for a putative **5**-like product. In fact, relaxed potential energy scan calculations with respect to (Mn)H-C(CO_2) distance indicate that a H-bound formate complex does not correspond to a local minimum. This is in contrast with the HT reactivity of **3** and we tried to understand the reason behind it. When

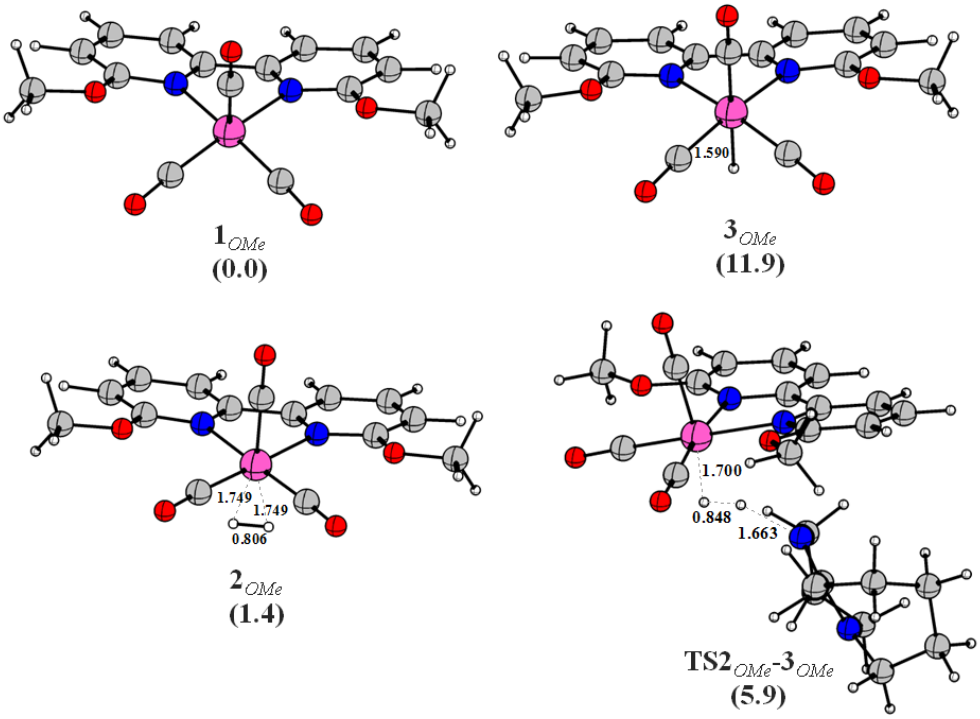

Figure 6.9: Geometry optimised structures of the key stationary points for heterolytic cleavage of H_2 during hydrogenation of CO_2 to FA catalysed by **1**. All distances are given in Å. Solvent-corrected Gibbs free energy values (in kcal/mol) are given in parentheses.

we compared the HDFE values (-4.6 kcal/mol and 12.8 kcal/mol for **3** and $\mathbf{3}_{OMe}$ respectively), $\mathbf{3}_{OMe}$ is found to be much weaker hydride donor compared to **3**. This is reflected in the energetics of the HT step, which is strikingly different for **3** and $\mathbf{3}_{OMe}$. While the HT step ($\mathbf{3}/\mathbf{3}_{OMe} + CO_2 \rightarrow \mathbf{1}/\mathbf{1}_{OMe} + HCO_2^-$) is -3.0 kcal/mol exergonic for **3**, it is found to be 14.7 kcal/mol endergonic for $\mathbf{3}_{OMe}$. Intuitively, the anionic oxygens in **3** have better electron donating ability compared to the methoxy oxygens in $\mathbf{3}_{OMe}$. This is supported by the NPA atomic charges on H atom, which is found to be more negative in **3** (0.033) than that in $\mathbf{3}_{OMe}$ (0.077), indicating that the former is a stronger hydride donor than latter. Thus, the weak hydride donating ability in $\mathbf{3}_{OMe}$ prohibits the hydrogenation reactivity of the **Mn-DMBP** complex, which corroborates with the experimental observation. It is evident that, in these Mn-complexes, the pendant oxygens participate neither in the H_2 cleavage step nor directly during the HT step. Their effect is rather indirect; they help in modulating

the electron density on the metal centre and in turn, control the hydricity of the Mn-hydride. Therefore, the presence of the deprotonated pendant hydroxyl groups are crucial for the hydrogenation reactivity of the **Mn-DHBP** complex.

6.3.3 H_2 cleavage: P_A *vs.* P_B pathway

Having settled the mechanism of CO_2 hydrogenation catalysed by **Mn-DHBP**, we look back and re-examine the H_2 cleavage steps in $\mathbf{P}_A$ and $\mathbf{P}_B$. Unlike in $\mathbf{P}_B$, $\mathbf{P}_A$ does not involve direct participation of the pendant oxygen atoms; rather they merely help in modulating the electron density on the Mn centre. While **TS2-3** lies 7.1 kcal/mol below **TS2-4** in the relative free energy profile, on the basis of electronic energy, the stabilization is even more (16.0 kcal/mol). Although **TS2-4** and **TS^{alt}2-3** lie very close in free energy, we noticed that excluding the entropic correction, latter is 6.8 kcal/mol more stable than former in terms of electronic energy. Clearly, the higher entropic cost in **TS^{alt}2-3** is associated with the intermolecular H_2 activation process in going from two components to one and the entropic penalty is even higher at elevated temperature as in the present case. In fact, while at 298.15 K, **TS^{alt}2-3** is 2.1 kcal/mol more stable in free energy than **TS2-4**, **TS^{alt}2-3** is only 0.8 kcal/mol more stable than **TS2-4** at 338.15 K. In light of this, we rethink the origin of the relatively higher energy barrier in the pendant oxygen-assisted H_2 cleavage. Apparently, the difference in activation energy barrier directly correlates to the strength of the base component responsible for H_2 clevage; (pendant) oxygen has weaker eletron donating ability compared to nitrogen (DBU). Nevertheless, a closer look at the structure of **TS2-4** reveals significant distortion in the bpy moiety as the oxygen makes an effort to reach for the H_2 molecule in the axial position. We argue that the energy cost associated with this geometric distortion also contributes substantially to the high barrier obtained in **TS2-4**. In case of DBU-assisted H_2 cleavage, the bpy core is as such not affected since an external base is deprotonating the Mn-bound H_2 molecule. In order to rationalize the argument, we have computed the deformation energy (DE) of the catalyst in the **TS2-4**, **TS2-3** and **TS^{alt}2-3** geometries. The deformation

energies are calculated in the following manner; in the TS structures, the H_2 and the base molecule are deleted keeping the rest of the structure intact. The single point energies of the resulting distorted catalyst structures are then calculated (at the M06/BS-II level) and compared with the ground state optimized structure of **1**.The DE for **TS2-3**, **TS**^{alt}**2-3** and **TS2-4** are found to be 5.6, 0.2 and 13.1 kcal/mol, suggesting a greater distortion in the catalyst structure for pendant oxygen assisted H_2 cleavage. The higher DE in **TS2-3** compared to **TS**^{alt}**2-3** can be associated with slightly distorted catalyst structure owing to several noncovalent contacts with the DBU methylene hydrogens.

6.3.4 H_2 cleavage by $\mathbf{1}_{iso}$

The above computational results made us contemplate about Mn-complexes having slightly different geometric design. The idea is to exploit the full utility of the pendant oxygen ligands by keeping it on the same plane as the vacant coordination site. We surmised that such geometric arrangements would help in reducing the distortion in the TS for pendant oxygen-assisted H_2 cleavage. At this point, it is interesting to point out that the configurational isomer, $\mathbf{1}_{iso}$, fits well with the aforementioned geometric criterion. In the structure of $\mathbf{1}_{iso}$, two of the CO ligands occupy the axial position while the remaining CO ligand occupies the equatorial position. As the vacant coordination site is shifted to equatorial plane, we expect that the Mn-bound H_2 would be located in close proximity to the pendant oxygen, rendering the activation barrier for the oxygen-assisted H_2 cleavage somewhat lower than that in **1**. Although we discarded the isomerisation pathway in the mechanism of Mn-DHBP catalysed CO_2 hydrogenation reaction, further pursuit along this route could provide some insights into our conjecture that we discussed above. Thus, as a proof-of-principle study, we examined the pendant oxygen assisted heterolytic cleavage of H_2 by $\mathbf{1}_{iso}$. The corresponding Gibbs free energy profile and the geometry optimized structures of the relevant intermediates and TSs are depicted in Figure 6.10. For the sake of clear representation, we maintained similar nomenclatures (to

describe the key intermediates and TS) as that of **1**-mediated H_2 cleavage pathway. The Mn-H_2 σ complex, $\mathbf{2}_{iso}$, lies 7.1 kcal/mol below $\mathbf{1}_{iso}$. The H_2 molecule is found

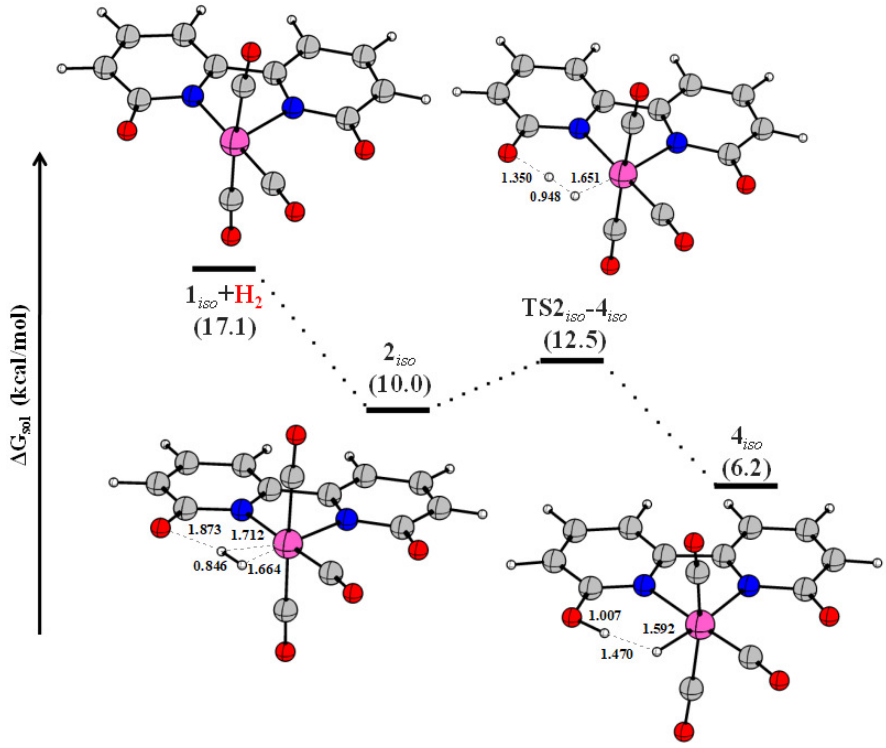

Figure 6.10: Mechanism of H_2 splitting by $\mathbf{1}_{iso}$ along with the corresponding relative Gibbs free energy profile. Solvent-corrected Gibbs free energy values (in kcal/mol) at T=338.15 K are given in the parentheses. The free energies are reported with respect to **1**+H_2 as the zero-point-reference. All the complexes are monoanioninc.

to be significantly elongated to 0.845 Å in $\mathbf{2}_{iso}$. The interaction between the pendant oxygen and a nearby H atom is apparent from the close O-H distance of 1.873 Å. As per our anticipation, the H_2 cleavage barrier is lowered significantly. The TS for H-H cleavage, $\mathbf{TS2}_{iso}$**-** $\mathbf{4}_{iso}$, lies only 2.5 kcal/mol above $\mathbf{2}_{iso}$. $\mathbf{TS2}_{iso}$-$\mathbf{4}_{iso}$ features a H-H distance of 0.948 Å. The H_2 splitting is found to be exergonic by 3.8 kcal/mol. The calculated DE for $\mathbf{TS2}_{iso}$-$\mathbf{4}_{iso}$ is much lower (3.4 vs 13.1 kcal/mol in **TS2-4**) compared to that of **TS2-4**. Overall, the low activation barrier in pendant oxygen assisted H_2 cleavage in $\mathbf{1}_{iso}$ proves that bringing the pendant oxygen closer to the coordinated H_2 can significantly affects the kinetics of the H_2 cleavage step.

6.3.5 Mn-AcPy complexes as CO_2 hydrogenation catalysts

These notions inspired us to design new Mn-based catalysts for CO_2 hydrogenation. To this end, we sought for different ligand frameworks with similar pendant oxygen ligands such as **1**. Specifically, our interest was drawn into acylmethylpyridinol (AcPy) ligand, which is also found in the active site of Fe-hydrogenase [33]. Inspired by the framework, Yang *et al.* computationally designed a series of Fe and Co-complexes bearing AcPy ligands and these complexes are shown to be promising CO_2 hydrogenation catalysts [16, 17]. They have also shown that the ligand plays an important role in the heterolytic hydrogen activation step during the hydrogenation process. Therefore, we have chosen AcPy [34] and CO ligands to build Mn(I)-complexes for hydrogenation of CO_2 to FA. In general, these complexes are denoted as **Mn-AcPy** and the corresponding structural framework is schematically shown in Figure 6.11. In **Mn-AcPy**, both the pendant oxygen and the vacant coordination

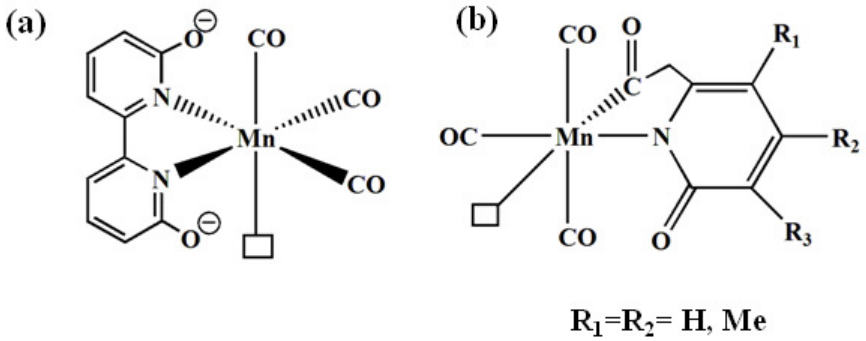

Figure 6.11: Structural frameworks of (a) **Mn-DHBP** (active form) and (b) **Mn-AcPy** complexes. The square box represents vacant coordination site.

site lie in the equatorial plane and therefore, we anticipate that the oxygen would actively participate in the H_2 splitting process.

In order to find out the catalytic activity of **Mn-AcPy**, we have investigated mechanism of CO_2 hydrogenation catalysed by a model complex **9** (R_1=R_2=H). Anticipating a Mn/O-mediated FLP-type H_2 activation, we explored an external base-free mechanism. The first step comprises of heterolytic H_2 cleavage which requires the Mn and the pendant oxygen to act cooperatively, leading to the formation of a

Mn-hydride. Subsequently, the hydride and proton delivery to CO_2 would complete the hydrogenation process. Figure 6.12 shows the mechanism for the hydrogenation of CO_2 to FA catalysed by **1** along with the corresponding relative Gibbs free energy profile. The optimized structures of the key stationary points involved in the catalytic cycle are shown in Figure 6.13.

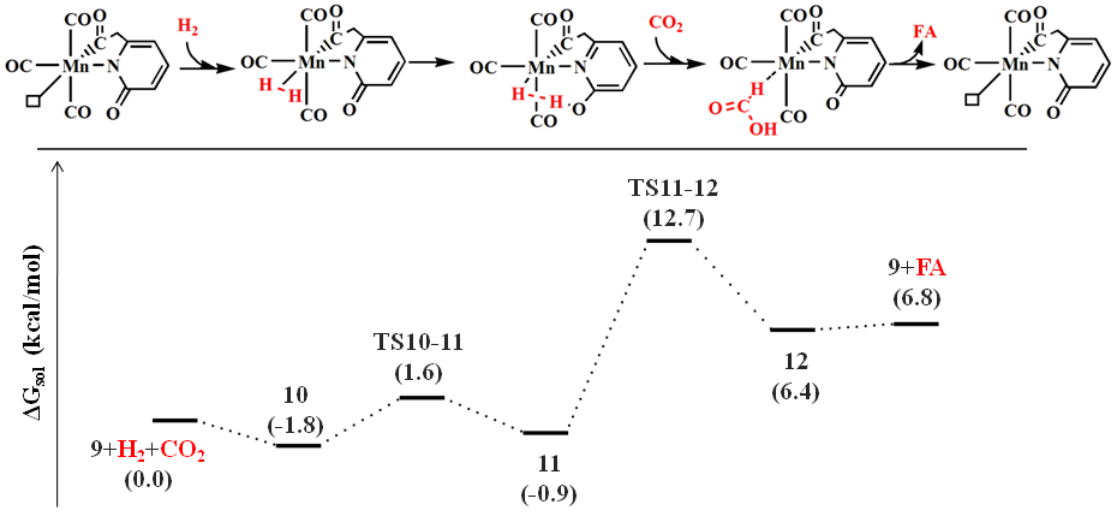

Figure 6.12: Mechanism of hydrogenation of CO_2 to FA catalysed by **9** along with the corresponding relative Gibbs free energy profile. The square box represents vacant coordination site. Solvent-corrected Gibbs free energy values (in kcal/mol) at T=298.15 K are given in the parentheses. All the complexes are monoanioninc.

The reaction begins with the coordination of H_2 molecule to the vacant site, resulting in Mn-H_2 σ-complex, **10**. The H-H distance in **10** is found to be 0.829 Å, which is slightly higher than that in **2** (0.802 Å). This is due to an additional interaction of the H_2 molecule with the proximal pendant oxygen in **10**; the O-H distance is found to be 1.906 Å. NBO analysis confirms a donor-acceptor interaction (E_{int}=11.8 kcal/mol) between the oxygen lone pair and the σ^* antibonding orbital of H_2 molecule. Formation of **10** is 1.8 kcal/mol downhill in free energy with respect to **9**. H_2 cleavage in **10** occurs through a FLP-type cooperative electron transfer processes via **TS10-11**, leading to the formation of hydride complex, **11**. In **TS10-11**, the H-H distance is 0.990 Å, similar as that of **TS2-4**. The computed activation barrier for H_2 cleavage is much lower than that in the **Mn-DHBP**-catalysed reaction (vide

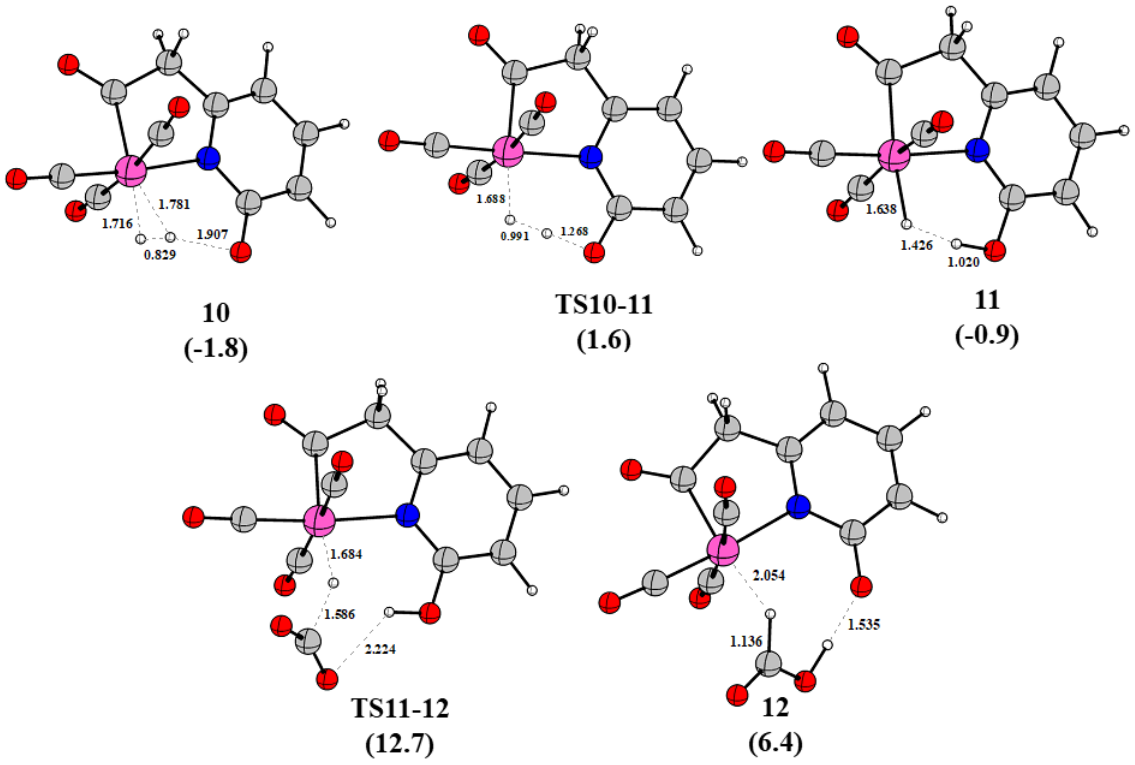

Figure 6.13: Geometry optimised structures of the key stationary points in the **9**-catalysed hydrogenation of CO_2 to FA. All distances are given in Å. Solvent-corrected Gibbs free energy values (in kcal/mol) are given in parentheses.

supra). Such low barrier is consistent with the small distortion in the catalyst moiety. The DE for the catalyst in the **TS10-11** geometry is computed to be 3.6 kcal/mol, which is 9.5 kcal/mol lower than **TS2-4**; this is evident from the easy accessibility of the H_2 molecule for the pendant oxygen as they lie in the same plane. The H atoms in **11** are only 1.436 Å apart indicating a Mn-H$\cdots$H-O diydrogen bonding interaction. Note that, similar dihydrogen bond distances are also reported in the study of related Fe and Co-complexes by Yang *et al* [16, 17].

Following H_2 cleavage, the hydride and the proton is transferred to CO_2 in a single, concerted TS, **TS11-12**, which lies 13.6 kcal/mol above **11**. In **TS11-12**, the dihydrogen bond is weakened to 1.660 Å as the hydride begins to establish interaction with the CO_2 carbon atom while the Mn-H and C-H distances are found to be 1.684 and 1.584 Å. The CO_2 molecule becomes bent due to interaction with the hydride. After HT and PT, **12** is formed in which FA remains weakly bound to the

Table 6.1: Substituent effect on the total free energy activation barrier of the hydrogenation of CO_2 to FA catalysed by **Mn-AcPy** complexes. All energy values are given in kcal/mol.

Catalysts	Substituents		ΔG_{tot}^{act}
	R_1	R_2	
9-a	H	H	14.5
9-b	H	Me	14.6
9-c	H	OMe	14.1
9-d	Me	H	12.7
9-e	Me	Me	11.7
9-f	Me	OMe	14.3

Mn-catalyst. The hydroxyl group in FA is engaged in O-H$\cdots$O hydrogen-bonding interaction with the pendant oxygen of the catalyst. After dissociation of the FA, the catalst is regenerated; the process is nearly thermoneutral in terms of free energy change. Nevertheless, **FA**+**9** lies about 6.8 kcal/mol highter than **9**+H_2+CO_2; Note that, similar endergonicity was also previously reported in the CO_2 hydrogenation catalysed by related Fe and Co complexes in organic solvents [16, 17]. Evidently, FA, being a polar molecule, is more stabilised in a polar solvent like water. In fact, considering water as the solvent, the reaction H_2+CO_2 $\rightarrow$ FA is only 2.0 kcal/mol endergonic at the present theoretical level. Therefore, the formation of FA can be facilitated by either addition of water in the reaction medium or some external base (as seen in the case of **Mn-DHBP**) which would stabilise the FA in the form of formate.

The total free energy activation barrier (ΔG_{tot}^{act}) for CO_2 hydrogenation catalysed by **9** is estimated from the difference in free energy between **10** and **TS10-11**, which is computed to be 12.7-(-1.8)=14.5 kcal/mol. In order to examine the effect of substituents (R_1 and R_2) in the catalytic activity of **Mn-AcPy** complexes, we have replaced R_1 and R_2 groups in AcPy ligand with a few functionalities and computed the ΔG_{tot}^{act} in each case. These substitutions result in six complexes as listed in Table 6.1. The complexes with R_1=H has slightly higher ΔG_{tot}^{act} compared to the complexes with R_1=Me groups. In fact, the total activation barriers remain within only 2-3

kcal/mol of the model complex **9**. The complex, **9-d**, with R_1=R_2=Me is shown to have the lowest ΔG_{tot}^{act} of 11.7 kcal/mol, which is about 3 kcal/mol lower than that of **9**. Thus, a proper choice of substitutions in the meta and para positions of the AcPy ligand is important for improved catalytic activity. The computed activation barriers suggests that these newly designed **Mn-AcPy** complexes could catalyse the hydrogenation of CO_2 to FA under mild reaction conditions.

6.4 Conclusion

In summary, we have performed a comprehensive DFT study to elucidate the mechanism for hydrogenation of CO_2 to formate catalysed by **Mn-DHBP** complex. The hydrogenation consists of two basic reaction steps; heterolytic H_2 activation followed by hydride transfer to CO_2. Heterolytic H_2 activation can occur through two conceptually different pathways. It may proceed through the deprotonation of the initially formed Mn-$H_2\sigma$-complex by an external base, resulting in the formation of the Mn-hydride. An alternative base-free H_2 activation mechanism, which exploits the synergy between Mn centre and the pendant oxygen atom to cleave H_2, is also charaterised. On the basis of computed free energy barrier, H_2 activation is predicted to proceed through the base-assisted pathway under experimental condition. After H_2 activation, the Mn-hydride complex transfers the hydride to CO_2 to complete the hydrogenation process. One key point emerging out from our computational mechanistic model is the significant geometric distortion of the catalyst in the base-free H_2 activation mode caused by the fact that the pendant oxygen and the H_2 molecule occupies equatorial and axial sites, respectively. And we surmised that keeping these two close by in the same equatorial plane could reduce the structural distortion and make H_2 activation more facile. We tested our hypothesis with a different ligand framework, acylmethylpyridinol, around the Mn centre. Indeed, the pendant oxygen assisted H_2 splitting barrier for **Mn-AcPy** complexes are much lower than that in **Mn-DHBP** complex. Considering the overall free energy activation

barrier, **Mn-AcPy** complexes could act as promising catalysts for hydrogenation of CO_2.

Bibliography

[1] Schneider, J.; Jia, H.; Muckerman, J. T.; Fujita, E. *Chemical Society Reviews* **2012**, *41*, 2036–2051.

[2] Benson, E. E.; Kubiak, C. P.; Sathrum, A. J.; Smieja, J. M. *Chemical Society Reviews* **2009**, *38*, 89–99.

[3] Johnson, T. C.; Morris, D. J.; Wills, M. *Chemical Society Reviews* **2010**, *39*, 81–88.

[4] Joó, F. *ChemSusChem* **2008**, *1*, 805–808.

[5] Leitner, W. *Angewandte Chemie International Edition* **1995**, *34*, 2207–2221.

[6] Grasemann, M.; Laurenczy, G. *Energy & Environmental Science* **2012**, *5*, 8171–8181.

[7] Schaub, T.; Paciello, R. A. *Angewandte Chemie International Edition* **2011**, *50*, 7278–7282.

[8] Tanaka, R.; Yamashita, M.; Nozaki, K. *Journal of the American Chemical Society* **2009**, *131*, 14168–14169.

[9] Schmeier, T. J.; Dobereiner, G. E.; Crabtree, R. H.; Hazari, N. *Journal of the American Chemical Society* **2011**, *133*, 9274–9277.

[10] Hull, J. F.; Himeda, Y.; Wang, W.-H.; Hashiguchi, B.; Periana, R.; Szalda, D. J.; Muckerman, J. T.; Fujita, E. *Nature chemistry* **2012**, *4*, 383–388.

[11] Filonenko, G. A.; Conley, M. P.; Coperet, C.; Lutz, M.; Hensen, E. J.; Pidko, E. A. *ACS Catalysis* **2013**, *3*, 2522–2526.

[12] Federsel, C.; Boddien, A.; Jackstell, R.; Jennerjahn, R.; Dyson, P. J.; Scopelliti, R.; Laurenczy, G.; Beller, M. *Angewandte Chemie International Edition* **2010**, *49*, 9777–9780.

[13] Ziebart, C.; Federsel, C.; Anbarasan, P.; Jackstell, R.; Baumann, W.; Spannenberg, A.; Beller, M. *Journal of the American Chemical Society* **2012**, *134*, 20701–20704.

[14] Federsel, C.; Ziebart, C.; Jackstell, R.; Baumann, W.; Beller, M. *Chemistry-A European Journal* **2012**, *18*, 72–75.

[15] Langer, R.; Diskin-Posner, Y.; Leitus, G.; Shimon, L. J.; Ben-David, Y.; Milstein, D. *Angewandte Chemie International Edition* **2011**, *50*, 9948–9952.

[16] Yang, X. *Chemical Communications* **2015**, *51*, 13098–13101.

[17] Ge, H.; Jing, Y.; Yang, X. *Inorganic chemistry* **2016**, *55*, 12179–12184.

[18] Ge, H.; Chen, X.; Yang, X. *Chemistry-A European Journal* **2017**,

[19] Yang, X. *ACS Catalysis* **2011**, *1*, 849–854.

[20] Bertini, F.; Glatz, M.; Gorgas, N.; Stöger, B.; Peruzzini, M.; Veiros, L. F.; Kirchner, K.; Gonsalvi, L. *Chemical Science* **2017**,

[21] Rawat, K. S.; Mahata, A.; Choudhuri, I.; Pathak, B. *The Journal of Physical Chemistry C* **2016**, *120*, 16478–16488.

[22] Rawat, K. S.; Pathak, B. *Catalysis Science & Technology* **2017**,

[23] Dubey, A.; Nencini, L.; Fayzullin, R. R.; Nervi, C.; Khusnutdinova, J. R. *ACS Catalysis* **2017**, *7*, 3864–3868.

[24] Himeda, Y.; Miyazawa, S.; Hirose, T. *ChemSusChem* **2011**, *4*, 487–493.

[25] Himeda, Y.; Onozawa-Komatsuzaki, N.; Sugihara, H.; Kasuga, K. *Organometallics* **2007**, *26*, 702–712.

[26] Suna, Y.; Ertem, M. Z.; Wang, W.-H.; Kambayashi, H.; Manaka, Y.; Muckerman, J. T.; Fujita, E.; Himeda, Y. *Organometallics* **2014**, *33*, 6519–6530.

[27] Hou, C.; Jiang, J.; Zhang, S.; Wang, G.; Zhang, Z.; Ke, Z.; Zhao, C. *ACS Catalysis* **2014**, *4*, 2990–2997.

[28] Zhao, Y.; Truhlar, D. G. *Theoretical Chemistry Accounts: Theory, Computation, and Modeling (Theoretica Chimica Acta)* **2008**, *120*, 215–241.

[29] Marenich, A. V.; Cramer, C. J.; Truhlar, D. G. *The Journal of Physical Chemistry B* **2009**, *113*, 6378–6396.

[30] Frisch, M. J. et al. Gaussian 16 Revision A.03. 2016; Gaussian Inc. Wallingford CT.

[31] Das, S.; Pati, S. K. *Chemistry-A European Journal* **2017**, *23*, 1078–1085.

[32] Kozuch, S.; Shaik, S. *Accounts of chemical research* **2010**, *44*, 101–110.

[33] Tard, C.; Pickett, C. J. *Chemical Reviews* **2009**, *109*, 2245–2274.

[34] *Infact, we have chosen a deprotonated form of the AcPy ligand*.

Chapter 7

Summary and Outlook

7.1 Retrospect

The past decade has witnessed an incredible development in the chemistry of the FLPs. Their remarkable abilities to cleave molecular hydrogen and catalyse the hydrogenation of unsaturated organic substrates have revolutionalized the field of metal-free catalytic hydrogenation, which was mostly considered to be a hypothetical area of research even a decade ago. Since their discovery in 2007, the initial years were devoted to understanding the fundamental concepts underlying FLP reactivity and catalysis in which theoretical studies played its own part to establish a reliable mechanistic picture. In the last five years, researchers in this community are looking to enhance the scope and practicality of the FLP catalysis focusing on developing air-stable, moisture tolerant catalytic protocols with a wide range of substrate scope. This has led to modified strategies for boron-based FLP catalysis and more importantly, alternative Sn-based FLP LAs for catalytic hydrogenation. Our contribution in this field, which we have reported in the previous five work chapters, was to provide a conceptual understanding of the fundamental mechanisms in these recently developed systems and to design new systems whenever possible. In the concluding chapter of this thesis, we recollect and summarize the key findings of our computational studies. Also, in the next section, we wish to mention a few aspects, which might provide new

avenues for future studies.

Our studies on $B(C_6F_5)_3$-catalysed hydrogenation of carbonyl compounds delineates the critical role of the ether solvent as an active participant throughout the entire reaction pathway beginning with H_2 activation and the subsequent steps involving Brønsted acid activation of the substrate, proton transfer, and hydride transfer. In addition, the computed decomposition routes for the aqua-complex of $B(C_6F_5)_3$ explain the observed moisture tolerance of the catalyst in commercial solvents.

Subsequently, we have proposed that H_2 activation by iPr$_3$SnOTf/amine Lewis pairs follow dual pathways decided by the mutual positioning of the counter anion and amine LB. We have extended this idea to understand the full mechanism of the catalytic hydrogenation of carbonyl compounds using Sn-based FLPs. Our calculations revealed that a LA activation pathway, instead of the Brønsted acid activation of the substrate proposed for corresponding $B(C_6F_5)_3$-catalysed process, operates under the reaction condition. In addition to H_2 activation, the counter anion to LA fragment was shown to play a crucial role in the hydride transfer step of the hydrogenation pathway. Continuing along the same line, based on these molecular-level understanding, we designed a new series of intramolecular Sn/N Lewis pairs for H_2 activation and catalytic hydrogenation. During H_2 cleavage, these intramolecular candidates constitute a rare example of directly accessing FLP reactivity from a classical Lewis adduct state avoiding the formal dissociation of the LA/LB centre. The subsequent release of the active hydrogens to unsaturated organic substrates imply that they might find suitable catalytic applications, calling for experimental realization.

Finally, we explored the mechanism of CO_2 hydrogenation to formate catalysed by dihydroxybipyridine-decorated Mn(I)-complexes. We find that notwithstanding the perceived role in H_2 cleavage, the pendant oxygens remains as spectators during the entire reaction pathway although their presence is crucial to retain the catalytic activity. The reluctance of these pendant ligands to participate in H_2 splitting was

attributed to a significant structural distortion in the transtion state structure, leading to a higher activation energy barrier. To circumvent this, we have designed a series of new Mn-complexes built with acylmethylpyridol ligand so that the pendant oxygens take part in the H_2 cleavage to reduce the energy barrier. The proposed Mn-complexes can be potential catalyst for hydrogenation of CO_2 to formic acid. Interestingly, the generic mechanism of hydrogenation by these newly designed Mn-complexes shares a number of common features with that of intramolecular Sn/N Lewis pairs. The similarities in the TS for H_2 activation and concerted hydride/proton transfers are easily noticeable, indicating the high generality of the concept of Lewis pair cooperativity in the main group and TM chemistry.

7.2 Prospects

From here, the future research could be propagated to many possible directions. Despite the success of the tin-based FLPs to overcome many of the existing limitations of the conventional boron-based catalysts, there remains significant scope for improvements. Since the organyl groups and the counteranion attached in these Sn(IV)-LA controls the reactivity, a systematic screening of these two entities could possibly point out to optimal combinations that can bring out maximum catalytic efficiency out of these systems. For intramolecular Sn-based FLPs, we might achieve improved reactivity with a different backbone, a different linker and possibly, a different LB centre. We expect that the success of the Sn-based LAs would spur research activities towards searching for alternative LAs derived from the p-block elements. Given the reports on Si and Sn-based LAs, it is surprising that Ge-based LAs are not reported in FLP chemistry yet. With the mechanistic models proposed in Chapter 3 and 4, it should be possible to assess the ability of Ge-based FLPs towards H_2 activation and subsequent hydrogenation catalysis. While it is truly exciting to explore new options for promising LA candidates, equal importance should be given to modifying and optimizing the existing catalysts to achieve improved reactivities and selectivies.

Systematic computational studies might play an important part by identifying the critical influencing factors, which might point to prospective candidates more rapidly instead of a trial and error approach. It is worth pointing out that although the prospect of metal-free hydrogenation is very appealing, the FLP catalysts are often inferior than the existing TM-catalysts. A possible solution lies in the design of heterogeneous versions of FLPs, which might eventually carry FLP catalysis from laboratory research to the domain of industrial applications. We hope that the results reported in this thesis will help FLP chemistry to move forward and eventually reach to its full potential.